Dynamic Properties of Fluids from Molecular Simulations and Entropy Scaling

Von der Fakultät Energie-, Verfahrens- und Biotechnik der
Universität Stuttgart und dem Stuttgart Center for
Simulation Science (SC SimTech) zur Erlangung der Würde eines
Doktor-Ingenieurs (Dr.–Ing.) genehmigte Abhandlung

Vorgelegt von
Matthias Fischer
aus Stuttgart

Hauptberichter: Prof. Dr.-Ing. Joachim Groß

Mitberichter: Prof. Dr.-Ing. habil. Jadran Vrabec

Tag der mündlichen Prüfung: 04. November 2022

Institut für Technische Thermodynamik und Thermische Verfahrenstechnik
Universität Stuttgart

2022

Sometimes science is a lot more art than science.
A lot of people don't get that.

Rick Sanchez
Earth Dimension C-137

Contents

Abstract

The design of most processes in chemical industry depends on reliable estimates of the transport properties of fluids. Various approaches exist for the prediction of these quantities, which can be used to compensate for insufficient experimental data. The present work deals with two of the approaches: *Molecular simulations* and *entropy scaling*. According to the latter approach, transport coefficients, such as shear viscosity, thermal conductivity or self diffusion coefficients, defined as dimensionless quantities using a suitable reference, are univariant functions of only the residual entropy of the fluid. The two methods, molecular simulations and entropy scaling are used jointly in order to achieve synergistic effects. A suitable mixture-model for entropy scaling models was investigated in molecular simulations as part of this work. Mixtures of simple model fluids, namely Lennard-Jones mixtures, are regarded and it is found that the principle of entropy scaling holds also for mixtures, to excellent approximation. Entropy scaling, in turn, is used to more efficiently design and evaluate molecular simulations. In this context, the *TAMie* force field developed in Stuttgart is assessed with respect to the accuracy of predicted transport coefficients. The *TAMie* model, like many other force fields developed for thermodynamic properties, uses rigid bond lengths between interaction sites within a molecule. In order to ensure a meaningful assessment of transport coefficients in Molecular Dynamic simulations, an analysis of bond-length models is conducted: what is the influence of the model for intramolecular atomic bonds on the predicted static and dynamic fluid properties? It is shown that it is possible to obtain the same results for transport coefficients with flexible atomic bonds, within statistical accuracy, as with the same force field but using a rigid description of the bonds. Within the context of the simulation studies carried out in this thesis, a workflow has been developed that enables efficient evaluation of simulations for determining transport properties. In combination with entropy scaling, this work presents a methodology that can be used to efficiently determine transport quantities from molecular simulations, thus enabling extensive simulation studies for either predicting fluid properties or to enable force field development where transport coefficients are considered in the objective function.

Kurzfassung

Für die Entwicklung und Auslegung der meisten Prozesse der chemischen Industrie ist die verlässliche Vorhersage der Transporteigenschaften von Fluiden eine unverzichtbare Grundvoraussetzung. Dafür gibt es verschiedene Ansätze, mit denen fehlende experimentelle Daten kompensiert werden können. Diese Arbeit behandelt zwei dieser Ansätze: *Molekularsimulationen* und die *Entropieskalierung*. Transportkoeffizienten, wie Scherviskosität, Wärmeleitfähigkeit und Selbstdiffusionskoeffizienten, sind nach dem Entropieskalierungsansatz univariante Funktionen einzig der residuellen Entropie des Fluids, sofern sie mit einer geeigneten Referenz als dimensionslose Größen definiert werden. Die beiden Methoden, Molekularsimulationen und Entropieskalierung, werden kombiniert eingesetzt um Synergieeffekte zu erzielen. So wird in dieser Arbeit ein geeignetes Mischungsmodell für Entropieskalierungsmodelle untersucht. Dafür wurden Gemische einfacher Modellflüssigkeiten, insbesondere Lennard-Jones-Gemische, in Molekularsimulationen betrachtet. Dabei zeigt sich, dass das Prinzip der Entropieskalierung in hervorragender Näherung auch für Gemische gilt. Die Entropieskalierung wird wiederum dafür genutzt, Molekularsimulationen effizienter zu gestalten und zu bewerten. Dabei wird das in Stuttgart entwickelte *TAMie* Kraftfeld hinsichtlich der Güte seiner Vorhersage von Transportkoeffizienten untersucht. Das *TAMie*-Modell verwendet – wie viele andere für die Bestimmung thermodynamischer Eigenschaften entwickelte Kraftfelder auch – starre Bindungslängen zwischen Wechselwirkungszentren innerhalb eines Moleküls. Um eine aussagekräftige Bewertung der Transportkoeffizienten in molekulardynamischen Simulationen zu gewährleisten, wird eine Analyse der Bindungslängenmodelle durchgeführt: Welchen Einfluss hat die Modellierung der intramolekularen Atombindungen auf die Vorhersage von statischen und dynamischen Fluideigenschaften? Es wird gezeigt, dass es möglich ist, mit flexiblen Atombindungen innerhalb statisticher Genauigkeit die gleichen Ergebnisse für Transportkoeffizienten zu erzielen, wie mit einer starren Beschreibung der Bindungen. Im Rahmen der für diese Arbeit durchgeführten Simulationsstudien wurde ein Workflow entwickelt, der eine effiziente Auswertung der Simulationen für die Bestimmung der Transportgrößen ermöglicht. In Kombination mit der Entropieskalierung wird in dieser Arbeit damit eine Methodik vorgestellt, mit der sehr effizient Transportgrößen aus Molekularsimulationen bestimmt werden können. Dies ermöglicht umfangreiche Simulationsstudien zur Vorhersage von Fuideigenschaften oder zur Kraftfeldentwicklung, bei der Transportkoeffizienten in der Zielfunktion berücksichtigt werden.

Journal publications

This thesis led to the following publications:

- Chapter 2: M. Fischer, G. Bauer, J. Gross: Force Fields with Fixed Bond Lengths and with Flexible Bond Lengths: Comparing Static and Dynamic Fluid Properties. *Journal of Chemical & Engineering Data*, **65**:1583-1593, 2020. doi:10.1021/acs.jced.9b01031
- Chapter 3: M. Fischer, G. Bauer, J. Gross: Transferable Anisotropic United-Atom Mie (TAMie) Force Field: Transport Properties from Equilibrium Molecular Dynamic Simulations. *Industrial & Engineering Chemistry Research*, **59**:8855-8869, 2020. doi:10.1021/acs.iecr.0c00848

The chapters 2 and 3 present literal quotes of the published work. Any addition with respect to the published work is marked. Any deletion is indicated with square brackets as "[...]". Cross-references between chapters of this thesis are added to the published version of the text to increase readability. The Supporting Information to the published work is presented in the Appendix of this thesis.

1 Introduction

Dynamic properties of gases and liquids are decisive for processes from the nanoscale, such as the folding of proteins[1,2] or the transport of drugs in cells[3,4], up to global scale phenomena, like for climate and weather.[5–7] Knowledge regarding dynamic properties is also crucial for the design and optimization of processes in engineering applications in chemical industry, like chemical reactions, distillation, and absorption. The present work focuses on this chemical engineering aspect, in particular on the dynamic properties of hydrocarbons as they are used in various chemical processes. Dynamic properties are needed for the optimization of already established processes in chemical industry.[8] Moreover, they are essential for the development of new technologies, such as the synthesis of climate-neutral fuels,[9–11] or the storage of the greenhouse gas CO_2.[12,13] The accurate prediction of dynamic properties furthermore enables the integrated design and optimization of processes and working fluids. This allows for already known processes, such as the Organic Rankine Cycle, to be operated more effectively.[14–16]

In this work I refer to shear viscosity, thermal conductivity and self-diffusion coefficients as *dynamic properties*. Shear viscosity and thermal conductivity are transport coefficients, i.e. they appear in constitutive (force-flux) equations as linear coefficients.[17] Self-diffusion is not a transport phenomenon driven by a driving force. It describes the averaged translocation of molecules per unit time due to thermal motion of molecules for a system in equilibrium.[18,19]

Transport coefficients act as the proportionality factors relating the thermodynamic driving forces to the flux densities.[17,20] These coefficients thus describe how a system responds to a small external disturbance, namely a perturbation out of equilibrium.[21] For small disturbances, the relation is linear and the proportionality of a given flux J towards the conjugate driving force, expressed as (negative) gradient ∇f, can be described in general terms by the equation[18–21]

$$J = -\gamma \nabla f. \tag{1.1}$$

Here, γ is the transport coefficient, which defines the proportional relation of flux and gradient. For some transport phenomena and their associated transport coefficient, eq. (1.1) reveals widely known relationships for mass, heat and momentum transport, summarized in table 1.1.[20] The flux equations listed here and discussed in this work are solely uncoupled

Table 1.1: Common constitutive (flux-force) equations

	Gradient	Flux	Transport Coefficient
Fourier's law $J_\mathrm{q} = -\lambda \frac{\partial T}{\partial x}$	T: temperature	J_q: heat flux	λ: thermal conductivity
Fick's law $J_i = -D \frac{\partial \rho_i}{\partial x}$	ρ_i: mass density of i	J_i: mass flux of i	D: diffusion coefficient
Newton's law $J_\mathrm{p}^{xy} = -\eta \frac{\partial v_x}{\partial y}$	$\boldsymbol{v}$: velocity	$\boldsymbol{J}_\mathrm{p}$: shear pressure tensor	η: shear viscosity

terms. Coupled fluxes are also possible.[20,22] One example is the Soret coefficient, which describes the transport of mass due to the temperature gradient. Even though several relevant applications can be found for the coupled coefficients,[20] they will not be subject of this work.

The thermal conductivity λ and the shear viscosity η are characteristic of pure substances and mixtures and as such they are content of this work. For the case of diffusion, I do not consider the Fickian diffusion coefficient shown in table 1.1, but the self-diffusion coefficient D_self. Self-diffusion describes the movement of a labeled molecule in the pure substance, in other words, the diffusion of a substance within itself.[18] Self-diffusion of course also occurs in mixtures. The corresponding coefficient is then sometimes referred to as tracer diffusion coefficient D_A^T of component A.[18] With known tracer diffusion coefficients, Maxwell-Stefan diffusion coefficients $Đ_\mathrm{AB}$ can be approximated[23] by approaches from Darken and Vignes.[18]

Once the transport coefficients are available, they can be used in force-flux equations within the balance equations for mass of each species, linear momentum and energy.[17] Or the transport coefficients can be used to predict the entropy production of a process.[20] Reliable and accurate knowledge of transport properties is therefore indispensible for the accurate prediction of dynamic processes, not only in the chemical industry.

This thesis deals specifically with the prediction of dynamic fluid properties from *molecular simulations* and from *entropy scaling*. Both methods can be used to predict η, λ, and D_self over a very wide range of temperatures and pressures (or densities) in both, the vapor and liquid phases, at state points for which no experimental data are available.[24–32] The challenges addressed in this thesis through means of molecular simulations and entropy scaling can be broadly condensed into three objectives:

1. Evaluation of the effects of specific force field properties on the results of molecular simulations of dynamic properties.

2. Development of methods for efficient calculation of transport coefficients from molecular simulations and the robust evaluation of results obtained with force fields adjusted exclusively to phase equilibria data.

3. Coupling of molecular simulations with the entropy scaling method to achieve synergy effects in order to minimize the simulation effort and to gain new insights for entropy scaling.

The following sections of chapter 1 are devoted to a brief introduction of the two central methods applied in this thesis: Section 1.1 gives an overview of the fundamentals of molecular simulations and classical force fields and presents the relevant methods and models used in this work. Section 1.2 describes how dynamic quantities can be determined from equilibrium molecular simulations. To conclude the introductory section, section 1.3 presents the basics of the entropy scaling correlation method.

1.1 Molecular Simulations & Force Fields

Statistical mechanics offers the possibility to determine macroscopic thermodynamic quantities (and the dynamic properties, as will be shown in the following sections) by averaging over microscopic states.[33] These molecular states are characterized by the positions of all N molecules ($\boldsymbol{r}_1, \boldsymbol{r}_2, \ldots, \boldsymbol{r}_N \equiv \boldsymbol{r}^N$) and their momenta ($\boldsymbol{p}_1, \boldsymbol{p}_2, \ldots, \boldsymbol{p}_N \equiv \boldsymbol{p}^N$).[21] For molecular fluids, $\boldsymbol{r}_1$ defines not only a (say) center of mass coordinate of molecule 1, but the entire configuration of that molecule. Analogously $\boldsymbol{p}^N$ defines all momenta, including the intramolecular contributions. $\boldsymbol{p}^N$ and $\boldsymbol{r}^N$ span the *phase space* in which microscopic states are defined. The average A of a state variable a can be determined as integrals over all positions and momenta via[34]

$$A = \langle a \rangle = \int a\left(\boldsymbol{r}^N, \boldsymbol{p}^N\right) P\left(\boldsymbol{r}^N, \boldsymbol{p}^N\right) \mathrm{d}\boldsymbol{p}^N \mathrm{d}\boldsymbol{r}^N \tag{1.2}$$

with the phase space density distribution function $P\left(\boldsymbol{r}^N, \boldsymbol{p}^N\right)$, which is the probability density of encountering the system with its molecules positioned in the configuration $\boldsymbol{r}^N$ with the molecules carrying momenta $\boldsymbol{p}^N$. The phase space density distribution function is related to the non-normalized phase space probability function $f\left(\boldsymbol{r}^N, \boldsymbol{p}^N\right)$ by[35]

$$P\left(\boldsymbol{r}^N, \boldsymbol{p}^N\right) = \frac{f\left(\boldsymbol{r}^N, \boldsymbol{p}^N\right)}{\int f\left(\boldsymbol{r}^N, \boldsymbol{p}^N\right) \mathrm{d}\boldsymbol{r}^N} \tag{1.3}$$

The integral in the denominator is the partition function, which is a measure of the total "number" of accessible microscopic states. It is a high-dimensional integral that cannot be solved directly for the applications considered in this work. Therefore, it is generally not possible to calculate the thermodynamic quantities analytically.

In the context of molecular simulations, eq. (1.2) thus rather describes the average value over occurring configurations in phase space. For this purpose, the integral in eq. (1.2) is approximated by a finite sum which allows us to determine averages of thermodynamic quantities without explicitly knowing the partition function. For generating the configurations to be averaged, molecular simulations provide two techniques to explore the phase space, both discussed in the following sections: *Monte Carlo* simulations (MC) and *Molecular Dynamics* simulations (MD). In both methods, macroscopic thermodynamic properties are determined by simulating a finite, managable number of molecules in a simulation volume. Bulk systems are emulated by ensuring the simulation volume is surrounded by infinite copies of itself using periodic boundary conditions (PBC). The interactions between the observed molecules are defined by *force fields*, which are addressed in the following section.

1.1.1 Classical Force Fields

In classical molecular simulations, force fields are used to describe interactions between atoms of a configuration $\boldsymbol{r}^N$. A force field defines a set of equations and parameters that is used to calculate the distinct contributions to the potential energy E_{pot} of a system. The potential energy is used in MC simulations to evaluate the acceptance criterion of a new configuration, while in MD the force acting on molecules ($\boldsymbol{F} = -\partial E_{\mathrm{pot}}/\partial \boldsymbol{r}^N$) is used to determine the time evolution of the system. The quality of simulation results depends heavily on the quality and suitability of the force field used, and hence the development and improvement of force fields is the subject of a great number of research efforts.[36–49] The field of applications ranges from relatively general to very specific. On one side of the spectrum are force fields designed for good transferability of parameters to different substances. Examples for transferable force fields are the AUA[36] force field, TraPPE,[37] and GROMOS.[38–41] On the other hand, there are force fields optimized precisely for a specific substance and even for the description of some peculiar substance quantities, such as specific protein solvents.[48]

In the present work, the Transferable Anisotropic United-Atom Mie Potential force field (*TAMie*) developed by Hemmen *et al.*,[42,43] Weidler and Gross,[44–46] and Baz *et al.*[47] is used to evaluate the potential energy. The force field uses an united-atom (UA) approach, in which hydrogen atoms are grouped together with larger atoms and treated as a single interaction site. For example, methyl (CH_3) and methylen (CH_2) groups are considered as single interaction

sites, which significantly reduces the computational effort while yielding good predictions. TAMie is an anisotropic force field, because the bond length between the methylen and the methyl end groups of the hydrocarbon molecules is increased by Δl.

Like other common force fields, TAMie calculates E_{pot} as a sum of various contributions to the potential energy of a system as[50]

$$E_{\mathrm{pot}}(\boldsymbol{r}^N) = E_{\mathrm{VdW}}(\boldsymbol{r}^N) + E_{\mathrm{charge}}(\boldsymbol{r}^N) + E_{\mathrm{bond}}(\boldsymbol{r}^N) + E_{\mathrm{bend}}(\boldsymbol{r}^N) + E_{\mathrm{torsion}}(\boldsymbol{r}^N) \tag{1.4}$$

The contributions can be broken down into two categories. The Van-der-Waals interactions E_{VdW} and the Coulombic interactions E_{charge} characterize the *nonbonded* interactions between atoms of different molecules and between atoms of the same molecule that are sufficiently far apart. The *covalent* terms describe the intramolecular contributions due to stretching of bond lengths E_{bond}, bond angles E_{bend}, and torsion angles E_{torsion}. In the case of the TAMie force field, the individual energy contributions are calculated as[44]

$$\begin{aligned} E_{\mathrm{pot}}(\boldsymbol{r}^N) = & \underbrace{\sum_{\text{pairs } i,j} c_{ij}\varepsilon_{ij}\left[\left(\frac{\sigma_{ij}}{r_{ij}}\right)^{n_{ij}} - \left(\frac{\sigma_{ij}}{r_{ij}}\right)^{6}\right]}_{E_{\mathrm{VdW}}} + \underbrace{\sum_{\text{pairs } i,j} \frac{q_i q_j}{4\pi\epsilon_0 r_{ij}}}_{E_{\mathrm{charge}}} \\ & + \underbrace{\sum_{\text{bonds}} k^{1}_{ij}\left(r_{ij} - r^{0}_{ij}\right)^2}_{E_{\mathrm{bond}}} + \underbrace{\sum_{\text{angles}} \frac{k^{\theta}_{ijk}}{2}\left(\theta_{ijk} - \theta^{0}_{ijk}\right)^2}_{E_{\mathrm{bend}}} \\ & + \underbrace{\sum_{\text{prop. dih.}} \sum_{n=0}^{3} c_{n,ijkl}\left[1 + d_{n,ijkl}\cos\left(n\phi_{ijkl}\right)\right] + \sum_{\text{imp. dih.}} \frac{d^{0}_{ijkl}}{2}\left(\phi_{ijkl} - \phi^{0}_{ijkl}\right)^2}_{E_{\mathrm{torsion}}} \end{aligned} \tag{1.5}$$

where $r_{ij} = \left|\boldsymbol{r}_j - \boldsymbol{r}_i\right|$ is the distance between two interaction sites i and j, located at position $\boldsymbol{r}_i$ and $\boldsymbol{r}_j$, respectively.

The Mie-n-6 potential given in eq. (1.5) that is used to describe E_{VdW} in the TAMie force field is defined by the energy parameter ε_{ij}, a size parameter σ_{ij}, and the exponent n_{ij}. The parameters of interactions between different types of UA centers are calculated via Lorentz-Berthelot rules.[51,52] Furthermore, an additional cross-interaction parameter k_{ij} can be introduced for mixtures.[46] A more detailed description of the potential and the calculated prefactor c_{ij} will be given in a later chapter. Electrostatic interactions are modelled as Coulomb interactions by placing point charges q_i, q_j on the centers of the VdW interactions or as additional off-center sites, where q_i is a fixed point charge (given as a factor of the electron charge) and ϵ_0 is the dielectric constant in vacuum. Applying multiple charges effectively leads

to multipole interactions. That way, dipole-dipole and quadrupole-quadrupole interactions can also be modeled using point charges.

The covalent terms in eq. (1.5) assign energy penalties for the displacements in distance (E_{bond}) and angle (E_{bend}) between bound interaction sites from a defined bond length r_{ij}^0 by r_{ij}, or from a defined angle θ_{ijk}^0 by the angle θ_{ijk}. The energy that results from torsion of dihedral angles ϕ_{ijk} between i, j, k, and l also adds to this contribution. The magnitude of the intramolecular contributions to the potential energy is defined by the respective force constants k_{ij}^{l}, k_{ijk}^{θ}, $c_{n,ijkl}$, and d_{ijkl}^0.

The force field parameters of the intramolecular potentials, namely equilibrium values and force constants, are typically determined either from experimental data or from quantum mechanics calculations.[53–56] For a number of reasons, many force fields use certain length or angle constraints.[57,58] Also the original version of TAMie uses fixed bond lengths between neighboring interaction sites $i-j$, instead of a harmonic potential $k_{ij}^{\text{l}}\left(r_{ij}-r_{ij}^0\right)^2$, as in eq. (1.5). Fixed bond lengths can be justified in certain cases[35] and are convenient in Monte Carlo simulations, but also in molecular dynamics simulations, because the high-frequency vibrations of typical interatomic bond-lengths then do not have to be resolved numerically.[59–61] Consequently, for rigid bond lengths, the time step can be significantly increased, enabling longer simulation times. At the same time, the bond length vibrations do not significantly contribute to many physical properties.[35]

However, there are downsides when using constant bond lengths, that can be subtle. The averages obtained in a system with rigid bonds are different from those obtained in a system of infinitely strong but non-rigid bonds.[21] For the heat capacity c_{v}, as well as for the thermal conductivity λ, vibrational contributions have to be considered and hence correction terms have to be introduced to "correct" for rigid bonds.[33,62] Furthermore, modifying parts of the intramolecular interactions can significantly change the dynamic properties of a fluid.[63–65] It is difficult to predict how or to which degree individual parameters influence these properties. For some substances, such as water, the influence of, for example, bond flexibility on static and dynamic properties has been investigated.[66,67] Other studies show, that the parameterization of the torsional energy contribution E_{torsion} has a strong influence on the viscosity without affecting other properties, such as the VLE.[68]

Several questions addressed in this thesis concern force fields and the influence of their parameters on dynamic properties. Chapter 2 investigates the influence of bond strength (defined by k_{ij}^{l}) on the transport quantities for various hydrocarbons and answers the question whether simulations with rigid and flexible bond lengths yield sufficiently similar results within typical statistical uncertainty. Chapter 3 considers the TAMie force field and addresses the

question: How well can a force field predict transport properties of fluids, whose parameters were fitted solely to VLE data (vapor pressure and liquid density), with no information on dynamic properties included in the optimization process? In chapter 4, simulations of simple model fluids are used to assess the concept of entropy scaling for mixtures. The force fields of the atomic Lennard-Jones fluids used in this study feature only a comparably small number of parameters, allowing the influence of individual parameters on the properties of the mixtures to be thoroughly investigated. In order to answer such questions, this work employs force fields in molecular simulations of both techniques, MC and MD, which are therefore briefly outlined in the following section.

1.1.2 Molecular Simulations

The historically earlier molecular simulation method is the **Monte Carlo** method, which was proposed by Metropolis *et al.*[69] The method uses *importance sampling*, to generate configurations according to the probability of their occurrence $P\left(\boldsymbol{r}^N\right)$ by stepping through phase space in distinct moves.[35] This allows the ensemble averages A of a macroscopic quantity a of the system to be calculated simply by averaging over the sampled values of a for all moves.[34]

$$A = \langle a \rangle = \frac{1}{N_{\text{moves}}} \sum_{i=1}^{N_{\text{moves}}} a_i \tag{1.6}$$

In simulations in the canonical ensemble – the one natural to MC – each move is a displacement of one or more arbitrary atoms to a random new position according to the principle of importance sampling.[34] The MC simulations in this work are performed in the grand canonical ensemble. Such simulations, at constant μ, V, and T, are realized by introducing deletion and insertion of molecules as additional moves besides the displacement moves.[35] Grand canonical MC simulations (GCMC) provide efficient methods for determining vapor-liquid equilibria (VLE) via molecular simulations,[42,70] which are also used in this work and will be therefore introduced in chapter 4. Mainly, however, GCMC simulations are used in this work to determine entropy values along isotherms via the Gibbs equation, as described in section 4.2.3. Here, only a single GCMC simulation is needed at each temperature. The entropy at different pressures along the isotherm is then determined via histogram reweighting, which significantly reduces the computational effort.[71] As such, Monte Carlo simulations and histogram reweighting provide us with very efficient methods for the determination of static thermodynamic quantities.

However, if one is interested in dynamic properties, like viscosity, thermal conductivity, or

diffusion, one must rely on **Molecular Dynamics** simulations, in which a system is allowed to evolve in time. In this method, the motion of molecules in the system is estimated along a temporal trajectory by integrating Newton's equation of motion.[35] In a simulation at constant number of molecules, volume and energy (NVE), the trajectory thereby conserves the Hamiltonian $\mathcal{H}$, being the operator describing the total energy of the system (potential energy E_{pot} and kinetic energy E_{kin}) as a function of the phase space variables $\boldsymbol{r}^N$ and $\boldsymbol{p}^N$.[34]

$$\mathcal{H}\left(\boldsymbol{r}^N, \boldsymbol{p}^N\right) = E_{\text{kin}}\left(\boldsymbol{p}^N\right) + E_{\text{pot}}\left(\boldsymbol{r}^N\right) \tag{1.7}$$

For a Hamiltonian system in cartesian coordinates the following relations, known as Hamilton's equations of motion, apply.[21]

$$\dot{\boldsymbol{r}}^N = \frac{\partial \mathcal{H}}{\partial \boldsymbol{p}^N} = \frac{\boldsymbol{p}^N}{m} \tag{1.8}$$

$$\dot{\boldsymbol{p}}^N = -\frac{\partial \mathcal{H}}{\partial \boldsymbol{r}^N} = -\frac{\partial E_{\text{pot}}(\boldsymbol{r}^N)}{\partial \boldsymbol{r}^N} = \boldsymbol{F}\left(\boldsymbol{r}^N\right) \tag{1.9}$$

where $\boldsymbol{F}$ is the vector of forces on each molecule of a system with the configuration $\boldsymbol{r}^N$. The dots above $\dot{\boldsymbol{r}}^N$ and $\dot{\boldsymbol{p}}^N$ symbolize the time derivative of the respective quantity.

Thermodynamic properties can be determined directly from the time integration of these equations of motion as an average over the time trajectories of the sampled quantities.[35] Yet there are several details that must be taken into account when simulating in order to ensure reliable results.[31,72] For instance, the algorithm used for time integration and the applied time step size may affect the result of a simulation.[73] In order to perform MD simulations at constant temperature or pressure, a thermostat or barostat, respectively, is required.[34] Selecting an unsuitable method for this purpose can lead to incorrect results, especially when investigating dynamic properties.[74] When determining dynamic properties in MD simulations, there are generally some additional caveats to consider compared to static quantities. For example, in order to determine transport coefficients, either the equations of motion have to be extended or additional quantities have to be sampled and processed.[21,31] Being a central subject of this thesis, the following chapter will introduce in more detail the specifics of determining dynamic coefficients via molecular simulations.

1.2 Dynamic Properties from Molecular Dynamics

Two general approaches are possible for determining transport coefficients using molecular simulations, both of which are MD methods. In addition to the equilibrium MD simulations

already introduced in section 1.1, an alternative technique are non-equilibrium MD simulations (NEMD), which will be regarded first.

1.2.1 Non-Equilibrium Molecular Dynamics

The NEMD approach appears to be the more intuitive one, since the transport properties are determined in a way comparable to related experiments.[21] A gradient is induced on the system and the corresponding transport quantity can be determined from the response of the system to this perturbation of the equilibrium. For this purpose, in the computer experiment, the equations of motion (eqs. (1.8) and (1.9)) are extended, as[21]

$$\dot{\boldsymbol{r}} = \frac{\partial \mathcal{H}}{\partial \boldsymbol{p}} + C(\boldsymbol{r},\boldsymbol{p})\,F_e(t) \tag{1.10}$$

$$\dot{\boldsymbol{p}} = -\frac{\partial \mathcal{H}}{\partial \boldsymbol{r}} + D(\boldsymbol{r},\boldsymbol{p})\,F_e(t) \tag{1.11}$$

$F_e(t)$ is a time-dependent driving force, $C(\boldsymbol{r},\boldsymbol{p})$ and $D(\boldsymbol{r},\boldsymbol{p})$ are functions of the phase space, which are specified by the respective perturbation.

Taking the example of the viscosity of a Couette flow in the x direction, this yields a set of equations of motion known as the SLLOD algorithm.[75]

$$\dot{\boldsymbol{r}} = \boldsymbol{p}/m + \gamma_{yx}\left(\boldsymbol{r}\cdot\bar{\boldsymbol{e}}_y\right)\bar{\boldsymbol{e}}_x \tag{1.12}$$

$$\dot{\boldsymbol{p}} = \boldsymbol{F} - \gamma_{yx}\left(\boldsymbol{p}\cdot\bar{\boldsymbol{e}}_y\right)\bar{\boldsymbol{e}}_x \tag{1.13}$$

Here, $\bar{\boldsymbol{e}}_\alpha$ with $\alpha = x,y,z$ is the unit vector in α direction and γ_{yx} is the shear rate $\frac{\partial v_x}{\partial y} = \gamma_{yx}$, the change in the velocity in y direction (orthogonal to the direction of the flow). The systems response can be determined, manifesting as response of the non-diagonal entries of the pressure tensor J_{p}^{xy}. Using with Newton's shear law from table 1.1, the viscosity can be obtained as[34]

$$\eta = -\lim_{t\to\infty} \frac{\left\langle J_{\mathrm{p}}^{xy}\right\rangle_t}{\gamma_{yx}} \tag{1.14}$$

The non-equilibrium average $\left\langle J_{\mathrm{p}}^{xy}\right\rangle_t$ can be determined as the time average of a trajectory following the equations of motion according to eqs. (1.12) and (1.13). It is necessary to apply certain specific periodic boundary conditions that take into account both the deformation of the simulation box due to shear, as well as the flow.[76] Moreover, high shear rates are required to ensure a low noise-to-signal ratio. To reach the viscosity at the shear rate of interest (often

the viscosity at $\gamma_{yx} = 0$) it is necessary to extrapolate from several simulations at different γ_{yx}.[77] Furthermore, since the perturbation of the equations of motion introduces energy into the system from external sources, a thermostat must be used in this case for NEMD simulation.[78]

Some of the problems mentioned are overcome by a different non-equilibrium method, the Reverse NEMD (RNEMD).[78,79] In this approach, cause and effect are interchanged. A flux is artificially created in the system, which results in a gradient in the simulated system. In the example of viscosity, a momentum flux is applied by swapping the velocities of two particles by a Maxwell daemon. For this purpose, the simulation box is divided into slices in the y direction. The daemon now regularly exchanges the velocities of two particles with opposed velocities, which are located in two slices that are half a box length apart. This way, momentum is transferred artificially, which results in a physical momentum flux that compensates for this disturbance. A linear velocity profile evolves in the system in y direction, from which the viscosity can be determined. RNEMD generally converges comparatively well[80] and is considered to conserve energy, so no (or only a very weak) thermostat has to be used. Moreover, ordinary periodic boundary conditions can be applied. For high momentum fluxes, nonlinear velocity profiles are exhibited, leading to incorrect values for η.

A drawback – which RNEMD has in common with other NEMD methods – is that a dedicated flux (or driving force) has to be applied for any transport coefficient. Besides the viscosity shown above, thermal conductivity and diffusion can also be calculated via NEMD using the appropriate $C(\boldsymbol{r}, \boldsymbol{p})$, $D(\boldsymbol{r}, \boldsymbol{p})$ and $F_e(t)$ terms in eqs. (1.10) and (1.11). This is where the equilibrium approach for determining the transport properties in MD has a strong advantage: The method determines the transport coefficients from equilibrium simulations and can thus calculate all coefficients simultaneously.

1.2.2 Transport Coefficients from Equilibrium MD Simulations

Along with the NEMD methods shown, dynamic quantities such as the transport coefficients can also be determined in simulations in the equilibrium ensemble in which no perturbations are imposed. The method is based on the fact that all the information about the response of a system to a perturbation is contained in the *equilibrium time correlation function* (TCF), which can be determined in equilibrium simulations. The origin of the TCF, as well as its relation to the dynamic properties, will be briefly presented in this section. The argumentation follows a chapter of the text book by Tuckerman,[21] where the interested reader can find a more detailed derivation.

The initial point for the derivation is – as for NEMD – the perturbed equations of motion, shown in eqs. (1.10) and (1.11). At this point, we assume just a small perturbation from equilibrium, so that the driving forces lead only to a small perturbation of Hamilton's equations. For the time-dependent phase space density distribution function of the non-equilibrium ensemble a perturbation approach can then be applied as

$$P(\chi, t) = P_0(\mathcal{H}(\chi)) + \Delta P(\chi, t) \tag{1.15}$$

where χ abbreviates the phase space vector $\chi = (\boldsymbol{r}, \boldsymbol{p})$ for a more compact notation. P_0 describes the equilibrium phase space density distribution function as a function of the Hamiltonian $\mathcal{H}(\chi)$ of the undisturbed system; $\Delta P(\chi, t)$ denotes the time-dependent perturbation. For the average of an arbitrary phase space function $a(\chi)$ this perturbation approach yields

$$\langle a \rangle_t = \int a(\chi) P(\chi, t) \, \mathrm{d}\chi \tag{1.16}$$

$$= \int a(\chi) P_0(\mathcal{H}(\chi)) \, \mathrm{d}\chi + \int a(\chi) \Delta P(\chi, t) \, \mathrm{d}\chi \tag{1.17}$$

$$= \langle a \rangle + \int a(\chi) \Delta P(\chi, t) \, \mathrm{d}\chi \tag{1.18}$$

$\langle a \rangle_t$ is the average in the non-equilibrium ensemble and corresponds to the time-dependent macroscopic quantity $A(t)$, whereas $\langle a \rangle$ is the average of $a(\chi)$ in equilibrium (see eq. (1.2)). Since the disturbance of the system due to the driving force is assumed to be small, the perturbation term can be linearized. This approach is the basis of the linear response theory, which allows to solve the Liouville equation of the system. As result, the following equation is obtained for $\langle a \rangle_t$.

$$\langle a \rangle_t = \langle a \rangle - \beta \int_0^t F_e(s) \, \mathrm{d}s \int P_0(\mathcal{H}(\chi)) \, a(\chi_{t-s}(\chi)) \, j(\chi) \, \mathrm{d}\chi \tag{1.19}$$

The integration over the time variable s in eq. (1.19) originates from the solution of the Liouville equation. $F_e(s)$ is the driving force from eqs. (1.10) and (1.11) with respect to the time s. Equation (1.19) further introduces the *dissipative flux* $j(\chi)$, which is defined by the equation

$$j(\chi) = -\sum_{i=1}^{3N} \left[D_i(\chi) \frac{\partial \mathcal{H}}{\partial \boldsymbol{p}_i} + C_i(\chi) \frac{\partial \mathcal{H}}{\partial \boldsymbol{r}_i} \right] \tag{1.20}$$

Also note, that for eq. (1.19) the system is assumed to be in equilibrium by time $t \leq 0$. So the

driving forces are zero for $t < 0$, giving also $\Delta P(\chi, t = 0) = 0$ and $\langle a \rangle_{t=0} = \langle a \rangle$.

For the second integral in eq. (1.19), Tuckerman gives a quite accessible interpretation:[21] Each point χ in the phase space is considered as a starting point. The system is then allowed to evolve from this point for a time $t - s$ according to Hamilton's equations of motion. After this time a new point in the phase space is reached: χ_{t-s}. As a solution of Hamilton's equations of motion, χ_{t-s} depends solely on the respective starting point χ, which is why it is denoted as $\chi_{t-s}(\chi)$ in eq. (1.19). The integral has the form of an average, similar to that in eq. (1.2). It corresponds to the average of $a(\chi_{t-s}(\chi))\, j(\chi)$ over all possible initial conditions, with respect to the phase space density distribution function of the unperturbed ensemble $P_0(\mathcal{H}(\chi))$. The resulting average is multiplied with $F_e(s)$. s is then integrated from 0 to t to obtain the time-dependent non-equilibrium average of a at time t: $\langle a \rangle_t = A(t)$.

It is noteworthy at this point that, with eq. (1.19), it is possible to determine the non-equilibrium-average, exclusively via averages of the equilibrium ensemble, characterized by $P_0(\mathcal{H}(\chi))$. The average value calculated in the second part of eq. (1.19) is the aforementioned *equilibrium time correlation function* (TACF). By expressing the equilibrium TACF as an average, eq. (1.19) can be rewritten.

$$A(t) = \langle a \rangle_t = \langle a \rangle - \beta \int_0^t F_e(s) \langle a(t-s)\, j(0) \rangle \, \mathrm{d}s \tag{1.21}$$

All quantities in this equation – the equilibrium average $\langle a \rangle$, just as the quantities in the TACF – can be sampled in an equilibrium MD simulation. In order to be able to calculate the transport quantities via TACFs, the respective perturbation terms F_e, $C(\chi)$ and $D(\chi)$ still have to be identified. They can be expressed in quantities that are captured during the simulation. Using the example of viscosity, this step will be illustrated in the following.

The perturbed equations of motion of a Couette flow in the x direction (eqs. (1.12) and (1.13)) again serve as a basis. By comparison with the unperturbed equations of motion (eqs. (1.8) and (1.9)) and the extended form of the equations of motion from eqs. (1.10) and (1.11), C and D can be identified as

$$C(\boldsymbol{r}, \boldsymbol{p}) = \gamma_{yx} \left(\boldsymbol{r} \cdot \bar{\boldsymbol{e}}_y \right) \bar{\boldsymbol{e}}_x \tag{1.22}$$

$$D(\boldsymbol{r}, \boldsymbol{p}) = \gamma_{yx} \left(\boldsymbol{p} \cdot \bar{\boldsymbol{e}}_y \right) \bar{\boldsymbol{e}}_x \tag{1.23}$$

with a resulting value of $F_e(t) = 1$. As a matter of that, the dissipative flux is calculated as

$$\begin{aligned} j(\chi) = j(\boldsymbol{r},\boldsymbol{p}) &= \sum_{i=1}^{3N}\left[C_i(\boldsymbol{r},\boldsymbol{p})\,\boldsymbol{F}_i - D_i(\boldsymbol{r},\boldsymbol{p})\,\frac{\boldsymbol{p}_i}{m_i}\right] \\ &= \gamma_{yx}\sum_{i=1}^{3N}\left[\left(\boldsymbol{r}\cdot\bar{\boldsymbol{e}}_y\right)\left(\bar{\boldsymbol{e}}_x\cdot\boldsymbol{F}_i\right) + \left(\boldsymbol{p}\cdot\bar{\boldsymbol{e}}_y\right)\left(\bar{\boldsymbol{e}}_x\cdot\frac{\boldsymbol{p}_i}{m_i}\right)\right] \\ &= \gamma_{yx} V J_{\mathrm{p}}^{xy} \end{aligned} \tag{1.24}$$

with J_{p}^{xy} as a non-diagonal entry of the instantaneous pressure tensor

$$\boldsymbol{J}_{\mathrm{p}}(\boldsymbol{r},\boldsymbol{p}) = \frac{1}{3V}\sum_{i=1}^{N}\left[\frac{\boldsymbol{p}_i^2}{m_i} + \boldsymbol{r}_i\cdot\boldsymbol{F}_i\right] \tag{1.25}$$

As a result, the non-equilibrium-average of the non-diagonal entry of the pressure tensor $\left\langle J_{\mathrm{p}}^{xy}\right\rangle_t$ can be calculated according to eq. (1.21) as

$$\left\langle J_{\mathrm{p}}^{xy}\right\rangle_t = \left\langle J_{\mathrm{p}}^{xy}\right\rangle - \beta\gamma_{yx}V\int_0^t \left\langle J_{\mathrm{p}}^{xy}(0)\,J_{\mathrm{p}}^{xy}(t-s)\right\rangle \mathrm{d}s \tag{1.26}$$

With the definition of viscosity from eq. (1.14) as $\eta = -\lim_{t\to\infty}\left\langle J_{\mathrm{p}}^{xy}\right\rangle_t/\gamma_{yx}$ and the fact that $\left\langle J_{\mathrm{p}}^{xy}\right\rangle$ equals zero according to the virial theorem, one obtains the famous Green-Kubo[81,82] equation for viscosity

$$\eta = \beta V\int_0^\infty \left\langle J_{\mathrm{p}}^{xy}(0)\,J_{\mathrm{p}}^{xy}(\tau)\right\rangle \mathrm{d}\tau \tag{1.27}$$

introducing a change of variables $\tau = t - s$ into the integral. The Green-Kubo equations can also be derived for thermal conductivity and self-diffusion. The corresponding quantities of the TACF are the heat flux J_{q} for λ and the velocities of the particles $\boldsymbol{v}_i$ for $D_{\text{self, i}}$.

According to Onsager's regression hypothesis, any TACF decays to zero after a sufficiently long time.[83] Thus, essentially constant values for the transport coefficients of a fluid with low molecular mass can be determined from finite integration times in eq. (1.21). How long the decay time (correlation time) actually is, in the specific case, depends strongly on the nature of the system under study. In most cases considered in this work, the TACF decayed to zero after only a few simulation time steps. When using the Green-Kubo equations, it is crucial to record the required values for the TACF (i.e., J_{p}^{xy}, J_{q}, and $\boldsymbol{v}_i$) at a high frequency, because

the values at very small times τ substantially contribute to the value of the integral of the autocorrelation function, eq. (1.27). For higher values of τ, the noise-to-signal ratio of the TACF becomes significantly worse. Accordingly, for the evaluation of the Green-Kubo integrals, it is necessary to balance between selecting an integration time τ_{max} that is long enough to ensure that the TACF has decayed while still providing good statistics for the integral.

Associated with each Green-Kubo equation is a corresponding Einstein relation, into which the long-time behavior of the trajectories enters, in contrast to the short correlation times which are relevant for the Green-Kubo equations. Green-Kubo and Einstein relation can be straightforwardly transformed into each other.[34] In the present work, the diffusion coefficient is determined from an Einstein relation that calculates D_{self} from the Mean Squared Displacement (MSD) of the molecule center of mass, according to[35]

$$D_{\mathrm{self}} = \frac{1}{6N} \lim_{\tau \to \infty} \frac{\mathrm{d}}{\mathrm{d}\tau} \sum_{i=1}^{N} \left\langle |\boldsymbol{r}_i(\tau) - \boldsymbol{r}_i(0)|^2 \right\rangle \tag{1.28}$$

We use the Einstein equation instead of the velocity autocorrelation function in this case as it only requires storing the positions of the molecules at comparatively large time intervals and does not require additional sampling of the molecule velocities at high frequency.

In general, the Green-Kubo and Einstein relations shown here can be used to determine dynamic properties from quantities that can be sampled in ordinary equilibrium MD simulations. This is where the advantages of this method over NEMD methods become apparent. The equations of motion do not need to be modified, no special periodic boundary conditions need to be applied, and no (additional) thermostating is required. And most significantly, all three transport coefficients can be determined from one and the same simulation, which reduces the simulation effort. The evaluation of the dynamic properties can be done in post-processing; in fact, the simulation is independent of the evaluation of the coefficients – as long as the required quantities are recorded at a sufficiently high frequency during the simulation. A particular challenge in post-processing lies in a statistically optimized analysis of the data in order to improve the noise-to-signal ratio, which has long been considered the major weakness in the determination of transport properties from EMD simulations.[84] There have been advancements in this field in recent years, and new algorithms have been developed to efficiently compute the TACF and to improve and accurately quantify statistical uncertainties. Some examples of such techniques, such as the moving window algorithm,[85] the time decomposition method,[86] and bootstrapping methods for determining error bars are collected in the Best Practice Paper for Computing η and D_{self} with EMD by Maginn *et al.*,[31] which gives a highly recommended overview of the subject. The best statistics at the highest efficiency can be achieved by computing the TACF using the Fast Fourier Transform

(FFT) algorithm.[21] Here, the TACF are computed as convolutions in Fourier space and are subsequently transformed back. No data is omitted in the process and the calculation is performed in a fraction of the time required by conventional algorithms, while at the same time, requiring comparatively little memory resources.

One goal of the present work is to build an efficient framework for robust determination of transport coefficients from EMD simulations. It addresses both, optimal post-processing and the rigorous setup of simulation sets. By combining Fast Fourier Transform algorithms with best-practice methods, I have developed a workflow that allows – especially in combination with the entropy scaling methods that will be introduced in section 1.3 – to determine dynamic properties over a wide range of states easily and in a comparably short time. A detailed description of the workflow and techniques used can be found in chapters 2 and 3 of this work.

1.3 Entropy Scaling

In determining transport properties, the present thesis is not limited to molecular simulations alone. The goal of this work is to combine simulations with the entropy scaling method in various ways in order to achieve synergy effects on multiple levels.

Entropy scaling is a semi-empirical correlation approach by which transport properties can be determined based on the residual entropy s_{res} of a given state defined by ρ and T. The residual entropy is the entropy minus the entropy of an ideal gas at the same temperature T and density ρ, as

$$s_{\mathrm{res}}(T,\rho) = s(T,\rho) - s_{\mathrm{id.\,gas}}(T,\rho) \tag{1.29}$$

The connection between s_{res} and dynamic properties was discovered and first researched by Yaakov Rosenfeld already in the 1970s.[87] However, the method received little attention until it was brought back into spotlight by a study by Dzugutov[88] published in Nature in 1996. Without providing a complete physical derivation, Rosenfeld's original article was the first to describe a monovariable relationship between excess entropy and a transport property $\zeta = (\eta, \lambda, D_{\mathrm{self}})$ in reduced form $\zeta^{\#}$, i.e. the property divided by a 'reference' property. Rosenfeld initially demonstrated the principle only for viscosity and diffusion; it was later applied to thermal conductivity as well.[89] Rosenfeld's investigations included model fluids based on Lennard-Jones and hard sphere potentials, whose dynamic properties were determined in molecular simulations. Subsequent work on entropy scaling also continued using molecular simulations

to demonstrate the applicability of the principle.[25,90–92] Thus, entropy scaling has historically been closely related to molecular simulation.

The rather involved property behavior of transport coefficients for varying state variables, such as temperature and pressure, makes the development of engineering correlations difficult – especially across phase boundaries. Using Rosenfled's approach, transport coefficients can be described as a function of a single state variable as

$$\zeta^{\#}(T,\rho) = \frac{\zeta(T,\rho)}{\zeta^{\mathrm{ref}}(T,\rho)} = \zeta^{\#}(s_{\mathrm{res}}(T,\rho)) \tag{1.30}$$

where $\zeta^{\mathrm{ref}}(T,\rho)$ stands for a suitable reference for each specific transport coefficient, which is used to obtain a dimensionless property. Several approaches using different references can be found in literature, which yield more or less satisfactory results. Rosenfeld's original approach was to define ζ^{ref} in such a way that $\zeta^{\#}$ becomes dimensionless, using combinations of thermodynamic quantities and constants, such as ρ, T, k_{B}. Towards the low-density limit (for which eq. (1.29) gives $s_{\mathrm{res}} \to 0$), this approach, however, leads to a diverging increase of $\zeta^{\#}$ for gases.[24] This behavior can be avoided for η and D_{self} by using the Chapman-Enskog approximation as a reference – a first-order approximation of the Boltzmann-equation, as proposed by Novak[93] and Lötgering-Lin and Gross,[24] as well as Hopp *et al.*[26] for self-diffusion. The new reference leads to finite values at the low density limit and a simple parameterization of correlation functions.

In recent years, entropy scaling has received increased attention, partly in connection with the *isomorph theory*, giving a lead for the physical derivation of the entropy scaling approach. The theory, developed by the *Glass & Time* group from Roskilde, describes the occurrence of special lines in the thermodynamic state space, so-called *isomorphs*. Isomorphs occur in fluids whose fluctuations in energy U and virial W (from the virial equation $pV = \frac{N}{\beta} + W$) are strongly correlated. Fluids with a correlation factor of $R = \frac{\langle \Delta W \Delta U \rangle}{\sqrt{\langle \Delta W^2 \rangle \langle \Delta U^2 \rangle}} > 0.9$ are called *Roskilde fluids*[94] and can be characterized by some interesting behaviors and invariants of structural, thermodynamic and dynamic properties, which hold along an isomorph I.[95] For example, the radial pair distribution function in reduced coordinates $\tilde{g}(\tilde{r})$ does not change along isomorph I.[94] The isomorph can thereby cover states of different pressures, temperatures and densities. Another fascinating phenomenon is the aging behavior of a system along an isomorph I. After a jump from an equilibrated state point on the isomorph to another state on the same isomorph (for example in a molecular simulation), the system is *instantaneously* back in equilibrium. Isomorphs thus can be thought of as *"wormholes in phase space"*.[95]

In the context of entropy scaling, though, the following two invariants are most interesting:

Both, the residual entropy and the TACF are considered constant in reduced coordinates along isomorph I.[94,96] From the immediate relationship between transport coefficients and the TACF as used in the Green-Kubo relations (see, e.g., eq. (1.27) for viscosity), it can be deduced that the reduced transport coefficients are also constant along isomorph I.[97] That means, that entropy scaling holds along isomorphs. Consequently, a number of studies of entropy scaling have already been carried out from the perspective of isomorph theory.[98] For the isomorph theory, model fluids have been extensively studied by means of molecular simulations.[97–100] Instead of a reference, dimensionless transport coefficients are usually considered directly in this context, similar to those also used in this work in chapter 4 (see table 4.1).

However, entropy scaling is not only applicable to Roskilde fluids. Monovariable correlation of transport coefficients and s_{res} also occurs for fluids and state points where ΔU and ΔW are not correlated. Therefore the isomorph theory does not give a conclusive derivation for entropy scaling.

Although the fundamental physical derivation for entropy scaling has not yet been uncovered – what speaks for the approach is that it works very convincingly in application and provides a powerful engineering tool. Beyond model fluids and proofs of concepts, entropy scaling can be used for real fluids and applications in industrial practice.[14–16] With a suitable choice of reference fluid, the monovariable profile of a reduced transport coefficient over residual entropy $\ln\left(\zeta^{\#}\left(s_{\mathrm{res}}\right)\right)$ is so benign that a simple correlation function can be adjusted to match it. In the simplest case, for shear viscosity, even a linear Ansatz function can give good results. Once the correlation function and its parameters are determined, the corresponding transport coefficient is accessible for any state point for which the residual entropy is known.

In this work, the entropy scaling variant developed in Stuttgart by members of the Thermodynamics group is used. Approaches for viscosity,[24,25] self-diffusion,[26] and thermal conductivity[27–29] have already been published and further research is ongoing. In the mentioned studies, an ideal gas approximation of the respective transport quantity (e.g., the mentioned CE viscosity[19] for $\eta^{\#}$ [25]) is chosen as reference, and entropies are determined from the PC-SAFT equation of state.[101] This choice ensures a great flexibility in terms of the range of substances and accessible state points. For all transport coefficients, correlations were adjusted to a rather extensive set of experiments, e.g. from the Dortmund database.[102] Using a PC-SAFT group contribution method (the GC-PC-SAFT[103]), it was possible to develop a group contribution method for entropy scaling of viscosity[24] and thermal conductivity,[27] which provides remarkable results, even for substances to which the method was not adapted in the first place. The excellent results of the method are not limited to pure substances. Using mixing rules for the parameters of the η correlations of the pure substances, the viscosity of their mixture can also be predicted in very good agreement with experiment, without adjusting

further parameters.[25] The Stuttgart entropy scaling variant reaches its limits, among others, for the viscosity of associating substances[25] and the diffusion coefficients in the gas phase[26], which in the latter case is due to the sparse data available. Apart from the fundamental question of an underlying physical theory, there is thus a need for further research in the field of applied entropy scaling.

In the present work, entropy scaling is combined with molecular simulations in several ways:

1. *The use of entropy scaling for selecting meaningful state points at which transport coefficients of real fluids are calculated from MD simulations.* For this purpose, the state points are chosen to be equidistant in residual entropy s_{res} based on the entropy scaling. Simulations at a few state points are then sufficient to allow the adjustment of a correlation function for the respective transport coefficient of the concidered force field. The correlation function can then be used to estimate the transport property of the force field for any other state point, provided s_{res} is known.

2. *The efficient assessment of the performance of a force field in the determination of transport coefficients.* By estimating the transport properties using a correlation from entropy scaling, associated to the force field (as described in point 1), the results of the simulations can be compared against all experimental data available. To do this, the corresponding transport coefficient of the force field's correlation is simply estimated at each state point where experiments are available. This avoids having to simulate at all experimental state points, and the comparison with a large number of data provides an assessment of the performance of the force field.

3. *The assessment and further development of entropy scaling for mixtures using results from molecular simulations for mixtures of simple model fluids as a reference.* For this purpose, mixtures of Lennard-Jones fluids are simulated, which differ only in one parameter of eq. (1.5). In this particular case, both, the transport coefficient and the entropy of the mixtures are determined from molecular simulations. Thus, GCMC simulations are used in addition to MD simulations.

On the one hand, molecular simulations are thus used to further explore and evaluate the entropy scaling method, as it has been done in studies since the beginning of the theory. On the other hand, entropy scaling is used vice versa to make molecular simulation of transport properties simpler and more efficient.

1.4 Outline of this Thesis

Chapter 2 investigates whether classical force fields with *rigid bond lengths* yield equivalent results (within statistical uncertainty) to models with *harmonic bond length* potentials that are identical in all other respects. Static and dynamic physical properties, namely pressure, viscosity, self-diffusion, and thermal conductivity of homogeneous phases, are analyzed under varying force constants of the harmonic bond length potentials for ethane, propane, and dimethyl ether described with the TAMie potential. The anticipated offset in the thermal conductivity of the force field with rigid bond lengths compared to the harmonic bond length models, is approximated by an analytical correction term. The study examines different time steps for solving the equations of motion, and investigates the question of whether an integrator that allows a separate, shorter time step for rather high frequency bond vibrations offers advantages over a simple velocity Verlet integrator.

Chapter 3 gives an assessment of the Transferable Anisotropic united-atom Mie (TAMie) force field for predicting dynamic properties. Equilibrium molecular dynamics simulations are used to calculate three dynamic properties ($\eta, D_{\text{self}}, \lambda$) in one MD simulation using the corresponding Green-Kubo methods. The simulated state points are distributed in temperature and pressure based on an entropy scaling approach, using the PC-SAFT equation of state to calculate the residual entropy. As a result, few simulations are sufficient to parameterize a correlation function that allows comparison with experimental data over a wide range of T and p. The combination of a few simulations with the entropy scaling method therefore allows a very efficient estimation of the transport properties for a large temperature and pressure range, while at the same time providing a consistent evaluation of the results by comparing them with experiments.

The study in **chapter 4** uses molecular simulations of model-mixtures to systematically validate the applicability of entropy scaling for viscosities of mixtures. The considered binary mixtures are composed of two LJ-fluids only differing in ε or σ, respectively. We further focus on non-ideal mixtures of two identical LJ-fluids with $\varepsilon_{11} = \varepsilon_{22} \neq \varepsilon_{12}$ which are known to show a strongly non-ideal phase behavior. We determine the viscosity η of several binary mixtures of Lennard-Jones fluids in equilibrium molecular dynamic simulations at different state points. Expanding a study[25] published together with Lötgering-Lin (first author), I calculate the dimensionless viscosity $\eta^{\#}$ for mixtures. Using the residual entropy of the mixtures s_{res}, which I determined in grand canonical MC simulations, an entropy-scaled representation shows a monovariable dependence of the reduced transport coefficient with s_{res}, so that all results of the study indeed collapse onto a single line.

Bibliography

[1] D. K. Klimov and D. Thirumalai. Viscosity Dependence of the Folding Rates of Proteins. *Physical Review Letters*, **79**(2):317–320, 1997. doi:10.1103/physrevlett.79.317.

[2] R. Swaminathan, C. Hoang, and A. Verkman. Photobleaching recovery and anisotropy decay of green fluorescent protein GFP-S65T in solution and cells: cytoplasmic viscosity probed by green fluorescent protein translational and rotational diffusion. *Biophysical Journal*, **72**(4):1900–1907, 1997. doi:10.1016/s0006-3495(97)78835-0.

[3] J. J. Schmidt, J. Rowley, and H. J. Kong. Hydrogels used for cell-based drug delivery. *Journal of Biomedical Materials Research Part A*, **87A**(4):1113–1122, 2008. doi:10.1002/jbm.a.32287.

[4] M. Sefidgar, M. Soltani, K. Raahemifar, H. Bazmara, S. M. Nayinian, and M. Bazargan. Effect of tumor shape, size, and tissue transport properties on drug delivery to solid tumors. *Journal of Biological Engineering*, **8**(1):12, 2014. doi:10.1186/1754-1611-8-12.

[5] S. Rahmstorf. Thermohaline circulation: The current climate. *Nature*, **421**(6924):699–699, 2003. doi:10.1038/421699a.

[6] G. Hughes and R. Griffiths. A simple convective model of the global overturning circulation, including effects of entrainment into sinking regions. *Ocean Modelling*, **12**(1-2):46–79, 2006. doi:10.1016/j.ocemod.2005.04.001.

[7] S. E. Huisman, M. den Toom, H. A. Dijkstra, and S. Drijfhout. An Indicator of the Multiple Equilibria Regime of the Atlantic Meridional Overturning Circulation. *Journal of Physical Oceanography*, **40**(3):551–567, 2010. doi:10.1175/2009jpo4215.1.

[8] J. A. Wesselingh and R. Krishna. *Mass Transfer in Multicomponent Mixtures*. VSSD, Delft, first edition edition, 2006. ISBN 9071301583.

[9] N. Yilmaz. Temperature-dependent viscosity correlations of vegetable oils and biofuel–diesel mixtures. *Biomass and Bioenergy*, **35**(7):2936–2938, 2011. doi:10.1016/j.biombioe.2011.03.026.

[10] B. Esteban, J.-R. Riba, G. Baquero, A. Rius, and R. Puig. Temperature dependence of density and viscosity of vegetable oils. *Biomass and Bioenergy*, **42**:164–171, 2012. doi:10.1016/j.biombioe.2012.03.007.

[11] A. Vidal, C. Rodriguez, P. Koukouvinis, M. Gavaises, and M. A. McHugh. Modelling

of Diesel fuel properties through its surrogates using Perturbed-Chain, Statistical Associating Fluid Theory. *International Journal of Engine Research*, **21**(7):1118–1133, 2018. doi:10.1177/1468087418801712.

[12] L.-B. Ouyang. New Correlations for Predicting the Density and Viscosity of Supercritical Carbon Dioxide Under Conditions Expected in Carbon Capture and Sequestration Operations. *The Open Petroleum Engineering Journal*, **5**(1):13–21, 2011. doi:10.2174/1874834101104010013.

[13] N. I. Diamantonis, G. C. Boulougouris, D. M. Tsangaris, M. J. E. Kadi, H. Saadawi, S. Negahban, and I. G. Economou. Thermodynamic and transport property models for carbon capture and sequestration (CCS) processes with emphasis on CO2 transport. *Chemical Engineering Research and Design*, **91**(10):1793–1806, 2013. doi:10.1016/j.cherd.2013.06.017.

[14] J. Schilling, D. Tillmanns, M. Lampe, M. Hopp, J. Gross, and A. Bardow. Integrating working fluid design into the thermo-economic design of ORC processes using PC-SAFT. *Energy Procedia*, **129**:121–128, 2017. doi:10.1016/j.egypro.2017.09.179.

[15] J. Schilling, D. Tillmanns, M. Lampe, M. Hopp, J. Gross, and A. Bardow. From molecules to dollars: integrating molecular design into thermo-economic process design using consistent thermodynamic modeling. *Molecular Systems Design and Engineering*, **2**(3):301–320, 2017. doi:10.1039/c7me00026j.

[16] M. Lampe, M. Stavrou, J. Schilling, E. Sauer, J. Gross, and A. Bardow. Computer-aided molecular design in the continuous-molecular targeting framework using group-contribution PC-SAFT. *Computers & Chemical Engineering*, **81**:278–287, 2015. doi:10.1016/j.compchemeng.2015.04.008.

[17] R. B. Bird, W. E. Stewart, and E. N. Lightfoot. *Transport phenomena*. J. Wiley, New York, 2002. ISBN 9780470115398.

[18] B. E. Poling, J. M. Prausnitz, and J. P. O'Connell. *The Properties of Gases and Liquids*. McGraw-Hill Professional, 2000. ISBN 9780071499996.

[19] J. O. Hirschfelder, C. F. Curtiss, and R. B. Bird. *Molecular Theory of Gases and Liquids*. John Wiley & Sons, Inc, 1954.

[20] S. Kjelstrup, D. Bedeaux, E. Johannessen, and J. Gross. *Non-Equilibrium Thermodynamics for Engineers*. WORLD SCIENTIFIC, 2017. ISBN 9789813200302. doi:10.1142/10286.

[21] M. Tuckerman. *Statistical Mechanics: Theory and Molecular Simulation*. OXFORD UNIV PR, 2010. ISBN 0198525265.

[22] S. R. D. Groot, P. Mazur, and S. R. de Groot. *Non-Equilibrium Thermodynamics*. DOVER PUBN INC, New York, 1984. ISBN 978-0-486-64741-8.

[23] X. Liu, S. K. Schnell, J.-M. Simon, P. Krüger, D. Bedeaux, S. Kjelstrup, A. Bardow, and T. J. H. Vlugt. Diffusion Coefficients from Molecular Dynamics Simulations in Binary and Ternary Mixtures. *International Journal of Thermophysics*, **34**(7):1169–1196, 2013. doi:10.1007/s10765-013-1482-3.

[24] O. Lötgering-Lin and J. Gross. Group Contribution Method for Viscosities Based on Entropy Scaling Using the Perturbed-Chain Polar Statistical Associating Fluid Theory. *Ind. Eng. Chem. Res.*, **54**(32):7942–7952, 2015. doi:10.1021/acs.iecr.5b01698.

[25] O. Lötgering-Lin, M. Fischer, M. Hopp, and J. Gross. Pure Substance and Mixture Viscosities Based on Entropy Scaling and an Analytic Equation of State. *Ind. Eng. Chem. Res.*, **57**(11):4095–4114, 2018. doi:10.1021/acs.iecr.7b04871.

[26] M. Hopp, J. Mele, and J. Gross. Self-Diffusion Coefficients from Entropy Scaling Using the PCP-SAFT Equation of State. *Ind. Eng. Chem. Res.*, **57**(38):12942–12950, 2018. doi:10.1021/acs.iecr.8b02406.

[27] M. Hopp and J. Gross. Thermal Conductivity from Entropy Scaling: A Group-Contribution Method. *Ind. Eng. Chem. Res.*, **58**(44):20441–20449, 2019. doi:10.1021/acs.iecr.9b04289.

[28] M. Hopp and J. Gross. Thermal Conductivity of Real Substances from Excess Entropy Scaling Using PCP-SAFT. *Ind. Eng. Chem. Res.*, **56**(15):4527–4538, 2017. doi:10.1021/acs.iecr.6b04289.

[29] M. Hopp, J. Mele, R. Hellmann, and J. Gross. Thermal Conductivity via Entropy Scaling: An Approach That Captures the Effect of Intramolecular Degrees of Freedom. *Ind. Eng. Chem. Res.*, **58**(39):18432–18438, 2019. doi:10.1021/acs.iecr.9b03998.

[30] R. A. Messerly, M. C. Anderson, S. M. Razavi, and J. R. Elliott. Improvements and limitations of Mie λ-6 potential for prediction of saturated and compressed liquid viscosity. *Fluid Phase Equilib.*, **483**:101–115, 2019. doi:10.1016/j.fluid.2018.11.002.

[31] E. J. Maginn, R. A. Messerly, D. J. Carlson, D. R. Roe, and J. R. Elliott. Best Practices for Computing Transport Properties 1. Self-Diffusivity and Viscosity from Equilibrium Molecular Dynamics [Article v1.0]. *Living J. Comput. Mol. Sci.*, **1**(1):6324–, 2018. doi:10.33011/livecoms.1.1.6324.

[32] M. Fischer, G. Bauer, and J. Gross. Transferable Anisotropic United-Atom Mie (TAMie) Force Field: Transport Properties from Equilibrium Molecular Dynamic Simulations. *Ind. Eng. Chem. Res.*, **59**(18):8855–8869, 2020. doi:10.1021/acs.iecr.0c00848.

[33] D. McQuarrie. *Statistical Mechanics*. University Science Books, 2000. ISBN 9781891389153.

[34] M. Allen and D. Tildesley. *Computer Simulation of Liquids*. Oxford science publications. Clarendon Press, 1987. ISBN 9780198553755.

[35] D. Frenkel and B. Smit. *Understanding molecular simulations: from algorithms to applications*.

Academic, San Diego, 1996.

[36] P. Ungerer, C. Beauvais, J. Delhommelle, A. Boutin, and B. Rousseau. Optimization of the Anisotropic United Atoms Intermolecular Potential for n-Alkanes, Gibbs Ensemble. *J. Chem. Phys.*, **112**:5499–5510, 2000.

[37] M. G. Martin and J. I. Siepmann. Transferable potentials for phase equilibria. 1. United-atom description of n-alkanes. *J. Phys. Chem. B*, **102**(14):2569–2577, 1998. doi:10.1021/jp972543+.

[38] L. D. Schuler, X. Daura, and W. F. Van Gunsteren. An improved GROMOS96 force field for aliphatic hydrocarbons in the condensed phase. *J. Comput. Chem.*, **22**(11):1205–1218, 2001. doi:10.1002/jcc.1078.

[39] C. Oostenbrink, A. Villa, A. E. Mark, and W. F. V. Gunsteren. A biomolecular force field based on the free enthalpy of hydration and solvation: The GROMOS force-field parameter sets 53A5 and 53A6. *J. Comput. Chem.*, **25**(13):1656–1676, 2004. doi:10.1002/jcc.20090.

[40] T. A. Soares, P. H. Hünenberger, M. A. Kastenholz, V. Kräutler, T. Lenz, R. D. Lins, C. Oostenbrink, and W. F. van Gunsteren. An improved nucleic acid parameter set for the GROMOS force field. *J. Comput. Chem.*, **26**(7):725–737, 2005. doi:10.1002/jcc.20193.

[41] N. Schmid, A. P. Eichenberger, A. Choutko, S. Riniker, M. Winger, A. E. Mark, and W. F. van Gunsteren. Definition and testing of the GROMOS force-field versions 54A7 and 54B7. *Eur. Biophys. J.*, **40**(7):843–856, 2011. doi:10.1007/s00249-011-0700-9.

[42] A. Hemmen, A. Z. Panagiotopoulos, and J. Gross. Grand Canonical Monte Carlo Simulations Guided by an Analytic Equation of State - Transferable Anisotropic Mie Potentials for Ethers. *J. Phys. Chem. B*, **119**(23):7087–7099, 2015.

[43] A. Hemmen and J. Gross. Transferable Anisotropic United-Atom Force Field Based on the Mie Potential for Phase Equilibrium Calculations: n-Alkanes and n-Olefins. *J. Phys. Chem. B*, **119**(35):11695–11707, 2015.

[44] D. Weidler and J. Gross. Transferable Anisotropic United-Atom Force Field Based on the Mie Potential for Phase Equilibria: Aldehydes, Ketones, and Small Cyclic Alkanes. *Ind. Eng. Chem. Res.*, **55**(46):12123–12132, 2016. doi:10.1021/acs.iecr.6b02182.

[45] D. Weidler and J. Gross. Individualized force fields for alkanes, olefins, ethers and ketones based on the transferable anisotropic Mie potential. *Fluid Phase Equilib.*, **470**:101–108, 2018. doi:10.1016/j.fluid.2018.02.012.

[46] D. Weidler and J. Gross. Phase equilibria of binary mixtures with alkanes, ketones, and esters based on the Transferable Anisotropic Mie force field. *Fluid Phase Equilib.*, **490**:123–132, 2019. doi:10.1016/j.fluid.2019.02.009.

[47] J. Baz, N. Hansen, and J. Gross. Transferable Anisotropic Mie-Potential Force Field for n-Alcohols: Static and Dynamic Fluid Properties of Pure Substances and Binary Mixtures. *Ind. Eng. Chem. Res.*, **59**(2):919–929, 2019. doi:10.1021/acs.iecr.9b05323.

[48] D. Markthaler, J. Zeman, J. Baz, J. Smiatek, and N. Hansen. Validation of Trimethylamine-N-oxide (TMAO) Force Fields Based on Thermophysical Properties of Aqueous TMAO Solutions. *J. Phys. Chem. B*, **121**(47):10674–10688, 2017. doi:10.1021/acs.jpcb.7b07774.

[49] S. Riniker. Fixed-Charge Atomistic Force Fields for Molecular Dynamics Simulations in the Condensed Phase: An Overview. *J. Chem. Inf. Model.*, **58**(3):565–578, 2018. doi:10.1021/acs.jcim.8b00042.

[50] A. R. Leach. *Molecular Modelling - Principles and Applications*. Longman, New York, 1996. ISBN 978-0-582-23933-3.

[51] H. A. Lorentz. Ueber die Anwendung des Satzes vom Virial in der kinetischen Theorie der Gase. *Ann. Phys.*, **248**(1):127–136, 1881. doi:10.1002/andp.18812480110.

[52] D. Berthelot. Sur le mélange des gaz. *C. R. Hebd. Seanc. Acad. Sci. (Paris)*, **126**:1703–1706, 1898.

[53] B. R. Brooks, R. E. Bruccoleri, B. D. Olafson, D. J. States, S. Swaminathan, and M. Karplus. CHARMM: A program for macromolecular energy, minimization, and dynamics calculations. *J. Comput. Chem.*, **4**(2):187–217, 1983. doi:10.1002/jcc.540040211.

[54] J. Wang, R. M. Wolf, J. W. Caldwell, P. A. Kollman, and D. A. Case. Development and testing of a general amber force field. *J. Comput. Chem.*, **25**(9):1157–1174, 2004. doi:https://doi.org/10.1002/jcc.20035.

[55] A. K. Malde, L. Zuo, M. Breeze, M. Stroet, D. Poger, P. C. Nair, C. Oostenbrink, and A. E. Mark. An Automated Force Field Topology Builder (ATB) and Repository: Version 1.0. *J. Chem. Theory Comput.*, **7**(12):4026–4037, 2011. doi:10.1021/ct200196m.

[56] K. B. Koziara, M. Stroet, A. K. Malde, and A. E. Mark. Testing and validation of the Automated Topology Builder (ATB) version 2.0: prediction of hydration free enthalpies. *J. Comput.-Aided Mol. Des.*, **28**(3):221–233, 2014. doi:10.1007/s10822-014-9713-7.

[57] W. van Gunsteren and H. Berendsen. Algorithms for macromolecular dynamics and constraint dynamics. *Mol. Phys.*, **34**(5):1311–1327, 1977. doi:10.1080/00268977700102571.

[58] W. van Gunsteren. Constrained dynamics of flexible molecules. *Mol. Phys.*, **40**(4):1015–1019, 1980. doi:10.1080/00268978000102101.

[59] J.-P. Ryckaert, G. Ciccotti, and H. J. Berendsen. Numerical integration of the cartesian equations of motion of a system with constraints: molecular dynamics of n-alkanes. *J. Comput. Phys.*,

23(3):327–341, 1977. doi:10.1016/0021-9991(77)90098-5.

[60] H. C. Andersen. Rattle: A "velocity" version of the shake algorithm for molecular dynamics calculations. *J. Comput. Phys.*, **52**(1):24–34, 1983. doi:10.1016/0021-9991(83)90014-1.

[61] B. Hess, H. Bekker, H. J. C. Berendsen, and J. G. E. M. Fraaije. LINCS: A linear constraint solver for molecular simulations. *J. Comput. Chem.*, **18**(12):1463–1472, 1997. doi:10.1002/(sici)1096-987x(199709)18:12<1463::aid-jcc4>3.0.co;2-h.

[62] Z. Liang and H.-L. Tsai. The vibrational contribution to the thermal conductivity of a polyatomic fluid. *Mol. Phys.*, **108**(13):1707–1714, 2010. doi:10.1080/00268976.2010.489520.

[63] C. G. Aimoli, E. J. Maginn, and C. R. A. Abreu. Transport properties of carbon dioxide and methane from molecular dynamics simulations. *J. Chem. Phys.*, **141**(13):134101, 2014. doi:10.1063/1.4896538.

[64] M. Zhang, E. Lussetti, L. E. de Souza, and F. Müller-Plathe. Thermal conductivities of molecular liquids by reverse nonequilibrium molecular dynamics. *J. Phys. Chem. B*, **109**(31):15060–15067, 2005. doi:10.1021/jp0512255.

[65] E. Lussetti, T. Terao, and F. Müller-Plathe. Nonequilibrium molecular dynamics calculation of the thermal conductivity of amorphous polyamide-6, 6. *J. Phys. Chem. B*, **111**(39):11516–11523, 2007. doi:10.1021/jp0737956.

[66] G. Raabe and R. J. Sadus. Influence of bond flexibility on the vapor-liquid phase equilibria of water. *J. Chem. Phys.*, **126**(4):044701, 2007. doi:10.1063/1.2428302.

[67] G. Raabe and R. J. Sadus. Molecular dynamics simulation of the effect of bond flexibility on the transport properties of water. *J. Chem. Phys.*, **137**(10):104512, 2012. doi:10.1063/1.4749382.

[68] C. Nieto-Draghi, P. Ungerer, and B. Rousseau. Optimization of the anisotropic united atoms intermolecular potential for n-alkanes: Improvement of transport properties. *J. Chem. Phys.*, **125**(4):044517, 2006. doi:10.1063/1.2219114.

[69] N. Metropolis, A. W. Rosenbluth, M. N. Rosenbluth, A. H. Teller, and E. Teller. Equation of State Calculations by Fast Computing Machines. *The Journal of Chemical Physics*, **21**(6):1087–1092, 1953. doi:10.1063/1.1699114.

[70] J. R. Errington and V. K. Shen. Direct evaluation of multicomponent phase equilibria using flat-histogram methods. *J. Chem. Phys.*, **123**(16):164103, 2005. doi:10.1063/1.2064628.

[71] A. M. Ferrenberg and R. H. Swendsen. New Monte Carlo technique for studying phase transitions. *Phys. Rev. Lett.*, **61**(23):2635, 1988. doi:10.1103/physrevlett.61.2635.

[72] A. Grossfield, P. N. Patrone, D. R. Roe, A. J. Schultz, D. Siderius, and D. M. Zuckerman. Best Practices for Quantification of Uncertainty and Sampling Quality in Molecular Simulations

[Article v1.0]. *Living J. Comput. Mol. Sci.*, **1**(1):5067–, 2018. doi:10.33011/livecoms.1.1.5067.

[73] P. A. Gordon. Influence of simulation details on thermodynamic and transport properties in molecular dynamics of fully flexible molecular models. *Mol. Simul.*, **29**(8):479–487, 2003. doi:10.1080/0892702031000106669.

[74] J. E. Basconi and M. R. Shirts. Effects of Temperature Control Algorithms on Transport Properties and Kinetics in Molecular Dynamics Simulations. *J. Chem. Theory Comput.*, **9**(7):2887–2899, 2013. doi:10.1021/ct400109a.

[75] D. J. Evans and G. P. Morriss. Nonlinear-response theory for steady planar Couette flow. *Physical Review A*, **30**(3):1528–1530, 1984. doi:10.1103/physreva.30.1528.

[76] A. W. Lees and S. F. Edwards. The computer study of transport processes under extreme conditions. *Journal of Physics C: Solid State Physics*, **5**(15):1921–1928, 1972. doi:10.1088/0022-3719/5/15/006.

[77] B. L. Holian and D. J. Evans. Shear viscosities away from the melting line: A comparison of equilibrium and nonequilibrium molecular dynamics. *J. Chem. Phys.*, **78**(8):5147–5150, 1983. doi:10.1063/1.445384.

[78] F. Müller-Plathe. Reversing the perturbation in nonequilibrium molecular dynamics: An easy way to calculate the shear viscosity of fluids. *Phys. Rev. E*, **59**(5):4894, 1999. doi:10.1103/PhysRevE.59.4894.

[79] F. Müller-Plathe and P. Bordat. *Reverse Non-equilibrium Molecular Dynamics*, pages 310–326. Springer Berlin Heidelberg, Berlin, Heidelberg, 2004. ISBN 978-3-540-39895-0. doi:10.1007/978-3-540-39895-0_10.

[80] C. M. Tenney and E. J. Maginn. Limitations and recommendations for the calculation of shear viscosity using reverse nonequilibrium molecular dynamics. *The Journal of Chemical Physics*, **132**(1):014103, 2010. doi:10.1063/1.3276454.

[81] M. S. Green. Markoff Random Processes and the Statistical Mechanics of Time-Dependent Phenomena. II. Irreversible Processes in Fluids. *J. Chem. Phys.*, **22**(3):398–413, 1954.

[82] R. Kubo. Statistical-Mechanical Theory of Irreversible Processes. I. General Theory and Simple Applications to Magnetic and Conduction Problems. *J. Phys. Soc. Jpn.*, **12**(6):570–586, 1957. doi:10.1143/jpsj.12.570.

[83] L. Onsager. Reciprocal Relations in Irreversible Processes. I. *Physical Review*, **37**(4):405–426, 1931. doi:10.1103/physrev.37.405.

[84] T. Chen, B. Smit, and A. T. Bell. Are pressure fluctuation-based equilibrium methods really worse than nonequilibrium methods for calculating viscosities? *The Journal of Chemical Physics*,

131(24):246101, 2009. doi:10.1063/1.3274802.

[85] D. Dubbeldam, D. C. Ford, D. E. Ellis, and R. Q. Snurr. A new perspective on the order-n algorithm for computing correlation functions. *Mol. Simul.*, **35**(12-13):1084–1097, 2009.

[86] Y. Zhang, A. Otani, and E. J. Maginn. Reliable Viscosity Calculation from Equilibrium Molecular Dynamics Simulations: A Time Decomposition Method. *J. Chem. Theory Comput.*, **11**(8):3537–3546, 2015. doi:10.1021/acs.jctc.5b00351.

[87] Y. Rosenfeld. Relation between the transport coefficients and the internal entropy of simple systems. *Phys. Rev.*, **15**(6):2545, 1977.

[88] M. Dzugutov. A universal scaling law for atomic diffusion in condensed matter. *Nature*, **381**:137, 1996. doi:10.1038/381137a0.

[89] Y. Rosenfeld. A quasi-universal scaling law for atomic transport in simple fluids. *J. Phys.: Condens. Matter*, **11**(28):5415, 1999.

[90] T. Goel, C. N. Patra, T. Mukherjee, and C. Chakravarty. Excess entropy scaling of transport properties of Lennard-Jones chains. *J. Chem. Phys.*, **129**(16):164904, 2008. doi:10.1063/1.2995990.

[91] G. Galliéro and C. Boned. Thermal conductivity of the Lennard-Jones chain fluid model. *Phys. Rev. E*, **80**(6):061202, 2009. doi:10.1103/PhysRevE.80.061202.

[92] R. Chopra, T. M. Truskett, and J. R. Errington. Excess entropy scaling of dynamic quantities for fluids of dumbbell-shaped particles. *J. Chem. Phys.*, **133**(10):104506, 2010.

[93] L. T. Novak. Fluid viscosity-residual entropy correlation. *Int. J. Chem. Reactor Eng.*, **9**(1), 2011. doi:10.2202/1542-6580.2839.

[94] J. C. Dyre. Hidden scale invariance in condensed matter. *J. Phys. Chem. B*, **118**(34):10007–10024, 2014. doi:10.1103/PhysRevE.88.042139.

[95] N. Gnan, T. B. Schrøder, U. R. Pedersen, N. P. Bailey, and J. C. Dyre. Pressure-energy correlations in liquids. IV. "Isomorphs" in liquid phase diagrams. *J. Chem. Phys.*, **131**(23):234504, 2009. doi:10.1063/1.3265957.

[96] L. Bøhling, T. S. Ingebrigtsen, A. Grzybowski, M. Paluch, J. C. Dyre, and T. B. Schrøder. Scaling of viscous dynamics in simple liquids: theory, simulation and experiment. *New J. Phys.*, **14**(11):113035, 2012. doi:10.1088/1367-2630/14/11/113035.

[97] D. M. Heyes, D. Dini, L. Costigliola, and J. C. Dyre. Transport coefficients of the Lennard-Jones fluid close to the freezing line. *J. Chem. Phys.*, **151**(20):204502, 2019. doi:10.1063/1.5128707.

[98] J. C. Dyre. Perspective: Excess-entropy scaling. *J. Chem. Phys.*, **149**(21):210901, 2018. doi:10.1063/1.5055064.

[99] A. A. Veldhorst, J. C. Dyre, and T. B. Schrøder. Scaling of the dynamics of flexible Lennard-Jones chains. *J. Chem. Phys.*, **141**(5):054904, 2014. doi:10.1063/1.4888564.

[100] A. A. Veldhorst, J. C. Dyre, and T. B. Schrøder. Scaling of the dynamics of flexible Lennard-Jones chains: Effects of harmonic bonds. *J. Chem. Phys.*, **143**(19):194503, 2015. doi:10.1063/1.4934973.

[101] J. Gross and G. Sadowski. Perturbed-chain SAFT: An equation of state based on a perturbation theory for chain molecules. *Ind. Eng. Chem. Res.*, **40**(4):1244–1260, 2001. doi:10.1021/ie0003887.

[102] Dortmund Data Bank. 2018.

[103] E. Sauer, M. Stavrou, and J. Gross. Comparison between a Homo- and a Heterosegmented Group Contribution Approach Based on the Perturbed-Chain Polar Statistical Associating Fluid Theory Equation of State. *Industrial & Engineering Chemistry Research*, **53**(38):14854–14864, 2014. doi:10.1021/ie502203w.

2 Force Fields with Fixed Bond Lengths and with Flexible Bond Lengths: Comparing Static and Dynamic Fluid Properties

The content of this chapter is a literal quote of the publication:

M. Fischer, G. Bauer, J. Gross: Force Fields with Fixed Bond Lengths and with Flexible Bond Lengths: Comparing Static and Dynamic Fluid Properties. *Journal of Chemical & Engineering Data*, **65**:1583-1593, 2020. doi:10.1021/acs.jced.9b01031

Abstract

This study investigates the equivalence or differences between classical force fields with rigid bond lengths and the same models but with (harmonic) bond length potentials. For ethane, propane and dimethyl ether described with the Transferable Anisotropic Mie potential we vary the force constant of the harmonic bond length potentials and analyze static and dynamic physical properties, namely pressure, viscosity, self-diffusion, and thermal conductivity of homogeneous phases. We find a range of values for the force constant of the bond length potentials (expressed in terms of the period-length of bond-oscillations) where force fields with harmonic bond lengths give equivalent results as the model with rigid bond lengths for static properties, for viscosity and for self-diffusion coefficients. The thermal conductivity of the force field with rigid bond lengths has an offset compared to the harmonic bond length models, which can be approximated through an analytic correction term. After adding the correction term results of the rigid model and the flexible models are in rather close agreement. Our study varies time-steps for solving the equations of motion and investigates whether the rRESPA integrator with a small time step associated to the (rather high frequency) bond length potentials has advantages compared to a simple velocity Verlet integrator. Furthermore, this work proposes a fast and memory efficient prescription to calculate autocorrelation functions for the calculation of Green-Kubo integrals. We then estimate average values and meaningful error bars for dynamic physical properties based on the time-decomposition approach [Zhang, Y.; Otani, A.; Maginn, E.J.: Reliable Viscosity Calculation from Equilibrium Molecular Dynamics Simulations: A Time Decomposition Method, *J. Chem. Theory Comput.* **2015**, 11, 3537–3546].

2.1 Introduction

Reliable prediction of transport coefficients for fluids, such as viscosity, thermal conductivity and diffusion is an important prerequisite for process design. Next to experimental measurements and semi-empirical models, molecular simulations are an attractive alternative for the determination of dynamic properties of fluids. Simulations are used where experiments are expensive, time-consuming and particularly challenging, for example at extreme temperatures or pressures. Semi-empirical models, such as the entropy scaling method[1–3], require a set of experimental data as basis for predicting transport properties, which may not be available for many substances. Also in this case, molecular simulations can be used to provide data where no experiments are available for which the models can be parameterized. The quality of results from molecular simulations strongly depends on the used force field, as corroborated in recent studies.[4] Force fields are composed of potentials that describe the interaction between molecules and the interaction between atoms within these molecules, such as binding forces, binding angles and torsion angles. Some parameters of force fields are adjusted to experimental data, especially those corresponding to Van der Waals interactions, because they are usually defined to effectively capture multi-body corrections. Numerous force fields can be found in literature for a wide variety of applications; for condensed liquids some of the most commonly used are TraPPE[5], GAFF[6], OPLS[7], CHARMM[8,9] and GROMOS[10–13].

In this work we study the influence of the way bonds are modeled with an emphasis on the influence on transport properties. In most force fields, harmonic potentials are used to model the bond energy between two neighboring atoms or atom groups. The two required parameters, the reference length r_0 and force constant k_l, are determined *a priori* for many force fields, for example, from crystallographic experiments, microwave data, and vibration frequencies[8]. Alternatively, *ab initio* quantum mechanics calculations can be used to parameterize the potential[6,14,15]. In either case, these parameters are not part of the optimization used to determine intermolecular parameters of a force field. The high frequency of the bond vibrations limit the time step that can be used for the integration of the equations of motion in the simulation. This also affects the calculation of transport properties. A study by Gordon[16] showed an influence of the time step and the chosen integration method on the simulated viscosity η of fully flexible *n*-octane and *n*-dodecane. Using multi-time step integration schemes allows the simulation of high-frequency bond vibrations with larger time steps[17,18]. In this context, the influence of the frequency of the bonds of a Lennard-Jones dimer on the energy conservation of the integration approach[18,19] as well as dynamic properties such as the velocity autocorrelation function and the friction kernel of the model fluid were investigated[20,21].

In practice, bonds are often constrained to a constant bond length in order to increase the time step[22–24]. A further simplification are so-called united atom force fields, in which bonds including hydrogen atoms are implicitly considered: the hydrogen atoms are combined with neighboring atoms to pseudo atoms, which act as single centres of interaction. These simplifications are justified in many cases, because the bond vibrations are not excited quantum mechanically at room temperature[25,26]. Importantly, these constraints also show little influence on the dynamics in molecular simulations[27,28]. The comparability of the two approaches in describing bonds has earlier been investigated in literature. Considering viscosity, Bird *et al.*[29] showed the equivalence of bead-spring molecules and of bead-rod molecules whose atoms are connected by infinitely stiff springs. Chandler and Berne[30] found differences in the conformational structure of rigid and flexible models of *n*-butane. Tironi *et al.*[31] discussed the relative merits of either rigid or flexible models of water. The authors concluded that introducing flexibility is possible but not recommended. The quality of the results could not be improved, whereas flexible bonds increase the danger of introducing further artifacts. The velocity autocorrelation function of flexible and rigid water models was also compared by Hess *et al.*[32] who proposed flexible constraints as an alternative approach for the calculation of intramolecular bonds.

The difference in transport properties between fixed and flexible bonds were compared for N_2 and H_2O by Bordat and Müller-Plathe[33]. Differences for the viscosity were found to be within statistical uncertainties. Other studies for water show more accurate results for flexible molecules in diffusion and viscosity[34–36] compared to a rigid model. However, in these cases, results were compared to fully rigid water models. The effects of flexible bond lengths and flexible bond angles were not considered separately in these studies. Aimoli *et al.*[37] found, that a flexible TraPPE description of CO_2 is able to estimate transport properties with accuracies comparable to that of rigid models. However, the authors report higher deviations to experimental data for the thermal conductivity calculated with the flexible TraPPE force field. Considerable deviations from the respective force field with rigid bonds were also found for the thermal conductivity in flexible models of *n*-hexane[38] and polyamide-6,6[39].

MD simulations with bond length constraints require iterative adjustment of molecules' space coordinates for every time step which is particularly undesired for large simulations. That is why force fields with fixed bond lengths were in several studies converted to a "flexible" equivalent force field. A corresponding "flexible" model is usually defined by assuming harmonic bond length potentials with force constant k_l and zero-force length r_0 defined equal to the fixed bond length. For example, studies in the literature show flexible TraPPE variants for CO_2[40,41], for *n*-alkanes[16,42], for propane[43] and for *n*-octane, cyclohexane, squalane, and other hydrocarbons[44]. The origin of the k_l values in the *TraPPE-flex* force fields is often not

quite clear. Usually, the force constants are taken over from other force fields, like AMBER[6], as in the force field of Rane *et al.*[44] Depending on the originating force field, the k_l value for the same bond type may differ significantly between the two force fields.

In this work we systematically investigate how the force constant k_l of bond length potentials influences the static and transport properties of short-chain hydrocarbons. We thereby regard the pressure p, the shear viscosity η, the self-diffusion coefficient D_{self} and the thermal conductivity λ of ethane, propane and dimethyl ether as determined from equilibrium molecular dynamics (MD) simulations. We introduce a harmonic bond potential in the Transferable Anisotropic Mie (TAMie) force field, which was originally parameterized for fixed bond lengths[45,46]. The (inverse) bond length constants are thereby scaled with the mass of the two corresponding interaction sites, leading to the period time of single bond length vibrations. Expressing bond length constants in this way makes the results transferable to other force fields and allows for a meaningful comparison of different substances. The "flexible force field" is studied for a range of k_l values. For varying force constants of the harmonic bond length potentials we investigate different time steps and MD-integration schemes and observe how the results for static and dynamic properties change for increasing large time steps.

2.2 Methods

2.2.1 Molecular Model

The united atom TAMie force field[45–48] is considered in this study. TAMie originally utilizes fixed bond lengths whereas angles and torsions are modeled as flexible potentials. Intermolecular interactions are described as Mie (n–6) potentials (vdW), and fixed point charge (Coulombic) potentials, as

$$u_{ij}(r) = c_{ij}\varepsilon_{ij}\left[\left(\frac{\sigma_{ij}}{r}\right)^{n_{ij}} - \left(\frac{\sigma_{ij}}{r}\right)^{6}\right] + \frac{q_i q_j}{4\pi\epsilon_0 r} \tag{2.1}$$

with the prefactor

$$c_{ij} = \left(\frac{n_{ij}}{n_{ij}-6}\right)\left(\frac{n_{ij}}{6}\right)^{6/\left(n_{ij}-6\right)} \tag{2.2}$$

where r_{ij} denotes the distance between two interaction sites i and j. The size parameter σ_{ij}, the well depth ε_{ij} and the repulsive exponent n_{ij} characterize the vdW interactions. These parameters were adjusted to experimental data of vapor-liquid equilibria (VLE). Lorentz-

Berthelot combining rules are applied[49,50], where repulsive exponents are combined arithmetically as $n_{ij} = (n_{ii} + n_{jj})/2$[51]. Coulombic interactions are calculated with the partial charge q_i, given as a factor of an electron charge $|e|$, and the dielectric constant ϵ_0.

Molecules regarded in this study consist of three or less interaction sites. The intramolecular potential of the molecules is composed of the bending angle potential of the original force field and the bond length potential investigated in this study. Bending angles are generated according to a harmonic potential

$$u_{\text{bend}}(\theta) = k_\theta/2(\theta - \theta_0)^2 \tag{2.3}$$

where k_θ is the force constant, θ is the bending angle, and θ_0 is the zero-force angle. TAMie was originally parameterized for fixed bond lengths. In order to study the influence of the bond vibrations on static and dynamic fluid properties, we introduce flexible bond lengths according to a harmonic bond potential

$$u_{\text{bond}} = k_l(r - r_0)^2 \tag{2.4}$$

The zero-force distance r_0 is adopted from the original TAMie force field. k_l denotes a force constant with unit $\text{kcal mol}^{-1}\,\text{Å}^{-2}$. Note, that we use k_l in eq. (2.4) instead of $k_l/2$, in agreement to the notation in LAMMPS[52]. We investigate how the stiffness of the harmonic potential influences different static and harmonic properties of fluids.

An overview of all TAMie parameters used in this study is given in table 2.1 and table 2.2.

2.2.2 Data Analysis

Dynamic properties in this study were determined from equilibrium molecular dynamics simulations. The three investigated dynamic properties (shear viscosity η, thermal conductiv-

bond type	r_0/Å
CH_3—CH_3	1.94
CH_3—CH_2	1.74
CH_3—O	1.61

angle type	θ_0/deg	k_θ/kcal mol^{-1}
CH_3—CH_2—CH_3	114.0	124.20
CH_3—O—CH_3	112.0	120.03

Table 2.1: Intramolecular Parameters

united atom i	ε_{ii}/kcal mol^{-1}	σ_{ii}/Å	n_{ii}	q_i/e
$-CH_3-$	0.270 89	3.6034	14	0.175 (next to ether O)
$-CH_3-$ (ethane)	0.259 89	3.6463	14	—
$-CH_2-$	0.105 15	4.0400	14	—
$-O-$ (DME)	0.108 02	3.213	12	−0.35

Table 2.2: Intermolecular Parameters

ity λ, and self-diffusion coefficient D_{self}) for a given state point can be obtained in a single simulation run.

Shear viscosity and thermal conductivity are determined through Green-Kubo relations[53,54]. Green-Kubo integrals associate dynamic properties with autocorrelation functions (ACF) of quantities sampled during simulation. The ACF of the sampled time series, R_{JJ}, of a general quantity J is calculated as

$$R_{JJ}(\tau) = \lim_{\Theta\to\infty} \frac{1}{2\Theta} \int_{-\Theta}^{\Theta} J(t+\tau)J(t)\mathrm{d}t \tag{2.5}$$

where τ is the time lag between two evaluations of J and t is the instantaneous time. Integration of R_{JJ} (with consideration of a corresponding prefactor C) yields the cumulative transport property

$$\zeta_{\text{run}}(\tau) = C \int_{0}^{\tau} R_{JJ}(\tau')\mathrm{d}\tau' \tag{2.6}$$

as function of the lag time. The ACF's decay to zero in the limit of infinite lag times τ and the respective transport coefficient ζ is therefore derived from the limit of infinite integration times of the running integral as

$$\zeta = \zeta_{\text{run}}(\tau \to \infty) \tag{2.7}$$

In the specific case of the the shear viscosity, the Green-Kubo relation uses the ACF of off-diagonal elements of the shear-stress tensor in the simulation box, $J_p^{\alpha\beta}$, (with $\alpha, \beta \in (x, y, z)$ and $\alpha \neq \beta$), calculated as

$$R_{J_pJ_p}(\tau) = \lim_{\Theta\to\infty} \frac{1}{2\Theta} \int_{-\Theta}^{\Theta} J_p^{\alpha\beta}(t+\tau)J_p^{\alpha\beta}(t)\,\mathrm{d}t \tag{2.8}$$

The shear viscosity as function of τ is then

$$\eta_{\text{run}}(\tau) = \frac{1}{V k_{\text{B}} T} \int_0^{\tau} R_{J_p J_p}(\tau') \mathrm{d}\tau' \tag{2.9}$$

where the shear viscosity is formally obtained as the limit $\eta = \eta_{\text{run}}(\tau \to \infty)$. The stress tensor is calculated during the simulation using the molecule velocities $v_i, i \in x, y, z$ and the virial $\mathbf{r_{ij}}(\partial u(r_{ij})/\partial \mathbf{r_{ij}})$, according to

$$J_p^{\alpha\beta} = \sum_{i=1}^{N} m_i v_i^{\alpha} v_i^{\beta} - \sum_{i=1}^{N} \sum_{j>i}^{N} r_{ij}^{\alpha} \frac{\partial u(r_{ij})}{\partial r_{ij}^{\beta}} \tag{2.10}$$

In order to improve the statistic of each simulation, we use the six independent shear components[55,56] of the stress tensor.

The correlated quantities needed for the calculation of the thermal conductivity are the three spatial entries of the heat flux $\boldsymbol{J}_q = \left(J_q^x, J_q^y, J_q^z\right)$. The thermal conductivity is determined via the ACF $R_{J_q J_q}$, analogous to the viscosity. Details of the calculation are shown in the Supporting Information.

For computing the self-diffusion coefficient D_{self} we use the Einstein relation, that calculates $D_{\text{self, run}}$ from the mean-squared displacement (MSD) of the centre-of-mass (COM) positions $W_i(t')$ of each molecule i, according to

$$W_i(\tau) = \lim_{\Theta \to \infty} \int_0^{\Theta} \left[\boldsymbol{r}_i^{\text{COM}}(\tau + t) - \boldsymbol{r}_i^{\text{COM}}(t)\right]^2 \mathrm{d}t \tag{2.11}$$

The transport coefficient is defined as the limit of the running value ($D_{\text{self}} = D_{\text{self, run}}(\tau \to \infty)$), which is calculated as the slope of the average of the MSD over all molecules, according to

$$D_{\text{self, run}}(\tau) = \frac{1}{6N} \frac{\mathrm{d}}{\mathrm{d}\tau} \sum_{i=1}^{N} W_i(\tau) \tag{2.12}$$

During molecular simulations, the time series of $J_p^{\alpha\beta}(t)$, $\boldsymbol{J}_q(t)$ and $\boldsymbol{r}_i^{\text{COM}}(t)$ are sampled as described in the Simulation Details section. The autocorrelation of $J_p^{\alpha\beta}$ and $\boldsymbol{J}_q$, as well as the mean-squared displacement are calculated in a post-processing step.

The autocorrelation integral is defined as

$$(f * f)(\tau) = \int_{-\infty}^{\infty} f(t+\tau) f(t) \mathrm{d}t \tag{2.13}$$

and can be calculated using efficient Fourier transform algorithms. This allows us to calculate the ACF in three steps[57].

1. Calculate the Fourier transform of the time series.

   $\hat{J}(f) = \mathcal{F}\{J(t)\}$

2. Multiply the transform with its complex conjugate $\hat{J}^*(f)$.

   $\hat{R}_{JJ}(f) = \hat{J}(f)\hat{J}^*(f)$

3. Calculate the ACF as inverse Fourier transform of the result.

   $R_{JJ}(\tau) = \mathcal{F}^{-1}\left\{\hat{R}_{JJ}(f)\right\}$

Using the fast Fourier transform algorithm (FFT), the computational complexity depending on the number of observations N_t is reduced from $\mathcal{O}\left(N_t^2\right)$, for the direct calculation, to $\mathcal{O}(N_t \log_2(N_t))$[58]. FFT algorithms assume periodicity of the transformed functions, and the sequence has to be zero-padded to twice the length before the calculation of the autocorrelation. The first half of the resulting sequence is the desired ACF. This approach allows us to calculate the ACF very efficiently without having to apply a moving window scheme as typically used[59], which, in practice, would reduce the number of considered data points. Our approach rigorously correlates all observations with all other observations, whereby every observation is also a starting point for a new time series. We therefore do not have to consider any parameters, such as window width, lag time, or the complexity due to the use of multiple time origins.

Although the mean-squared displacement is not an autocorrelation function in the first place, it can be determined more efficiently using FFT algorithms as well. For this purpose eq. (2.11) is decomposed into two parts, where one part is solved by FFT algorithms and the second part is calculated by a simple recursion. Details on efficient computation of mean-squared displacements are reported by Calandrini *et al.*[58].

The Green-Kubo method suffers from increasingly high statistical uncertainties and numerical noise for increasing lag times τ. Therefore, one typically truncates data after a certain correlation time $\tau_{\max}$. The time decomposition method proposed by Zhang *et al.*[60] helps us identify a suitable trade-off between too low values for $\tau_{\max}$, where the ACF has not

sufficiently dropped to zero and too high $\tau_{\max}$ values, where statistical uncertainty degrades the calculation results. We generate several independent replicate trajectories for each state point and calculate a running standard deviation $\sigma(\tau)$ and a running average $A(\tau)$ of η_{run}, λ_{run} and $D_{\text{self, run}}$ of all replicates. An on-the-fly algorithm is used for this purpose in order to save memory[61]. The cut-off time $\tau_{\max}$ is set to the time when the ratio of standard deviation and running average, $\sigma(\tau_{\max})/A(\tau_{\max})$, reaches a heuristic value of $\sigma^*_{\max} = 0.4$[60]. The data with $\tau > \tau_{\max}$ is ignored for the further procedure. An exponential function for the estimated standard deviation

$$\sigma_{\text{fit}}(\tau) = A\tau^b \tag{2.14}$$

is then fitted to $\sigma(\tau)$. In the next step, a double exponential function[62,63] is adjusted to the running average $A(\tau)$. We rearranged it to the following form[64]

$$\eta_{\text{fit}}(\tau) = \eta \frac{\alpha\beta_1\left(1-\mathrm{e}^{-\tau/\beta_1}\right) + (1-\alpha)\,\beta_2\left(1-\mathrm{e}^{-\tau/\beta_2}\right)}{\alpha\beta_1 + (1-\alpha)\,\beta_2} \tag{2.15}$$

with the adjustable parameters η, α, and the decay times β_1 and β_2. These parameters are identified by minimizing the objective function

$$f = \sum_{i=N_\tau^{\min}}^{N_\tau^{\max}} \left((\eta_{\text{fit}}(\tau_i) - \eta_{\text{run}}(\tau_i))w(\tau_i)\right)^2 \tag{2.16}$$

where index i runs over observations of $\eta_{\text{run}}(\tau)$. Adjusting the double exponential ansatz function to the sampled data is done with weight function $w(\tau) = 1/\tau^b$ in order to account for the increasing statistical uncertainty with increasing decay time where parameter b is from eq. (2.14). At very short decay times, large fluctuations make the fitting difficult due to the heavy weight in this τ range, which is why we adjust the function for decay times greater than $\tau_{i=N_\tau^{\min}} = 2\,\text{ps}$ determining the lower bound index $i = N_\tau^{\min}$.[60] The upper bound index is given as $\tau_{i=N_\tau^{\max}} = \tau_{\max}$, with the cut-off time $\tau_{\max}$ as defined above. To prevent nonphysical decay times longer than $\tau_{\max}$, the parameters β_1 and β_2 are limited to $\beta_1, \beta_2 < 0.01\tau_{\max}$ during the fitting procedure. The desired transport coefficient is determined by parameter η in eq. (2.15). Thermal conductivity λ is evaluated analogously.

As the value of $D_{\text{self, run}}$ is an average over all N molecules, the statistical uncertainty is much lower than for η_{run} and λ_{run}. We do not apply an elaborate adjustment procedure for determining D_{self}. The adjustment of one constant parameter to $D_{\text{self, run}}(\tau)$ with a weight of $1/\sigma(\tau)$ is sufficient. The data is truncated at $\tau_{\max,D} = \max\left(\tau_{\max,\eta}, \tau_{\max,\lambda}\right)$. The value of D_{self} is corrected for finite size effects applying the analytic correction factor proposed by Yeh and

Hummer[65].

Because the running standard deviation based on replicate trajectories is used for estimating the transport quantities in terms of the weight function $w(\tau)$ and for choosing of the cut-off time $\tau_{\max}$ of the fitting procedure, the method yields an estimate for the transport property, and it is not straight forward in determining statistical uncertainties. We propose an approach to estimate statistical uncertainties of the calculated transport properties by using a bootstrapping method[4,66]. One bootstrap sample is a random set of the replicate simulations, generated by randomly selecting (with replacement) 30 time series of the complete set of replicates. Transport properties are calculated for each bootstrap sample using the methods described above. In order to account for the uncertainty of the heuristic value of $\sigma^*_{\max} = 0.4$, a new value for $\sigma^*_{\max}$ is randomly selected between 0.4 and 0.6 for each subset. The procedure is repeated 500 times to generate a distribution of η, λ and D_{self} values, differing in the time series used as well as in $\sigma^*_{\max}$. We then construct the 95 % confidence interval of the distribution using the percentile method[67]. The results given below are mean values of the bootstrap distributions and error bars are defined as 95 % confidence interval.

The reported errors for the pressure are calculated as the standard error of the mean of p of $n = 10$ independent replicate simulations as $s(\bar{p}) = s(p)/\sqrt{n}$, where $s(p)$ is the unbiased estimate of the standard deviation as obtained from the independent replicates. The reported 95 % confidence interval is then calculated as $\bar{p} \pm 2.262\, s(\bar{p})$, where the factor 2.262 comes from the t-distribution using $(n-1)$ degrees of freedom.[68]

2.2.3 Simulation Details

Dynamic as well as equilibrium properties are obtained from equilibrium molecular dynamics simulations using the MD code LAMMPS. General simulation specifications are given in table 2.3.

Table 2.3: General Simulation Specifications.

equilibration time/ns	20
production time/ns	10
cut-off length/Å	14
number of molecules	1000
tail-corrections	U and P
constrained bonds	SHAKE[22]
long range solver	PPPM[69] with $1.0 \cdot 10^{-5}$ desired relative error in forces

We regard two substances (ethane and propane) where partial charges q_i are zero and dimethyl ether as a polar species. Besides the original TAMie force field with constant bond lengths, we simulated "flexible" versions with varying constants k_l of the harmonic bond length potential as given in eq. (2.4). We investigated 10 values for k_l varying from loose bonds ($k_l = 50\,\mathrm{kcal\,Å^{-2}}$) to very stiff bonds ($k_l = 10\,000\,\mathrm{kcal\,Å^{-2}}$).

Two liquid state points were simulated for each investigated force field variation. Properties are calculated at fixed temperatures T and densities ρ. T and ρ were taken from VLE calculations with the original TAMie force field as obtained from the literature[45,46]. An overview of the simulations is given in table 2.4.

The same simulation stages were applied to all state points. 1000 molecules are placed on a lattice as the initial configuration. After conducting an energy minimization, all systems run through a 10 ns *NVT* equilibration, proceeded by another 10 ns *NVE* equilibration. We added this step to make sure that energy is sufficiently conserved for the selected integration algorithm and time step. The production step of the simulation is carried out in the *NVT* ensemble. Temperature is controlled using a Nosé-Hoover thermostat, with a coupling time of 2000 fs. In order to improve statistical precision and provide estimates of uncertainties, we utilize 10 to 20 replicate simulations for the production stage. A single equilibrated configuration is used as the initial configuration for each replicate where different randomized initial velocities are taken from a Boltzmann distribution for each replicate simulation. Every second time step during the production stage, the pressure tensor entries and the entries of the heat flux are written to a file. The centre-of-mass positions of each molecule, used in the calculation of mean-squared displacement in eq. (2.11), are sampled every 100 steps.

Two types of numeric methods were used in this study to integrate the equations of motion. For the analysis of the fixed bonds, we use a velocity Verlet (VV) algorithm[70]. Bonds are constrained using the SHAKE algorithm[22]. For the simulation of the molecules with flexible bonds, we used the rRESPA multi-time step integrator[18]. rRESPA allows using different time

Table 2.4: Overview over Simulated States for Different Substances. For all Simulations, $N = 1000$ Molecules were Used

Substance	T/K	ρ/kg m^{-3}
ethane	205.0	512.83
	300.0	315.44
propane	295.0	497.24
	360.0	361.27
dimethyl ether	300.0	648.93
	380.0	482.04

steps for the calculation of different contributions of the potential-energy function. If not stated otherwise, we use a maximum time step of $1 \times \Delta t = 1\,\mathrm{fs}$ for all simulations using rRESPA. Intermolecular interactions and angle potentials are evaluated at this outer level. Forces due to bond-stretching are calculated with an "inner" time step of $\frac{1}{n} \times \Delta t$ with $n = 2$ and $n = 10$. This is meant to allow for sufficiently small time steps for the calculation of (high frequency) bond vibrations without exerting high computational costs in calculating expensive vdW interactions or Coulombic interactions. For $n = 1$ the rRESPA time integrator is equivalent to the VV integrator. For propane, we performed additional simulations of the flexible molecules with the VV algorithm, using time steps $\Delta t = 0.5\,\mathrm{fs}$ and $\Delta t = 2.0\,\mathrm{fs}$ for comparison.

2.3 Results and Discussion

The properties of three substances were investigated in this study: ethane, propane and dimethyl ether (DME). Ethane has a simple geometry with only one bond and no bonding angle. For ethane, it is easy to single out the influence of the bond interactions on simulation results. The number of rigid bonds that can be simulated with LAMMPS using the SHAKE algorithm is limited to two adjacent bonds. Propane with two bonds is the longest alkane for which we are able to determine a reference calculation with rigid bond lengths. The third substance, dimethyl ether, has a similar topology as propane but carries partial charges on each of the three united atom interaction sites.

We emphasize that this study is not committed to assess how well the chosen force field reproduces experimental data. We are focused on the equivalence or difference between force fields with rigid bond lengths and models with (harmonic) bond length potentials. Two saturated liquid state points were investigated for all substances. One state is at a temperature near the critical point and one condition is at a lower temperature, as summarized in table 2.4. The near-critical temperature was chosen because changes in the force field often lead to strong responses in observed quantities near the critical point. If not mentioned otherwise, all results presented below were calculated at a near critical temperature ($360\,\mathrm{K}/T^{\mathrm{crit}} = 0.97$ for propane, $300\,\mathrm{K}/T^{\mathrm{crit}} = 0.98$ for ethane, and $380\,\mathrm{K}/T^{\mathrm{crit}} = 0.95$ for dimethyl ether). Results for the lower temperature are given in the Supporting Information.

One static property (pressure p) and three transport properties (shear viscosity η, self-diffusion coefficient D_{self}, and thermal conductivity λ) are analyzed in this study. Figure 2.1 illustrates results for calculated pressures of propane plotted over the period of the bond

oscillations

$$\mathcal{T} = 2\pi\sqrt{\bar{M}/k_l} \tag{2.17}$$

with reduced molar mass $\bar{M} = (M_i M_j)/(M_i + M_j)$ of the two bonded united atom groups i and j. Presenting results in terms of $\mathcal{T}$ allows for comparison of different molecular bonds where low $\mathcal{T}$ values correspond to high values for k_l, indicating stiff bonds. The limit $\mathcal{T} = 0$ represents rigid bonds. It is noteworthy that for the limit $k_l \to \infty$, flexible bonds differ energetically and entropically from fixed bonds.[28] However, the thermal equation of state as well as calculated dynamic properties may well be practically equivalent.

Each point in fig. 2.1 is the result of one set of replicate simulations. Lines between points are merely visual aids. The red dashed horizontal line represents the result of a set of simulations with rigid bonds, as calculated using the VV algorithm with a time step of 1 fs and the SHAKE algorithm to ensure the bond length constraints. Other colors are results for propane with flexible bonds, obtained with different integration schemes and different time steps.

The first observation in fig. 2.1 is the high spread as well as statistical uncertainty for short $\mathcal{T}$ values, that is, for high values of k_l. For $\mathcal{T} < 0.035$ ps, we expect that the pressure from the flexible model should approach the pressure from the rigid bond force field. However, for periods below a $\mathcal{T}_{\text{min}}$ of 0.035 ps, the large frequency of the bonds' oscillations, $1/\mathcal{T}$, cannot be sufficiently solved by the integration algorithms. As a result, the pressure cannot be properly estimated and tends to be overestimated or underestimated compared to fixed bond length simulations. It is remarkable that the two-stage integration scheme rRESPA is also suffering

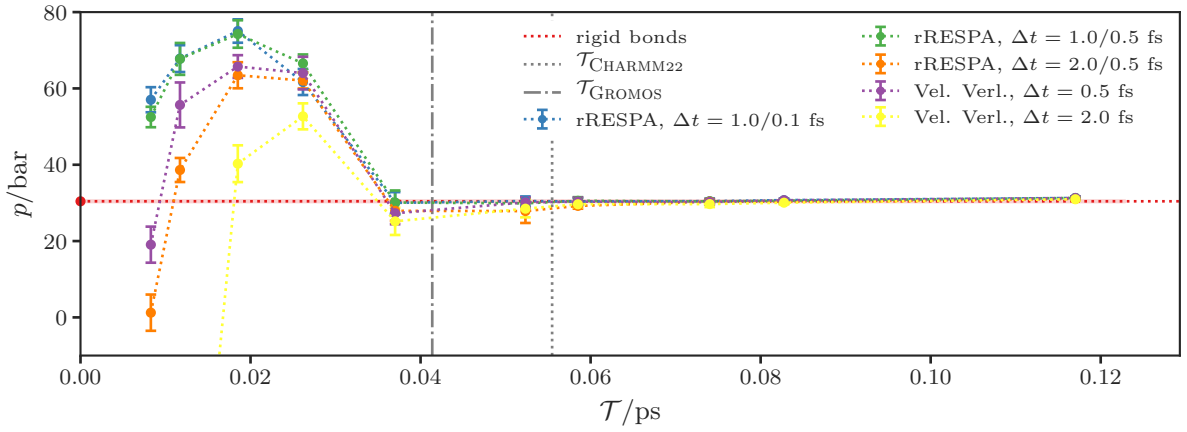

Figure 2.1: Pressure p of propane at $T = 360$ K over the period of the bond vibrations $\mathcal{T}$. Colors represent different integration schemes with different time steps Δt. The red horizontal line shows result of rigid bonds. Vertical lines highlight $\mathcal{T}$ values of the CHARMM (dotted) and the GROMOS force field (dashed).

from this issue at low values of $\mathcal{T}$. For $\mathcal{T} > 0.1\,\text{ps}$, the k_l values are small and therefore the flexible bonds are so loose that results of the flexible bond model deviate from results of a rigid bond model. The results at $\mathcal{T} = 0.12\,\text{ps}$ are no longer equivalent to the results of the stiff bonds within statistical uncertainty. The scale of fig. 2.1 is too coarse to clearly confirm this statement, which is why the Supporting Information gives the results of fig. 2.1, but shown on a finer scale.

For a wide range of moderate values of $\mathcal{T}$ (0.035 ps to 0.085 ps), the pressures as determined from the force field with flexible bonds agree within statistical uncertainties with the pressure p_{rigid} as determined for the rigid bonded molecule. The exact choice of k_l is not important, the k_l values in this plateau region result in statistically equivalent pressures, independent of time steps and integration schemes used.

Grey vertical lines in fig. 2.1 highlight $\mathcal{T}$ values for C—C bonds of the CHARMM22[8] (dotted line) and GROMOS[11] (dashed line) force field, determined from experimental crystallographic and microwave data. The $\mathcal{T}$ values of these two models are located in the plateau region for all considered time steps. We conclude, that for liquid-phase pressure as a rather sensitive static property, a time resolution of 1.0 fs or even 2.0 fs appears to be sufficient for the simulation of bond potentials with force constants in the range $100\,\text{kcal}\,\text{mol}^{-1}\,\text{Å}^{-2} < k_l < 500\,\text{kcal}\,\text{mol}^{-1}\,\text{Å}^{-2}$. For this range we find equivalent results of the flexible force field to the model with rigid bond lengths.

In the preceding discussion we argued that the rigid bond end of the plateau of constant p values at $p = p_{\text{rigid}}$, that is, for high values of $\mathcal{T}$ or low values of k_l, is reached when the flexible bonds are so loose that the results for the flexible model deviate from results of the rigid

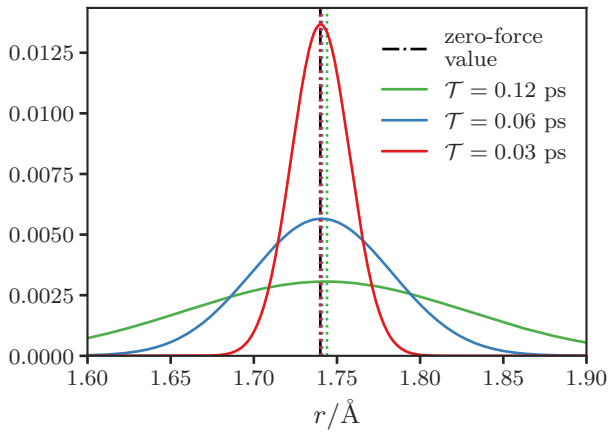

Figure 2.2: Distribution of bond lengths of liquid propane at $T = 360\,\text{K}$ and $\rho = 361.27\,\text{kg}\,\text{m}^{-3}$ (rRESPA with inner time step $\Delta t = 0.1\,\text{fs}$) for different values of bonding force constant k_l. Vertical colored lines represent the respective maximum value of the distribution. The black vertical line shows the reference length r_0.

force field. This explanation is supported by fig. 2.2 which shows the distribution of the bond lengths of propane for three simulations with different k_l values. The higher the k_l values get, the more stiff are the bonds and the more narrow are the bond length distributions. The maximum of the distributions are shown as vertical dashed lines. For loose flexible bonds with $\mathcal{T} = 0.12\,\text{ps}$ and $k_l = 50\,\text{kcal}\,\text{mol}^{-1}\,\text{Å}^{-2}$, which is only one-eighth of the k_l value of GROMOS, one sees deviations of the maximum from the zero-force value (black line). For too low k_l values one can not expect to yield the equivalent results of a rigid force field with bond length defined as the vertical red line.

Figure 2.3 compares results for pressure obtained for propane with the results for the other two substances, ethane and dimethyl ether. The previous results for propane showed that the chosen time step (in the range of 0.1 fs to 2 fs) and the integration scheme have no significant impact on the results. For the other substances, these observations are confirmed. In Figure 2.3 we show results using the rRESPA integrator with an outer time step $\Delta t = 1.0\,\text{fs}$ and an inner time step of 0.1 fs for ethane and propane and of 0.5 fs for dimethyl ether, respectively. To be able to compare different substances, in fig. 2.3 we scale the pressure by the pressure obtained for the model with rigid bond lengths, p/p_{rigid}. The figure shows that for all three substances, the flexible bond model and the rigid bond model are statistically equivalent for sufficiently high values of $\mathcal{T}$, while deviations appear for low values of $\mathcal{T}$. The lowest period of the bond vibrations $\mathcal{T}_{\text{min}}$ for which the flexible bond model can be regarded equivalent to a rigid bond force field is higher for ethane ($\approx 0.052\,\text{ps}$) than for propane or dimethyl ether ($\approx 0.035\,\text{ps}$). The higher number of bonds in a molecule appears to be more well-behaved in the time-integration scheme. We observe no influence of the presence of partial charges in dimethyl ether on the numerical stability of the problem. It is noteworthy that the period of the bond vibrations $\mathcal{T}_{\text{GROMOS}}$ calculated for the bond-energy constant k_l of the GROMOS force

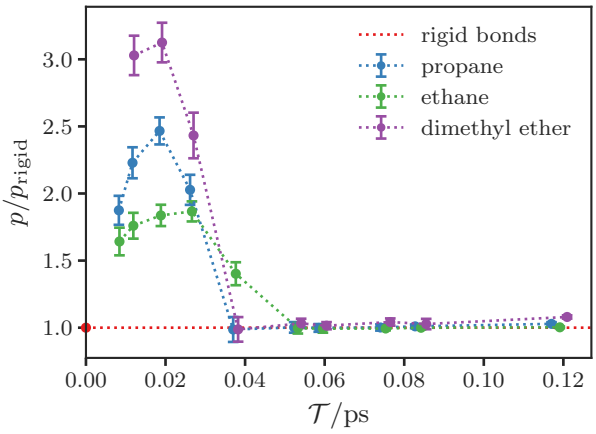

Figure 2.3: Reduced pressure p/p_{rigid} of ethane, propane and dimethyl ether over the period of the bond vibrations $\mathcal{T}$. The red horizontal line shows the result of rigid bonds as reference.

field is below the left end of the plateau $\mathcal{T}_{\text{min}}$, where time steps below $\Delta t = 0.5\,\text{fs}$ are needed.

The main focus of this work is on transport properties. To investigate dynamic properties we regard viscosity, self-diffusion, and thermal conductivity. Figure 2.4 depicts the shear viscosity of propane for varying $\mathcal{T}$ values. The dashed red horizontal line is for the result of the force field with rigid bond lengths, and the 95 % confidence interval is indicated by the red-shaded region. For models with flexible bond lengths, we regard different time steps and different integration methods. As before, we observe a plateau with a viscosity η that is constant within error bars where all computed viscosities are statistically equivalent. We see high deviations for short periods of the bond vibrations ($\mathcal{T} < 0.035\,\text{ps}$) where the integrators (with time steps considered in this work) are not any more appropriate for the high frequent bond vibrations. The rRESPA integrator with a small time step allocated to the harmonic bond length potential does not improve the numerical stability at low $\mathcal{T}$ values. The viscosity of propane from models with flexible bond lengths (for $0.035 > \mathcal{T}$) is equal to the viscosity of the model with rigid bonds within statistical uncertainty.

Figure 2.5 confirms that results for viscosity of propane are transferable to ethane and dimethyl ether. All viscosities of molecules with flexible bonds of $\mathcal{T} > 0.35$ within the error bars agree with the results of molecules with rigid bonds. The normalized 95 % confidence interval around the red dotted line representing the rigid molecules is indicated for each substance by the region shaded in the respective color.

An analysis of the diffusion coefficient D_{self} for the three substances is given in fig. 2.6. The range in $\mathcal{T}$ for which a plateau in self-diffusion coefficient occurs is comparable to the range found for pressure and viscosity above. The lowest period $\mathcal{T}_{\text{min}}$, which yields stable results,

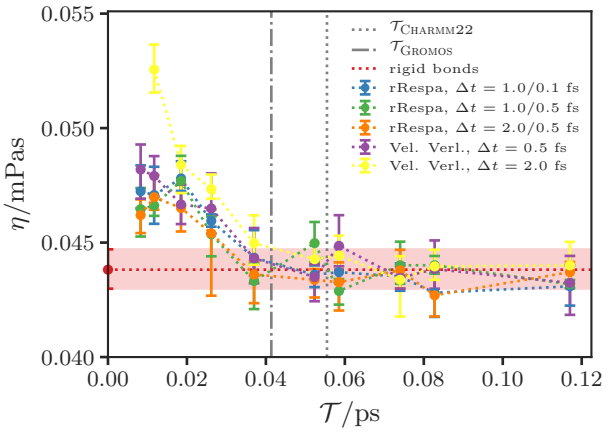

Figure 2.4: Viscosity η of propane at $T = 360\,\text{K}$ over the period of the bond vibrations $\mathcal{T}$. Different colors represent different integration schemes with different time steps Δt. The red horizontal line shows result of rigid bonds. Vertical lines show $\mathcal{T}$ values of common force fields.

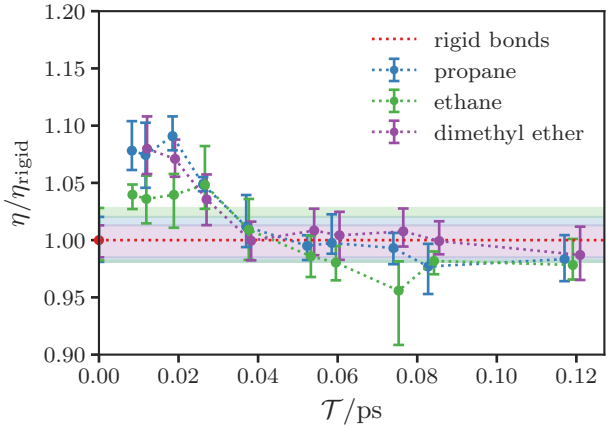

Figure 2.5: Reduced viscosity η/η_{rigid} of ethane, propane and dimethyl ether over the period of the bond vibrations $\mathcal{T}$. The red horizontal line shows the result of rigid bonds as reference.

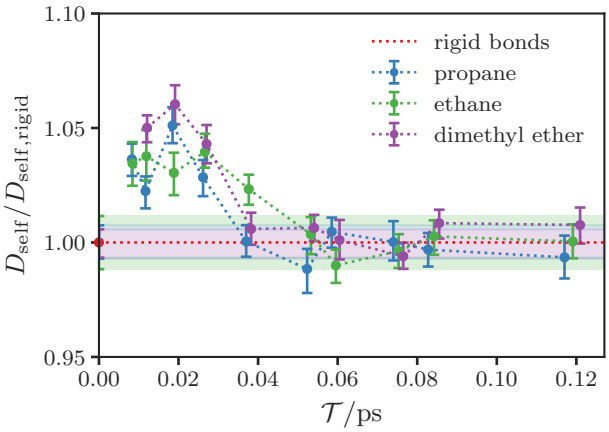

Figure 2.6: Reduced self-diffusion coefficient $D_{\text{self}}/D_{\text{self, rigid}}$ of ethane, propane and dimethyl ether over the period of the bond vibrations $\mathcal{T}$. The red horizontal line shows the result of rigid bonds as reference.

can apparently be observed in several quantities. For the diffusion coefficient, we do not observe higher deviations of flexible bond models from the fixed-bond length models for molecules with two bonds as compared to molecules with only a single bond. For all considered substances, the diffusion coefficient of the original rigid bond force field is reproduced by the flexible bond models within statistical errors, provided that the force constant is appropriately chosen.

Now, we consider thermal conductivity, which is different from the other transport properties, in that the rigid bond length model suppresses intramolecular vibrations. However, these degrees of freedom must be taken into account in order to to properly compare thermal conductivity. We approximately correct the fixed-bond model for intramolecular bond-vibrational degrees of freedom, by adding an analytic vibrational thermal conductivity λ^{vib}, to the thermal

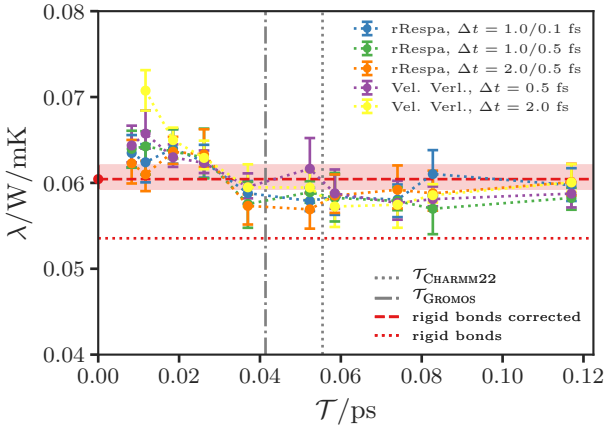

Figure 2.7: Thermal conductivity λ of propane at $T = 360\,\mathrm{K}$ over the period of the bond vibrations $\mathcal{T}$. Different colors represent different integration schemes with different time steps Δt. The red dashed horizontal lines show uncorrected (thin line) and corrected (thick line) result of rigid bonds. Vertical lines show $\mathcal{T}$ values of common force fields.

conductivity determined from molecular simulations, with

$$\lambda^{\mathrm{vib}} = c_v^{\mathrm{vib}} \rho D_{\mathrm{self}} \tag{2.18}$$

as proposed by Liang and Tsai[71]. The expression accounts for the conductivity of thermal energy stored in intramolecular vibrational modes of the considered molecule in the form of the heat capacity c_v^{vib} whereby the transport mechanism is self-diffusion. The density ρ and the self-diffusion coefficient D_{self} are determined from the simulations. The vibrational contribution of the heat capacity is approximated as $c_v^{\mathrm{vib}} = k_{\mathrm{B}} N_{\mathrm{bonds}}$, which means, we assume independent harmonic oscillators for all rigid bonds N_{bonds}[72]. Especially for molecules with several rigid bond length potentials, this is a somewhat coarse approximation. The statistical error of the two quantities, D_{self} and c_v^{vib}, is negligible, as compared to that of the thermal conductivity.

Figure 2.7 presents results for the thermal conductivity. The lower dashed horizontal line represents the results from molecular simulations determined for the rigid bond model. The upper dashed horizontal line is shifted by λ^{vib} corresponding to the results of the corrected rigid bond model. Comparable to other transport coefficients, the thermal conductivity as calculated for the flexible bond force field exhibits a plateau within $0.035\,\mathrm{ps} < \mathcal{T} < 0.1\,\mathrm{ps}$. For bond-energy constants k_l corresponding to $\mathcal{T} < 0.035\,\mathrm{ps}$, we observe a systematic deviation from the values for $\mathcal{T} > 0.035\,\mathrm{ps}$, as we have noticed for the other transport properties. The investigated time steps of 0.5 and 2 fs and both types of integration schemes only act weakly on the results. The plateau value for the thermal conductivity of the flexible bond model agrees within the statistical uncertainty to the corrected rigid bond force field. However, the

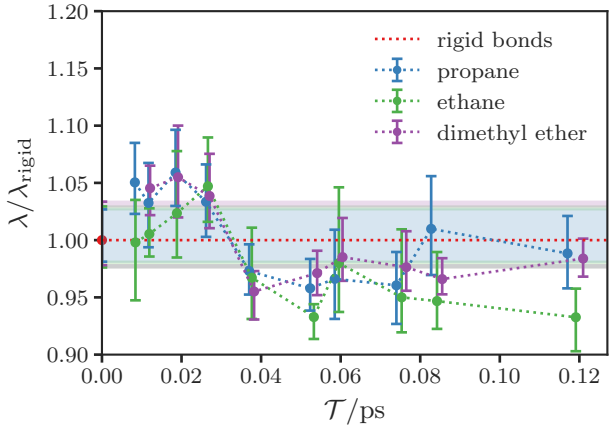

Figure 2.8: Reduced thermal conductivity $\lambda/\lambda_{\mathrm{rigid}}$ of ethane, propane and dimethyl ether over the period of the bond vibrations $\mathcal{T}$. The red dashed horizontal line shows the result of rigid bonds corrected by λ^{vib}, eq. (2.18), as a reference.

error bars of thermal conductivity are significantly wider than those of the other properties because, as described above, the ACF $R_{J_qJ_q}$ can only be averaged over fewer samples as opposed to viscosity or self-diffusion.

Figure 2.8 compares thermal conductivities for three different components, relative to the results of their fixed-bond counter part. Flexible bond force fields of ethane and propane lead to lower values of λ, compared to the fixed-bond models, if we ignore the region of insufficient time step resolution at $\mathcal{T} < 0.035$. Because the results of the rigid bond models seem to systematically underestimate results from models with flexible bonds for all substances and all time steps, it seems that the rigid bond value is overcorrected by the consideration of λ^{vib}. Nevertheless, it is evident in fig. 2.7 that the correction leads to a better agreement of the λ results of molecules with rigid and flexible bonds.

The results shown for liquids at near critical temperature could also be confirmed for the lower temperatures for each substance. Tables with all results of these simulations can be found in the Supporting Information. Also, for exemplary simulations of the gas phase of propane at the VLE at 360 K, the exact same statements can be made as for the results of the liquids: molecules with harmonic binding potentials provide statistically equivalent results as models with rigid bonds. The corresponding simulation results are also summarized in tables in the Supporting Information.

2.4 Conclusion

This study investigates whether a force field with rigid bond lengths can be applied with harmonic bond length potentials and how static and transport properties are thereby affected. Introducing harmonic bond length potentials leads to results for thermodynamic properties and transport properties that are in good agreement to results obtained for the model with rigid bond lengths, provided that the bond-energy constants k_l are appropriately chosen. Suitable values for k_l are in the range of those from fully flexible united atom force fields. We consider ethane and propane as substances with one and two bond length potentials as well as dimethyl ether as a species with (partial) point charges. These substances are described with the TAMie force field, which was developed with rigid bond lengths. The same force field but with flexible bond lengths reproduces results of the rigid bond counterpart to within the overlap of the corresponding 95 % confident intervals for (liquid phase) pressure, shear viscosity, and self-diffusion coefficient. For thermal conductivity a force field with rigid bond lengths and a model with flexible bond lengths are conceptually different. For a flexible bond length model, a certain part of the thermal conductivity is due to the energy stored in intramolecular vibrational bond length modes of the considered molecule, which is transported through self-diffusion of the considered species. We use an approximation for this contribution of the thermal conductivity to correct the rigid bond length model for missing degrees of freedom, which makes the “corrected rigid bond” model and the model with flexible bond lengths comparable. Both models lead to satisfyingly similar values in thermal conductivity.

With increasingly large k_l values, an integration scheme, such as the velocity Verlet integration with a time step of 2 fs, leads at some point to deviations from the expected results, because the highly frequent bond length vibrations can no longer be resolved. The rRESPA integrator offers the possibility of assigning a shorter (inner) time step to the bond length potential and a longer (outer) time step for the other contributions of the force field. The rRESPA integrator with this setting, however, does not improve on the velocity Verlet integrator with the same outer time step. Smaller steps for the integration of the binding potentials did not lead to improvements.

Acknowledgement

The authors acknowledge the support by the state of Baden-Württemberg through bwHPC and the German Research Foundation (DFG) through grant no INST 40/467-1 FUGG (clusters JUSTUS and BinAC).

Supporting Information

Tables with a summary of temperatures, pressures, viscosities, diffusion coefficients and thermal conductivities for all integration methods and time steps; tables with results for a lower temperature for each substance and the results of gas phase simulations of propane at 360K calculated with rRESPA; more detailed description of the thermal conductivity calculation.

Bibliography

[1] O. Lötgering-Lin, M. Fischer, M. Hopp, and J. Gross. Pure Substance and Mixture Viscosities Based on Entropy Scaling and an Analytic Equation of State. *Ind. Eng. Chem. Res.*, **57**(11):4095–4114, 2018. doi:10.1021/acs.iecr.7b04871.

[2] M. Hopp and J. Gross. Thermal conductivity of real substances from excess entropy scaling using PCP-SAFT. *Ind. Eng. Chem. Res.*, **56**(15):4527–4538, 2017. doi:10.1021/acs.iecr.6b04289.

[3] M. Hopp, J. Mele, and J. Gross. Self-Diffusion Coefficients from Entropy Scaling Using the PCP-SAFT Equation of State. *Ind. Eng. Chem. Res.*, **57**(38):12942–12950, 2018. doi:10.1021/acs.iecr.8b02406.

[4] R. A. Messerly, M. C. Anderson, S. M. Razavi, and J. R. Elliott. Improvements and limitations of Mie λ-6 potential for prediction of saturated and compressed liquid viscosity. *Fluid Phase Equilib.*, **483**:101–115, 2019. doi:10.1016/j.fluid.2018.11.002.

[5] M. G. Martin and J. I. Siepmann. Transferable potentials for phase equilibria. 1. United-atom description of n-alkanes. *J. Phys. Chem. B*, **102**(14):2569–2577, 1998. doi:10.1021/jp972543+.

[6] J. Wang, R. M. Wolf, J. W. Caldwell, P. A. Kollman, and D. A. Case. Development and testing of a general amber force field. *J. Comput. Chem.*, **25**(9):1157–1174, 2004. doi:https://doi.org/10.1002/jcc.20035.

[7] W. L. Jorgensen, D. S. Maxwell, and J. Tirado-Rives. Development and testing of the OPLS all-atom force field on conformational energetics and properties of organic liquids. *J. Am. Chem. Soc.*, **118**(45):11225–11236, 1996. doi:10.1021/ja9621760.

[8] B. R. Brooks, R. E. Bruccoleri, B. D. Olafson, D. J. States, S. Swaminathan, and M. Karplus. CHARMM: A program for macromolecular energy, minimization, and dynamics calculations. *J. Comput. Chem.*, **4**(2):187–217, 1983. doi:10.1002/jcc.540040211.

[9] K. Vanommeslaeghe, E. Hatcher, C. Acharya, S. Kundu, S. Zhong, J. Shim, E. Darian, O. Guvench, P. Lopes, I. Vorobyov, and A. D. Mackerell. CHARMM general force field: A force field for drug-like molecules compatible with the CHARMM all-atom additive biological force fields. *J. Comput. Chem.*, pages 671–690, 2009. doi:10.1002/jcc.21367.

[10] T. A. Soares, P. H. Hünenberger, M. A. Kastenholz, V. Kräutler, T. Lenz, R. D. Lins, C. Oostenbrink, and W. F. van Gunsteren. An improved nucleic acid parameter set for the GROMOS force field. *J.*

Comput. Chem., **26**(7):725–737, 2005. doi:10.1002/jcc.20193.

[11] L. D. Schuler, X. Daura, and W. F. Van Gunsteren. An improved GROMOS96 force field for aliphatic hydrocarbons in the condensed phase. *J. Comput. Chem.*, **22**(11):1205–1218, 2001. doi:10.1002/jcc.1078.

[12] C. Oostenbrink, A. Villa, A. E. Mark, and W. F. V. Gunsteren. A biomolecular force field based on the free enthalpy of hydration and solvation: The GROMOS force-field parameter sets 53A5 and 53A6. *J. Comput. Chem.*, **25**(13):1656–1676, 2004. doi:10.1002/jcc.20090.

[13] N. Schmid, A. P. Eichenberger, A. Choutko, S. Riniker, M. Winger, A. E. Mark, and W. F. van Gunsteren. Definition and testing of the GROMOS force-field versions 54A7 and 54B7. *Eur. Biophys. J.*, **40**(7):843–856, 2011. doi:10.1007/s00249-011-0700-9.

[14] A. K. Malde, L. Zuo, M. Breeze, M. Stroet, D. Poger, P. C. Nair, C. Oostenbrink, and A. E. Mark. An Automated Force Field Topology Builder (ATB) and Repository: Version 1.0. *J. Chem. Theory Comput.*, **7**(12):4026–4037, 2011. doi:10.1021/ct200196m.

[15] K. B. Koziara, M. Stroet, A. K. Malde, and A. E. Mark. Testing and validation of the Automated Topology Builder (ATB) version 2.0: prediction of hydration free enthalpies. *J. Comput.-Aided Mol. Des.*, **28**(3):221–233, 2014. doi:10.1007/s10822-014-9713-7.

[16] P. A. Gordon. Influence of simulation details on thermodynamic and transport properties in molecular dynamics of fully flexible molecular models. *Mol. Simul.*, **29**(8):479–487, 2003. doi:10.1080/0892702031000106669.

[17] M. E. Tuckerman, G. J. Martyna, and B. J. Berne. Molecular dynamics algorithm for condensed systems with multiple time scales. *J. Chem. Phys.*, **93**(2):1287–1291, 1990. doi:10.1063/1.459140.

[18] M. Tuckerman, B. J. Berne, and G. J. Martyna. Reversible multiple time scale molecular dynamics. *J. Chem. Phys.*, **97**(3):1990–2001, 1992. doi:10.1063/1.463137.

[19] M. E. Tuckerman and B. J. Berne. Molecular dynamics in systems with multiple time scales: Systems with stiff and soft degrees of freedom and with short and long range forces. *J. Chem. Phys.*, **95**(11):8362–8364, 1991. doi:10.1063/1.461263.

[20] B. J. Berne, M. E. Tuckerman, J. E. Straub, and A. L. R. Bug. Dynamic friction on rigid and flexible bonds. *J. Chem. Phys.*, **93**(7):5084–5095, 1990. doi:10.1063/1.458647.

[21] M. Tuckerman and B. J. Berne. Vibrational relaxation in simple fluids: Comparison of theory and simulation. *J. Chem. Phys.*, **98**(9):7301–7318, 1993. doi:10.1063/1.464723.

[22] J.-P. Ryckaert, G. Ciccotti, and H. J. Berendsen. Numerical integration of the cartesian equations of motion of a system with constraints: molecular dynamics of n-alkanes. *J. Comput. Phys.*, **23**(3):327–341, 1977. doi:10.1016/0021-9991(77)90098-5.

[23] H. C. Andersen. Rattle: A "velocity" version of the shake algorithm for molecular dynamics calculations. *J. Comput. Phys.*, **52**(1):24–34, 1983. doi:10.1016/0021-9991(83)90014-1.

[24] B. Hess, H. Bekker, H. J. C. Berendsen, and J. G. E. M. Fraaije. LINCS: A linear constraint solver for molecular simulations. *J. Comput. Chem.*, **18**(12):1463–1472, 1997. doi:10.1002/(sici)1096-987x(199709)18:12<1463::aid-jcc4>3.0.co;2-h.

[25] W. van Gunsteren and H. Berendsen. Algorithms for macromolecular dynamics and constraint dynamics. *Mol. Phys.*, **34**(5):1311–1327, 1977. doi:10.1080/00268977700102571.

[26] W. van Gunsteren. Constrained dynamics of flexible molecules. *Mol. Phys.*, **40**(4):1015–1019, 1980. doi:10.1080/00268978000102101.

[27] W. F. Van Gunsteren and M. Karplus. Effect of constraints on the dynamics of macromolecules. *Macromolecules*, **15**(6):1528–1544, 1982. doi:10.1021/ma00234a015.

[28] D. Frenkel and B. Smit (editors). *Understanding molecular simulation: from algorithms to applications*. Computational science series ; 1. Academic Press, San Diego [u.a.], 2. ed. edition, 2002. ISBN 0-12-267351-4.

[29] R. B. Bird, M. W. Johnson, and C. F. Curtiss. Potential Flows of Dilute Polymer Solutions by Kramers' Method. *J. Chem. Phys.*, **51**(7):3023–3026, 1969. doi:10.1063/1.1672451.

[30] D. Chandler and B. J. Berne. Comment on the role of constraints on the conformational structure of n-butane in liquid solvents. *J. Chem. Phys.*, **71**(12):5386, 1979. doi:10.1063/1.438326.

[31] I. G. Tironi, R. M. Brunne, and W. F. van Gunsteren. On the relative merits of flexible versus rigid models for use in computer simulations of molecular liquids. *Chem. Phys. Lett.*, **250**(1):19–24, 1996. doi:10.1016/0009-2614(95)01434-9.

[32] B. Hess, H. Saint-Martin, and H. J. C. Berendsen. Flexible constraints: An adiabatic treatment of quantum degrees of freedom, with application to the flexible and polarizable mobile charge densities in harmonic oscillators model for water. *J. Chem. Phys.*, **116**(22):9602–9610, 2002. doi:10.1063/1.1478056.

[33] P. Bordat and F. Müller-Plathe. The shear viscosity of molecular fluids: A calculation by reverse nonequilibrium molecular dynamics. *J. Chem. Phys.*, **116**(8):3362–3369, 2002. doi:10.1063/1.1436124.

[34] D. M. Ferguson. Parameterization and evaluation of a flexible water model. *J. Comput. Chem.*, **16**(4):501–511, 1995. doi:10.1002/jcc.540160413.

[35] J. S. Medina, R. Prosmiti, P. Villarreal, G. Delgado-Barrio, G. Winter, B. González, J. V. Alemán, and C. Collado. Molecular dynamics simulations of rigid and flexible water models: Temperature dependence of viscosity. *Chem. Phys.*, **388**(1-3):9–18, 2011. doi:10.1016/j.chemphys.2011.07.001.

[36] G. Raabe and R. J. Sadus. Molecular dynamics simulation of the effect of bond flexibility on the transport properties of water. *J. Chem. Phys.*, **137**(10):104512, 2012. doi:10.1063/1.4749382.

[37] C. G. Aimoli, E. J. Maginn, and C. R. A. Abreu. Transport properties of carbon dioxide and methane from molecular dynamics simulations. *J. Chem. Phys.*, **141**(13):134101, 2014. doi:10.1063/1.4896538.

[38] M. Zhang, E. Lussetti, L. E. de Souza, and F. Müller-Plathe. Thermal conductivities of molecular liquids by reverse nonequilibrium molecular dynamics. *J. Phys. Chem. B*, **109**(31):15060–15067, 2005. doi:10.1021/jp0512255.

[39] E. Lussetti, T. Terao, and F. Müller-Plathe. Nonequilibrium molecular dynamics calculation of the thermal conductivity of amorphous polyamide-6, 6. *J. Phys. Chem. B*, **111**(39):11516–11523, 2007. doi:10.1021/jp0737956.

[40] M. E. Perez-Blanco and E. J. Maginn. Molecular Dynamics Simulations of CO2at an Ionic Liquid Interface: Adsorption, Ordering, and Interfacial Crossing. *J. Phys. Chem. B*, **114**(36):11827–11837, 2010. doi:10.1021/jp103862v.

[41] C. G. Aimoli, E. J. Maginn, and C. R. Abreu. Force field comparison and thermodynamic property calculation of supercritical CO2 and CH4 using molecular dynamics simulations. *Fluid Phase Equilib.*, **368**:80–90, 2014. doi:10.1016/j.fluid.2014.02.001.

[42] P. A. Gordon. Development of intermolecular potentials for predicting transport properties of hydrocarbons. *J. Chem. Phys.*, **125**(1):014504, 2006. doi:10.1063/1.2208359.

[43] S. Patel, W. V. Wilding, and R. L. Rowley. The use of two-phase molecular dynamics simulations to determine the phase behavior and critical point of propane molecular models. *J. Chem. Phys.*, **134**(2):024101, 2011. doi:10.1063/1.3528117.

[44] K. S. Rane, S. Murali, and J. R. Errington. Monte Carlo Simulation Methods for Computing Liquid–Vapor Saturation Properties of Model Systems. *J. Chem. Theory Comput.*, **9**(6):2552–2566, 2013. doi:10.1021/ct400074p.

[45] A. Hemmen, A. Z. Panagiotopoulos, and J. Gross. Grand Canonical Monte Carlo Simulations Guided by an Analytic Equation of State - Transferable Anisotropic Mie Potentials for Ethers. *J. Phys. Chem. B*, **119**(23):7087–7099, 2015. doi:10.1021/acs.jpcb.5b01806.

[46] A. Hemmen and J. Gross. Transferable Anisotropic United-Atom Force Field Based on the Mie Potential for Phase Equilibrium Calculations: n-Alkanes and n-Olefins. *J. Phys. Chem. B*, **119**(35):11695–11707, 2015. doi:10.1021/acs.jpcb.5b01354.

[47] D. Weidler and J. Gross. Transferable Anisotropic United-Atom Force Field Based on the Mie Potential for Phase Equilibria: Aldehydes, Ketones, and Small Cyclic Alkanes. *Ind. Eng. Chem. Res.*, **55**(46):12123–12132, 2016. doi:10.1021/acs.iecr.6b02182.

[48] D. Weidler and J. Gross. Phase equilibria of binary mixtures with alkanes, ketones, and esters based on the Transferable Anisotropic Mie force field. *Fluid Phase Equilib.*, **490**:123–132, 2019. doi:10.1016/j.fluid.2019.02.009.

[49] H. A. Lorentz. Ueber die Anwendung des Satzes vom Virial in der kinetischen Theorie der Gase. *Ann. Phys.*, **248**(1):127–136, 1881. doi:10.1002/andp.18812480110.

[50] D. Berthelot. Sur le mélange des gaz. *C. R. Hebd. Seanc. Acad. Sci. (Paris)*, **126**:1703–1706, 1898.

[51] J. J. Potoff and D. A. Bernard-Brunel. Mie Potentials for Phase Equilibria Calculations: Application to Alkanes and Perfluoroalkanes. *J. Phys. Chem. B*, **113**(44):14725–14731, 2009. doi:10.1021/jp9072137.

[52] S. Plimpton. Fast parallel algorithms for short-range molecular dynamics. *J. Comput. Phys.*, **117**(1):1–19, 1995. doi:10.1006/jcph.1995.1039.

[53] M. S. Green. Markoff Random Processes and the Statistical Mechanics of Time-Dependent Phenomena. II. Irreversible Processes in Fluids. *J. Chem. Phys.*, **22**(3):398–413, 1954. doi:10.1063/1.1740082.

[54] R. Kubo. Statistical-mechanical theory of irreversible processes. I. General theory and simple applications to magnetic and conduction problems. *J. Phys. Soc. Jpn.*, **12**(6):570–586, 1957. doi:10.1143/JPSJ.12.570.

[55] B. L. Holian and D. J. Evans. Shear viscosities away from the melting line: A comparison of equilibrium and nonequilibrium Molecular Dynamics. *J. Chem. Phys.*, **78**(8):5147–5150, 1983. doi:10.1063/1.445384.

[56] P. J. Daivis and D. J. Evans. Comparison of constant pressure and constant volume nonequilibrium simulations of sheared model decane. *J. Chem. Phys.*, **100**(1):541–547, 1994. doi:10.1063/1.466970.

[57] M. T. Humbert, Y. Zhang, and E. J. Maginn. PyLAT: Python LAMMPS Analysis Tools. *J. Chem. Inf. Model.*, **59**(4):1301–1305, 2019. doi:10.1021/acs.jcim.9b00066.

[58] V. Calandrini, E. Pellegrini, P. Calligari, K. Hinsen, and G. R. Kneller. nMoldyn - Interfacing spectroscopic experiments, molecular dynamics simulations and models for time correlation functions. *JDN*, **12**:201–232, 2011. doi:10.1051/sfn/201112010.

[59] D. Dubbeldam, D. C. Ford, D. E. Ellis, and R. Q. Snurr. A new perspective on the order-n algorithm for computing correlation functions. *Mol. Simul.*, **35**(12-13):1084–1097, 2009. doi:10.1080/08927020902818039.

[60] Y. Zhang, A. Otani, and E. J. Maginn. Reliable Viscosity Calculation from Equilibrium Molecular

Dynamics Simulations: A Time Decomposition Method. *J. Chem. Theory Comput.*, **11**(8):3537–3546, 2015. doi:10.1021/acs.jctc.5b00351.

[61] P. P. Pebay. Formulas for robust, one-pass parallel computation of covariances and arbitrary-order statistical moments. Technical Report SAND2008-6212, U.S. Department of Energy, Office of Scientific and Technical Information, 2008. doi:10.2172/1028931. Office of Scientific and Technical Information.

[62] B. Hess. Determining the shear viscosity of model liquids from molecular dynamics simulations. *J. Chem. Phys.*, **116**(1):209–217, 2002. doi:10.1063/1.1421362.

[63] C. Rey-Castro and L. F. Vega. Transport properties of the ionic liquid 1-ethyl-3-methylimidazolium chloride from equilibrium molecular dynamics simulation. The effect of temperature. *J. Phys. Chem. B*, **110**(29):14426–14435, 2006. doi:10.1021/jp062885s.

[64] D. Markthaler, J. Zeman, J. Baz, J. Smiatek, and N. Hansen. Validation of Trimethylamine-N-oxide (TMAO) Force Fields Based on Thermophysical Properties of Aqueous TMAO Solutions. *J. Phys. Chem. B*, **121**(47):10674–10688, 2017. doi:10.1021/acs.jpcb.7b07774.

[65] I.-C. Yeh and G. Hummer. System-Size Dependence of Diffusion Coefficients and Viscosities from Molecular Dynamics Simulations with Periodic Boundary Conditions. *J. Phys. Chem. B*, **108**(40):15873–15879, 2004. doi:10.1021/jp0477147.

[66] E. J. Maginn, R. A. Messerly, D. J. Carlson, D. R. Roe, and J. R. Elliott. Best Practices for Computing Transport Properties 1. Self-Diffusivity and Viscosity from Equilibrium Molecular Dynamics [Article v1.0]. *Living J. Comput. Mol. Sci.*, **1**(1):6324–, 2018. doi:10.33011/livecoms.1.1.6324.

[67] B. Efron. Bootstrap Methods: Another Look at the Jackknife. *Ann. Stat.*, **7**(1):1–26, 1979. doi:10.1214/aos/1176344552.

[68] A. Grossfield, P. N. Patrone, D. R. Roe, A. J. Schultz, D. Siderius, and D. M. Zuckerman. Best Practices for Quantification of Uncertainty and Sampling Quality in Molecular Simulations [Article v1.0]. *Living J. Comput. Mol. Sci.*, **1**(1):5067–, 2018. doi:10.33011/livecoms.1.1.5067.

[69] R. Hockney and J. Eastwood. *Computer Simulation Using Particles*. Taylor & Francis, 1988. doi:10.1201/9781439822050.

[70] L. Verlet. Computer "Experiments" on Classical Fluids. I. Thermodynamical Properties of Lennard-Jones Molecules. *Phys. Rev.*, **159**(1):98–103, 1967. doi:10.1103/physrev.159.98.

[71] Z. Liang and H.-L. Tsai. The vibrational contribution to the thermal conductivity of a polyatomic fluid. *Mol. Phys.*, **108**(13):1707–1714, 2010. doi:10.1080/00268976.2010.489520.

[72] D. McQuarrie. *Statistical Mechanics*. University Science Books, 2000. ISBN 9781891389153.

3 Transferable Anisotropic United-Atom Mie (TAMie) Force Field: Transport Properties from Equilibrium Molecular Dynamic Simulations

The content of this chapter is a literal quote of the publication:

M. Fischer, G. Bauer, J. Gross: Transferable Anisotropic United-Atom Mie (TAMie) Force Field: Transport Properties from Equilibrium-MD-Simulations. *Industrial & Engineering Chemistry Research*, **59**(18):8855–8869, 2020. doi:10.1021/acs.iecr.0c00848

Abstract

Reliable prediction of transport coefficients for fluids, such as the viscosity, thermal conductivity and diffusion coefficients, is an important prerequisite for process design. Besides experimental measurements and semiempirical correlations, molecular simulations are a promising method to estimate transport properties of fluids over wide ranges of temperatures and pressures. Transport properties are sensitive to the underlying intermolecular potentials. In this work we assess the Transferable Anisotropic united-atom Mie (TAMie) force field regarding the calculation of transport properties. The force field was parametrized for thermodynamic properties with emphasis on vapor–liquid coexistence properties. Equilibrium molecular dynamic simulations are used to calculate all transport properties in a single simulation, using the corresponding Green–Kubo methods. The simulated state points were distributed in the temperature and pressure based on an entropy scaling approach, where the PC-SAFT equation of state is used to calculate residual entropy. Utilizing the favorable behavior of dynamic properties when plotted over the residual entropy, only few simulations are needed to parametrize a correlation function that furthermore enables comparison with experimental data over a wide range of temperatures and pressures. TAMie yields good results for all transport properties and substances investigated (with average absolute deviations of 13 % for viscosity, 18 % for diffusion, and 10 % for thermal conductivity), given that only static properties were considered in the parametrization of the force field. Combining few simulations with the entropy scaling method enables very efficient prediction of transport properties for a large temperature and pressure region.

3.1 Introduction

Transport coefficients such as viscosity, thermal conductivity, or diffusion coefficients are essential for process and apparatus design in chemical engineering. Data for these transport coefficients are less abundant as compared to many static properties, say density to prescribed temperature and pressure. Molecular simulations offer the possibility of predicting these quantities for pure substances and for mixtures.

Transport coefficients can be determined from various molecular dynamics (MD) techniques. In nonequilibrium MD approaches one maintains or creates driving forces and samples the resulting fluxes[1–3], or in reverse nonequilibrium MD one imposes fluxes and samples the resulting gradients of conjugate field variables[4,5]. For viscosity, Maginn and co-workers suggested a method where the relaxation of an initially imposed momentum impulse is observed within a system, and they showed good statistical results with a modest computational (wall-clock time) demand[6]. Alternatively, transport coefficients can be determined from systems in equilibrium, given a suitable ensemble, as a time-dependent response to spontaneous fluctuations. All transport coefficients can thereby be obtained from a single simulation or, for practical reasons, more likely from a set of statistically independent simulations of the same state condition. Our work is concerned with MD simulations of systems in equilibrium, by determining autocorrelation functions according to the Green–Kubo formalism[7–9].

It was observed for Lennard-Jones fluids, that equilibrium MD simulations at fluid conditions give thermal conductivities[10] and viscosities[11] with a small dependence on system size. A comprehensive analysis for shear viscosity was recently given by Kim *et al.* who confirmed results for viscosity are weakly dependent on the size of the simulation box unless rather small simulation boxes are considered, where shear viscosity exhibits complex, oscillatory size-dependent behavior[12]. Self-diffusion coefficients as determined from equilibrium MD simulations, in contrast, show a rather pronounced dependence on the choice of the system size. Dünweg and Kremer found a linear dependence of the self-diffusion coefficient with inverse length of the simulation box[13]. Yeh and Hummer proposed an analytic expression for the size dependence that can conveniently be applied to estimate self-diffusion coefficients for the limit of infinite system size[14]. Their development is based on a hydrodynamic model of particles diffusing in a continuum with defined shear viscosity with periodic boundary conditions. The shear viscosity thus needs to be sampled and known. The correction of Yeh and Hummer is sufficiently reliable, so that Jamali *et al.* proposed applying the correction to determine the viscosity of a fluid by studying the system size dependence of the self-diffusion coefficients[15]. This approach is motivated from the fact that shear viscosities (like thermal conductivities) are sampled with higher statistical uncertainty than self-diffusion coefficients,

because the autocorrelation function of self-diffusion coefficients can be sampled for every molecule of a considered simulation, whereas shear viscosity only has six independent entries, namely the six independent cross-coefficients of the pressure tensor.

Transport coefficients are an important test for force fields and they can serve as training data for optimizing force fields. Our group has proposed the Transferable Anisotropic Mie (TAMie) force field optimized toward phase equilibrium properties, namely vapor pressure and liquid densities[16–20]. The force field has been shown to have considerable predictive capabilities for phase equilibria of mixtures[20,21]. It is a united-atom force field, where van der Waals interactions of hydrogen atoms are grouped together with larger neighboring atoms and the united-atom group is described as a single effective van der Waals interaction site[22–28]. A methylene group ($-CH_3$), for example, is treated as a single effective van der Waals interaction site. In order to better account for the presence of hydrogen atoms, the methylene groups in the TAMie model are moved outward from the position of the carbon atom, as proposed by Toxvaerd[29] and adopted in other force fields[30–32]. The Mie potential is considered for van der Waals interactions with a prescribed attractive exponent of $n = 6$, whereas the repulsive exponent is an adjustable parameter. The additional degree of freedom, compared to a Lennard-Jones potential, with predefined repulsive exponent of $m = 12$, leads to substantially better agreement of simulated properties with experimental properties[16–18,33–35].

It is well recognized that phase equilibrium properties are a meaningful test for force fields, or in turn, phase equilibrium properties are valuable ingredients of a training set for optimizing force fields. With this study, we wish to assess how a force field parametrized solely to (static) phase equilibrium properties predicts transport coefficients of pure fluids. Fernández *et al.* already found good agreement with experiments for transport properties of simple real fluids[36,37], quadrupolar fluids[38] and dipolar fluids[39], using force fields that were developed with no information on transport properties included in the optimization procedures. Guevara-Carrion *et al.* extended the studies on transport properties of force fields adjusted to static properties to methanol, ethanol[40] and water and their mixtures[41]. First assessments of the TAMie force fields were reported by Messerly *et al.*[42] with deviations of approximately 10 % for viscosities of linear alkanes and roughly 20 % for branched alkanes. Our work on 1-alcohols[21,43] showed reasonably good agreement of predicted transport coefficients to experimental data. The deviations from experimental data, however were systematic, i.e. too high diffusion coefficients and too low shear viscosities are found, as expected from a united-atom force field. Messerly *et al.*[44] investigated the force field proposed by Potoff and co-workers, which is also based on a Mie (m-6) potential for the van der Waals interactions[33,35]. They observe overestimated viscosities at rather high pressures, above 600 MPa, attributed to a too repulsive 16-6 Mie force field (with repulsive exponent of $m = 16$).

Our study is facilitated by recent developments in correlating transport coefficients using entropy scaling, as proposed by Rosenfeld[45,46]. Whereas Rosenfeld initially limited entropy scaling to simple, spherically symmetric atomic fluids, it was later observed that entropy scaling also holds for molecular species with complex intermolecular interactions[47–57], namely for substances with strongly nonspherical interactions or directional polar or hydrogen-bonding interactions and for mixtures of such substances[58]. Previous work from our group showed that entropy scaling can be used to develop models for transport properties. Those models allowed experimental viscosities of pure components[57] and of mixtures[58] to be correlated and predicted. Also thermal conductivities[59] and self-diffusion coefficients[60] of pure substances were were regarded. A strength of entropy scaling is that a model parametrized to a few data points (well-distributed in state conditions, as we will show below) can be used for predicting transport properties well outside the range of temperatures and pressures considered for training the model.

In this work, we assess the TAMie force field (initially developed for static thermodynamic properties and phase equilibria) for predicting transport coefficients. We regard self-diffusion coefficients, shear viscosity, and thermal conductivities of pure substances. For a meaningful comparison of the TAMie force field within the entire fluid region (with pressures below $\sim 100\,\mathrm{MPa}$), we select state points about equally distributed in residual entropy. Entropy scaling can then be used to estimate transport coefficients in wide ranges of gaseous and liquid states.

3.2 Methods

3.2.1 Molecular Model

The TAMie force field uses a united atom (UA) description of molecules. Carbon atoms and their adjacent hydrogen atoms are combined to single interaction sites, whereas other atoms are usually considered as individual interaction sites. The intermolecular interactions are described as sum of interactions between pairs of sites. The (nonbonded) interactions between two sites i and j are described by a Mie potential and by fixed point charges

$$u_{ij}\left(r_{ij}\right) = c_{ij}\varepsilon_{ij}\left[\left(\frac{\sigma_{ij}}{r_{ij}}\right)^{n_{ij}} - \left(\frac{\sigma_{ij}}{r_{ij}}\right)^{6}\right] + \frac{q_i q_j}{4\pi\epsilon_0 r_{ij}} \tag{3.1}$$

where r_{ij} denotes the distance between two interaction sites i and j and σ_{ij} and ε_{ij} are size and energy parameters of the Mie potential, respectively. Point charge q_i, defined as a unitless

negative factor of the electron charge, and vacuum permittivity ϵ_0 characterize the Coulombic interactions. The attractive exponent was set to $m_{ij} = 6$ for all sites, whereas the repulsive exponent n_{ij} was part of the parameter adjustment. The constant

$$c_{ij} = \left(\frac{n_{ij}}{n_{ij}-6}\right)\left(\frac{n_{ij}}{6}\right)^{6/\left(n_{ij}-6\right)} \tag{3.2}$$

ensures a minimum of the Mie potential at a value of $-\varepsilon_{ij}$. Two interaction sites located on the same molecule but separated by more than three bonds also interact through the potential, eq. (3.1). The parameters for nonbonded interactions of like (i–i) pairs were extracted from previous publications[16–18,20] and are given in the supporting information. For the parameters of unlike site pairs, Lorentz–Berthelot combining rules are applied as

$$\sigma_{ij} = \left(\sigma_i + \sigma_j\right)/2 \tag{3.3}$$

$$\varepsilon_{ij} = \sqrt{\varepsilon_i \varepsilon_j} \tag{3.4}$$

and the arithmetic mean

$$n_{ij} = \left(n_i + n_j\right)/2 \tag{3.5}$$

is used for the repulsive exponent. This combination rule may lead to fractional exponents if even and odd exponents are combined. There are alternative combination rules for the exponents discussed in literature that circumvent this issue.[61] The TAMie force field was constructed to only apply even exponents, precisely to circumvent fractional exponents, so that the arithmetic mean can be used in this work. It should be emphasized that parameters of the TAMie force field describing the intermolecular interactions were adjusted to experimental liquid–vapor equilibrium data (saturation pressure p_{sat} and liquid density ρ_{L}). The calculated dynamic quantities are predictions, since no transport properties were included in the parametrization of the TAMie force field.

The intramolecular (bonded) interactions are defined in the TAMie force field through potential functions for bond lengths, angle bending, and torsions. The angle bending potential is described by a harmonic potential as

$$u_{\mathrm{bend}}(\theta) = \frac{k_\theta}{2}(\theta - \theta_0)^2 \tag{3.6}$$

where θ_0 is the zero-force angle and k_θ is the force constant. For all substances considered in this study, the torsional potential is defined as

$$\begin{aligned} u_{\text{torsion}} = c_0 &+ c_1 [1 + \cos(\phi)] \\ &+ c_2 [1 - \cos(2\phi)] \\ &+ c_3 [1 + \cos(3\phi)] \end{aligned} \tag{3.7}$$

While the TAMie force field was originally proposed with fixed bond lengths, we here adopt harmonic potentials for the bond lengths. Constant bond lengths require additional, often iterative algorithms to enforce constraints. These constraints suppress vibrational degrees of freedom and consequently have to be accounted for when evaluating e.g. the thermal conductivity as discussed in our previous work.[62] When bonds are modeled with a harmonic potential, typically smaller time steps have to be used to properly sample the fast bond vibrations – a disadvantage we alleviate by using appropriate time steps.

The bond potentials are modeled as

$$u_{\text{bond}} = k_l (r - r_0)^2, \tag{3.8}$$

whereas the original force field uses fixed bond lengths between interaction sites[16–18]. The zero-force bond-length r_0 is set equal to the rigid bond-length of the TAMie model. Our previous study[62] regarded short-chain alkanes and ethers and showed that results of the TAMie force field with properly chosen force constants are equivalent to results of the TAMie model with fixed bond lengths. Equivalent results within reasonably small statistical uncertainties were found for the thermal equation of state, for self-diffusion coefficient and for viscosity. Thermal conductivity, as calculated from the original TAMie model with fixed bond lengths and from the TAMie force field with flexible bond lengths cannot expected to be equivalent. But both models can be brought to close agreement with one another when correcting for the thermal conductivity contribution from bond-vibrations by assuming independent harmonic oscillators[62] for every fixed bond-length. Entropic properties of a model with fixed bond lengths and the same model with flexible bond lengths, of course, cannot be equivalent. The force constant k_l is, in agreement to our earlier study[62], defined as $100\,644\,\mathrm{K\,\mathring{A}^{-2}}$ for all binding types. All bonded parameters of the substances used in this study are summarized in the supporting information.

3.2.2 Simulation Setup

We find it appealing to select state points for conducting simulations based on the principle of entropy scaling, which is briefly introduced here. Rosenfeld[45,46] first proposed that there exists, to excellent approximation, a univariate relation between dimensionless transport coefficients and the residual entropy $s_{\mathrm{res}} = s - s_{\mathrm{id.\,gas}}(T,\rho)$. The coefficients he originally regarded are the self-diffusion coefficient, shear viscosity, and thermal conductivity. The dimensionless transport coefficients are the simulated or experimental values of the transport coefficients divided by an adequate reference. Entropy scaling was initially proposed by Rosenfeld for simple fluids only, but in the meantime several studies showed that the principle also holds for strongly nonspherical, polar and hydrogen-bonding fluids and models were developed for viscosity η[57,58], thermal conductivity λ[59] and self-diffusion coefficient D_{self}[60]. With such a model, say for shear viscosity $\eta^*(s_{\mathrm{res}})$, one calculates $s_{\mathrm{res}}(T,\rho,x)$ for temperature T, composition x and density $\rho(p)$ (for given pressure p) from an equation of state and it is then possible to calculate the corresponding transport property η from $\eta^* = \eta/\eta_{\mathrm{ref}}$.

In this study we use entropy scaling in two ways. First, we select state points approximately equally spaced in residual entropy space. Doing so, we cover the entire fluid region of a considered substance with a defined number of simulations (here 5 simulations for each pure substance). Second, we conduct simulations and use the results to parametrize simple (univariate) models for each transport property for the TAMie force field. These models can subsequently be used for predicting transport properties for the considered substance at any fluid state point (with pressures below $\sim 100\,\mathrm{MPa}$), when combined with s^{res} from an equation of state.

The five state points simulated for each substance in this study are selected using the PC-SAFT[63] equation of state. For this we select pressures (in most cases $p_0 = 1\,\mathrm{MPa}$). The lower limit of the considered s_{res} range is determined by selecting a temperature close to the triple point temperature as $T_0 = T^{\mathrm{TP}} \cdot 1.1$ to 1.5. We use index 0 to indicate the state with the lowest value of s_{res}, corresponding to the highest density and to low temperatures of a liquid phase. With PC-SAFT we calculate the dimensionless entropy $s_0^* = s_{\mathrm{res}}(T_0,p_0)/(N_{\mathrm{A}}k_{\mathrm{b}}m)$, where m is the segment number parameter of PC-SAFT for the substance. We then divide the range of s^*, from s_0^* to $s_{\mathrm{id.\,gas}}^* = 0$, into four equal parts and determine the entropy values of the next three liquid state points, s_1^*, s_2^* and s_3^*. We use PC-SAFT to iterate the temperatures to T_1, T_2 and T_3 in such a way that the values $s^*(p_1,T_1)$, $s^*(p_2,T_2)$ and $s^*(p_3,T_3)$ are evenly distributed. We thereby ensure a liquid state by defining $p_i = \min(p_0, p^{\mathrm{sat}}(T_i)\cdot 1.25), i \in \{1,2,3\}$. The fifth state point is chosen in the gas phase and its entropy is determined as $s_4^* = s^*(T_3, 0.8\cdot p^{\mathrm{sat}}(T_3))$. p^{sat} values in this procedure are also calculated from PC-SAFT.

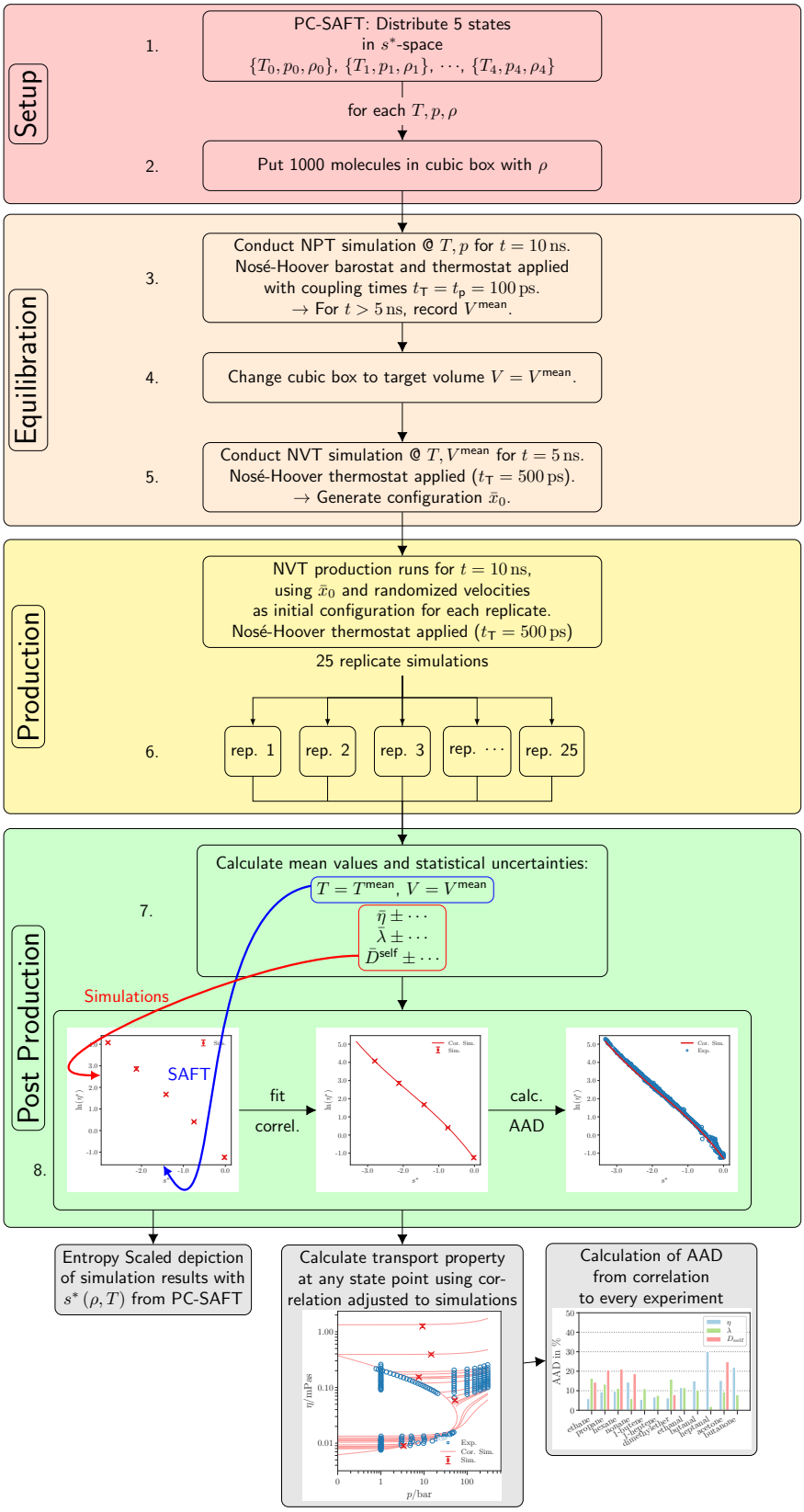

Figure 3.1: Visualization of the workflow used to calculate transport properties in equilibrium molecular dynamics simulations.

This approach yields five state conditions (T, p) that are used to conduct equilibrium MD simulations. All states used in this study are listed in the Supporting Information. We emphasize that calculations with the PC-SAFT equation of state are only used to deliver estimates for the initial conditions of simulations with the TAMie force field. Properties such as equilibrium pressures and densities that are used for analysis in this study are the results of the MD simulations described below and the values from simulations only approximately agree with the initial PC-SAFT state points. The properties as obtained from the simulations are used as input to PC-SAFT to recalculate s^*_{0-4} afterward.

After defining initial conditions T, p, ρ using PC-SAFT, the simulation setup is completed by placing 1000 molecules on a lattice as initial configuration in a box at the density ρ. For each state point found in the way described above, the same simulation procedure is now conducted as shown in the flowchart in fig. 3.1. Simulation details, such as simulation times t and choices for barostat and thermostat, including the coupling times t_p and t_T, are summarized in the flowchart of fig. 3.1. All simulations are performed using the simulation package LAMMPS[64].

The equilibration procedure comprises steps 3 to 5 of fig. 3.1. After conducting an energy minimization, the density of the system is equilibrated in an NpT simulation (step 3). The box volume V is sampled for the second half of the NpT equilibration time and a average equilibrium volume $V^{mean} = \langle V \rangle$ is calculated. After that, the size of cubic box is dynamically adjusted to V^{mean} (step 4). In step 5, the system undergoes another NVT equilibration, yielding a representative configuration which is used to initiate 25 replicate production simulations in NVT, each with different randomized initial velocities, taken from the Boltzmann distribution. In order to ensure a constant temperature over the whole simulation time we apply a Nosé-Hoover thermostat ($t_T = 500\,\mathrm{ps}$) with weak coupling. This thermostat does not influence the kinetics of MD simulations nor the calculation of transport properties.[65] To confirm this fact, we repeated the simulations for hexane without a thermostat in the production phase under otherwise identical simulation conditions. We obtain equivalent results within the statistical accuracy. The results of the NVE simulations are shown in the supporting information. During production (step 6), the pressure tensor entries and the entries of the heat flux, needed for the calculation of shear viscosity η and thermal conductivity λ are written to a file every second time step. The center of mass position of each molecule, used in the calculation of D^{self}, is sampled every 500 steps. For all simulations, the multiple-time-scale integrator rRESPA[66] is used to integrate the equations of motion. We evaluate the bond vibrations with an inner time step of 0.5 fs. All other interactions are calculated with an outer time step of 1.0 fs. An overview of general simulation specifications is given in table 3.1.

Time-step / fs (outer/inner)	1/0.5
Cut-off length / Å	14
Number of molecules	1000
Tail-corrections	U and p
Long range solver	PPPM[67] with $1.0 \cdot 10^{-5}$ desired relative error in forces

Table 3.1: General Simulation Specifications.

3.2.3 Data Analysis

We compute transport properties in this study in equilibrium MD simulations using Green–Kubo methods. Using these methods all transport coefficients, η, λ, and D_{self}, can be calculated from data that originates from the same simulation. The Green–Kubo equations relate transport coefficients to an integral of an autocorrelation function (ACF) of time series that are sampled during simulations. The viscosity η is given by the Green–Kubo equation

$$\eta = \frac{1}{V k_{\mathrm{B}} T} \int_0^\infty R_{J_p J_p}(\tau) \mathrm{d}\tau, \tag{3.9}$$

as the integral of the ACF $R_{J_p J_p}$ of the stress-tensor J_p, according to

$$R_{J_p J_p}(\tau) = \lim_{\Theta \to \infty} \frac{1}{2\Theta} \int_{-\Theta}^{\Theta} J_p^{\alpha\beta}(t+\tau) J_p^{\alpha\beta}(t) \, \mathrm{d}t \tag{3.10}$$

as a function of the lag time τ. $J_p^{\alpha\beta}$ is any off-diagonal element of the stress-tensor (with $\alpha, \beta \in x, y, z$ and $\alpha \neq \beta$). In order to improve the statistics of each simulation, we use the six independent shear components of the stress-tensor ($\left(J_p^{xy} + J_p^{yx}\right)/2$, $\left(J_p^{yz} + J_p^{zy}\right)/2$, $\left(J_p^{xz} + J_p^{zx}\right)/2$, $\left(J_p^{xx} - J_p^{yy}\right)/2$, $\left(J_p^{yy} - J_p^{zz}\right)/2$ and $\left(J_p^{xx} - J_p^{zz}\right)/2$) to calculate an averaged $R_{J_p J_p}(\tau)$[68]. $J_p^{\alpha\beta}$ is calculated from the molecule's center of mass (COM) velocity $\boldsymbol{v}_i$ and the virial $\mathbf{r_{ij}}(\partial u_{ij}(r_{ij})/\partial \mathbf{r_{ij}})$ as

$$J_p^{\alpha\beta} = \sum_{i=1}^{N^{\text{mol.}}} m_i v_i^\alpha v_i^\beta - \sum_{i=1}^{N^{\text{mol.}}} \sum_{j>i}^{N^{\text{mol.}}} r_{ij}^\alpha \frac{\partial u_{ij}(r_{ij})}{\partial r_{ij}^\beta}. \tag{3.11}$$

In the same manner, we can calculate the thermal conductivity as

$$\lambda = \frac{V}{3k_\mathrm{B}T^2}\int_0^\infty R_{J_qJ_q}(\tau)\mathrm{d}\tau \tag{3.12}$$

from the ACF

$$R_{J_qJ_q}(\tau) = \lim_{\Theta\to\infty}\frac{1}{2\Theta}\int_{-\Theta}^{\Theta}\boldsymbol{J}_q(t+\tau)\cdot\boldsymbol{J}_q(t)\,\mathrm{d}t \tag{3.13}$$

of the heat flux $\boldsymbol{J}_q$, which is determined through the per-atom energy e_i and the force $\boldsymbol{f}_{ij} = -\frac{\partial u_i}{\partial \boldsymbol{r}_j}$ due to the per-atom potential energy u_i as

$$\boldsymbol{J}_q = \frac{1}{V}\left[\sum_{i=1}^{N^\mathrm{at.}}\boldsymbol{v}_i e_i + \sum_{i=1}^{N^\mathrm{at.}}\sum_{j>i}^{N^\mathrm{at.}}\boldsymbol{r}_{ij}\left(\boldsymbol{v}_j\cdot\frac{\partial u_i}{\partial \boldsymbol{r}_j}\right)\right] \tag{3.14}$$

The self-diffusion coefficient was calculated using an Einstein relation (that can also be converted into a Green–Kubo equation). The Einstein relation formulates D_self in terms of the slope of the mean squared displacement as

$$D_\mathrm{self} = \frac{1}{6N}\lim_{\tau\to\infty}\frac{\mathrm{d}}{\mathrm{d}\tau}\sum_{i=1}^{N^\mathrm{mol.}}W_i(\tau), \tag{3.15}$$

where W_i denotes the mean squared displacement of the center of mass position $\boldsymbol{r}_i^\mathrm{COM}$ of molecule i at time τ relative to the initial time $\tau_0 = 0$, as

$$W_i(\tau) = \lim_{\Theta\to\infty}\int_0^\Theta\left[\boldsymbol{r}_i^\mathrm{COM}(t+\tau) - \boldsymbol{r}_i^\mathrm{COM}(t)\right]^2\mathrm{d}t. \tag{3.16}$$

The integration in eq. (3.16) averages over different initial times. Moreover, D_self is averaged over all N molecules and therefore has the best statistics of all transport coefficients. After evaluating eq. (3.15), the finite size correction of Yeh and Hummer[14] is applied to the values of D_self.

Calculation of the transport coefficients is done in post processing. We thereby follow the suggestions of Maginn *et al.*, who provided a very helpful and comprehensive summary of best practices in calculating transport properties from equilibrium MD simulations including estimates for statistical uncertainties using a bootstrapping procedure[69]. We use the *fast*

fourier transform algorithm to calculate the ACFs as a convolution in Fourier space.[70,71] The Fourier Transform is convenient because one can effortlessly correlate all samples to one another; i.e., every sample is also the starting point of another time series. This approach replaces elaborate methods to reduce memory demand and computation time in evaluating the autocorrelation function, like the staged time-interval sampling proposed by Dubbeldam *et al.*[72]. The evaluation of the Green–Kubo integrals is done using the *time decomposition method*, proposed by Zhang *et al.*, where the maximum time for the autocorrelation integral is determined by approximating the increasing uncertainty for increasingly long upper bounds of the autocorrelation integral[73]. Statistical errors are given as 95 % confidence interval as obtained from a bootstrapping procedure.[69,74] We generate bootstrap samples by randomly selecting (with replacement) 25 time series of the complete set of 25 replicate simulations. For each bootstrap sample we calculate the transport properties as described above. The procedure is repeated 500 times to generate a distribution of η, λ and D_{self} values, each based on a different subset of all simulated time series. The distributions are used to construct the 95 % confidence interval using the percentile method[74]. For a detailed description of the post processing procedure we refer the reader to our previous work.[62]

The transport coefficients resulting from the MD simulations are analyzed using the entropy scaling method. To do this, we first calculate the entropy for each of the five state points we have simulated per substance. We calculate $s^*(T^{\text{sim}}, \rho^{\text{sim}})$ with PC-SAFT and use the mean value of the temperature from the time series of the production simulation runs as T^{sim} and the constant density of these NVT simulations as ρ^{sim}. The dimensionless quantities $\lambda^* = \lambda/\lambda^{\text{ref}}$, $D^*_{\text{self}} = D_{\text{self}}/D^{\text{ref}}_{\text{self}}$ and $\eta^* = \eta/\eta^{\text{ref}}$, needed for the reference values for entropy scaling, are determined by the equations in table 3.2. The collision integrals $\Omega^{(1,1)*}$ and $\Omega^{(2,2)*}$ are calculated after Neufeld *et al.*[75]; the PC-SAFT parameters m_{ii}, σ_{ii} and ε_{ii}, needed for calculating the references are summarized in the supporting information. The critical reduced entropy s^*_c in the calculation of α is also calculated with PC-SAFT.

Having determined the reduced transport properties η^*, D^*_{self} and λ^* as well as the reduced entropy s^* at each simulated state point, we can adjust correlation functions known from the literature to our simulation results. The functions used for this purpose are listed in table 3.3. Three (η, λ) and four (D_{self}) parameters are adjusted with a least squares fit. Using the equations for the references from table 3.2 for each transport property, it is now straight forward to calculate an estimate for the viscosity $\eta^{\text{cor}}(s^*) = \eta^*(s^*) \cdot \eta^{\text{ref}}$, the thermal conductivity $\lambda^{\text{cor}}(s^*) = \lambda^*(s^*) \cdot \lambda^{\text{ref}}$ and the diffusion coefficient $D^{\text{cor}}_{\text{self}}(s^*) = D^*_{\text{self}}(s^*) \cdot D^{\text{ref}}_{\text{self}}$ corresponding to the TAMie force field, at state points that were not simulated explicitly.

We use this correlation in the residual entropy to compare the simulation results with a wide range of experimental data. Using PC-SAFT we determine $s^*(T, p)$ of a state point at which an

Transport Coefficient	Reference Value
Viscosity[58]	$\eta^{\mathrm{ref}} = \frac{5}{16}\frac{\sqrt{M_{ii}k_{\mathrm{b}}T/(N_{\mathrm{A}}\pi)}}{\sigma_{ii}^2\Omega_{ii}^{(2,2)*}}$
Self-diffusion[60]	$D_{\mathrm{self}}^{\mathrm{ref}} = \frac{3}{8\sigma^2\rho N_{\mathrm{A}}}\frac{1}{\Omega^{(1,1)*}}\sqrt{RT/(\pi M_{ii}m_{ii})}$
Thermal Conductivity[59]	$\lambda^{\mathrm{ref}} = \lambda_{\mathrm{CE}}^{\mathrm{ref}} + \alpha(s^*)\lambda^*$ with $\lambda_{\mathrm{CE}}^{\mathrm{ref}} = \frac{83.235}{10^3}\frac{\sqrt{T/(M_{ii}m_{ii})}}{\sigma^2\Omega_{ii}^{(2,2)*}m_{ii}}$ and $\alpha(s^*) = \exp\left(-s^*/s_{\mathrm{c}}^*\right)$

Table 3.2: Reference Transport Coefficients η^{ref}, $D_{\mathrm{self}}^{\mathrm{ref}}$ and λ^{ref} for the Calculation of Reduced Transport Properties.

Transport Coefficient	Entropy Correlation
Viscosity[58]	$\ln(\eta^*) = A_\eta + B_\eta s^* + C_\eta s^{*2} + D_\eta s^{*3}$
Self-diffusion[60]	$\ln\left(D_{\mathrm{self}}^*\right) = A_{D_{\mathrm{self}}} - B_{D_{\mathrm{self}}}(1.0-\exp(s^*))s^{*2} + C_{D_{\mathrm{self}}}s^{*3}$ with $C_{D_{\mathrm{self}}} \geq 0$
Thermal Conductivity[59]	$\ln(\lambda^*) = A_\lambda + B_\lambda s^* + C_\lambda(1.0-\exp(s^*)) + D_\lambda s^{*2}$

Table 3.3: Entropy correlations of reduced transport properties.

experimental value for a transport property is available. The transport property corresponding to the $s^*(T,p)$ condition can then be calculated. This allows us to estimate transport properties the force field would deliver at (T,p), where experiments are available, but which are not covered from the actually simulated state points. We illustrate this procedure for the viscosity of dimethyl ether (DME). The viscosity of dimethyl ether determined experimentally at pressure $p^{\mathrm{exp}} = 100\,\mathrm{bar}$ and at temperature $T^{\mathrm{exp}} = 293.14\,\mathrm{K}$ is $\eta^{\mathrm{exp}} = 0.145\,\mathrm{mPa\,s}$. Although neither pressure nor temperature of the simulated state points is close to this experimental point, we can estimate the deviation of the simulation from this experiment. We determine the residual entropy of the experimental state as $s^{*,\mathrm{exp}} = s^*(T^{\mathrm{exp}}, \rho(p^{\mathrm{exp}})) = -1.7481$ with PC-SAFT. Then, we evaluate the correlation function for $\ln(\eta^{*,\mathrm{cor}})(s^{*,\mathrm{exp}})$ from table 3.3, where parameters $A_{\eta,\mathrm{DME}}$, $B_{\eta,\mathrm{DME}}$, $C_{\eta,\mathrm{DME}}$, and $D_{\eta,\mathrm{DME}}$ were adjusted to the five simulated viscosities of dimethyl ether. Using the reference η^{ref} from table 3.2 we determine $\eta^{\mathrm{cor}}(s^{*,\mathrm{exp}}) = 0.157\,\mathrm{mPa\,s}$ and calculate its deviation from the experiment as $|\eta^{\mathrm{exp}} - \eta^{\mathrm{cor}}|/\eta^{\mathrm{exp}} = 7.97\,\%$. It is important to point out that the analytic PC-SAFT model is used to calculate the residual entropy for the simulated conditions and for the experimental conditions. Errors of the PC-SAFT model therefore cancel to some extent.

Following this procedure, we estimate absolute average deviations (AAD) of the correlations (adjusted to the simulations) and all experimental data, for which $s^{*,\mathrm{exp}}$ can be determined with PC-SAFT. For example, the AAD for viscosity is calculated for each substance as

$$AAD_\eta = \frac{1}{N_\mathrm{exp}} \sum_{i=1}^{N_\mathrm{exp}} \frac{\left|\eta_i^\mathrm{exp} - \eta_i^\mathrm{cor}\right|}{\eta_i^\mathrm{exp}}, \tag{3.17}$$

where N_exp is the number of experimental data points considered. The AADs of the other transport coefficients are calculated analogously.

3.3 Results and Discussion

In this study we simulated the transport properties of 13 different substances. The substances were selected based on availability of experimental data and existing TAMie parameters in the literature, and we can group them into five classes: alkanes, alkenes as nonpolar species, ketones, aldehydes, and ethers as polar substances. For each class, 1 to 5 substances were selected for which most experimental data is available in the Dortmund Data Bank[76] for η and λ and in several other sources[77–91] for D_self in order to compare the simulations with the largest possible data set using entropy scaling. Despite our selection criteria, for some substances experimental data for certain transport properties are not reported and in these cases it is not possible to quantitatively evaluate the simulation results through AAD values. In total 19 334 experimental data points were considered in the calculation of the AADs shown here, up to 3154 per substance.

The results of this study are organized per transport property and presented in the same way in each case. The structure will be explained in the following subsection.

3.3.1 Viscosity

Figures 3.2–3.6 show the entropy scaled representation of the simulation results, whereby the logarithm of the reduced viscosity is plotted over s^*, as calculated from PC-SAFT. Results of the simulations are represented as crosses with error bars, the correlations (table 3.3) adjusted to the simulation points are shown as solid lines and the experimental data – if available – is represented as circles. Each figure summarizes results of a chemical class, whereby different colors represent the individual substances.

Most substances were studied in the class of alkanes shown in fig. 3.2, namely ethane,

propane, hexane, and nonane. The figure illustrates that the qualitative behavior of the relation $\eta^*(s^*)$ from experimental points is well captured by both, the individual simulation results at five state conditions, and by the correlations (solid lines) adjusted to them. The rightmost simulated point corresponds to a gas phase, noting that ideal gas conditions are characterized by $s^* = 0$. Strongly negative values of s^* represent dense liquid states. In the range $s^* \leq -2$, we observe deviations of simulated results from experimental data exceeding the range, where experimental data scatters. Although state points at low values of residual entropy $s^* \leq -2$ are rather challenging to simulate, because they correspond to high densities and low temperatures, we are convinced the deviations are not due to deficiency in the simulation technique. Rather, deficiencies of the force field in predicting the dynamics of a fluid will be most prominently seen at state points at low temperatures and high densities. Results for ethane shows a typical behavior, already reported in an earlier study of Messerly *et al.* [42]. While the experimental viscosities are underestimated for the alkanes with longer chains, for ethane, in contrast, the predicted viscosities are overestimated.

Figure 3.2 illustrates the large number of experimental data with which we compare our simulation results. For alkanes in fig. 3.2 there are between 382 and 2606 points per substance for a temperature range of 88.1 K (for propane) to 222.15 K (for nonane) and a pressure range of 2.6 kPa (ethane) up to 400 MPa (propane). The experimental data originates from different sources and the entropy scaled representation reveals data that does not follow the univariate behavior and has to be considered as outlier. Entropy scaling can provide strong indications

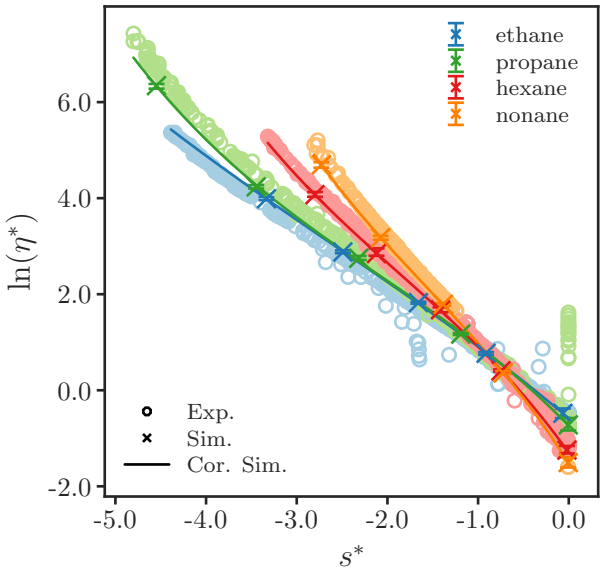

Figure 3.2: Logarithmic depiction of reduced viscosity η^* over the residual entropy s^* for different alkanes. Circles show experimental data from the DDB [76], and crosses represent simulation results. Lines are correlations adjusted to the simulation data.

of non-plausible or inconsistent experimental data[59], as can be seen for example for ethane in the range of $-3 \leq s^* \leq -1$. Nevertheless, to be conservative, all experimental data shown here are included in the calculation of the AAD according to eq. (3.17). The AADs for viscosity summarized in fig. 3.7 confirm rather good agreement with the experimental data for alkanes with AADs below 15 % for the entire fluid region, from gaseous state to liquid states at low temperature and high pressures. A systematic tendency towards higher deviations for longer alkane chains can be observed. There are two possible explanations for the weaker description of long alkane chains. Either the intramolecular force field (i.e. angle and torsion potentials as well as intramolecular van der Waals interactions) does not sufficiently reflect the actual behavior of alkanes. Or, increasing deviations are a result of a coarse-grained (united-atom) force field, where hydrogen interaction sites are not explicitly modeled. The effect of this coarse-graining may act more substantially on longer chains than on molecules with small aspect ratio. The results in fig. 3.2 support this hypothesis for increasingly long chains, because coarse-graining artificially increases the dynamic of the system, leading to too low viscosities and too high self-diffusion coefficients. In order to better assess the quality of results from the TAMie force field, fig. 3.7 also gives the AADs for the entropy scaling method from the literature[58], which resulted from adjusting correlations directly to experimental data. It is remarkable that the correlation from five simulation points for ethane delivers the same accuracy of the correlation as obtained from multiple hundred experimental data points. Also for other n-alkanes the accuracy of the model trained by the TAMie force field is in the same order of magnitude as results obtained by adjusting the model directly to the experimental data.

For the group of alkenes, fig. 3.3, there are noticeably fewer experimental data points available in literature. The simulated state points extend beyond the range of residual entropies s^* covered by the experimental data. In the s^*-ranges, where both, simulations and experiments are available, the simulated viscosities lie within the range of the experimental data. Correlations adjusted to all simulations represent the experimental data very satisfyingly, as also reflected by the AAD-value of less than 7 %, which for 1-butene is in the range of what can best be achieved with the entropy scaling method without filtering experimental data (as seen in fig. 3.7). In the case of 1-heptene, a potential application for the determination of transport properties by means of simulations can be identified. The entropy scaling method requires a broad set of data to reasonably adjust the correlations. For 1-heptene experimental data is scarce and limited to a small range in residual entropy, so that no viscosity model could be parametrized in our earlier work[58]. Results from the TAMie force field or from other force fields might be used to supplement experimental data in order to propose a model for the viscosity of such substances.

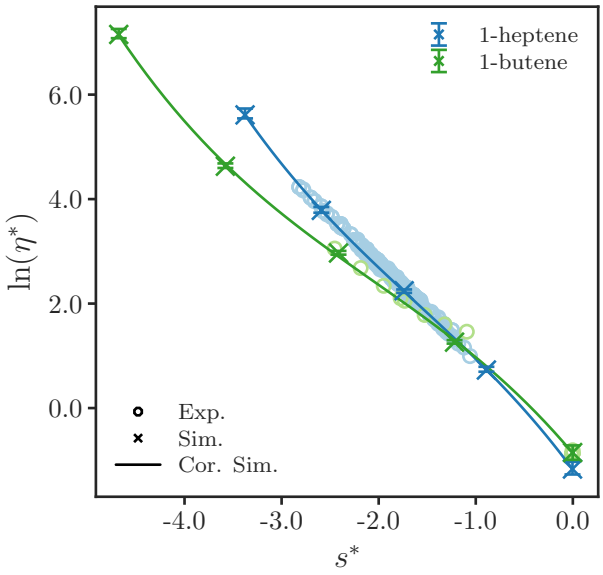

Figure 3.3: Logarithmic depiction of reduced viscosity η^* over the residual entropy s^* for different alkenes. Circles show experimental data from the DDB[76], and crosses represent simulation results. Lines are correlations adjusted to the simulation data.

Larger deviations from experimental data can be seen in fig. 3.4 for the viscosity of aldehydes, where also the qualitative behavior of the experiments is partly not represented by the simulations. Taking a closer look at experimental data for ethanal reveals two 'sets' of points with different courses of $\eta^*(s^*)$, in the range $s^* < -2.0$. One set is accurately traced by the

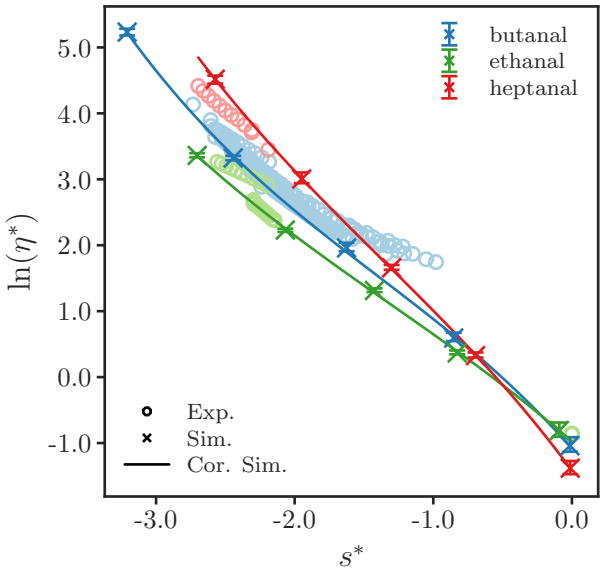

Figure 3.4: Logarithmic depiction of reduced viscosity η^* over the residual entropy s^* for different aldehydes. Circles show experimental data from the DDB[76], and crosses represent simulation results. Lines are correlations adjusted to the simulation data.

correlation adjusted to the simulations. The experimental data of this set comes from four different references. The data set with higher viscosities, that clearly contradicts predictions from the TAMie force field, originates from a single reference and was measured at high pressures of 137 bar to 1378.9 bar. If one chooses to exclude this data set, say by limiting the considered pressures to values $p \leq 100$ bar, the deviation of the TAMie-correlation to the experimental values drops to 4 %. Also 80 % of the experimental data shown in fig. 3.4 for heptanal, the substance with the highest AAD for the viscosity, were measured above 100 bar. For butanal, with an AAD of 15 %, a clear analysis of the TAMie results and of experimental data is difficult. The data shows rather pronounced spread in the entropy scaling diagram, where experimental data is partly contradicting with other experimental data, which also translates to relatively high AAD of 9 % of the original entropy scaling correlation in the literature, that was adjusted to the experiments[58].

The results for the next chemical group, ketones, are summarized in fig. 3.5. Qualitatively the simulations follow the $\eta^*(s^*)$ behavior of the experiments. The four rightmost state points of both substances, located in the range $s^* > -2.5$, show simulated viscosities in satisfying quantitative agreement with experimental values. The point furthest to the left, with the lowest entropy, however, overestimates the viscosity for both ketones. Correspondingly, the correlation runs above the experimental points, leading to comparatively high AADs of 15 % and 21 %, respectively.

As a representative for ethers, we here regard the viscosity of dimethyl ether, shown in fig. 3.6.

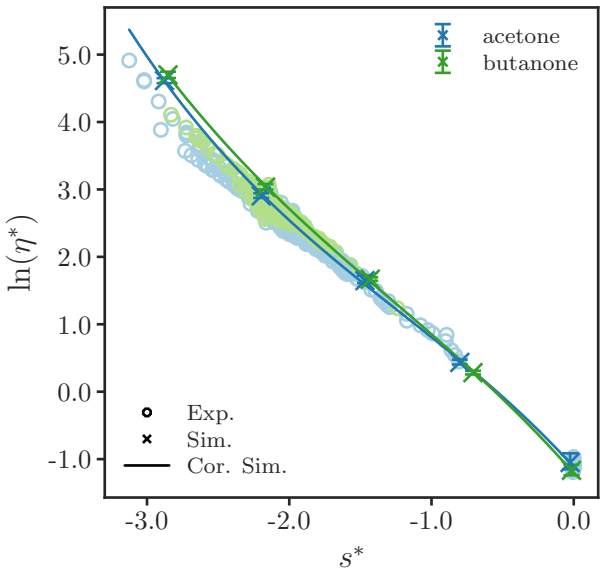

Figure 3.5: Logarithmic depiction of reduced viscosity η^* over the residual entropy s^* for acetone and butanone. Circles show experimental data from the DDB[76], and crosses represent simulation results. Lines are correlations adjusted to the simulation data.

The entropy scaled representation in fig. 3.6a illustrates that the experimental viscosities in both, the gas phase ($-0.1 < s^*$) and the liquid phase ($-2.5 < s^* < -1$) can be predicted very well with the TAMie force field. Figure 3.6b shows a double logarithmic representation of the unscaled viscosity versus pressure. Open circles symbolize experiments, red crosses the results of our simulations. The red lines in fig. 3.6b represent viscosities along isotherms as calculated from the TAMie-correlation. Although the isotherms are selected rather arbitrarily for the purpose of illustrating the course of isotherms in the fluid region, the figure reveals the appeal of the method used: from simulation results at five states (that do not even have to be close to the experimental data in the state space), the transport coefficients can be predicted for any T and p in the fluid region. From the diagram we see that the TAMie-correlation predicts experimental viscosities both at vapor liquid equilibrium (VLE) states – gas-side and liquid-side –, as well as liquid viscosities at high pressures up to 400 bar rather well. For dimethyl ether this visual assessment is also reflected in a low AAD value of 6 %.

The deviations of the viscosity correlations determined with TAMie are summarized for all substances in fig. 3.7. The mean of all AADs is 13 %. This value is surprising, (1) in view of the large number of experimental data that entered the AAD values, (2) considering the fact that we did not filter (non-plausible) experimental data, and (3) noticing that we conducted simulations at merely five state points.

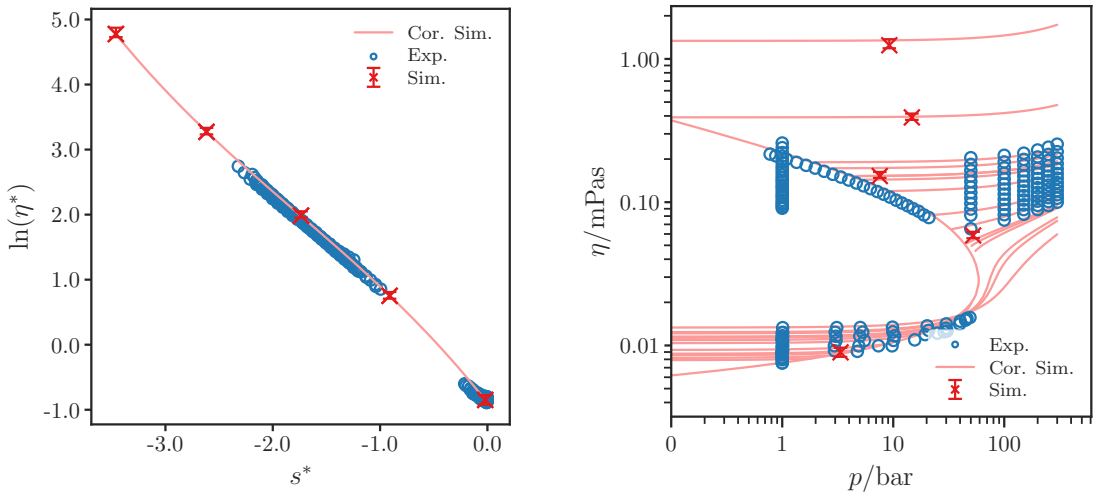

(a) **(b)**

Figure 3.6: Two logarithmic depictions of the results for the viscosity η of dimethyl ether. In both figures, circles show experimental data from the DDB[76], and crosses represent simulation results. (a) shows the reduced viscosity η^* over the residual entropy s^*. Lines in (a) are correlations adjusted to the simulation data. (b) shows viscosity η over pressure p. Lines in (b) are isotherms calculated with a correlation adjusted to the simulation data.

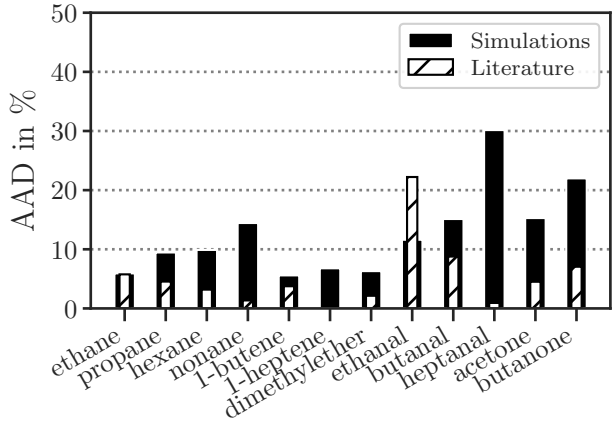

Figure 3.7: AAD in percent of the correlation adjusted to simulation compared to all experimental viscosities available. Additionally, AAD of correlations from the literature[58], adjusted directly to experiments are given.

3.3.2 Self-Diffusion

Results for the self-diffusion coefficients D_{self} are shown in figs. 3.8–3.13. For diffusion there are considerably fewer experimental data available than for the other transport properties. Data with which we can assess the TAMie force field are only available for seven of the substances investigated. Gas diffusion experiments are particularly scarce.

For alkanes, however, data for the gas phase is available, with the exception of nonane, as shown in fig. 3.8. The results of alkanes are therefore important for assessing the predictive quality of the simulations, especially for the gas phase. The qualitative behavior of $D^*_{\text{self}}(s^*)$ is reproduced by the simulated results. The scatter in experimental data is more pronounced for self-diffusion coefficients than for shear viscosity. In our earlier work on self-diffusion[60] we have come to belief the experimental scatter in the entropy scaling diagram is mainly rooted in contradicting data and does not necessarily reveal deficiencies of the entropy scaling principle. The simulated values D_{self} are in reasonable agreement to the experimental data. The simulations are for longer n-alkanes systematically overestimating experimental values of D_{self}, and for ethane they are underestimating D_{self}-values. This may hint either at a non-optimal choice for the anisotropic shift of the CH_3-group, or at the need for partial charges to better represent the quadrupolar charge distribution of ethane. Diffusion coefficients in the gas phase are determined within the experimental range, with a slight tendency to underestimate them.

From our simulation results for self-diffusion coefficients (fig. 3.8) it becomes apparent the ansatz function in table 3.3 for D_{self} is not well suitable for correlating the function $D_{\text{self}}(s^*)$ at low values of s^*, i.e. for the gas phase. The ansatz function enforces a slope of zero for

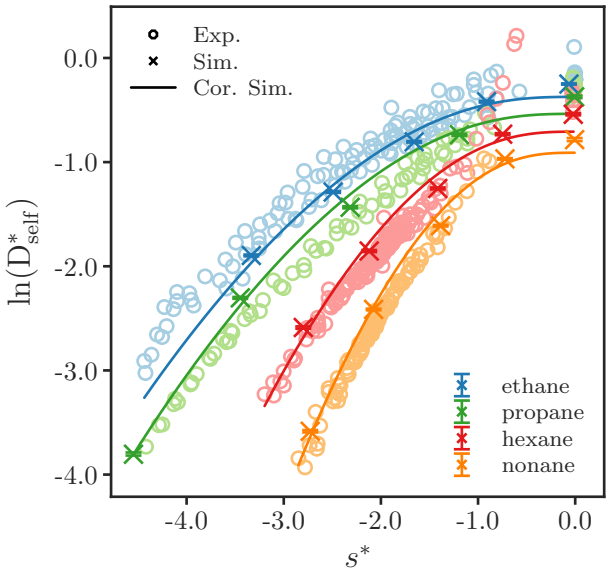

Figure 3.8: Logarithmic depiction of reduced self-diffusion coefficient D^*_{self} over the residual entropy s^* for different alkanes. Circles show experimental data from the literature[77–83,85,87–91], and crosses represent simulation results. Lines are correlations adjusted to the simulation data.

$s^* = 0$ which does not model the experiments nor the simulations adequately. That is an important finding. When we proposed the ansatz function, ref.[60], we had collected fewer experimental data for the vapor phase and had no results from molecular simulations. The few substances, where we had vapor phase data (xenon, argon, carbon dioxide, water) are spherical substances or only mildly elongated. For these species the slope of $D_{self}(s^*)$ at $s^* = 0$ is indeed close to zero. Now, with an extended database and with the results from the molecular simulations from the TAMie force field, we need to revise the ansatz function. For the same reason, namely the deficient ansatz function for D_{self}, the calculated AADs are worse than the simulation results would suggest.

The results for alkenes and aldehydes given in figs. 3.9 and 3.10 demonstrate the scarcity of experimental values for self-diffusion coefficients.

Figure 3.11 gives results of the TAMie force field for ketones, i.e. for acetone and for butanone. The experimental self-diffusion coefficients available for acetone are clearly underestimated by the force field.

Simulation results for dimethyl ether are shown in fig. 3.12. Predictions of TAMie are in good agreement to the experimental data in the liquid phase; experimental values for the gas phase are not available. The strength of expressing results of simulations in an entropy scaled form is evident from fig. 3.12b. The experiments all correspond to comparatively high pressures, whereas the simulations were performed at moderate 30 bar to 50 bar. The predictive power

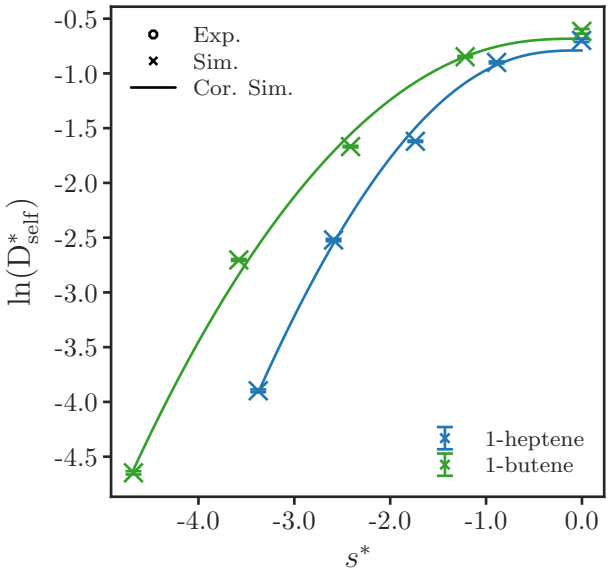

Figure 3.9: Logarithmic depiction of reduced self-diffusion coefficient D^*_{self} over the residual entropy s^* for different alkenes. Lines are correlations adjusted to the simulation data.

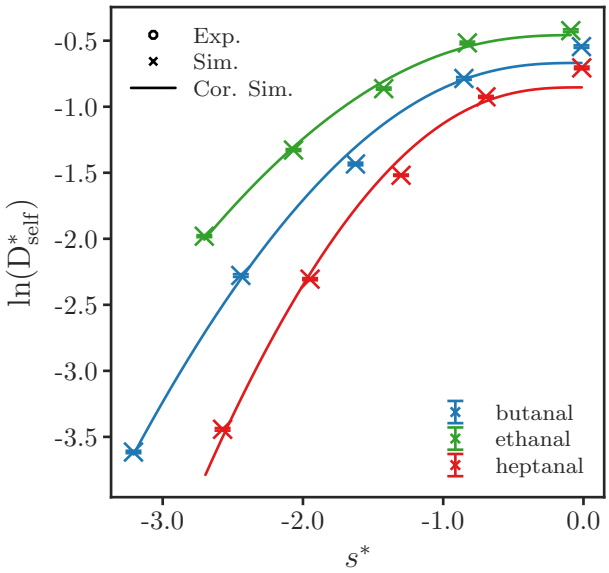

Figure 3.10: Logarithmic depiction of reduced self-diffusion coefficient D^*_{self} over the residual entropy s^* for different aldehydes. Lines are correlations adjusted to the simulation data.

of entropy scaling is remarkably good as seen from the isotherms in fig. 3.12b, reproducing the experimental isothermal data series.

The deviations of the TAMie-correlations from experimental data are summarized in fig. 3.13. We find AADs between 8 % and 25 %, a result that can be appreciated when compared to the native entropy scaling model based on PC-SAFT, also presented in fig. 3.13.

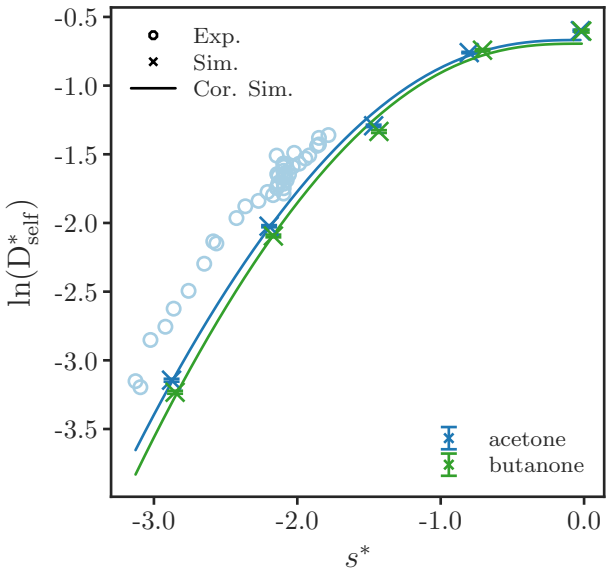

Figure 3.11: Logarithmic depiction of reduced self-diffusion coefficient D^*_{self} over the residual entropy s^* for acetone and for butanone. Circles show experimental data from the literature[91], and crosses represent simulation results. Lines are correlations adjusted to the simulation data.

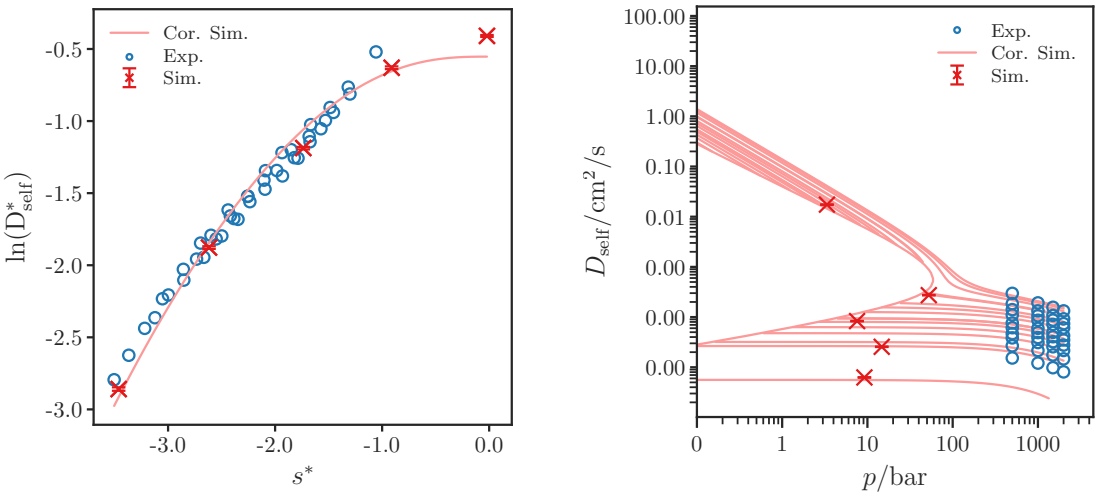

(a) **(b)**

Figure 3.12: Two logarithmic depictions of the results for the self-diffusion coefficient D_{self} of dimethyl ether. In both figures, circles show experimental data from the literature[91], and crosses represent simulation results. (a) shows the reduced self-diffusion coefficient D^*_{self} over the residual entropy s^*. Lines in (a) are correlations adjusted to the simulation data. (b) shows D_{self} over pressure p. Lines in (b) are isotherms calculated with a correlation adjusted to the simulation data.

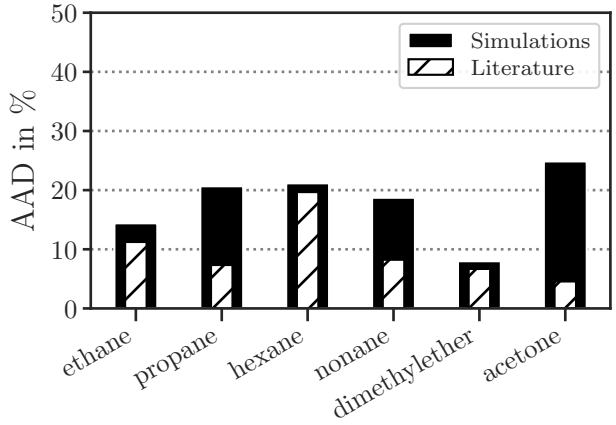

Figure 3.13: AAD in percent of the correlation adjusted to simulation compared to all experimental D_{self} values available. Additionally, AAD of correlations from the literature[60], adjusted directly to experiments are given.

3.3.3 Thermal Conductivity

Figures 3.14–3.19 show the results for the thermal conductivity, starting with the alkanes in fig. 3.14. Results from the TAMie force field reproduce the qualitative behavior of $\ln(\lambda^*)(s^*)$ of the experiments accurately. The simulation results lie within the distribution of the experiments in the entropy scaled diagram, both for the liquid state points as well as for the gas phase. For alkanes we find smaller deviations of the TAMie force field from experiments for longer chain molecules, with the lowest deviations of 6 % for nonane.

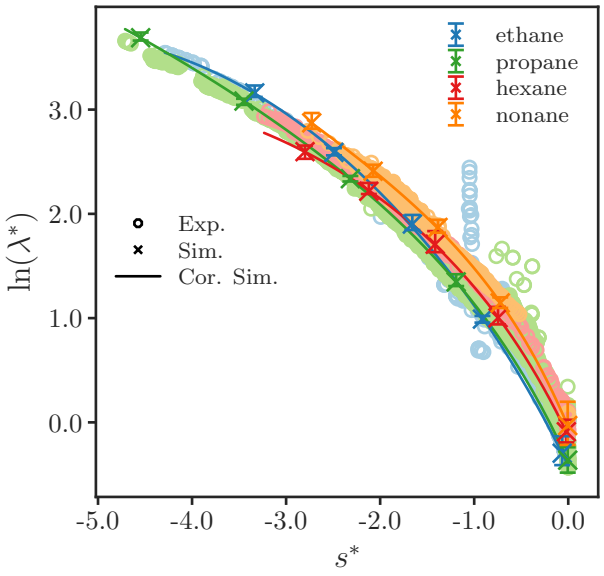

Figure 3.14: Logarithmic depiction of the reduced thermal conductivity λ^* over the residual entropy s^* for different alkanes. Circles show experimental data from the DDB[76], and crosses represent simulation results. Lines are correlations adjusted to the simulation data.

The results for the alkenes in fig. 3.15 are satisfying. In the liquid phase, the thermal conductivities tend to be underestimated, with a total AAD of 11 % for 1-butene. For 1-heptene the simulations underestimate the experimental values for λ, especially in the range $s^* < -2.5$, leading to a total deviation of below 8 %.

Experimental values of thermal conductivity for aldehydes are scarce, see fig. 3.16. The TAMie model is in rather good agreement with the available experimental data for the liquid phase, whereas some deviations are seen for the gas phase. The AAD of the TAMie-correlation is calculated to about 10 % for the aldehydes.

For the ketones, fig. 3.17 shows deviations from the experiments in the vicinity to the critical point ($s^* \approx 0.4$ for both ketones). Thermal conductivity is known significantly increase close to the critical point[92] and it was observed that the critical enhancement is not captured by entropy scaling[59]. However, the critical enhancement is seen for conditions rather close to the critical point and cannot explain the deviations of simulated thermal conductivities and experimental data for ketones. Good overall agreement of the gas phase and liquid phase simulations with experiments results in averaged deviations of less than 10 % for both ketones.

Very satisfying results for thermal conductivities are found for dimethyl ether, as seen in Figure 3.18a. The TAMie force field tends to underestimate the experimental data in the gas phase and overestimates thermal conductivities in the dense liquid phase. fig. 3.18b shows thermal conductivity of dimethyl ether versus pressure, where lines represent isotherms as

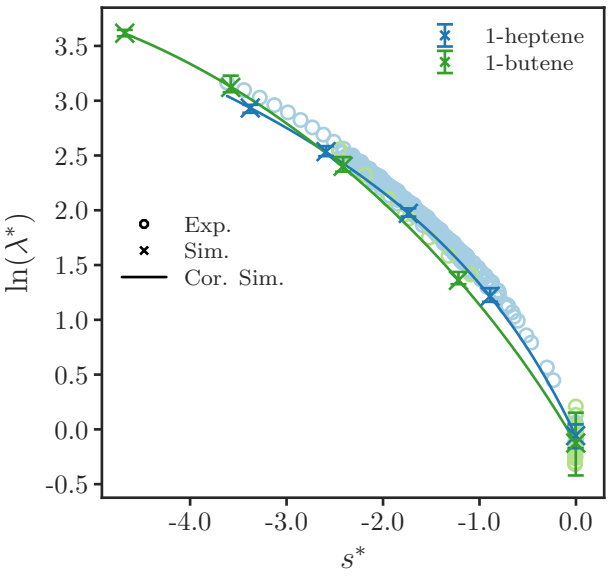

Figure 3.15: Logarithmic depiction of the reduced thermal conductivity λ^* over the residual entropy s^* for different alkenes. Circles show experimental data from the DDB[76], and crosses represent simulation results. Lines are correlations adjusted to the simulation data.

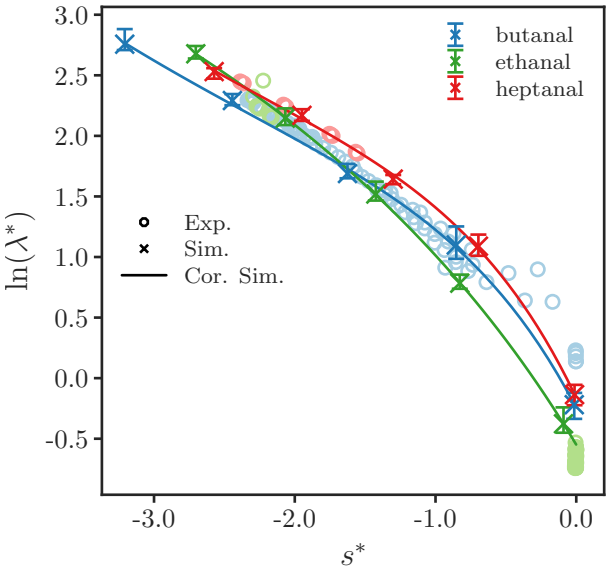

Figure 3.16: Logarithmic depiction of the reduced thermal conductivity λ^* over the residual entropy s^* for different aldehydes. Circles show experimental data from the DDB[76], and crosses represent simulation results. Lines are correlations adjusted to the simulation data.

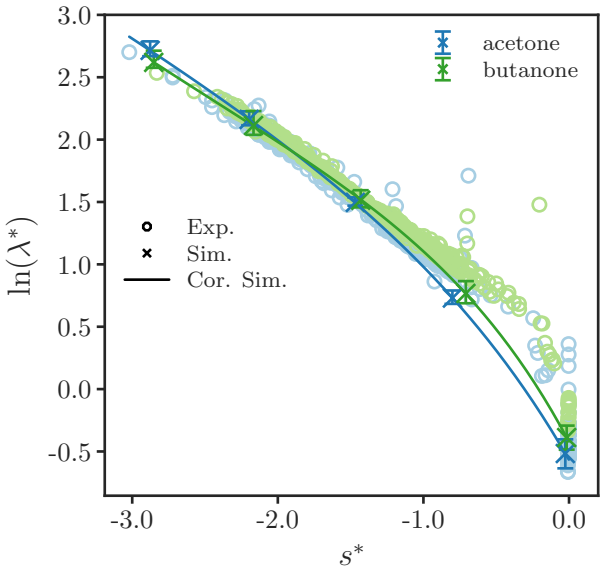

Figure 3.17: Logarithmic depiction of the reduced thermal conductivity λ^* over the residual entropy s^* for acetone and butanone. Circles show experimental data from the DDB[76], and crosses represent simulation results. Lines are correlations adjusted to the simulation data.

determined from TAMie-correlations.

Figure 3.19 summarizes the deviations of predicted thermal conductivities from TAMie-correlations to experimental data for all substances. The overall average AAD are 10 % for all substances, which we consider a very satisfactory result.

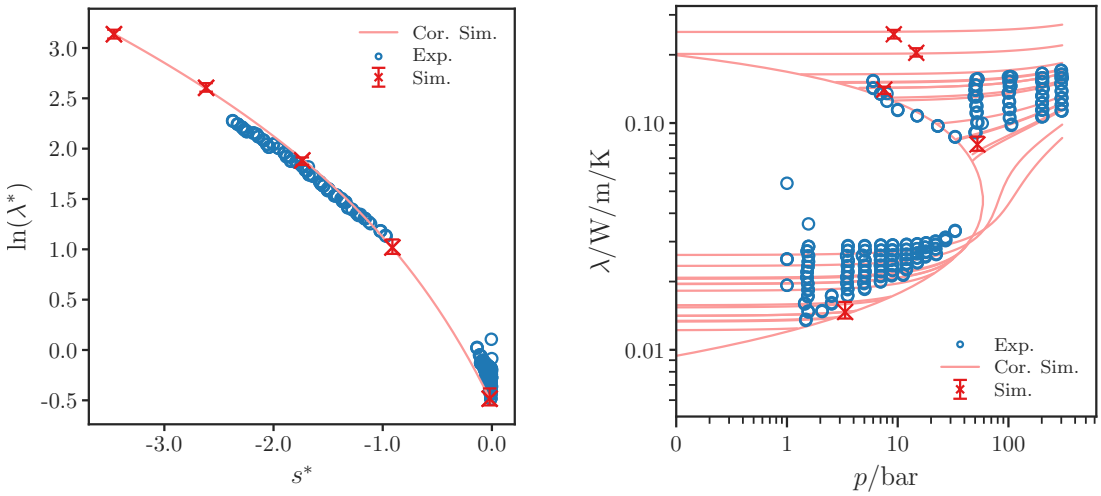

(a) (b)

Figure 3.18: Two logarithmic depictions of the results for the thermal conductivity λ of dimethyl ether. In both figures, circles show experimental data from the DDB[76], and crosses represent simulation results. (a) shows the reduced thermal conductivity λ^* over the residual entropy s^*. Lines in (a) are correlations adjusted to the simulation data. (b) shows λ over pressure p. Lines in (b) are isotherms calculated with a correlation adjusted to the simulation data.

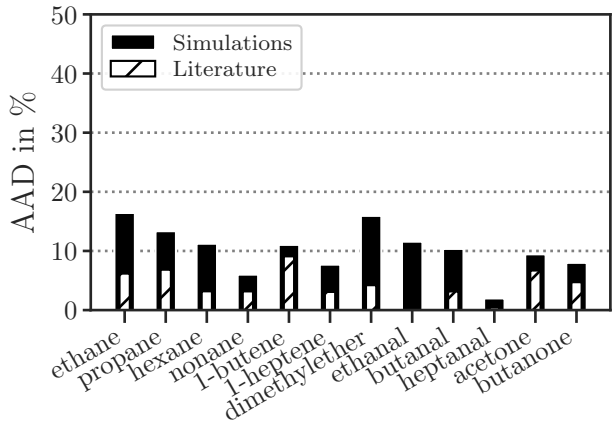

Figure 3.19: AAD in percent of the correlation adjusted to simulation compared to all experimental λ available. Additionally, AAD of correlations from the literature[59], adjusted directly to experiments are given.

3.4 Conclusion

The TAMie force field was originally parametrized using VLE data without considering any dynamic properties. In this study we investigate the predictive power of the TAMie force field for the transport properties, namely shear viscosity, self-diffusion coefficient and thermal conductivity. We conclude that the TAMie force field is rather well suited for the prediction of

transport coefficients.

Simulation results for all transport properties and their statistical uncertainties are obtained simultaneously from a series of equilibrium MD simulations. We propose a workflow, where the state points at which simulations are conducted are selected based on their residual entropy (which we estimate a priori using the PC-SAFT equation of state). We define five state points for each substance, approximately equally distributed in residual entropy. According to entropy scaling that ensures a meaningful distribution of states for conducting simulations covering the entire fluid region. The simulation results are used to adjust a simple correlation function for each transport property, based on the entropy scaling method. We assess predictions of the TAMie force field by comparing the correlation parametrized using simulations with all experimental data available in literature – even for thermodynamic states far from those we have simulated. We observe good agreement of the model, based on the TAMie force field with literature data for all transport coefficients, with AAD-values of 13 % for viscosity, 18 % for diffusion and 10 % for thermal conductivity. The deviations are only mildly higher as compared to an entropy scaling model that directly uses experimental data[57–60].

Generally, molecular simulations are seen to be promising for species with scarce or nonexistent experimental data for one of the transport coefficients. For self-diffusion it is particularly important to provide estimates for self-diffusion coefficients in the gaseous phase. In fact, with this study it became apparent that our ansatz function for the entropy-scaling correlation proposed in earlier work[60] (originally developed with rather limited experimental data for gas phases) does not adequately model the course of the simulation results.

Acknowledgement

This work was funded by Deutsche Forschungsgemeinschaft (DFG, German Research Foundation) under Germany's Excellence Strategy - EXC 2075-390740016. The authors further acknowledge support by the state of Baden-Württemberg through bwHPC and the German Research Foundation (DFG) through Grant No. INST 40/467-1 FUGG (clusters JUSTUS and BinAC).

Supporting Information

PC-SAFT parameters, as well as the parameters of the TAMie force field used in this study, are provided along with tables summarizing temperatures, pressures, viscosities, diffusion coefficients, and thermal conductivities for all simulated state points of all investigated substances; tables with the resulting parameters of the adjusted correlations; and the results of an NVE study of hexane.

Bibliography

[1] D. J. Evans and G. Morriss. *Statistical mechanics of nonequilibrium liquids*. Cambridge University Press, 2008. doi:10.1017/cbo9780511535307.

[2] B. D. Todd and P. J. Daivis. *Nonequilibrium molecular dynamics: theory, algorithms and applications*. Cambridge University Press, 2017. doi:10.1017/9781139017848.

[3] E. J. Maginn and J. R. Elliott. Historical Perspective and Current Outlook for Molecular Dynamics As a Chemical Engineering Tool. *Ind. Eng. Chem. Res.*, **49**(7):3059–3078, 2010. doi:10.1021/ie901898k.

[4] F. Müller-Plathe. A simple nonequilibrium molecular dynamics method for calculating the thermal conductivity. *J. Chem. Phys.*, **106**(14):6082–6085, 1997. doi:10.1063/1.473271.

[5] F. Müller-Plathe. Reversing the perturbation in nonequilibrium molecular dynamics: An easy way to calculate the shear viscosity of fluids. *Phys. Rev. E*, **59**(5):4894, 1999. doi:10.1103/physreve.59.4894.

[6] G. Arya, E. J. Maginn, and H.-C. Chang. Efficient viscosity estimation from molecular dynamics simulation via momentum impulse relaxation. *J. Chem. Phys.*, **113**(6):2079–2087, 2000. doi:10.1063/1.482019.

[7] M. S. Green. Markoff Random Processes and the Statistical Mechanics of Time-Dependent Phenomena. II. Irreversible Processes in Fluids. *J. Chem. Phys.*, **22**(3):398–413, 1954. doi:10.1063/1.1740082.

[8] R. Kubo. Statistical-Mechanical Theory of Irreversible Processes. I. General Theory and Simple Applications to Magnetic and Conduction Problems. *J. Phys. Soc. Jpn.*, **12**(6):570–586, 1957. doi:10.1143/jpsj.12.570.

[9] R. Zwanzig. Time-correlation functions and transport coefficients in statistical mechanics. *Annu. Rev. Phys. Chem.*, **16**(1):67–102, 1965. doi:10.1146/annurev.pc.16.100165.000435.

[10] G. V. Paolini, G. Ciccotti, and C. Massobrio. Nonlinear thermal response of a Lennard-Jones fluid near the triple point. *Phys. Rev. A*, **34**:1355–1362, 1986. doi:10.1103/physreva.34.1355.

[11] J.-P. Ryckaert, A. Bellemans, G. Ciccotti, and G. V. Paolini. Evaluation of transport coefficients of simple fluids by molecular dynamics: Comparison of Green-Kubo and nonequilibrium approaches

for shear viscosity. *Phys. Rev. A*, **39**:259–267, 1989. doi:10.1103/physreva.39.259.

[12] K.-S. Kim, M. H. Han, C. Kim, Z. Li, G. E. Karniadakis, and E. K. Lee. Nature of intrinsic uncertainties in equilibrium molecular dynamics estimation of shear viscosity for simple and complex fluids. *J. Chem. Phys.*, **149**(4):044510, 2018. doi:10.1063/1.5035119.

[13] B. Dünweg and K. Kremer. Molecular dynamics simulation of a polymer chain in solution. *J. Chem. Phys.*, **99**(9):6983–6997, 1993. doi:10.1063/1.465445.

[14] I.-C. Yeh and G. Hummer. System-Size Dependence of Diffusion Coefficients and Viscosities from Molecular Dynamics Simulations with Periodic Boundary Conditions. *J. Phys. Chem. B*, **108**(40):15873–15879, 2004. doi:10.1021/jp0477147.

[15] S. H. Jamali, R. Hartkamp, C. Bardas, J. Sohl, T. J. H. Vlugt, and O. A. Moultos. Shear Viscosity Computed from the Finite-Size Effects of Self-Diffusivity in Equilibrium Molecular Dynamics. *J. Chem. Theory Comput.*, **14**(11):5959–5968, 2018. doi:10.1021/acs.jctc.8b00625.

[16] A. Hemmen and J. Gross. Transferable Anisotropic United-Atom Force Field Based on the Mie Potential for Phase Equilibrium Calculations: n-Alkanes and n-Olefins. *J. Phys. Chem. B*, **119**(35):11695–11707, 2015. doi:10.1021/acs.jpcb.5b01354.

[17] A. Hemmen, A. Z. Panagiotopoulos, and J. Gross. Grand Canonical Monte Carlo Simulations Guided by an Analytic Equation of State - Transferable Anisotropic Mie Potentials for Ethers. *J. Phys. Chem. B*, **119**(23):7087–7099, 2015. doi:10.1021/acs.jpcb.5b01806.

[18] D. Weidler and J. Gross. Transferable Anisotropic United-Atom Force Field Based on the Mie Potential for Phase Equilibria: Aldehydes, Ketones, and Small Cyclic Alkanes. *Ind. Eng. Chem. Res.*, **55**(46):12123–12132, 2016. doi:10.1021/acs.iecr.6b02182.

[19] D. Weidler and J. Gross. Individualized force fields for alkanes, olefins, ethers and ketones based on the transferable anisotropic Mie potential. *Fluid Phase Equilib.*, **470**:101–108, 2018. doi:10.1016/j.fluid.2018.02.012.

[20] D. Weidler and J. Gross. Phase equilibria of binary mixtures with alkanes, ketones, and esters based on the Transferable Anisotropic Mie force field. *Fluid Phase Equilib.*, **490**:123–132, 2019. doi:10.1016/j.fluid.2019.02.009.

[21] J. Baz, N. Hansen, and J. Gross. Transferable Anisotropic Mie-Potential Force Field for n-Alcohols: Static and Dynamic Fluid Properties of Pure Substances and Binary Mixtures. *Ind. Eng. Chem. Res.*, **59**(2):919–929, 2019. doi:10.1021/acs.iecr.9b05323.

[22] W. L. Jorgensen, J. D. Madura, and C. J. Swenson. Optimized Intermolecular Potential Functions for Liquid Hydrocarbons. *J. Am. Soc.*, **106**:6638–6646, 1984. doi:10.1021/ja00334a030.

[23] W. L. Jorgensen and C. J. Swenson. Optimized Intermolecular Potential Functions for Amides

and Peptides. Structure and Properties of Liquid Amides. *J. Am. Soc.*, **107**:569–578, 1985. doi:10.1021/ja00289a008.

[24] W. L. Jorgensen. Optimized Intermolecular Potential Functions for Liquid Alcohols. *J. Phys. Chem.*, **90**:1276–1284, 1986. doi:10.1021/j100398a015.

[25] M. G. Martin and J. I. Siepmann. Transferable Potentials for Phase Equilibria. 1. United-Atom Description of n-Alkanes. *J. Phys. Chem. B*, **102**(14):2569–2577, 1998. doi:10.1021/jp972543+.

[26] M. G. Martin and J. I. Siepmann. Novel Configurational-Bias Monte Carlo Method for Branched Molecules. Transferable Potentials for Phase Equilibria. 2. United-Atom Description of Branched Alkanes. *J. Phys. Chem. B*, **103**(21):4508–4517, 1999. doi:10.1021/jp984742e.

[27] C. D. Wick, M. G. Martin, and J. I. Siepmann. Transferable Potentials for Phase Equilibria. 4. United-Atom Description of Linear and Branched Alkenes and Alkylbenzenes. *J. Phys. Chem. B*, **104**(33):8008–8016, 2000. doi:10.1021/jp001044x.

[28] B. Chen, J. J. Potoff, and J. I. Siepmann. Monte Carlo Calculations for Alcohols and Their Mixtures with Alkanes. Transferable Potentials for Phase Equilibria. 5. United-Atom Description of Primary, Secondary, and Tertiary Alcohols. *J. Phys. Chem. B*, **105**(15):3093–3104, 2001. doi:10.1021/jp003882x.

[29] S. Toxvaerd. Molecular dynamics calculation of the equation of state of alkanes. *J. Chem. Phys.*, **93**(6):4290–4295, 1990. doi:http://dx.doi.org/10.1063/1.458709.

[30] P. Ungerer, C. Beauvais, J. Delhommelle, A. Boutin, B. Rousseau, and A. H. Fuchs. Optimization of the anisotropic united atoms intermolecular potential forn-alkanes. *J. Chem. Phys.*, **112**(12):5499–5510, 2000. doi:10.1063/1.481116.

[31] N. Ferrando, V. Lachet, J.-M. Teuler, and A. Boutin. Transferable Force Field for Alcohols and Polyalcohols. *J. Phys. Chem. B*, **113**(17):5985–5995, 2009. doi:10.1021/jp810915z. PMID: 19344171.

[32] N. Ferrando, V. Lachet, J. Pérez-Pellitero, A. D. Mackie, P. Malfreyt, and A. Boutin. A Transferable Force Field To Predict Phase Equilibria and Surface Tension of Ethers and Glycol Ethers. *J. Phys. Chem. B*, **115**(36):10654–10664, 2011. doi:10.1021/jp203278t. PMID: 21800821.

[33] J. J. Potoff and D. A. Bernard-Brunel. Mie Potentials for Phase Equilibria Calculations: Application to Alkanes and Perfluoralkanes. *J. Phys. Chem. B*, **113**:14725–14731, 2009. doi:10.1021/jp9072137.

[34] J. J. Potoff and G. Kamath. Mie Potentials for Phase Equilibria: Application to Alkenes. *J. Chem. Eng. Data*, **59**(10):3144–3150, 2014. doi:10.1021/je500202q.

[35] J. R. Mick, M. Soroush Barhaghi, B. Jackman, L. Schwiebert, and J. J. Potoff. Optimized Mie

Potentials for Phase Equilibria: Application to Branched Alkanes. *J. Chem. Eng. Data*, **62**(6):1806–1818, 2017. doi:10.1021/acs.jced.6b01036.

[36] G. A. Fernández, J. Vrabec, and H. Hasse. A molecular simulation study of shear and bulk viscosity and thermal conductivity of simple real fluids. *Fluid Phase Equilib.*, **221**(1):157–163, 2004. doi:10.1016/j.fluid.2004.05.011.

[37] G. Fernández, J. Vrabec, and H. Hasse. Self diffusion and binary Maxwell-Stefan diffusion in simple fluids with the Green-Kubo method. *Int. J. Thermophys.*, **25**(1):175–186, 2004. doi:10.1023/b:ijot.0000022333.07168.c4.

[38] G. A. Fernández, J. Vrabec, and H. Hasse. Shear viscosity and thermal conductivity of quadrupolar real fluids from molecular simulation. *Mol. Simul.*, **31**(11):787–793, 2005. doi:10.1080/08927020500252599.

[39] G. A. Fernández, J. Vrabec, and H. Hasse. Shear viscosity and thermal conductivity of dipolar real fluids from equilibrium molecular dynamics simulation. *Cryogenics*, **46**(10):711–717, 2006. doi:10.1016/j.cryogenics.2006.05.004.

[40] G. Guevara-Carrion, C. Nieto-Draghi, J. Vrabec, and H. Hasse. Prediction of transport properties by molecular simulation: methanol and ethanol and their mixture. *J. Phys. Chem. B*, **112**(51):16664–16674, 2008. doi:10.1021/jp805584d.

[41] G. Guevara-Carrion, J. Vrabec, and H. Hasse. Prediction of self-diffusion coefficient and shear viscosity of water and its binary mixtures with methanol and ethanol by molecular simulation. *J. Chem. Phys.*, **134**(7):074508, 2011. doi:10.1063/1.3515262.

[42] R. A. Messerly, M. C. Anderson, S. M. Razavi, and J. R. Elliott. Improvements and limitations of Mie λ-6 potential for prediction of saturated and compressed liquid viscosity. *Fluid Phase Equilib.*, **483**:101–115, 2019. doi:10.1016/j.fluid.2018.11.002.

[43] J. Baz, N. Hansen, and J. Gross. On the use of transport properties to discriminate Mie-type molecular models for 1-propanol optimized against VLE data. *EPJ ST*, **227**(14):1529–1545, 2019. doi:10.1140/epjst/e2019-800178-4.

[44] R. A. Messerly, M. C. Anderson, S. M. Razavi, and J. R. Elliott. Mie 16–6 force field predicts viscosity with faster-than-exponential pressure dependence for 2, 2, 4-trimethylhexane. *Fluid Phase Equilib.*, **495**:76–85, 2019. doi:10.1016/j.fluid.2019.05.013.

[45] Y. Rosenfeld. Relation between the transport coefficients and the internal entropy of simple systems. *Phys. Rev. A*, **15**(6):2545, 1977. doi:10.1103/physreva.15.2545.

[46] Y. Rosenfeld. A quasi-universal scaling law for atomic transport in simple fluids. *J. Phys.: Condens. Matter*, **11**(28):5415, 1999. doi:10.1088/0953-8984/11/28/303.

[47] M. Dzugutov. A universal scaling law for atomic diffusion in condensed matter. *Nature*, **381**:137–139, 1996. doi:10.1038/381137a0.

[48] L. T. Novak. Self-Diffusion Coefficient and Viscosity in Fluids. *Int. J. Chem. React. Eng.*, **9**(A63):1–25, 2011. doi:10.1515/1542-6580.2640.

[49] J.-L. Bretonnet. Self-diffusion coefficient of dense fluids from the pair correlation function. *J. Chem. Phys.*, **117**(20):9370–9373, 2002. doi:10.1063/1.1516594.

[50] R. Chopra, T. M.Truskett, and J. R. Errington. On the Use of Excess Entropy Scaling to Describe the Dynamic Properties of Water. *J. Phys. Chem. B*, **114**(32):10558–10566, 2010. doi:10.1021/jp1049155.

[51] R. Chopra, T. M. Truskett, and J. R. Errington. Excess-entropy scaling of dynamics for a confined fluid of dumbbell-shaped particles. *Phys. Rev. E*, **82**:041201, 2010. doi:10.1103/physreve.82.041201.

[52] T. Goel, C. N. Patra, T. Mukherjee, and C. Chakravarty. Excess entropy scaling of transport properties of Lennard-Jones chains. *J. Chem. Phys.*, **129**(16):164904, 2008. doi:10.1063/1.2995990.

[53] W. P. Krekelberg, T. Kumar, J. Mittal, J. R. Errington, and T. M. Truskett. Anomalous structure and dynamics of the Gaussian-core fluid. *Phys. Rev. E*, **79**:031203, 2009. doi:10.1103/physreve.79.031203.

[54] W. P. Krekelberg, M. J. Pond, G. Goel, V. K. Shen, J. R. Errington, and T. M. Truskett. Generalized Rosenfeld scalings for tracer diffusivities in not-so-simple fluids: Mixtures and soft particles. *Phys. Rev.*, **80**(6):061205, 2009. doi:10.1103/physreve.80.061205.

[55] M. J. Pond, J. R. Errington, and T. M. Truskett. Communication: Generalizing Rosenfeld's excess-entropy scaling to predict long-time-diffusivity in dense fluids of Brownian particles: From hard to ultrasoft interactions. *J. Chem. Phys.*, **134**(8):081101, 2011. doi:10.1063/1.3559676.

[56] S. Pieprzyk, D. M. Heyes, and A. C. Brańka. Thermodynamic properties and entropy scaling law for diffusivity in soft spheres. *Phys. Rev. E*, **90**(1), 2014. doi:10.1103/physreve.90.012106.

[57] O. Lötgering-Lin and J. Gross. Group Contribution Method for Viscosities Based on Entropy Scaling Using the Perturbed-Chain Polar Statistical Associating Fluid Theory. *Ind. Eng. Chem. Res.*, **54**(32):7942–7952, 2015. doi:10.1021/acs.iecr.5b01698.

[58] O. Lötgering-Lin, M. Fischer, M. Hopp, and J. Gross. Pure Substance and Mixture Viscosities Based on Entropy Scaling and an Analytic Equation of State. *Ind. Eng. Chem. Res.*, **57**(11):4095–4114, 2018. doi:10.1021/acs.iecr.7b04871.

[59] M. Hopp and J. Gross. Thermal conductivity of real substances from excess entropy scaling using PCP-SAFT. *Ind. Eng. Chem. Res.*, **56**(15):4527–4538, 2017. doi:10.1021/acs.iecr.6b04289.

[60] M. Hopp, J. Mele, and J. Gross. Self-Diffusion Coefficients from Entropy Scaling using the PCP-SAFT equation of state. *Ind. Eng. Chem. Res.*, **57**(38):12942–12950, 2018. doi:10.1021/acs.iecr.8b02406.

[61] T. Stiegler and R. J. Sadus. Molecular simulation of fluids with non-identical intermolecular potentials: Thermodynamic properties of 10-5 + 12-6 Mie potential binary mixtures. *The Journal of Chemical Physics*, **142**(8):084504, 2015. doi:10.1063/1.4908530.

[62] M. Fischer, G. Bauer, and J. Gross. Force Fields with Fixed Bond Lengths and with Flexible Bond Lengths: Comparing Static and Dynamic Fluid Properties. *J. Chem. Eng. Data*, **65**(4):1583–1593, 2020. doi:10.1021/acs.jced.9b01031.

[63] J. Gross and G. Sadowski. Perturbed-chain SAFT: An equation of state based on a perturbation theory for chain molecules. *Ind. Eng. Chem. Res.*, **40**(4):1244–1260, 2001. doi:10.1021/ie0003887.

[64] S. Plimpton. Fast parallel algorithms for short-range molecular dynamics. *J. Comput. Phys.*, **117**(1):1–19, 1995. doi:10.1006/jcph.1995.1039.

[65] J. E. Basconi and M. R. Shirts. Effects of Temperature Control Algorithms on Transport Properties and Kinetics in Molecular Dynamics Simulations. *J. Chem. Theory Comput.*, **9**(7):2887–2899, 2013. doi:10.1021/ct400109a.

[66] M. Tuckerman, B. J. Berne, and G. J. Martyna. Reversible multiple time scale molecular dynamics. *J. Chem. Phys.*, **97**(3):1990–2001, 1992. doi:10.1063/1.463137.

[67] R. Hockney and J. Eastwood. *Computer Simulation Using Particles*. Taylor & Francis, 1988. doi:10.1201/9781439822050.

[68] B. L. Holian and D. J. Evans. Shear viscosities away from the melting line: A comparison of equilibrium and nonequilibrium molecular dynamics. *J. Chem. Phys.*, **78**(8):5147–5150, 1983. doi:10.1063/1.445384.

[69] E. J. Maginn, R. A. Messerly, D. J. Carlson, D. R. Roe, and J. R. Elliott. Best Practices for Computing Transport Properties 1. Self-Diffusivity and Viscosity from Equilibrium Molecular Dynamics [Article v1.0]. *Living J. Comput. Mol. Sci.*, **1**(1), 2019. doi:10.33011/livecoms.1.1.6324.

[70] V. Calandrini, E. Pellegrini, P. Calligari, K. Hinsen, and G. R. Kneller. nMoldyn-Interfacing spectroscopic experiments, molecular dynamics simulations and models for time correlation functions. *JDN*, **12**:201–232, 2011. doi:10.1051/sfn/201112010.

[71] M. T. Humbert, Y. Zhang, and E. J. Maginn. PyLAT: Python LAMMPS Analysis Tools. *J. Chem. Inf. Model.*, **59**(4):1301–1305, 2019. doi:10.1021/acs.jcim.9b00066.

[72] D. Dubbeldam, D. C. Ford, D. E. Ellis, and R. Q. Snurr. A new perspective on the order-n algorithm for computing correlation functions. *Mol. Simul.*, **35**(12-13):1084–1097, 2009.

doi:10.1080/08927020902818039.

[73] Y. Zhang, A. Otani, and E. J. Maginn. Reliable Viscosity Calculation from Equilibrium Molecular Dynamics Simulations: A Time Decomposition Method. *J. Chem. Theory Comput.*, **11**(8):3537–3546, 2015. doi:10.1021/acs.jctc.5b00351.

[74] B. Efron. Bootstrap Methods: Another Look at the Jackknife. *Ann. Stat.*, **7**(1):1–26, 1979. doi:10.1214/aos/1176344552.

[75] P. D. Neufeld, A. Janzen, and R. Aziz. Empirical Equations to Calculate 16 of the Transport Collision Integrals Ω (l, s)* for the Lennard-Jones (12–6) Potential. *J. Chem. Phys.*, **57**(3):1100–1102, 1972. doi:10.1063/1.1678363.

[76] Dortmund Data Bank. 2018.

[77] A. Boushehri, J. Bzowski, J. Kestin, and E. A. Mason. Equilibrium and Transport Properties of Eleven Polyatomic Gases At Low Density. *J. Phys. Chem. Ref. Data*, **16**(3):445–466, 1987. doi:10.1063/1.555800.

[78] C. R. Mueller and R. W. Cahill. Mass Spectrometric Measurement of Diffusion Coefficients. *J. Chem. Phys.*, **40**(3):651–654, 1964. doi:10.1063/1.1725184.

[79] A. Greiner-Schmid, S. Wappmann, M. Has, and H.-D. Lüdemann. Self-diffusion in the compressed fluid lower alkanes: Methane, ethane, and propane. *J. Chem. Phys.*, **94**(8):5643–5649, 1991. doi:10.1063/1.460474.

[80] M. Helbæk, B. Hafskjold, D. K. Dysthe, and G. H. Sørland. Self-Diffusion Coefficients of Methane or Ethane Mixtures with Hydrocarbons at High Pressure by NMR. *J. Chem. Eng. Data*, **41**(3):598–603, 1996. doi:10.1021/je950293p.

[81] M. Awan and J. Dymond. Transport Properties of Nonelectrolyte Liquid Mixtures. XI. Mutual Diffusion Coefficients for Toluene + n-Hexane and Toluene + Acetonitrile at Temperatures from 273 to 348 K and at Pressures up to 25 MPa. *Int. J. Thermophys.*, **22**:679–700, 2001. doi:https://doi.org/10.1023/A:1010714713468.

[82] D. McCall, D. Douglass, and E. Anderson. Self-Diffusion in Liquids: Paraffin Hydrocarbons. *Phys. Fluids*, **2**:87–91, 1959. doi:10.1063/1.1724398.

[83] K. R. Harris. Temperature and density dependence of the self-diffusion coefficient of n-hexane from 223 to 333 K and up to 400 MPa. *J. Chem. Soc., Faraday Trans. 1 F*, **78**(7):2265, 1982. doi:10.1039/f19827802265.

[84] M. Iwahashi, Y. Yamaguchi, Y. Ogura, and M. Suzuki. Dynamical Structures of Normal Alkanes, Alcohols, and Fatty Acids in the Liquid State as Determined by Viscosity, Self-Diffusion Coefficient, Infrared Spectra, and CNMR Spin-Lattice Relaxation Time Measurements. *Bull. Chem. Soc. Japan*,

63:2154–2158, 1990. doi:10.1246/bcsj.63.2154.

[85] C. D'Agostino, M. Mantle, L. Gladden, and G. Moggridge. Prediction of Binary Diffusion Coefficients in Non-Ideal Mixtures from NMR Data: Hexane-Nitrobenzene near its Consolute Point. *Chem. Eng. Sci.*, **66**:3898–3906, 2011. doi:10.1016/j.ces.2011.05.014.

[86] D. Douglass and D. McCall. Diffusion in Paraffin Hydrocarbons. *J. Phys. Chem.*, **62**:1102–1107, 1958. doi:10.1021/j150567a020.

[87] G. Panchenkov and V. Erchenkov. Temperature Variation of the Coordination Number and Diffusion Coefficient in a Liquid. *Russ. J. Phys. Chem.*, **36**:455–457, 1962.

[88] G. Panchenkov, N. Borisenko, and V. Erchenkov. Self-diffusion of n-paraffins in a wide temperature range. *Zh. Fiz. Khim*, **43**:2369–2370, 1969.

[89] P. Tofts, D. Lloyd, C. Clark, G. Barker, G. Parker, P. McConville, C. Baldock, and J. Pope. Test liquids for quantitative MRI measurements of self-diffusion coefficient in vivo. *Magn. Reson. Med.*, **43**(3):368–374, 2000. doi:10.1002/(SICI)1522-2594(200003)43:3<368::AID-MRM8>3.0.CO;2-B.

[90] D. W. McCall, D. C. Douglass, and E. W. Anderson. Diffusion in Liquids. *J. Chem. Phys.*, **31**(6):1555–1557, 1959. doi:10.1063/1.1730651.

[91] O. Suárez-Iglesias, I. Medina, M. de los Ángeles Sanz, C. Pizarro, and J. L. Bueno. Self-Diffusion in Molecular Fluids and Noble Gases: Available Data. *J. Chem. Eng. Data*, **60**(10):2757–2817, 2015. doi:10.1021/acs.jced.5b00323.

[92] K. Madzhidov. Thermal conductivity of ketones as a function of temperature and pressure. *J. Eng. Phys. Thermophys.*, **47**(2):933–939, 1984. doi:10.1007/bf00869697.

4 Assessing Entropy Scaling for Mixture Viscosities using Molecular Simulations

Abstract

The present work uses molecular simulations of model-mixtures to systematically validate the applicability of entropy scaling for mixtures. I determine the viscosity η of several binary mixtures of simple Lennard-Jones fluids in equilibrium molecular dynamic simulations at different state points. The extended Chapman-Enskog viscosity for mixtures is considered as reference viscosity η^{CE} in order to define the dimensionless viscosity $\eta^{\#}$. Grand-Canonical Monte Carlo simulations are used to determine residual entropy s_{res} in order to avoid assumptions inherent to any analytic EoS, but remain consistent within molecular simulations. The considered binary mixtures are composed of two LJ-fluids differing in their ε or σ parameters. The study further focuses on non-ideal mixtures of two identical LJ-fluids with $\varepsilon_{11} = \varepsilon_{22} \neq \varepsilon_{12}$ which can be parameterized to show a strongly non-ideal phase behavior. In an entropy scaled depiction, the viscosities of all considered mixtures collapse well onto a universal curve and show a monovariable dependence of $\eta^{\#}$ on residual entropy. The results of the non-ideal mixtures of two identical LJ-fluids enabled us to formulate a general mixing rule for the correlation parameters of pure components.

4.1 Introduction

Approaches for correlating or predicting transport coefficients of mixtures proposed in literature are based on the principle of corresponding states[1–5], the free volume theory[6–12], friction theory[13–15] and thermodynamic scaling[16–21]. A broad overview of the existing correlation methods for viscosity is given in the recent review of Baled et al.[22]. The authors compare established methods and find unsatisfactorily high deviations between predicted viscosities and experiments, especially in temperature and pressure ranges with scarce experimental data. The most precise and promising predictive results were provided by a group contribution entropy scaling method of Lötgering-Lin and Gross[23]. This method will be assessed in this work with regard to the entropy scaling behavior of the viscosity of mixtures. For this purpose

simple model mixtures are investigated using molecular simulations. Simulation results allow the distinct analysis of the influence of individual model parameters on fluid properties.

This benefit of molecular simulation of model fluids has been used in the literature for a long time to develop and assess different approaches for the calculation of dynamic properties of mixtures. Several studies considered the influence of different parameters defining Lennard-Jones fluids (LJ) and Mie fluid mixtures on the viscosity. Investigated were mixtures, where two Mie fluids have different mass[24], or energy parameters, or size parameters of the intermolecular potentials,[25] or different repulsive exponents of the Mie potential[26]. The model mixtures helped to develop correlation functions for transport coefficients of mixtures, based on various approaches, such as thermodynamic scaling[26] or the corresponding-state principle[24,25,27–29]. Another interesting approach that allows to predict dynamic properties is the isomorph theory, introduced in chapter 1. At this point it is worth recalling two specifics of isomorphs which are of particular interest in the context of this work: Both, the residual entropy s_{res} and the reduced dynamic quantities $\tilde{D}_{\mathrm{self}}$, $\tilde{\lambda}$, and $\tilde{\eta}$ are invariant along isomorphs. These two observations support the basic idea of entropy scaling: The reduced dynamic properties are a monovariable function of residual entropy. Numerous simple model fluids, such as the LJ fluid and the dumbbell fluid, have been identified as *Roskilde fluids* and exhibit isomorph properties.[30] Also mixtures of model fluids, like the Kob-Andersen binary LJ fluid, behave like *Roskilde fluids*.[31] Although isomorph theory seeks approaches to explain entropy scaling, a full understanding can not be provided.[32] It has been shown that the monovariable relationship between entropy and dynamic properties is also valid for fluids and regions in phase space to which $R < 0.9$ applies and where therefore no isomorphs occur[33]. The relation between entropy and dynamic properties therefore exceeds the isomorph theory and has been discovered long before the isomorphs.

In later studies, dynamic properties of more complex model fluids, like LJ chains[34,35] and Dumbbell particles[36], were investigated using entropy scaling. The findings regarding model fluids were applied to molecular simulation studies of real fluids, for example water[37], n-alkanes[38] and polyethylene[39]. One advantage of the investigation of simple model fluids is that s_{res} is accessible through well established and highly accurate equations of state[34,35,38–41], or even directly through molecular simulations[36,37]. The approach was also used to investigate mixtures. Results based on Dzugotov's scaling approach implied a general scaling law for LJ-mixtures.[42,43] Recently, I used molecular simulations of LJ model mixtures to find a mixing rule that takes the correlation parameters of the pure fluids as input, as published jointly in Lötgering-Lin *et al.*[44]. The mixing rule leads to excellent predictions for viscosities of mixtures containing non-polar and polar fluids, without any further adjustment of parameters.

In this chapter I extend on our previous work[44] in analyzing the scaling behavior of mixture

viscosities. For a consistent assessment, I calculate $\eta^{\#} = \eta/\eta_{CE,mix}$ as well as s_{res} using molecular simulations. This approach circumvents any inaccuracy underlying analytical equation-of-state models. Additionally, also the reference quantity $\eta_{CE,mix}$ can be calculated using the molecular parameters of the considered force fields. The mixtures investigated here consist of two LJ fluids, that differ in one model parameter, which allows the dedicated investigation of the influence of individual parameters. In addition, a mixture of two identical LJ fluids with a non-Berthelot cross-interaction is studied to assess the influence of non-idealities.

4.2 Methods

This section discusses the methodical background of this work. First, the molecular model and the model mixtures are described and a brief overview of entropy scaling and the required reference quantities is given. Subsequently, it is explained how entropy and viscosity are calculated from molecular simulations.

4.2.1 Molecular Model

The mixtures investigated in this work are composed of spherical mono-atomic model fluids. The interactions two interaction sites are modeled by a Lennard–Jones potential,

$$\phi^{\mathrm{LJ}}\left(r_{ij}\right) = 4\varepsilon_{ij}\left[\left(\frac{\sigma_{ij}}{r_{ij}}\right)^{12} - \left(\frac{\sigma_{ij}}{r_{ij}}\right)^{6}\right], \tag{4.1}$$

with r_{ij} as the distance of two centers of interaction i and j. Here, the size parameter σ_{ii} and the energy parameter ε_{ii} are the parameters that distinguish the pure components of the mixtures. Unless otherwise specified, the parameters of the unlike site pairs of the mixture are calculated using a Lorentz combining rule and an non–Berthelot cross-energy parameter ε_{ij}, as

$$\sigma_{ij} = \frac{\sigma_{ii} + \sigma_{jj}}{2} \tag{4.2}$$

$$\varepsilon_{ij} = \sqrt{\varepsilon_{ii}\varepsilon_{jj}}\left(1 - k_{ij}\right), \tag{4.3}$$

where the binary interaction parameter k_{ij} (with $k_{ii} = 0$) acts as a deviation from the geometric Berthelot combining rule. The parameters σ_{11} and ε_{11} of the first component of each mixture are used to define reduced (dimensionless) quantities. All results are given in these reduced

LJ units that are summarized in table 4.1.

A well studied example for a binary mixture of LJ fluids is the Kob-Andersen model[45,46], that has also been investigated with respect to entropy scaling and is known as a *Roskilde fluid* in isomorph theory.[31] The two LJ components of the Kob-Andersen fluid differ in σ_{22}/σ_{11} as well as in $\varepsilon_{22}/\varepsilon_{11}$ and a non-zero binary interaction parameter k_{ij}.[47] Since the aim of this study is to systematically analyze the impact of the parameters of the LJ potential on viscosity and entropy, two LJ fluids are mixed, differing only in their ε or σ-values, respectively. Mixture I is therefore designed as a mixture of two LJ fluids with a ratio of the energy parameters of $\varepsilon_{22} = \varepsilon_{11} \cdot 0.7$. The other parameters are identical for both components of the mixture ($\sigma_{11} = \sigma_{22}$, $m_1 = m_2$). In a second mixture II, only the size parameters differ ($\varepsilon_{11} = \varepsilon_{22}$, $m_1 = m_2$, but $\sigma_{22} = \sigma_{11} \cdot 1.5$). For both mixtures, the Lorentz-Berthelot combining rules eq. (4.2) and eq. (4.3) with $k_{ij} = 0$ are applied. The viscosity of mixtures comparable to I and II have been investigated using a one-fluid model, which defines one pseudo-component based on the parameters of the two involved LJ fluids[25]. The study showed the limitations of the one-fluid model regarding size asymmetric mixtures. It is thus of interest how well mixture II can be described with entropy scaling.

The third mixture III is a mixture of two LJ-fluids with an identical set of parameters ($\varepsilon_{11} = \varepsilon_{22}, m_1 = m_2, \sigma_{11} = \sigma_{22}$), but with a non-ideal cross interaction term for the energy parameter of $k_{12} = 0.25$. This mixture is of special interest, as both boundaries of the composition, $x_1 = 0$ and $x_1 = 1$, are well defined as the regular LJ fluid, whereas the non-pure compostions will show a different behavior. All parameters of defining the three investigated model mixtures are summarized in table 4.2

Table 4.1: Reduced Lennard-Jones units

Quantity	Symbol	Reduced units
Time	t	$t^* = t\sqrt{\varepsilon_{11}/\left(M_1\sigma_{11}^2\right)}$
Distance	r	$r^* = r/\sigma_{11}$
Energy	u	$u^* = u/\varepsilon_{11}$
Temperature	T	$T^* = T/(\varepsilon_{11}/k_\mathrm{b})$
Volume	V	$V^* = V/\sigma_{11}^3$
Particle Density	ρ	$\rho^* = \rho\sigma_{11}^3$
Pressure	p	$p^* = p\sigma_{11}^3/\varepsilon_{11}$
Viscosity	η	$\eta^* = \eta\sigma_{11}^2/\sqrt{\varepsilon_{11}M_1}$

Table 4.2: Parameters of the LJ potential of the investigated model mixtures

Mixture	σ_{22}/σ_{11}	$\varepsilon_{22}/\varepsilon_{11}$	k_{12}
I	1	0.7	0
II	1.5	1	0
III	1	1	0.25

4.2.2 Entropy Scaling

Rosenfeld's Ansatz allows for calculating transport properties of a substance at any fluid state point, using a simple correlation function. For a wide range of substances, a third order polynomial in terms of reduced viscosity $\eta^{\#} = \eta/\eta_{ref}$ is sufficient to calculate the viscosity η for a wide range of thermodynamic conditions. For spherical fluids, even a linear correlation gives good results[40,41,48]. The monovariable dependence of $\eta^{\#}$ on s_{res}, and thus the applicability of entropy scaling, critically depends on the choice of the reference viscosity η^{ref}. For pure fluids, Novak[48] proposed the Chapman-Enskog viscosity as a reference, which was shown to lead to accurate predictions of viscosities of various real substances[23,44,49]. The CE-viscosity for a pure substance of index i is defined as[50]

$$\eta_{CE,i} = \frac{5}{16}\frac{\sqrt{M_i k_{\mathrm{b}} T/(N_A \pi)}}{{\sigma_{ii}}^2\,\Omega_i^{(2,2)^*}}, \tag{4.4}$$

with the molecular mass M_i, Boltzmann's constant k_{b}, temperature T, Avogadro's constant N_{A} and the molecular diameter σ_{ii}. The collision integral $\Omega_i^{(2,2)^*}$ is calculated using the empirical correlation of Neufeld et al[51]. In this study the approximation of Wilke[52,53] is used to define the Chapman-Enskog viscosity for mixtures, $\eta_{CE,mix}$.

$$\eta_{CE,mix} = \sum_{i=1}^{N} \frac{x_i \eta_{CE,i}}{\sum_{j=1}^{N} x_j \phi_{ij}} \tag{4.5}$$

where

$$\phi_{ij} = \frac{\left(1 + \left(\eta_{CE,i}/\eta_{CE,j}\right)^{1/2}\left(M_j/M_i\right)^{1/4}\right)^2}{\left(8\left(1 + M_i/M_j\right)\right)^{1/2}}. \tag{4.6}$$

Since this study is concerned with LJ mixtures only, the reference values can also be given in

reduced units (cf. table 4.1). The CE viscosity in eq. (4.4) is then reduced to

$$\eta^*_{CE,i} = \frac{5}{16}\frac{\sqrt{T^*/(\pi)}}{\Omega_i^{(2,2)^*}}. \tag{4.7}$$

For the case $M_i = M_j$, eq. (4.6) simplifies to

$$\phi_{ij} = \frac{\left(1+\left(\eta_{CE,i}/\eta_{CE,j}\right)^{1/2}\right)^2}{4}. \tag{4.8}$$

A second prerequisite for the precise prediction of η via entropy scaling is an accurate estimate of the molar residual entropy s_{res}, which is defined as the molar entropy minus the molar ideal gas entropy, according to $s_{\text{res}}(T,\rho) = s(T,\rho) - s_{\text{id. gas}}(T,\rho)$. For the application to real substances, the calculation of s_{res} is relatively straightforward, and can be done based on a suitable equations of state (EoS)[23,44,48,49], such as PC-SAFT[54]. In principle, such an approach is also applicable to mixtures, provided that the used EoS is applicable to mixtures; however, the use of an EoS leads to approximate, i.e. non-exact mixture properties. All properties are therefore calculated based on molecular simulations.

4.2.3 Calculation of Residual Entropy

I calculate the residual entropy of the investigated model mixtures using Grand Canonical Monte Carlo (GCMC) simulations applying transition matrix sampling, following the scheme proposed by Errington and Shen[55]. The GCMC simulations are performed at constant temperature T, volume V and μ_i for each component i, whereas the particle numbers N_1 and N_2 are fluctuating. Temperature and volume are defined a priori for every simulation, estimates for excess chemical potentials μ_1 and μ_2 suiting the simulated temperature are taken from the PC-SAFT EoS[54]. Estimates of $\boldsymbol{\mu} = (\mu_1, \mu_2)$ are thereby sufficient, as earlier studies have shown[56]. The thermodynamic quantities, including residual entropy s_{res}, of a mixture at a certain pressure p^* and composition $\mathbf{x}$ are calculated in post processing using histogram reweighting[57]. For a more detailed description of the implementation I refer to the work of Hemmen *et al.*[56].

The simulations are carried out in a triangle in the (N_1, N_2) plane with $(N_1 = N_2 = 0)$, $N_1^{\max}$ and $N_2^{\max}$ as vertices. As this study focuses on state points in a homogeneous liquid, the maximum numbers of N_1 and N_2 are chosen in a way that the region of liquid densities is included in the sampling area. The triangle also includes the gas phase and the two phase region of the mixtures. The vapor liquid equilibrium (VLE) of each mixture can be calculated in post

processing using the simulation results. In order to allow parallel computation, the sampled (N_1, N_2) space is divided in squared windows of a fixed size $\Delta N_1 \times \Delta N_2$ with an overlap of one particle to each neighboring window[58].

In each window, every $\mathbf{N} = (N_1, N_2)$ point is sampled for a fixed number of trail moves. The following types of trial moves are thereby considered: particle displacements, particle insertion, particle deletion and particle identity swaps. All trial moves that might change the particle numbers are never accepted until the desired number of samples is reached in this particular (N_1, N_2) point. Only then will the simulation proceed on to an adjacent point in the $\mathbf{N}$ plane (e.g. $(N_1 + 1, N_2)$). In this way, the simulation meanders over the $\mathbf{N}$ plane and it is ensured that each point is sampled equally. All transition probabilities, including those of the trivially rejected moves, are recorded in a transition matrix (TM). From the TM the probability distribution of a particle composition $P(N_1, N_2; \mu_1, \mu_2, V, T)$ in this window for a given $(\boldsymbol{\mu}, V, T)$ can be calculated[55,59]. Combining the results of all windows a histogram of the normalized probability density $P(N_1, N_2; \boldsymbol{\mu}, V, T)$ is obtained over the complete predefined (N_1, N_2) triangle. Besides the probability P, the histogram of the average energy of a state $\langle U \rangle (N_1, N_2; \boldsymbol{\mu}, V, T)$ is sampled throughout the simulation.

The resulting histogram is then post processed using histogram reweighing[57], which is used to determine VLE data from GCMC simulations. In this procedure, $P(N_1, N_2; \boldsymbol{\mu}, V, T)$, simulated at T and the before estimated $\boldsymbol{\mu}$ is reweighted to a probability distribution at a desired $\boldsymbol{\mu}^{\text{target}}$ not too far away from the sampled $\boldsymbol{\mu}$, via the relation

$$P(\mathbf{N}, T, \boldsymbol{\mu}^{\text{target}}) = P(T, \mathbf{N}, \boldsymbol{\mu}) \exp\left[\beta \mathbf{N} \cdot (\boldsymbol{\mu}^{\text{target}} - \boldsymbol{\mu})\right] \tag{4.9}$$

with $\beta = \frac{1}{k_B T}$. An iterative approach is used. The $\mathbf{N}$-domain needs to be divided into a vapor and a liquid domain. The equilibrium requires equal pressure p for both phases. This condition is fulfilled if the sum under the peak in the vapor domain of the distribution $I^{\text{vap}} = \sum_{N_1, N_2}^{\text{vap}} P(\mathbf{N}, T, \boldsymbol{\mu}^{\text{coex}})$ is equal to the corresponding sum under the liquid peak I^{liq}. The two chemical potentials μ_1^{coex} and μ_2^{coex} are determined iteratively by two requirements, $I^{\text{vap}} = I^{\text{liq}}$ and the compostion of species 1 is equal to a target value, $x_1 = x_1^{\text{target}}$.

For determining the thermodynamic properties along an isobar for various compositions, P is iteratively reweighted to a $\boldsymbol{\mu}^{\text{isobar}}$ belonging to a state point at the desired pressure p^{target} and the required composition $\mathbf{x}^{\text{target}}$. p^{target} is selected in such a way that a state in the liquid-like phase is established. In each iteration step pressure p is calculated via the ideal gas limit as[60]

$$p = -\frac{1}{\beta V} \ln\left(P\left(N_1 = 0, N_2 = 0; \boldsymbol{\mu}, V, T\right)\right) \tag{4.10}$$

and the number of particles of species i, corresponding to the target composition is

$$\langle N_i \rangle = \sum_{N_1=0,N_2=0}^{N_{1,\max},N_{2,\max}} N_i \cdot P\left(N_1, N_2; \boldsymbol{\mu}, V, T\right) \tag{4.11}$$

$\boldsymbol{\mu}^{\text{isobar}}$ is thereby iterated in a way that the target composition

$$x_i^{\text{target}} = \frac{\left\langle N_i^{\text{target}} \right\rangle}{\left(\left\langle N_1^{\text{target}} \right\rangle + \left\langle N_2^{\text{target}} \right\rangle\right)} \tag{4.12}$$

and the pressure condition p^{target} are fulfilled simultaneously. This procedure is repeated for several $\mathbf{x}^{\text{target}}$ along an isobar. At each state point, it is now also possible to determine the average intermolecular energy of the system from the sampled energy histogram, as

$$\langle U_{\text{res}} \rangle = \sum_{N_1=0,N_2=0}^{N_{1,\max},N_{2,\max}} U\left(N_1, N_2; \boldsymbol{\mu}, V, T\right) \cdot P\left(N_1, N_2; \boldsymbol{\mu}, V, T\right) \tag{4.13}$$

The internal energy U coming from a GCMC simulation does not include the kinetic contribution and is therefore a residual quantity. The specific residual entropy s^* can now be calculated starting from the residual Gibbs Free Energy

$$G_{\text{res}} = \langle U \rangle + p_{\text{res}} V - T S_{\text{res}} \tag{4.14}$$

The residual pressure has to be calculated by subtracting the ideal gas contribution. For pressure p as determined from eq. (4.10), one gets the residual pressure from

$$p_{\text{res}} V = \left(pV - \frac{\langle N \rangle}{\beta} \right) \tag{4.15}$$

The residual Gibbs energy can be expressed by the residual chemical potential of the components, as

$$G_{\text{res}} = \sum_{i=1}^{N_{comp}} N_i \mu_{\text{res},i} \tag{4.16}$$

A chemical potential of species i contains the de Broglie wavelength Λ_i with $\beta\mu_i = \ln\left(\rho_i \Lambda_i^3\right) + \mu_{\text{res}}\left(T, \boldsymbol{\rho}\right)$. Without loss of generality, Λ_i can be set to σ_i in this chapter, so that

$$\beta\mu_{\text{res},i}\left(\mathbf{N}, V, T\right) = \beta\mu_i - \ln\left(\frac{\langle N_i \rangle}{V^*} \right) \tag{4.17}$$

Combining these equations finally gives the residual entropy.

$$S_{\mathrm{res}}(\mathbf{N},V,T)=\frac{1}{T}\langle U_{\mathrm{res}}\rangle+(\beta pV-\langle N\rangle)-\sum_{i=1}^{N_{comp}}N_i\left(\beta\mu_{\mathrm{res},i}\right) \tag{4.18}$$

The dimensionless and molar specific form s^* is used in the following for the entropy scaling of the viscosity results.

$$s^*=\frac{S_{\mathrm{res}}}{\langle N\rangle k_{\mathrm{b}}}=\beta\frac{\langle U_{\mathrm{res}}\rangle}{\langle N\rangle}+\left(\frac{\beta pV}{\langle N\rangle}-1\right)-\sum_{i=1}^{N_{comp}}x_i\left(\beta\mu_{\mathrm{res},i}\right). \tag{4.19}$$

Note that although non-reduced units are used in the equations of this chapter for the sake of convenience, the equations are also valid when using dimensionless quantities.

4.2.4 Calculation of Viscosity

The viscosity of the mixtures is calculated in equilibrium Molecular Dynamics (MD) simulations using the MD package DL_POLY_4[61]. NVT simulations are performed at constant particle number $\mathbf{N}$, Volume V^* and temperature T^*. The simulations were carried out at densities in the liquid region along several isotherms at one specific pressure p^* for each mixture and varying compositions $\mathbf{x}$. The density ρ^* corresponding to each simulated state point at $(p^*,T^*,\mathbf{x})$ are taken from the results of the GCMC simulations at the respective isobaric line. MC and MD, provide the same pressures for a simulation at the same density. The initial configurations for the NVT MD simulations are generated each in a short MC NVT simulation. This MC configuration is used as starting point for multiple MD NVT simulations at each considered state point using a velocity Verlet integrator with a time step of $\Delta t^*=4.6374e-04$. Initial particle velocities are drawn from the Boltzmann distribution for the considered temperature, with a different random seed for each replicate simulation. Each MD replicate is equilibrated for 10^6 time steps. The shear components of the stress tensor are then sampled for another 10^6 time steps. T^* is held constant using a weakly coupled Berendsen thermostat, which has been shown to preserve realistic dynamics[62]. An overview of general simulation specifications of the MD simulations is given in table 4.3.

The Green-Kubo approach[63,64] is used to calculate viscosities. The method determines $\eta*$ by integrating the auto correlation function (ACF) of the stress tensor, according to

$$\eta=\frac{1}{Vk_{\mathrm{B}}T}\int_0^\infty R_{J_pJ_p}(\tau)\mathrm{d}\tau, \tag{4.20}$$

integration method	Velocity Verlet
time-step Δt^*	$4.6374 \cdot 10^{-4}$
equilibration steps	$1 \cdot 10^6$
production steps	$1 \cdot 10^6$
number of molecules	1000
thermostat (coupling time t_T^*)	Berendsen ($4.6374 \cdot 10^{-6}$)
cut-off length / σ	4.112
tail-corrections	applied on U and p

Table 4.3: General Specifications of the MD Simulations.

with the ACF $R_{J_pJ_p}$ of the stress tensor $\boldsymbol{J}_p$, according to

$$R_{J_pJ_p}(\tau) = \lim_{\Theta\to\infty} \frac{1}{2\Theta} \int_{-\Theta}^{\Theta} J_p^{\alpha\beta}(t+\tau) J_p^{\alpha\beta}(t)\,\mathrm{d}t \tag{4.21}$$

as a function of the lag time τ. $J_p^{\alpha\beta}$ (with $\alpha,\beta = x,y,z$) are entries of the shear-stress tensor of the simulation box. The stress tensor is calculated using the particle velocities v_i and the virial $\mathbf{r_{ij}}(\partial\phi(r_{ij})/\partial\mathbf{r_{ij}})$.

$$J_p^{\alpha\beta} = \sum_{i=1}^{N} m_i v_i^\alpha v_i^\beta - \sum_{i=1}^{N}\sum_{j>i}^{N} r_{ij}^\alpha \frac{\partial\phi(r_{ij})}{\partial r_{ij}^\beta} \tag{4.22}$$

In order to improve the statistic of each simulation, $J_p^{\alpha\beta}$ is calculated as the average of the six independent shear components $1/2\left(J_p^{xy}+J_p^{yx}\right)$, $1/2\left(J_p^{yz}+J_p^{zy}\right)$, $1/2\left(J_p^{xz}+J_p^{zx}\right)$, $1/2\left(J_p^{xx}-J_p^{yy}\right)$, $1/2\left(J_p^{yy}-J_p^{zz}\right)$ and $1/2\left(J_p^{xx}-J_p^{zz}\right)$. The last three terms are determined from 45° rotations of the stress tensor about all axes[65,66].

As the the Green-Kubo method suffers from a high level of noise, statistics are improved by generating 100 replicate trajectories at each state point. The autocorrelation function (ACF) of each time series is computed in post processing. According to the Wiener-Khinchin Theorem[67,68], the correlation integrals can be calculated very efficiently in Fourier-space.[69,70] Using the *Fast Fourier Transform* algorithm, the computational complexity depending on the number of samples N_t is reduced from $\propto N_t^2$ to $\propto N_t \log_2(N_t)$ compared to the direct calculation[71]. This procedure allows us to evaluate ACFs very efficiently and without sacrificing any data points. Therefore, the autocorrelations of every sampled time step with all other time steps of the simulation is considered. The Green-Kubo integrals are evaluated with the Time Decomposition Method of Zhang *et al.*[72], a fitting method where the statistical uncertainty is part of the evaluation. The stated statistical uncertainties of the results are

95 % confidence intervals, obtained from a bootstrapping technique.[73–75] For this purpose 500 bootstrap samples are evaluated, generated by randomly drawing (with replacement) 50 times from the complete set of replicate simulations. For a more detailed description of the analysis of the viscosity data I refer to our recent work[75,76].

4.3 Results

The central result of the study of the model mixtures is the analysis of entropy scaling of mixture-viscosities. In order to lead to this result, this section first separately considers the calculated properties needed for entropy scaling – entropy s^* and viscosity η^*. The results are presented successively for the different mixtures. For a more comprehensive appraisal of the individual mixtures, I also show phase equilibrium properties of the mixtures. The vapour-liquid equilibria (VLE) can be computed from the data generated for the calculation of entropy. The VLEs are determined via histogram reweighting, as described in section 4.2.3, at the temperatures at which the GCMC simulations for the entropy calculation were performed. Therefore no additional simulations are required to determine the VLEs.

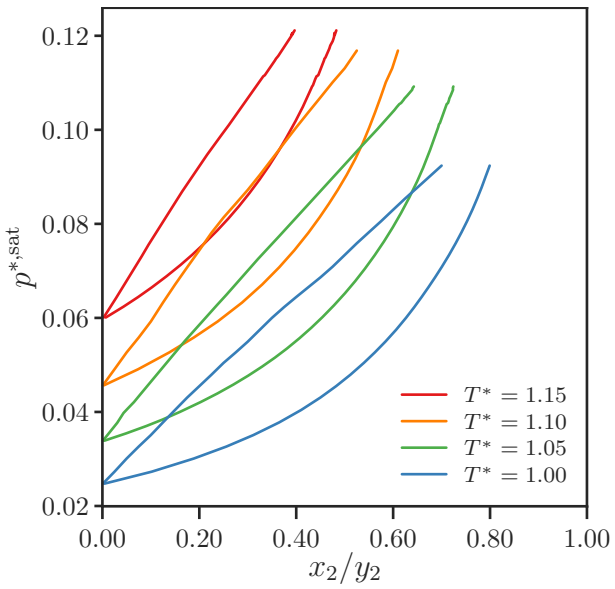

Figure 4.1: Vapor-liquid equilibrium of the energy asymmetric mixture I ($\sigma_{22} = \sigma_{11}$, $\varepsilon_{22} = 0.7 \cdot \varepsilon_{11}$, and $\varepsilon_{12} = \sqrt{\varepsilon_{11}\varepsilon_{22}}$) at four temperatures. For reduced units refer to table 4.1.

Figure 4.1 shows the VLE of the energy asymmetric mixture I. As the second component of the mixture is supercritical at all considered temperatures, a closed-loop phase behavior is observed for all shown VLEs. Component 2 is the low boiling component, due to its less attractive interactions ($\varepsilon_{22} = 0.7 \cdot \varepsilon_{11}$). Thus, a liquid phase, rich in component 1, and a gas phase, enriched with component 2, are obtained in the phase equilibrium. The phase

envelopes in fig. 4.1 do not close towards the critical point, because in regions near the critical pressure, phase equilibria can no longer be determined using simple histogram rescaling. The probability surfaces of the two phases increasingly overlap towards the critical point.[77] Although the critical point can be estimated using other methods[56,78], the required finite-size analysis was not performed in this work, as it is not a focus of this study. Since the two-phase region should be avoided for the investigation of entropy scaling of the mixture, the VLE in fig. 4.1 was also used to determine a pressure at which a homogeneous phase is ensured for the determination of s^* and η^*. In order to ensure a homogeneous phase for a wide range of T^* and $\mathbf{x}$, the pressure for the further studies was chosen supercritical for both components, but moderate with $p^* = 0.2$. This pressure results in densities in the liquid regime at the regarded temperatures.

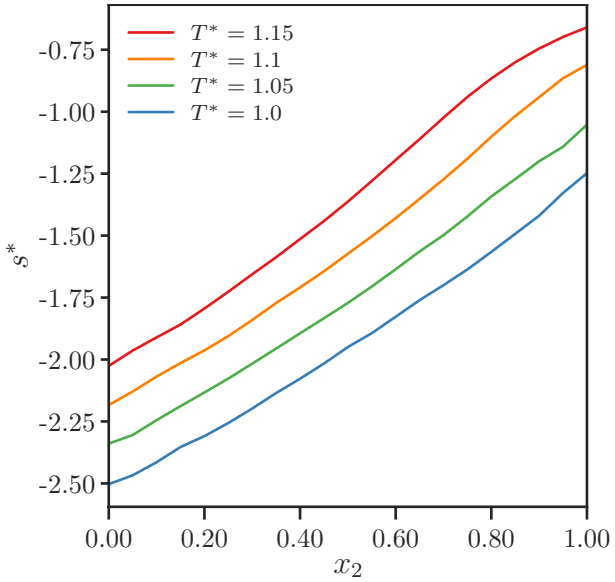

Figure 4.2: GCMC results for the energy asymmetric mixture I ($\sigma_{22} = \sigma_{11}$, $\varepsilon_{22} = 0.7 \cdot \varepsilon_{11}$, and $\varepsilon_{12} = \sqrt{\varepsilon_{11}\varepsilon_{22}}$): Reduced entropy s^* as a function of compostition x_2 at $p^* = 0.20$ and four temperatures.

Figure 4.2 shows the composition dependence of s^* of mixture I at different T^*. For each composition, entropy increases with rising temperature, as suggested by he partial derivative $(\partial s^{\mathrm{res}}/\partial T)_{p,\boldsymbol{x}} = c_p^{\mathrm{res}}/T$. With increasing composition of component 2 (with $\varepsilon_{22} = 0.7 \cdot \varepsilon_{11}$), the entropy s^* of the mixture tends to higher values. Component 1, the high boiler, has significantly more negative entropies ($s^* \sim -2$ to -2.5), which are typical values of liquids. The values of the pure component 2 ($s^* \sim -0.7$ to -1.3) are in a range close to the critical point of pure Lennard-Jones fluids.

Figure 4.3 depicts the temperature dependence of the viscosity of mixture I for several lines of constant compositions (isopleths). The viscosity in this figure is the dimensionless quantity $\eta^* = \eta\sigma_{11}^2/\sqrt{\varepsilon_{11}M_1}$, not to be mistaken with the reduced viscosity $\eta^{\#}$ in entropy scaling. While

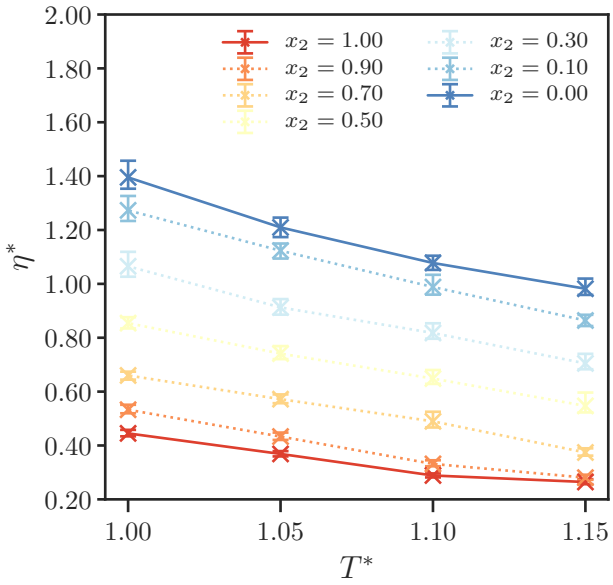

Figure 4.3: MD simulation results for the viscosities η^* of mixtures I ($\sigma_{22} = \sigma_{11}$, $\varepsilon_{22} = 0.7 \cdot \varepsilon_{11}$, and $\varepsilon_{12} = \sqrt{\varepsilon_{11}\varepsilon_{22}}$) at a pressure of $p^* = 0.2$ and several temperatures. Different colors represent different compositions, solid lines representing the pure fluids. Lines are a guide to the eyes.

the results of entropy are derived from histogram reweighting and can therefore be determined for any composition, the viscosity points are derived from individual MD simulations at discrete state points. The conditions (T^*, v^* and $\mathbf{x}$) at which the MD simulations are conducted were chosen in such a way that GCMC results are available for each viscosity. The isopleths of mixtures of varying composition lay between the lines of the pure components. The viscosities decrease for higher concentrations of the low boiling component 2 with $\varepsilon_{22} = 0.7\varepsilon_{11}$. This behavior seems plausible as the second component has a lower energy parameter ε, which defines the attractive interactions. With a higher concentration of this component, the interaction between the particles of the mixture is less attractive and therefore the viscosity decreases.

Figures 4.4–4.6 analyze the results of the size-asymmetric mixture II. This kind of mixture is known to show a thin VLE envelope in contrast to mixture I[60]. The small difference in vapor pressure between the two components impedes GCMC simulations of this mixture and necessitates a high number of samples. This has also been reported in the literature for Gibbs-ensemble calculations of similar mixtures dominated by size-asymmetric effects.[79]. As can be seen in the VLEs at several temperatures shown in fig. 4.4, both pure components remain subcritical for temperatures below $T^* = 1.2$. At a concentration of $x_2 = 0$ the same pure LJ fluid is present as in mixture I in fig. 4.1. So at the same temperature the same vapor pressures should be obtained for the left boundary of both mixtures. However, the vapor

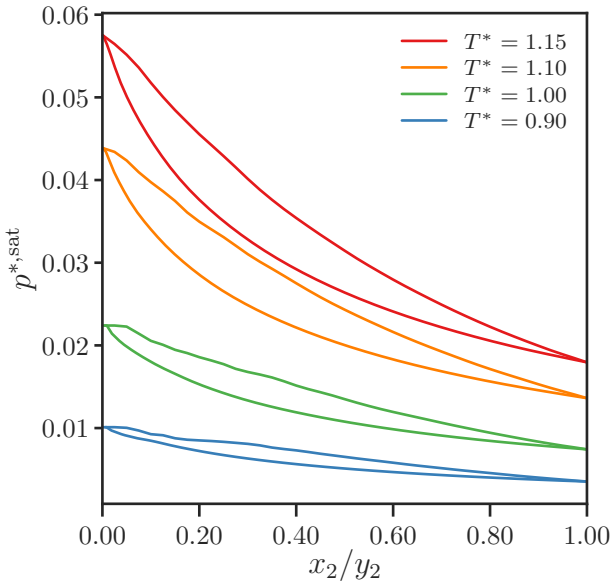

Figure 4.4: Vapor-liquid equilibrium of the size asymmetric mixture II ($\sigma_{22} = 1.5 \cdot \sigma_{11}$, $\varepsilon_{22} = \varepsilon_{11}$, and $\varepsilon_{12} = \sqrt{\varepsilon_{11}\varepsilon_{22}}$) at four temperatures.

pressures of the pure LJ fluid in mixture II are predicted slightly too low, which indicates the difficulties in sampling the size-asymmetric mixture. The low boiler in this mixture is component 1. The larger particles of component 2 tend rather to remain in the liquid phase. Based on fig. 4.4, a pressure is selected for the entropy calculation which is again far from the two-phase region, in the case of mixture II it is set to $p^* = 0.4$.

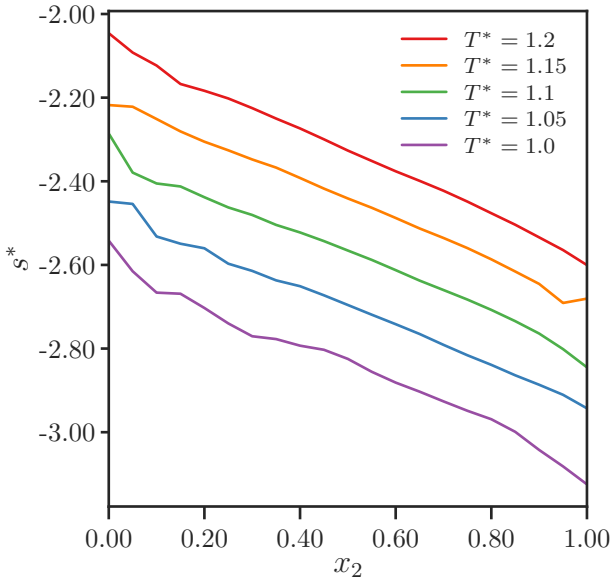

Figure 4.5: GCMC results for the size asymmetric mixture II ($\sigma_{22} = 1.5 \cdot \sigma_{11}$, $\varepsilon_{22} = \varepsilon_{11}$, and $\varepsilon_{12} = \sqrt{\varepsilon_{11}\varepsilon_{22}}$): Reduced entropy s^* as a function of concentration x_2 at $p^* = 0.40$ and five temperatures. For reduced units refer to table 4.1.

Figure 4.5 exhibits a similar concentration dependence for entropy as for mixture I, if one considers that component 1 is the low-boiling component of the mixture in this case. If the fraction of high boiler increases with x_2, the entropy s^* of the mixtures becomes more negative. Also for entropy, near the pure substances and for low temperatures, deviations from the nearly linear course are observed, which was already seen for mixture I.

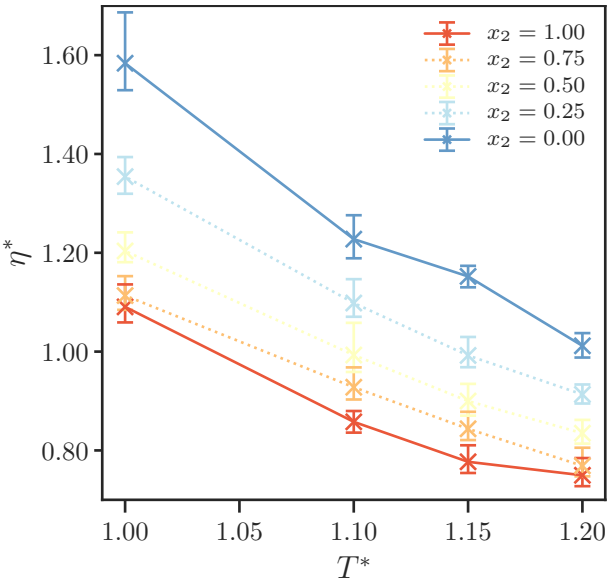

Figure 4.6: MD simulation results for the viscosities η^* of the size asymmetric mixtures II ($\sigma_{22} = 1.5 \cdot \sigma_{11}$, $\varepsilon_{22} = \varepsilon_{11}$, and $\varepsilon_{12} = \sqrt{\varepsilon_{11}\varepsilon_{22}}$) at a pressure of $p^* = 0.4$ and several temperatures. Different colors represent different compositions, solid lines representing the pure fluids. Lines are a guide to the eyes.

The viscosity in fig. 4.6 decreases for each temperature as the proportion of component 2 in the mixture increases. So I obviously find a clear dependence of η^* on the composition at the moderate pressure $p^* = 0.4$, unlike earlier studies of the viscosity of size asymmetric LJ-mixtures[29] at a high pressure of $p^* = 4.18$.

Mixture III is a mixture of two LJ fluids with identical σ and ε parameters, but with a cross-energy parameter $\varepsilon_{12} = 0.75\sqrt{\varepsilon_{11}\varepsilon_{22}}$. This mixture is known for a symmetric phase behavior with an VLE azeotrope at equimolar composition and a liquid-liquid equilibrium[60] at temperatures $T^* < 1.0$. Figure 4.7 shows the calculated vapor liquid equilibrium of the mixture at various temperatures. According to the character of the mixture a symmetrical behavior of the VLEs can be seen over the composition with the azeotropic point in the centre at $x_2 = 0.5$. The left ($x_2 = 0$), as well as the right boundary ($x_2 = 1$) of mixture III corresponds to the LJ fluid. The vapour pressures for the pure species boundaries ($x_1 = 1$ and $x_2 = 1$) are in good agreement with those of mixture I at $x_2 = 0$ in fig. 4.1. As before, using the VLE from fig. 4.7, a pressure is selected, that ensures conditions well away from the two-phase region

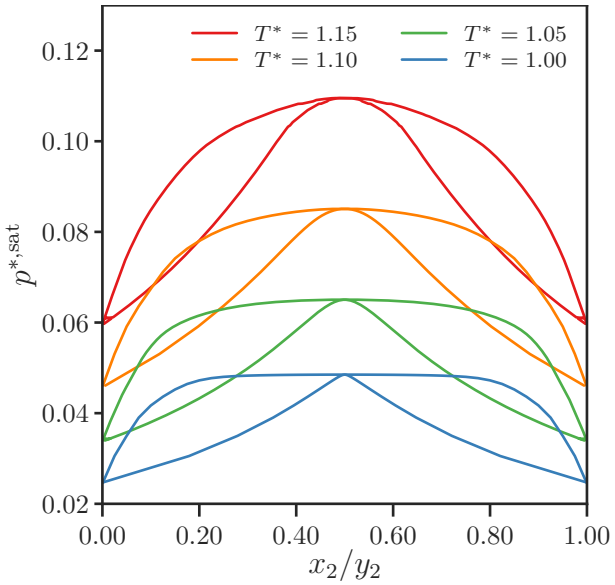

Figure 4.7: Vapor-liquid equilibrium of mixture III with non-Berthelot cross-energy parameters ($\sigma_{22} = \sigma_{11}$, $\varepsilon_{22} = \varepsilon_{11}$, and $\varepsilon_{12} = 0.75 \cdot \sqrt{\varepsilon_{11}\varepsilon_{22}}$) at four temperatures.

at which the analysis is carried out. For mixture III the pressure is set to $p^* = 0.15$. The value was chosen moderately enough to avoid high densities at which the pure components tend to form solids at lower temperatures.

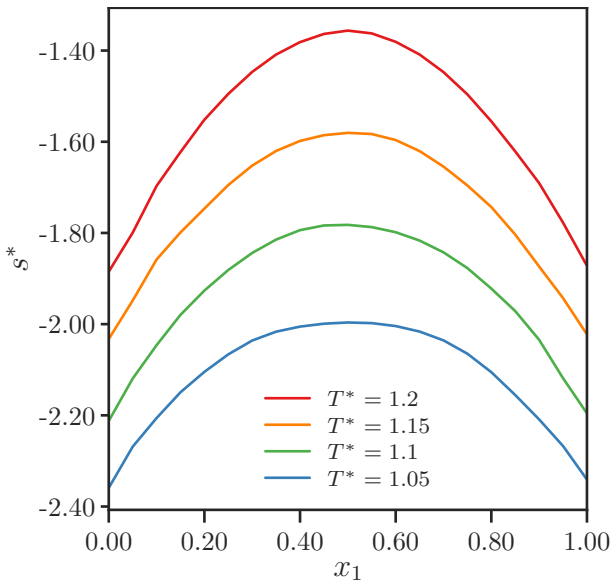

Figure 4.8: GCMC results for mixture III with non-Berthelot cross-energy parameters ($\sigma_{22} = \sigma_{11}$, $\varepsilon_{22} = \varepsilon_{11}$, and $\varepsilon_{12} = 0.75 \cdot \sqrt{\varepsilon_{11}\varepsilon_{22}}$): Reduced entropy s^* as a function of concentration x_2 at $p^* = 0.20$ and four temperatures.

In fig. 4.8 one can see the entropy of mixture III, which is also symmetric with the composition. As can be seen in fig. 4.8, the highest value for s^* at each temperature is reached at equimolar

composition. This reflects the behavior of the other model mixtures being considered. For the "low boiler" – here the azeotropic mixture at $x_2 = 0.5$ – the entropy is less negative, towards the high boilers – here the two pure substances – the entropy decreases.

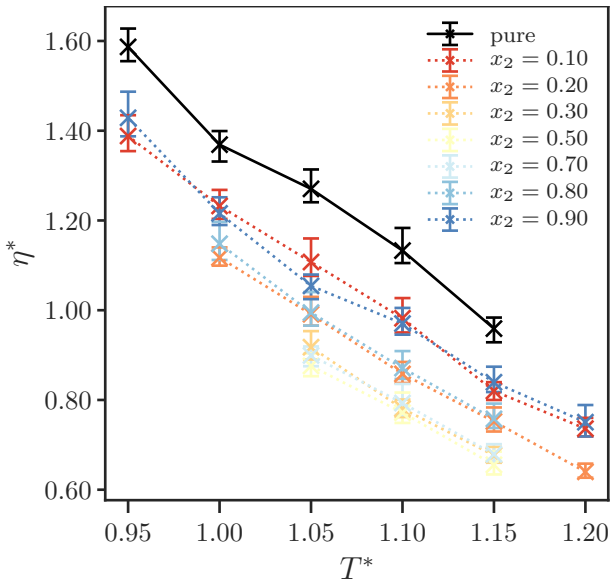

Figure 4.9: MD simulation results for the viscosities η^* of mixtures III ($\sigma_{22} = \sigma_{11}$, $\varepsilon_{22} = \varepsilon_{11}$, and $\varepsilon_{12} = 0.75 \cdot \sqrt{\varepsilon_{11}\varepsilon_{22}}$) at a pressure of $p^* = 0.15$ and several temperatures. Different colors represent different compositions, solid lines representing the pure fluids. Lines are a guide to the eyes.

The fact that the low boiler in mixture III is at equimolar composition leads to an interesting symmetric behavior also in viscosity, which can be seen in fig. 4.9 and was already noticed in our previous work.[44] The viscosity decreases with increasing amount of component 2 until it reaches its lowest value at the azeotropic composition. With further addition of component 2, η^* rises again. In the depiction of the isopleths versus temperature in fig. 4.9, this symmetry can be seen in the superimposed isopleths of complementary composition. Thus, for example, the viscosities at $x_2 = 0.1$ and $x_2 = 0.9$ ($x_2 = 0.2$ and $x_2 = 0.8$, and so on) are the same within the error bars for each temperature. The isopleths of the azeotropic mixture and those of the pure LJ fluids limit the viscosity at the bottom and top, respectively.

Figure 4.10 summarizes and visualizes the central result of the study on the model mixtures. The diagram combines the results presented in the figures above and shows the viscosity of all three mixtures in an entropy scaled analysis. On the y-axis of each figure, the logarithm of the dimensionless viscosity $\eta^\# = \eta^*/\eta_{CE,mix}$ is shown, using the Chapman-Enskog viscosity of the mixture (eq. (4.5)) as reference. On the x-axis is the related s^* value of each state point, respectively. Figures 4.10a–4.10c show the results of the individual mixtures, (a) gives the results of mixture I, (b) the results of mixture II, and (c) the results of of mixture III. The different colors in each figure indicate different temperatures. At each temperature several

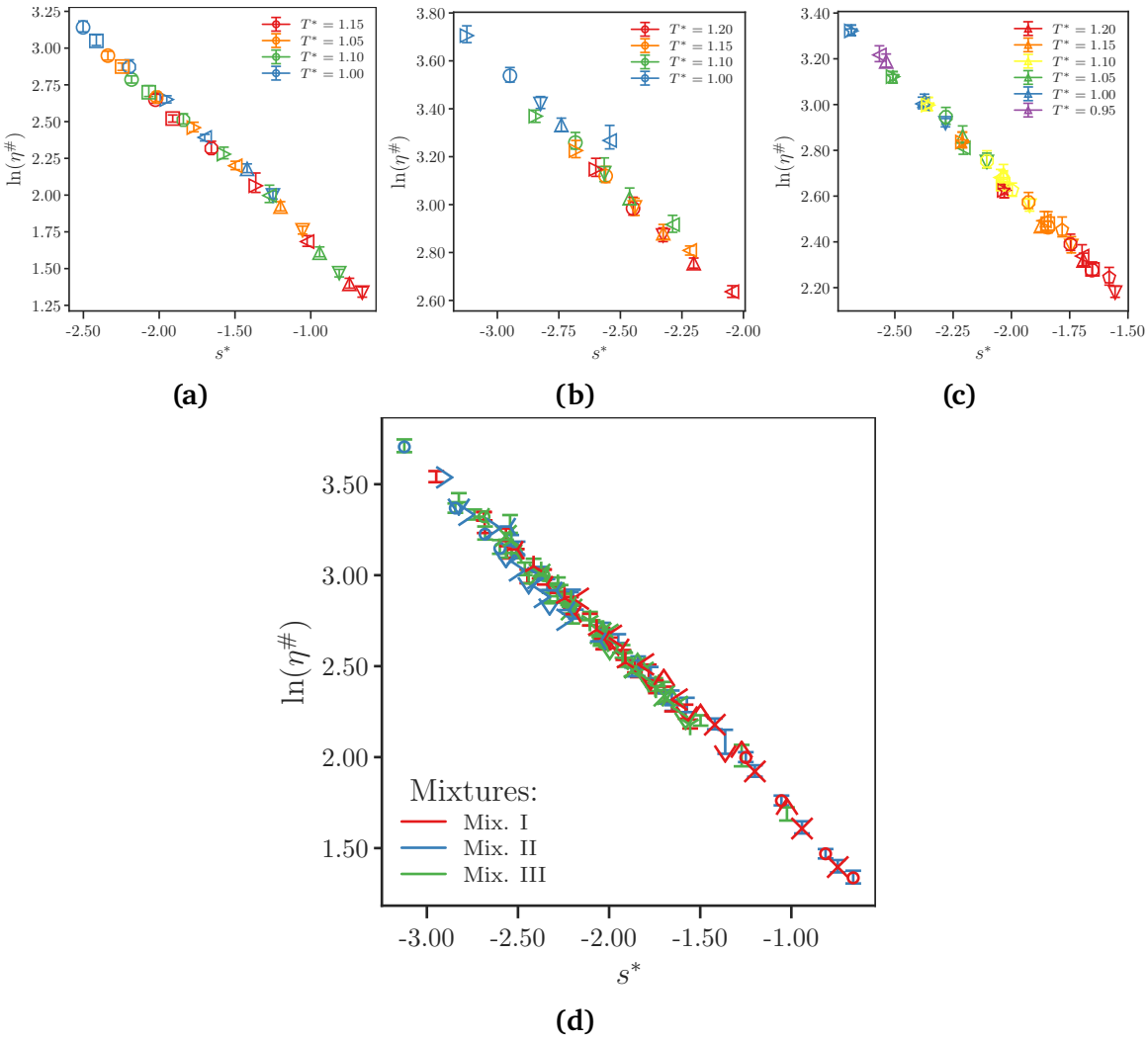

Figure 4.10: Dimensionless mixture viscosities $\ln(\eta^{\#})$ as a function of the residual entropy s^* of all non-associating mixtures I-III. Simulated temperatures and pressures of each mixture refer to figs. 4.3, 4.6 and 4.9. In (a), (b), and (c) different colors represent different temperatures; different symbols represent different compositions. (a) shows the results of mixture I, (b) the results of mixture II, and (c) the results of of mixture III. (d) shows the results of *all* three mixtures in one diagram. Here, different colors represent the three different types of mixtures. Different symbols show different compositions.

compositions are shown, represented by different symbols.

All mixtures follow the monovariable (almost linear) relationship of $\eta^{\#}$ and s^*. For mixture II, which has proven to be difficult to sample, an outlier from this linear course can be seen in (b). The point (at $s^* \sim -2.5, T^* = 1.0$ and $x_2 = 1$) is one at which both the GCMC simulations of entropy and the MD simulations of viscosity showed results deviating from the overall trend and I consider this point as an “outlier”. It is worth noting that the results in (a) - (c) extend over various s^* ranges that only partially overlap. All results combined in one figure

cover a very wide range of liquid entropies.

Figure 4.10d contains all datapoints calculated in this study. It contains state points at various compositions and temperatures for three different mixtures. The remarkable result is that the dimensionless viscosity of all data points collapse on one mastercurve. A universal behavior can be seen for *all* LJ mixtures, not only for each mixture individually. The mastercurve can be accurately represented by a linear equation. The parameters defining the linear mastercurve can conveniently be obtained by adjustment to the viscosity results of pure LJ fluids. As a conclusion of these findings, it can be stated, that the viscosity of any mixture of LJ fluid equals the viscosity of a pseudo pure fluid at the same residual entropy as the mixture. The pseudo pure components can be described by general paramaters adjusted to the pure LJ fluid. The only quantity needed to predict the mixture viscosity of any combination of LJ fluids differing in σ_{ii}, ε_{ii} or ε_{ij} is the residual entropy s^* of the mixture.

4.4 Conclusion

In this study I investigated the entropy scaling behavior of LJ model mixtures consistently using molecular simulations. By considering three model mixtures at various temperatures and compositions, the influence of individual LJ parameters on VLE, entropy s^* and viscosity ($\eta^\#$) has been assessed. Using a Chapman-Enskog equation for defining a dimensionless viscosity $\eta^\#$ as the only model equation, I related $\eta^\#$ with the residual entropy s^* and found a general, nearly linear master curve that is valid for all state points of all mixtures. In the entropy scaling approach all LJ mixtures can thus be considered as a pseudo pure LJ substance.

This result confirms what has already been postulated by isomorph theory, declaring LJ mixtures as *Roskilde fluid* and thus suitable for entropy scaling. In the present study, scalability was shown even for states far outside the range in which the LJ fluid behaves like a *Roskilde fluid*.[33] The results also show that $\ln\left(\eta^\#\right)$ is approximately linear with s^* for all LJ mixtures using the Chapman-Enskog viscosity as reference for making $\eta^\#$ dimensionless. The CE reference is therefore very suited as a reference for viscosity of LJ fluids, contrary to what was claimed in a previous publication.[33]

Furthermore, GCMC simulations have been validated as a suitable method for determining the entropy of mixtures in the context of entropy scaling. In a previous work[44] it has been found that the combination of the PC-SAFT equation of state for the determination of s^* and the CE viscosity as a reference leads to well-defined courses in entropy-scaled depiction, which allows the adjustment of simple correlation functions for real mixtures. The present work

shows for LJ-mixtures that this also applies when residual entropy is determined consistently from molecular simulations.

The results also open exciting new applications for entropy scaling. If one knows the entropy scaling parameters (see equation for viscosity in table 3.3 in chapter 3) related to a force field (in our case this would correspond to the straight line equation for LJ fluids), the transport properties can be estimated from GCMC simulations and entropy scaling. Thus, efficient methods like histogram reweighting can be used to determine dynamic properties, which otherwise requires numerous individual MD simulations. This allows the dynamic properties to be taken into account in force field optimization, for example. A prerequisite for such a procedure is that entropy scaling parameters remain almost constant for mild changes in the force field parameters. First studies in this regard have shown that this requirement is fulfilled for simple hydrocarbons[80].

Bibliography

[1] J. F. Ely and H. Hanley. Prediction of transport properties. 1. Viscosity of fluids and mixtures. *Ind. Eng. Chem. Fundamen.*, **20**(4):323–332, 1981. doi:10.1021/i100004a004.

[2] A. Teja and P. Rice. Generalized corresponding states method for the viscosities of liquid mixtures. *Ind. Eng. Chem. Fundamen.*, **20**(1):77–81, 1981. doi:10.1021/i100001a015.

[3] K. S. Pedersen, A. Fredenslund, P. L. Christensen, and P. Thomassen. Viscosity of crude oils. *Chem. Eng. Sci.*, **39**(6):1011–1016, 1984. doi:10.1016/0009-2509(84)87009-8.

[4] A. S. Teja, P. A. Thurner, and B. Pasumarti. Calculation of transport properties of mixtures for synfuels process design. *Ind. Eng. Chem. Process Des. Dev.*, **24**(2):344–349, 1985. doi:10.1021/i200029a021.

[5] K. S. Pedersen and A. Fredenslund. An improved corresponding states model for the prediction of oil and gas viscosities and thermal conductivities. *Chem. Eng. Sci.*, **42**(1):182–186, 1987. doi:10.1016/0009-2509(87)80225-7.

[6] A. K. Doolittle. Studies in Newtonian flow. II. The dependence of the viscosity of liquids on free-space. *J. Appl. Phys.*, **22**(12):1471–1475, 1951. doi:10.1063/1.1699894.

[7] A. Allal, M. Moha-Ouchane, and C. Boned. A new free volume model for dynamic viscosity and density of dense fluids versus pressure and temperature. *Phys. Chem. Liq.*, **39**(1):1–30, 2001. doi:10.1080/00319100108030323.

[8] A. Allal, C. Boned, and A. Baylaucq. Free-volume viscosity model for fluids in the dense and gaseous states. *Phys. Rev. E*, **64**(1):011203, 2001. doi:10.1103/physreve.64.011203.

[9] F. Llovell, R. Marcos, and L. Vega. Free-volume theory coupled with soft-SAFT for viscosity calculations: comparison with molecular simulation and experimental data. *J. Phys. Chem. B*, **117**(27):8159–8171, 2013. doi:10.1021/jp401307t.

[10] F. Llovell, O. Vilaseca, N. Jung, and L. Vega. Water+ 1-alkanol systems: Modeling the phase, interface and viscosity properties. *Fluid Phase Equilib.*, **360**:367–378, 2013. doi:10.1016/j.fluid.2013.10.002.

[11] F. Llovell, R. Marcos, and L. Vega. Transport properties of mixtures by the soft-SAFT+ free-volume theory: application to mixtures of n-alkanes and hydrofluorocarbons. *J. Phys. Chem. B*,

117(17):5195–5205, 2013. doi:10.1021/jp401754r.

[12] I. Polishuk and A. Yitzhak. Modeling viscosities of pure compounds and their binary mixtures using the modified Yarranton–Satyro correlation and free volume theory coupled with SAFT+ Cubic EoS. *Ind. Eng. Chem. Res.*, **53**(2):959–971, 2014. doi:10.1021/ie4030352.

[13] S. E. Quiñones-Cisneros, C. K. Zéberg-Mikkelsen, and E. H. Stenby. The friction theory (f-theory) for viscosity modeling. *Fluid Phase Equilib.*, **169**(2):249–276, 2000. doi:10.1016/s0378-3812(00)00310-1.

[14] S. E. Quiñones-Cisneros, C. K. Zéberg-Mikkelsen, J. Fernández, and J. García. General friction theory viscosity model for the PC-SAFT equation of state. *AIChE J.*, **52**(4):1600–1610, 2006. doi:10.1002/aic.10755.

[15] S. E. Quiñones-Cisneros and U. K. Deiters. Generalization of the friction theory for viscosity modeling. *J. Phys. Chem. B*, **110**(25):12820–12834, 2006. doi:10.1021/jp0618577.

[16] W.-T. Ashurst and W. Hoover. Dense-fluid shear viscosity via nonequilibrium molecular dynamics. *Phys. Rev. A*, **11**(2):658, 1975. doi:10.1103/PhysRevA.11.658.

[17] C. Roland, S. Bair, and R. Casalini. Thermodynamic scaling of the viscosity of van der Waals, H-bonded, and ionic liquids. *J. Chem. Phys.*, **125**(12):124508, 2006. doi:10.1063/1.2346679.

[18] A. S. Pensado, A. A. Pádua, M. J. Comuñas, and J. Fernandez. Relationship between viscosity coefficients and volumetric properties using a scaling concept for molecular and ionic liquids. *J. Phys. Chem. B*, **112**(18):5563–5574, 2008. doi:10.1021/jp711752b.

[19] D. Fragiadakis and C. M. Roland. On the density scaling of liquid dynamics. *J. Chem. Phys.*, **134**(4):044504, 2011. doi:10.1063/1.3532545.

[20] E. R. López, A. S. Pensado, M. J. Comuñas, A. A. Pádua, J. Fernández, and K. R. Harris. Density scaling of the transport properties of molecular and ionic liquids. *J. Chem. Phys.*, **134**(14):144507, 2011. doi:10.1063/1.3575184.

[21] R. Macías-Salinas, M. A. Flores-Granados, M. Diaz-Cruz, and F. García-Sánchez. Modeling the dynamic viscosity of associating and polar fluids via the use of density scaling. *Fluid Phase Equilib.*, **458**:16–29, 2018. doi:10.1016/j.fluid.2017.10.032.

[22] H. O. Baled, I. K. Gamwo, R. M. Enick, and M. A. McHugh. Viscosity models for pure hydrocarbons at extreme conditions: A review and comparative study. *Fuel*, **218**:89–111, 2018. doi:10.1016/j.fuel.2018.01.002.

[23] O. Lötgering-Lin and J. Gross. Group Contribution Method for Viscosities Based on Entropy Scaling Using the Perturbed-Chain Polar Statistical Associating Fluid Theory. *Ind. Eng. Chem. Res.*, **54**(32):7942–7952, 2015. doi:10.1021/acs.iecr.5b01698.

[24] G. Galliéro, C. Boned, A. Baylaucq, and F. Montel. Influence of the mass ratio on viscosity in Lennard–Jones mixtures: The one-fluid model revisited using nonequilibrium molecular dynamics. *Fluid Phase Equilib.*, **234**(1):56–63, 2005. doi:10.1016/j.fluid.2005.05.016.

[25] G. Galliéro, C. Boned, A. Baylaucq, and F. Montel. The van der Waals one-fluid model for viscosity in Lennard–Jones fluids: Influence of size and energy parameters. *Fluid Phase Equilib.*, **245**(1):20–25, 2006. doi:10.1016/j.fluid.2006.03.006.

[26] S. Delage-Santacreu, G. Galliero, H. Hoang, J.-P. Bazile, C. Boned, and J. Fernandez. Thermodynamic scaling of the shear viscosity of Mie n-6 fluids and their binary mixtures. *J. Chem. Phys.*, **142**(17):174501, 2015. doi:10.1063/1.4919296.

[27] G. Galliéro, C. Boned, and A. Baylaucq. Molecular dynamics study of the Lennard-Jones fluid viscosity: application to real fluids. *Ind. Eng. Chem. Res.*, **44**(17):6963–6972, 2005. doi:10.1021/ie050154t.

[28] N. Ohtori and Y. Ishii. Explicit expressions of self-diffusion coefficient, shear viscosity, and the Stokes-Einstein relation for binary mixtures of Lennard-Jones liquids. *J. Chem. Phys.*, **143**(16):164514, 2015. doi:10.1063/1.4934627.

[29] N. Meyer, J.-F. Wax, and H. Xu. Viscosity of Lennard-Jones mixtures: A systematic study and empirical law. *J. Chem. Phys.*, **148**(23):234506, 2018. doi:10.1063/1.5034779.

[30] J. C. Dyre. Hidden scale invariance in condensed matter. *J. Phys. Chem. B*, **118**(34):10007–10024, 2014. doi:10.1103/PhysRevE.88.042139.

[31] N. P. Bailey, U. R. Pedersen, N. Gnan, T. B. Schrøder, and J. C. Dyre. Pressure-energy correlations in liquids. I. Results from computer simulations. *J. Chem. Phys.*, **129**(18):184507, 2008. doi:10.1063/1.2982247.

[32] J. C. Dyre. Perspective: Excess-entropy scaling. *J. Chem. Phys.*, **149**(21):210901, 2018. doi:10.1063/1.5055064.

[33] I. H. Bell, R. Messerly, M. Thol, L. Costigliola, and J. C. Dyre. Modified Entropy Scaling of the Transport Properties of the Lennard-Jones Fluid. *J. Phys. Chem. B*, **123**(29):6345–6363, 2019. doi:10.1021/acs.jpcb.9b05808.

[34] T. Goel, C. N. Patra, T. Mukherjee, and C. Chakravarty. Excess entropy scaling of transport properties of Lennard-Jones chains. *J. Chem. Phys.*, **129**(16):164904, 2008. doi:10.1063/1.2995990.

[35] G. Galliéro and C. Boned. Thermal conductivity of the Lennard-Jones chain fluid model. *Phys. Rev. E: Stat., Nonlinear, Soft Matter Phys.*, **80**(6):061202, 2009. doi:10.1103/PhysRevE.80.061202.

[36] R. Chopra, T. M. Truskett, and J. R. Errington. Excess entropy scaling of dynamic quantities for fluids of dumbbell-shaped particles. *J. Chem. Phys.*, **133**(10):104506, 2010.

doi:10.1063/1.3477767.

[37] R. Chopra, T. M. Truskett, and J. R. Errington. On the Use of Excess Entropy Scaling to Describe the Dynamic Properties of Water. *J. Phys. Chem. B*, **114**(32):10558–10566, 2010. doi:10.1021/jp1049155.

[38] G. Galliéro, C. Boned, and J. Fernández. Scaling of the viscosity of the Lennard-Jones chain fluid model, argon, and some normal alkanes. *J. Chem. Phys.*, **134**(6):064505, 2011. doi:10.1063/1.3553262.

[39] E. Voyiatzis, F. Müller-Plathe, and M. C. Böhm. Excess entropy scaling for the segmental and global dynamics of polyethylene melts. *Phys. Chem. Chem. Phys.*, **16**(44):24301–24311, 2014. doi:10.1039/c4cp03559c.

[40] Y. Rosenfeld. Relation between the transport coefficients and the internal entropy of simple systems. *Phys. Rev. A*, **15**(6):2545, 1977. doi:10.1103/physreva.15.2545.

[41] Y. Rosenfeld. A quasi-universal scaling law for atomic transport in simple fluids. *J. Phys.: Condens. Matter*, **11**(28):5415, 1999. doi:10.1088/0953-8984/11/28/303.

[42] M. Dzugutov. A universal scaling law for atomic diffusion in condensed matter. *Nature (London, U. K.)*, **381**:137–139, 1996. doi:10.1038/381137a0.

[43] A. Samanta, S. M. Ali, and S. K. Ghosh. Universal Scaling Laws of Diffusion in a Binary Fluid Mixture. *Phys. Rev. Lett.*, **87**(24):245901, 2001. doi:10.1103/physrevlett.87.245901.

[44] O. Lötgering-Lin, M. Fischer, M. Hopp, and J. Gross. Pure Substance and Mixture Viscosities Based on Entropy Scaling and an Analytic Equation of State. *Ind. Eng. Chem. Res.*, **57**(11):4095–4114, 2018. doi:10.1021/acs.iecr.7b04871.

[45] W. Kob and H. C. Andersen. Testing mode-coupling theory for a supercooled binary Lennard-Jones mixture I: The van Hove correlation function. *Phys. Rev. E*, **51**(5):4626–4641, 1995. doi:10.1103/physreve.51.4626.

[46] W. Kob and H. C. Andersen. Testing mode-coupling theory for a supercooled binary Lennard-Jones mixture. II. Intermediate scattering function and dynamic susceptibility. *Phys. Rev. E*, **52**(4):4134–4153, 1995. doi:10.1103/physreve.52.4134.

[47] W. Kob and H. C. Andersen. Scaling Behavior in the β-Relaxation Regime of a Supercooled Lennard-Jones Mixture. *Phys. Rev. Lett.*, **73**(10):1376–1379, 1994. doi:10.1103/physrevlett.73.1376.

[48] L. Novak. Self-diffusion coefficient and viscosity in fluids. *Int. J. Chem. Reactor Eng.*, **9**(1), 2011. doi:10.1515/1542-6580.2640.

[49] L. T. Novak. Fluid viscosity-residual entropy correlation. *Int. J. Chem. Reactor Eng.*, **9**(1), 2011.

doi:10.2202/1542-6580.2839.

[50] J. O. Hirschfelder, C. F. Curtiss, and R. B. Bird. *Molecular Theory of Gases and Liquids*. John Wiley & Sons, Inc, 1954.

[51] P. D. Neufeld, A. Janzen, and R. Aziz. Empirical Equations to Calculate 16 of the Transport Collision Integrals Ω (l, s)* for the Lennard-Jones (12–6) Potential. *J. Chem. Phys.*, **57**(3):1100–1102, 1972. doi:10.1063/1.1678363.

[52] C. Wilke. A viscosity equation for gas mixtures. *J. Chem. Phys.*, **18**(4):517–519, 1950. doi:10.1063/1.1747673.

[53] B. E. Poling, J. M. Prausnitz, and J. P. O'Connell. *The Properties of Gases and Liquids*. McGraw-Hill Professional, 2000. ISBN 9780071499996.

[54] J. Gross and G. Sadowski. Perturbed-chain SAFT: An equation of state based on a perturbation theory for chain molecules. *Ind. Eng. Chem. Res.*, **40**(4):1244–1260, 2001. doi:10.1021/ie0003887.

[55] J. R. Errington and V. K. Shen. Direct evaluation of multicomponent phase equilibria using flat-histogram methods. *J. Chem. Phys.*, **123**(16):164103, 2005. doi:10.1063/1.2064628.

[56] A. Hemmen, A. Z. Panagiotopoulos, and J. Gross. Grand Canonical Monte Carlo Simulations Guided by an Analytic Equation of State – Transferable Anisotropic Mie Potentials for Ethers. *J. Phys. Chem. B*, **119**(23):7087–7099, 2015. doi:10.1021/acs.jpcb.5b01806.

[57] A. M. Ferrenberg and R. H. Swendsen. New Monte Carlo technique for studying phase transitions. *Phys. Rev. Lett.*, **61**(23):2635, 1988. doi:10.1103/physrevlett.61.2635.

[58] P. Virnau and M. Müller. Calculation of free energy through successive umbrella sampling. *J. Chem. Phys.*, **120**(23):10925–10930, 2004. doi:10.1063/1.1739216.

[59] J. R. Errington. Direct calculation of liquid–vapor phase equilibria from transition matrix Monte Carlo simulation. *J. Chem. Phys.*, **118**(22):9915–9925, 2003. doi:10.1063/1.1572463.

[60] V. K. Shen and J. R. Errington. Determination of fluid-phase behavior using transition-matrix Monte Carlo: binary Lennard-Jones mixtures. *J. Chem. Phys.*, **122**(6):064508, 2005. doi:10.1063/1.1844372.

[61] I. T. Todorov, W. Smith, K. Trachenko, and M. T. Dove. DL_POLY_3: new dimensions in molecular dynamics simulations via massive parallelism. *J. Mater. Chem.*, **16**(20):1911–1918, 2006. doi:10.1039/b517931a.

[62] J. E. Basconi and M. R. Shirts. Effects of Temperature Control Algorithms on Transport Properties and Kinetics in Molecular Dynamics Simulations. *J. Chem. Theory Comput.*, **9**(7):2887–2899, 2013. doi:10.1021/ct400109a.

[63] R. Zwanzig. Time-correlation functions and transport coefficients in statistical mechanics. *Annu. Rev. Phys. Chem.*, **16**(1):67–102, 1965. doi:10.1146/annurev.pc.16.100165.000435.

[64] B. Hess. Determining the shear viscosity of model liquids from molecular dynamics simulations. *J. Chem. Phys.*, **116**(1):209–217, 2002. doi:10.1063/1.1421362.

[65] B. L. Holian and D. J. Evans. Shear viscosities away from the melting line: A comparison of equilibrium and nonequilibrium molecular dynamics. *J. Chem. Phys.*, **78**(8):5147–5150, 1983. doi:10.1063/1.445384.

[66] P. J. Daivis and D. J. Evans. Comparison of constant pressure and constant volume nonequilibrium simulations of sheared model decane. *J. Chem. Phys.*, **100**(1):541–547, 1994. doi:10.1063/1.466970.

[67] N. Wiener. Generalized harmonic analysis. *Acta Math.*, **55**(0):117–258, 1930. doi:10.1007/bf02546511.

[68] A. Khintchine. Korrelationstheorie der stationären stochastischen Prozesse. *Math. Ann.*, **109**(1):604–615, 1934. doi:10.1007/bf01449156.

[69] M. Tuckerman. *Statistical Mechanics: Theory and Molecular Simulation*. OXFORD UNIV PR, 2010. ISBN 0198525265.

[70] M. T. Humbert, Y. Zhang, and E. J. Maginn. PyLAT: Python LAMMPS Analysis Tools. *J. Chem. Inf. Model.*, **59**(4):1301–1305, 2019. doi:10.1021/acs.jcim.9b00066.

[71] V. Calandrini, E. Pellegrini, P. Calligari, K. Hinsen, and G. R. Kneller. nMoldyn-Interfacing spectroscopic experiments, molecular dynamics simulations and models for time correlation functions. *JDN*, **12**:201–232, 2011. doi:10.1051/sfn/201112010.

[72] Y. Zhang, A. Otani, and E. J. Maginn. Reliable Viscosity Calculation from Equilibrium Molecular Dynamics Simulations: A Time Decomposition Method. *J. Chem. Theory Comput.*, **11**(8):3537–3546, 2015. doi:10.1021/acs.jctc.5b00351.

[73] E. J. Maginn, R. A. Messerly, D. J. Carlson, D. R. Roe, and J. R. Elliott. Best Practices for Computing Transport Properties 1. Self-Diffusivity and Viscosity from Equilibrium Molecular Dynamics [Article v1.0]. *Living J. Comput. Mol. Sci.*, **1**(1), 2019. doi:10.33011/livecoms.1.1.6324.

[74] B. Efron. Bootstrap Methods: Another Look at the Jackknife. *Ann. Stat.*, **7**(1):1–26, 1979. doi:10.1214/aos/1176344552.

[75] M. Fischer, G. Bauer, and J. Gross. Force Fields with Fixed Bond Lengths and with Flexible Bond Lengths: Comparing Static and Dynamic Fluid Properties. *J. Chem. Eng. Data*, **65**(4):1583–1593, 2020. doi:10.1021/acs.jced.9b01031.

[76] M. Fischer, G. Bauer, and J. Gross. Transferable Anisotropic United-Atom Mie (TAMie) Force

Field: Transport Properties from Equilibrium Molecular Dynamic Simulations. *Ind. Eng. Chem. Res.*, **59**(18):8855–8869, 2020. doi:10.1021/acs.iecr.0c00848.

[77] A. Hemmen. *Entwicklung eines übertragbaren Kraftfeldes (TAMie) für Phasengleichgewichte mit Monte Carlo Simulationen im großkanonischen Ensemble*. Ph.D. thesis, University of Stuttgart, 2019. doi:10.18419/OPUS-10910.

[78] K. Binder. Computer simulations of critical phenomena and phase behaviour of fluids. *Molecular Physics*, **108**(14):1797–1815, 2010. doi:10.1080/00268976.2010.495734.

[79] V. Harismiadis, N. Koutras, D. Tassios, and A. Panagiotopoulos. How good is conformal solutions theory for phase equilibrium predictions?: Gibbs ensemble simulations of binary Lennard-Jones mixtures. *Fluid Phase Equilib.*, **65**:1–18, 1991. doi:10.1016/0378-3812(91)87014-Z.

[80] M. Lechner. *Robustheit der Entropieskalierung mit Hinblick auf Kraftfeldanpassungen*. Studienarbeit, Institute of Thermodynamics and Thermal Process Engineering ITT, University of Stuttgart, 2019.

5 Conclusion

In the present work, entropy scaling and molecular simulations, two methods of predicting transport coefficients of fluids, are jointly employed in several ways, to achieve synergistic effects. Molecular simulations are used, on the one hand, to gain new findings and deeper insights concerning the entropy scaling method. On the other hand, approaches from entropy scaling are used to better define and assess molecular simulations for transport properties. This work establishes a framework to both robustly and efficiently determine transport coefficients of technically relevant fluids over a wide range of pressures and temperatures, and to perform larger-scale simulation studies to be used in force field development.

The first part of this thesis investigates whether a force field with rigid bond lengths can be applied with harmonic bond length potentials and how static and transport properties are thereby affected. The substances studied in this study are described using the *TAMie* force field, which was originally developed with fixed bond lengths, and to which harmonic bonds are introduced in this study. The new "flexible" version of *TAMie* manages to reproduce the results for liquid phase pressure, shear viscosity, thermal conductivity, and self-diffusion coefficients of the original force field within the 95 % confidence interval, provided that the binding energy constant of the harmonic bond k_l is appropriately chosen. In the study, a wide range of values for k_l were examined at different time step sizes of the integration scheme to evaluate whether the high-frequency oscillation of the bond can still be resolved correctly. It has been shown that with a Velocity Verlet integrator and a common time step of 2 fs, suitable values for k_l are in the range of fully flexible united atom force fields reported in the literature. Bonds with excessively high bond constants can no longer be resolved, which results in deviations. As a practical result of this study, it was shown that "flexible" versions can be introduced for force fields that were originally parametrized with fixed bonds (including *TAMie*), making it more straightforward to compute transport properties in molecular simulations.

This insight is applied in the second part of the thesis, where the predictive power of the ("flexible") *TAMie* force field for transport properties, namely shear viscosity, self-diffusion coefficient and thermal conductivity is assessed in a broad molecular simulation study. *TAMie* was initially developed for static thermodynamic properties and phase equilibria. This work proposes a workflow, where the state points at which simulations are conducted are selected based on their residual entropy in order to ensure a meaningful distribution of states for

conducting simulations covering the entire fluid region. The three transport coefficients and their statistical uncertainties are then determined simultaneously in a series of equilibrium molecular dynamics simulations at each state point, respectively. A simple correlation function is then fitted to the simulation results for each transport property, based on the entropy scaling method. By the careful choice of the simulated state points, four points corresponding to liquid states and one point to a gas state are sufficient to parameterize robust correlations. Using these correlations, transport coefficients in the entire fluid region can be predicted. The *TAMie* force field could then be assessed by comparing them with all the data available in literature – even for thermodynamic states far from those that were simulated. The model based on the *TAMie* force field achieved good agreement with literature data, with AAD values of 13 % for shear viscosity, 18 % for self diffusion, and 10 % for thermal conductivity.

Further, this thesis investigates the entropy scaling behavior of LJ model mixtures using molecular simulations. By considering three model mixtures at various temperatures and compositions, the influence of individual LJ parameters on VLE, entropy s^* and viscosity ($\eta^\#$) has been assessed. All quantities are determined in molecular simulations; besides MD simulations for the determination of viscosity, GCMC simulations are conducted for the calculation of the mixture entropies and the VLE data. In the context of entropy scaling, GCMC simulations are a suitable choice for determining mixture entropies. Relating the dimensionless viscosity to the residual entropy from the GCMC simulations, a general, nearly linear master curve was found that is valid for all state points of all mixtures. The Chapman-Enskog viscosity is used as the only model equation in the study to define the dimensionless viscosity. The results of the study indicate that within the entropy scaling approach, all LJ mixtures can be considered as pseudo pure LJ substance.

The results obtained in this thesis open an exciting potential for future applications for the combination of molecular simulations and entropy scaling. The *TAMie* force field, is subject to further development and parameters for new substance classes have recently been published. The workflow proposed in this work can be used to efficiently evaluate the predictive power of *TAMie* for the transport coefficients of these compounds. The results obtained from the simulation of the model mixtures suggest that it can also be applied to real mixtures. Following the approach, it may even be possible to avoid the comparatively computationally intensive MD simulations for an initial estimate of transport properties: Knowing the entropy scaling parameters for a force field (as determined for *TAMie* in chapter 3) the transport properties can be estimated via entropy scaling and the results of GCMC simulations and histogram reweighting. My preliminary work on this subject indicated that the entropy scaling parameters remain nearly constant under slight changes in the force field parameters, suggesting the dynamical properties can be considered in force field optimization.

Appendices

A Supporting Information for: Force fields with fixed bond lengths and with flexible bond lengths: Comparing static and dynamic fluid properties

The content of this appendix is a literal quote of the supporting information:

M. Fischer, G. Bauer, J. Gross: Supporting Information for: Force Fields with Fixed Bond Lengths and with Flexible Bond lengths: Comparing Static and Dynamic Fluid Properties. *Journal of Chemical & Engineering Data*, **65**:1583-1593, 2020. doi:10.1021/acs.jced.9b01031

A.1 Details of the calculation of the Thermal Conductivity

The correlated quantities needed for the calculation of the thermal conductivity are the three spatial entries of the heat flux $\boldsymbol{J}_q = \left(J_q^x, J_q^y, J_q^z\right)$. $R_{J_qJ_q}$ is the mean of the autocorrelation functions (ACF) of the three entries and is calculated via the dot product as

$$R_{J_qJ_q}(\tau) = \lim_{\Theta\to\infty} \frac{1}{2\Theta} \int_{-\Theta}^{\Theta} \boldsymbol{J}_q(t+\tau)\cdot\boldsymbol{J}_q(t)\,\mathrm{d}t \tag{S1}$$

where $\boldsymbol{J}_q$ is defined as

$$\boldsymbol{J}_q = \frac{1}{V}\left[\sum_{i=1}^{N} \boldsymbol{v}_i e_i + \sum_{i=1}^{N}\sum_{j>i}^{N} \boldsymbol{r}_{ij}\left(\boldsymbol{v}_j \cdot \frac{\partial u_i}{\partial \boldsymbol{r}_j}\right)\right] \tag{S2}$$

which contains the per-atom (potential and kinetic) energy e_i and the force $\boldsymbol{f}_{ij} = -\frac{\partial u_i}{\partial \boldsymbol{r}_j}$ due to the per-atom potential energy u_i. Analogous to the viscosity, the running value of λ is calculated as integral of an ACF, according to

$$\lambda_{\mathrm{run}}(\tau) = \frac{V}{3k_{\mathrm{B}}T^2} \int_0^{\tau} R_{J_qJ_q}(\tau')\mathrm{d}\tau' \tag{S3}$$

and the thermal conductivity is calculated as the limit $\lambda = \lambda_{\mathrm{run}}(\tau \to \infty)$.

A.2 Distribution of Bond Lengths

Figure A.1 shows the distribution of the bond lengths of propane, which can also be seen in fig. 2.2 of the main text. In fig. A.1 the simulation results from fig. 2.2 of the main text are compared with an analytical distribution, which calculates as

$$P(r) = \sqrt{\frac{k_l \beta}{\pi}} \exp\left(-\beta k_l (r - r_0)^2\right) \tag{S4}$$

Each maximum value of $P(r)$ is adjusted to the maximum value of the respective distribution of the simulations. The considered molecule, propane, comprises two harmonic bond length

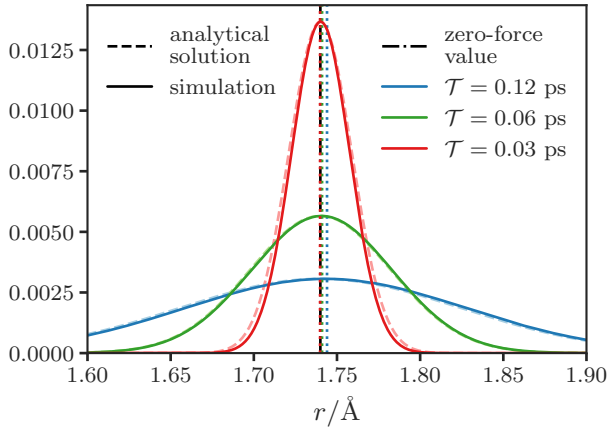

Figure A.1: Comparison of distributions of bond lengths from simulation (solid) and analytical solution (dashed). Results are shown for liquid propane at $T = 360\,\mathrm{K}$ and $\rho = 361.27\,\mathrm{kg\,m^{-3}}$ (rRESPA with inner time step $\Delta t = 0.1\,\mathrm{fs}$) for different values of bonding force constant k_l. Vertical colored lines represent the respective maximum value of the distribution. The black vertical line shows the reference length r_0.

potentials that are not independent from one another. The simple solution of a harmonic oscillator given in eq. (S4) can only be defended for uncorrelated harmonic oscillators of both bonds and no impact of surrounding molecules. These two assumptions are rather well justified, as we show in fig. A.1. For $k_l = 50$ / $\mathcal{T} = 0.12\,\mathrm{ps}$ the total distribution shifts to higher distances compared to the analytical solution, which confirms the offset maximum value. For $k_l = 1000$ / $\mathcal{T} = 0.03\,\mathrm{ps}$ the simulated distribution is slightly narrower than the analytical distribution.

A.3 Diagram of pressure of propane for high values of period time T

In the main text we explain that for $\mathcal{T} > 0.1\,\mathrm{ps}$, the k_l values are small and therefore the flexible bonds are so loose that results of the flexible bond model deviate from results of a rigid bond model. Figure A.2 illustrates this point by showing the section of high $\mathcal{T}$ values in Figure 1 from the main text in a finer scale.

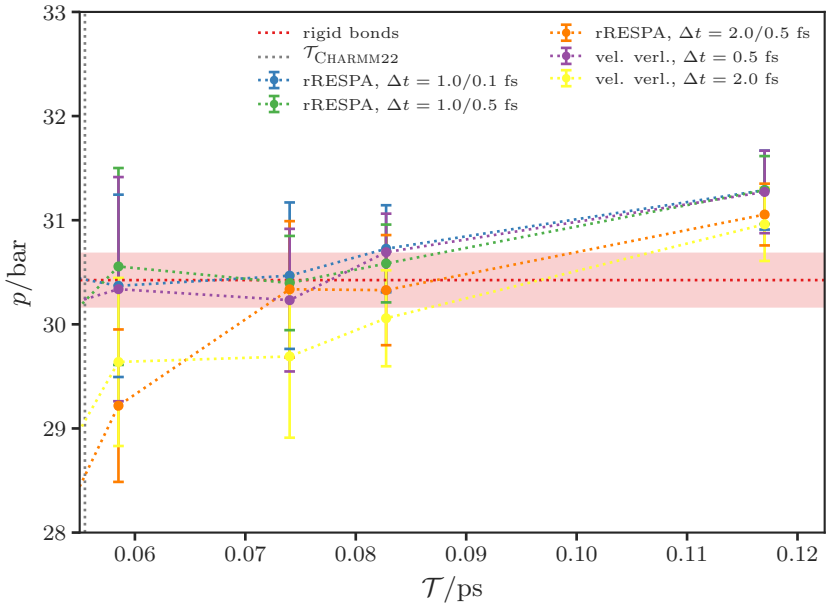

Figure A.2: Zoom into Figure 1 of the main text for high values of $\mathcal{T}$. Shown is the pressure p of propane at $T = 360\,\mathrm{K}$ over period of the bond vibrations $\mathcal{T}$. Colors represent different integration schemes with different time steps Δt. The red horizontal line shows result of rigid bonds. Vertical lines highlight $\mathcal{T}$ values of the CHARMM (dotted) and the GROMOS force field (dashed).

A.4 Simulation results in tables

This supporting information contains tables summarizing temperatures, pressures, viscosities, diffusion coefficients and thermal conductivities for the molecules with rigid bonds (table A.1) as well as for the models with flexible bonds, including all integration schemes and time steps (tables A.2–A.5). Additionally tables with results for one lower temperature for each substance (tables A.6–A.9) and the results of gas phase simulations of propane at 360 K, calculated with rRESPA (table A.10) are presented. The stated statistical uncertainties are the 95 % confidence interval, calculated as described in the main text.

Table A.1: Results of the rigid bonds, calculated with Velocity Verlet and SHAKE ($\Delta t = 1.0\,\mathrm{fs}$)

Substance	ρ/kg/m^3	T/K	p/bar	η/mPa s	λ/W m^{-1} K^{-1}	D_{self}/cm^2 s^{-1}
ethane	315.43	299.990(51)	38.677(240)	$3.75(9)\cdot10^{-2}$	$6.86(18)\cdot10^{-2}$	$3.38(4)\cdot10^{-4}$
ethane	512.82	205.000(53)	−0.659 48(68000)	$1.35(3)\cdot10^{-1}$	$1.58(5)\cdot10^{-1}$	$7.49(5)\cdot10^{-5}$
dimethylether	482.12	379.970(59)	31.868(290)	$5.91(8)\cdot10^{-2}$	$8.11(22)\cdot10^{-2}$	$2.53(2)\cdot10^{-4}$
dimethylether	649.04	299.980(64)	1.6168(6000)	$1.34(2)\cdot10^{-1}$	$1.34(4)\cdot10^{-1}$	$9.86(7)\cdot10^{-5}$
propane	361.24	360.010(56)	30.425(250)	$4.38(9)\cdot10^{-2}$	$6.04(14)\cdot10^{-2}$	$3.04(2)\cdot10^{-4}$
propane	497.2	294.980(48)	7.4815(4900)	$9.53(28)\cdot10^{-2}$	$9.35(32)\cdot10^{-2}$	$1.26(1)\cdot10^{-4}$
ethane	315.43	299.990(51)	38.677(240)	$3.75(9)\cdot10^{-2}$	$6.86(18)\cdot10^{-2}$	$3.38(4)\cdot10^{-4}$
propane (vapor)	18.481	295.000(24)	8.6049(74)	$8.08(120)\cdot10^{-3}$	$1.68(19)\cdot10^{-2}$	$6.19(4)\cdot10^{-3}$
propane (vapor)	94.323	359.990(51)	35.201(37)	$1.17(8)\cdot10^{-2}$	$2.75(19)\cdot10^{-2}$	$1.50(1)\cdot10^{-3}$

Table A.2: Results of ethane at 300 K, calculated with rRESPA

Δt/fs	ρ/kg/m^3	T/K	p/bar	$\mathcal{T}$/fs	η/mPa s	λ/W m^{-1} K^{-1}	D_{self}/cm^2 s^{-1}
1.0 / 0.1	315.43	299.990(51)	63.518(4000)	0.008 422 1	$3.90(4)\cdot10^{-2}$	$6.85(30)\cdot10^{-2}$	$3.50(3)\cdot10^{-4}$
1.0 / 0.1	315.43	300.000(64)	68.064(3700)	0.011 911	$3.89(8)\cdot10^{-2}$	$6.90(14)\cdot10^{-2}$	$3.51(4)\cdot10^{-4}$
1.0 / 0.1	315.43	300.000(52)	71.039(3100)	0.018 832	$3.90(9)\cdot10^{-2}$	$7.03(32)\cdot10^{-2}$	$3.48(3)\cdot10^{-4}$
1.0 / 0.1	315.43	300.000(47)	72.191(2900)	0.026 633	$3.93(10)\cdot10^{-2}$	$7.19(25)\cdot10^{-2}$	$3.51(3)\cdot10^{-4}$
1.0 / 0.1	315.43	300.000(41)	54.226(3300)	0.037 665	$3.79(10)\cdot10^{-2}$	$6.64(27)\cdot10^{-2}$	$3.46(2)\cdot10^{-4}$
1.0 / 0.1	315.43	300.000(58)	38.52(150)	0.053 266	$3.70(7)\cdot10^{-2}$	$6.40(10)\cdot10^{-2}$	$3.39(3)\cdot10^{-4}$
1.0 / 0.1	315.43	299.990(75)	38.388(1200)	0.059 553	$3.68(6)\cdot10^{-2}$	$6.73(37)\cdot10^{-2}$	$3.35(2)\cdot10^{-4}$

Continued on next page

Continued: Results of ethane at 300 K, calculated with rRESPA

Δt/fs	ρ/kg/m^3	T/K	p/bar	$\mathcal{T}$/fs	η/mPa s	λ/W m^{-1} K^{-1}	D_{self}/cm^2 s^{-1}
1.0 / 0.1	315.43	299.980(62)	38.443(540)	0.075 33	$3.59(14)\cdot10^{-2}$	$6.52(31)\cdot10^{-2}$	$3.37(2)\cdot10^{-4}$
1.0 / 0.1	315.43	300.000(51)	38.655(510)	0.084 221	$3.68(4)\cdot10^{-2}$	$6.50(23)\cdot10^{-2}$	$3.39(3)\cdot10^{-4}$
1.0 / 0.1	315.43	299.990(53)	38.785(240)	0.119 11	$3.67(7)\cdot10^{-2}$	$6.40(19)\cdot10^{-2}$	$3.38(3)\cdot10^{-4}$

Table A.3: Results of propane at 360 K, calculated with rRESPA

Δt/fs	ρ/kg/m^3	T/K	p/bar	$\mathcal{T}$/fs	η/mPa s	λ/W m^{-1} K^{-1}	D_{self}/cm^2 s^{-1}
2.0 / 0.5	361.24	360.01(7)	1.2363(47000)	0.008 274 8	$4.62(7)\cdot10^{-2}$	$6.23(25)\cdot10^{-2}$	$3.19(3)\cdot10^{-4}$
2.0 / 0.5	361.24	359.990(51)	38.625(3200)	0.011 702	$4.70(8)\cdot10^{-2}$	$6.10(18)\cdot10^{-2}$	$3.16(2)\cdot10^{-4}$
2.0 / 0.5	361.24	359.980(55)	63.451(3400)	0.018 503	$4.65(10)\cdot10^{-2}$	$6.36(16)\cdot10^{-2}$	$3.20(3)\cdot10^{-4}$
2.0 / 0.5	361.24	359.97(6)	62.065(2100)	0.026 167	$4.54(19)\cdot10^{-2}$	$6.33(22)\cdot10^{-2}$	$3.16(1)\cdot10^{-4}$
2.0 / 0.5	361.24	360.030(55)	27.924(2600)	0.037 006	$4.36(9)\cdot10^{-2}$	$5.73(18)\cdot10^{-2}$	$3.01(2)\cdot10^{-4}$
2.0 / 0.5	361.24	359.970(62)	27.853(3100)	0.052 334	$4.34(6)\cdot10^{-2}$	$5.69(21)\cdot10^{-2}$	$3.01(2)\cdot10^{-4}$
2.0 / 0.5	361.24	360.000(62)	29.219(730)	0.058 511	$4.33(11)\cdot10^{-2}$	$5.85(22)\cdot10^{-2}$	$3.04(2)\cdot10^{-4}$
2.0 / 0.5	361.24	360.000(52)	30.336(650)	0.074 012	$4.38(8)\cdot10^{-2}$	$5.92(25)\cdot10^{-2}$	$3.03(2)\cdot10^{-4}$
2.0 / 0.5	361.24	359.980(55)	30.328(530)	0.082 748	$4.27(10)\cdot10^{-2}$	$5.88(23)\cdot10^{-2}$	$3.05(2)\cdot10^{-4}$
2.0 / 0.5	361.24	359.990(78)	31.054(300)	0.117 02	$4.37(5)\cdot10^{-2}$	$6.01(18)\cdot10^{-2}$	$3.05(2)\cdot10^{-4}$
1.0 / 0.1	361.24	359.990(41)	57.036(3300)	0.008 274 8	$4.72(9)\cdot10^{-2}$	$6.35(19)\cdot10^{-2}$	$3.15(2)\cdot10^{-4}$
1.0 / 0.1	361.24	360.010(66)	67.816(3500)	0.011 702	$4.71(12)\cdot10^{-2}$	$6.24(22)\cdot10^{-2}$	$3.11(2)\cdot10^{-4}$
1.0 / 0.1	361.24	360.000(53)	75.041(3100)	0.018 503	$4.78(6)\cdot10^{-2}$	$6.40(20)\cdot10^{-2}$	$3.20(2)\cdot10^{-4}$
1.0 / 0.1	361.24	360.020(64)	61.681(3400)	0.026 167	$4.59(3)\cdot10^{-2}$	$6.25(19)\cdot10^{-2}$	$3.13(2)\cdot10^{-4}$

Continued on next page

Continued: Results of propane at 360 K, calculated with rRESPA

Δt/fs	ρ/kg/m^3	T/K	p/bar	$\mathcal{T}$/fs	η/mPa s	λ/W m^{-1} K^{-1}	D_{self}/cm^2 s^{-1}
1.0 / 0.1	361.24	359.990(65)	30.012(2800)	0.037 006	$4.43(10)\cdot10^{-2}$	$5.88(13)\cdot10^{-2}$	$3.04(2)\cdot10^{-4}$
1.0 / 0.1	361.24	359.970(48)	30.492(1200)	0.052 334	$4.36(5)\cdot10^{-2}$	$5.79(14)\cdot10^{-2}$	$3.01(3)\cdot10^{-4}$
1.0 / 0.1	361.24	359.990(66)	30.37(88)	0.058 511	$4.37(8)\cdot10^{-2}$	$5.84(24)\cdot10^{-2}$	$3.06(2)\cdot10^{-4}$
1.0 / 0.1	361.24	359.990(55)	30.467(700)	0.074 012	$4.35(6)\cdot10^{-2}$	$5.81(19)\cdot10^{-2}$	$3.04(3)\cdot10^{-4}$
1.0 / 0.1	361.24	360.00(7)	30.726(420)	0.082 748	$4.28(10)\cdot10^{-2}$	$6.10(26)\cdot10^{-2}$	$3.03(2)\cdot10^{-4}$
1.0 / 0.1	361.24	360.030(53)	31.289(380)	0.117 02	$4.31(9)\cdot10^{-2}$	$5.97(19)\cdot10^{-2}$	$3.02(3)\cdot10^{-4}$
1.0 / 0.5	361.24	359.970(51)	52.506(2700)	0.008 274 8	$4.65(11)\cdot10^{-2}$	$6.40(22)\cdot10^{-2}$	$3.19(1)\cdot10^{-4}$
1.0 / 0.5	361.24	359.980(58)	67.735(4200)	0.011 702	$4.66(4)\cdot10^{-2}$	$6.43(25)\cdot10^{-2}$	$3.21(3)\cdot10^{-4}$
1.0 / 0.5	361.24	360.000(35)	74.26(360)	0.018 503	$4.77(11)\cdot10^{-2}$	$6.37(17)\cdot10^{-2}$	$3.17(1)\cdot10^{-4}$
1.0 / 0.5	361.24	360.02(4)	66.556(2300)	0.026 167	$4.54(9)\cdot10^{-2}$	$6.30(29)\cdot10^{-2}$	$3.16(3)\cdot10^{-4}$
1.0 / 0.5	361.24	359.970(76)	30.101(3200)	0.037 006	$4.33(10)\cdot10^{-2}$	$5.75(27)\cdot10^{-2}$	$3.03(2)\cdot10^{-4}$
1.0 / 0.5	361.24	360.010(63)	29.882(1200)	0.052 334	$4.50(9)\cdot10^{-2}$	$5.89(13)\cdot10^{-2}$	$3.05(1)\cdot10^{-4}$
1.0 / 0.5	361.24	360.000(57)	30.556(950)	0.058 511	$4.29(6)\cdot10^{-2}$	$5.82(28)\cdot10^{-2}$	$3.00(2)\cdot10^{-4}$
1.0 / 0.5	361.24	360.000(53)	30.396(450)	0.074 012	$4.40(9)\cdot10^{-2}$	$5.79(13)\cdot10^{-2}$	$3.06(3)\cdot10^{-4}$
1.0 / 0.5	361.24	360.01(6)	30.584(370)	0.082 748	$4.40(4)\cdot10^{-2}$	$5.70(22)\cdot10^{-2}$	$3.04(1)\cdot10^{-4}$
1.0 / 0.5	361.24	360.000(79)	31.289(330)	0.117 02	$4.32(2)\cdot10^{-2}$	$5.82(13)\cdot10^{-2}$	$3.07(2)\cdot10^{-4}$

Table A.4: Results of propane at 360 K, calculated with Velocity Verlet

Δt/fs	ρ/kg/m^3	T/K	p/bar	$\mathcal{T}$/fs	η/mPa s	λ/W m^{-1} K^{-1}	D_{self}/cm^2 s^{-1}
2.0	361.24	360.000(59)	−116.75(820)	0.011 702	$5.26(10)\cdot10^{-2}$	$7.07(24)\cdot10^{-2}$	$3.16(3)\cdot10^{-4}$
2.0	361.24	360.010(49)	40.274(4800)	0.018 503	$4.84(10)\cdot10^{-2}$	$6.50(18)\cdot10^{-2}$	$3.19(3)\cdot10^{-4}$
2.0	361.24	360.000(55)	52.683(3400)	0.026 167	$4.73(5)\cdot10^{-2}$	$6.29(17)\cdot10^{-2}$	$3.16(2)\cdot10^{-4}$
2.0	361.24	360.020(66)	25.175(3600)	0.037 006	$4.50(11)\cdot10^{-2}$	$5.95(25)\cdot10^{-2}$	$3.01(3)\cdot10^{-4}$
2.0	361.24	359.990(42)	28.487(2300)	0.052 334	$4.43(7)\cdot10^{-2}$	$5.95(16)\cdot10^{-2}$	$3.07(3)\cdot10^{-4}$
2.0	361.24	359.990(64)	29.639(810)	0.058 511	$4.44(8)\cdot10^{-2}$	$5.73(20)\cdot10^{-2}$	$3.03(2)\cdot10^{-4}$
2.0	361.24	359.990(51)	29.692(780)	0.074 012	$4.34(13)\cdot10^{-2}$	$5.75(22)\cdot10^{-2}$	$3.03(3)\cdot10^{-4}$
2.0	361.24	359.990(74)	30.058(460)	0.082 748	$4.40(7)\cdot10^{-2}$	$5.86(11)\cdot10^{-2}$	$3.05(1)\cdot10^{-4}$
2.0	361.24	360.000(53)	30.961(350)	0.117 02	$4.40(9)\cdot10^{-2}$	$6.01(16)\cdot10^{-2}$	$3.03(2)\cdot10^{-4}$
0.5	361.24	360.000(65)	19.058(4700)	0.008 274 8	$4.82(12)\cdot10^{-2}$	$6.44(21)\cdot10^{-2}$	$3.17(2)\cdot10^{-4}$
0.5	361.24	360.000(59)	55.675(5900)	0.011 702	$4.79(9)\cdot10^{-2}$	$6.57(22)\cdot10^{-2}$	$3.16(2)\cdot10^{-4}$
0.5	361.24	360.030(53)	65.735(3000)	0.018 503	$4.67(9)\cdot10^{-2}$	$6.30(13)\cdot10^{-2}$	$3.11(3)\cdot10^{-4}$
0.5	361.24	360.010(61)	64.017(4300)	0.026 167	$4.65(13)\cdot10^{-2}$	$6.23(13)\cdot10^{-2}$	$3.14(3)\cdot10^{-4}$
0.5	361.24	359.990(83)	27.291(2900)	0.037 006	$4.43(12)\cdot10^{-2}$	$5.95(15)\cdot10^{-2}$	$3.02(2)\cdot10^{-4}$
0.5	361.24	359.990(67)	30.141(1300)	0.052 334	$4.35(8)\cdot10^{-2}$	$6.16(32)\cdot10^{-2}$	$3.03(3)\cdot10^{-4}$
0.5	361.24	359.98(7)	30.338(1100)	0.058 511	$4.49(11)\cdot10^{-2}$	$5.88(23)\cdot10^{-2}$	$3.03(2)\cdot10^{-4}$
0.5	361.24	360.010(53)	30.232(680)	0.074 012	$4.35(5)\cdot10^{-2}$	$5.77(23)\cdot10^{-2}$	$3.03(2)\cdot10^{-4}$
0.5	361.24	360.000(59)	30.692(370)	0.082 748	$4.38(11)\cdot10^{-2}$	$5.81(11)\cdot10^{-2}$	$3.07(2)\cdot10^{-4}$
0.5	361.24	359.980(79)	31.271(400)	0.117 02	$4.32(13)\cdot10^{-2}$	$5.88(15)\cdot10^{-2}$	$3.06(2)\cdot10^{-4}$

Table A.5: Results of dimethylether at 380 K, calculated with rRESPA

Δt/fs	ρ/kg/m^3	T/K	p/bar	$\mathcal{T}$/fs	η/mPa s	λ/W m^{-1} K^{-1}	D_{self}/cm^2 s^{-1}
1.0 / 0.5	482.12	380.03(8)	96.53(470)	0.012 094	$6.38(15)\cdot10^{-2}$	$8.48(18)\cdot10^{-2}$	$2.65(1)\cdot10^{-4}$
1.0 / 0.5	482.12	380.00(8)	99.587(4700)	0.019 123	$6.33(10)\cdot10^{-2}$	$8.55(33)\cdot10^{-2}$	$2.68(2)\cdot10^{-4}$
1.0 / 0.5	482.12	380.010(68)	77.516(5400)	0.027 044	$6.12(13)\cdot10^{-2}$	$8.42(26)\cdot10^{-2}$	$2.64(2)\cdot10^{-4}$
1.0 / 0.5	482.12	380.010(79)	31.465(2900)	0.038 245	$5.91(10)\cdot10^{-2}$	$7.74(17)\cdot10^{-2}$	$2.54(2)\cdot10^{-4}$
1.0 / 0.5	482.12	380.020(68)	32.886(1100)	0.054 087	$5.96(12)\cdot10^{-2}$	$7.87(16)\cdot10^{-2}$	$2.54(1)\cdot10^{-4}$
1.0 / 0.5	482.12	380.00(7)	32.34(85)	0.060 471	$5.94(12)\cdot10^{-2}$	$7.99(22)\cdot10^{-2}$	$2.53(2)\cdot10^{-4}$
1.0 / 0.5	482.12	380.000(66)	33.208(860)	0.076 491	$5.96(10)\cdot10^{-2}$	$7.92(21)\cdot10^{-2}$	$2.51(1)\cdot10^{-4}$
1.0 / 0.5	482.12	379.970(67)	32.733(1200)	0.085 519	$5.91(9)\cdot10^{-2}$	$7.83(13)\cdot10^{-2}$	$2.55(2)\cdot10^{-4}$
1.0 / 0.5	482.12	380.000(58)	34.411(380)	0.120 94	$5.84(14)\cdot10^{-2}$	$7.98(13)\cdot10^{-2}$	$2.55(2)\cdot10^{-4}$

Table A.6: Results of ethane at 205 K, calculated with rRESPA

Δt/fs	ρ/kg/m^3	T/K	p/bar	$\mathcal{T}$/fs	η/mPa s	λ/W m^{-1} K^{-1}	D_{self}/cm^2 s^{-1}
1.0 / 0.1	512.82	205.010(34)	81.712(7300)	0.008 422 1	$1.44(3)\cdot10^{-1}$	$1.71(4)\cdot10^{-1}$	$7.77(5)\cdot10^{-5}$
1.0 / 0.1	512.82	204.980(37)	84.29(660)	0.011 911	$1.40(3)\cdot10^{-1}$	$1.65(8)\cdot10^{-1}$	$7.79(7)\cdot10^{-5}$
1.0 / 0.1	512.82	205.010(33)	85.827(7400)	0.018 832	$1.39(3)\cdot10^{-1}$	$1.71(6)\cdot10^{-1}$	$7.73(5)\cdot10^{-5}$
1.0 / 0.1	512.82	205.010(43)	91.801(11000)	0.026 633	$1.39(1)\cdot10^{-1}$	$1.71(6)\cdot10^{-1}$	$7.78(6)\cdot10^{-5}$
1.0 / 0.1	512.82	205.000(38)	73.402(13000)	0.037 665	$1.37(2)\cdot10^{-1}$	$1.62(6)\cdot10^{-1}$	$7.68(4)\cdot10^{-5}$
1.0 / 0.1	512.82	205.000(37)	−1.9202(78000)	0.053 266	$1.33(2)\cdot10^{-1}$	$1.51(4)\cdot10^{-1}$	$7.44(7)\cdot10^{-5}$
1.0 / 0.1	512.82	205.000(37)	−5.2385(43000)	0.059 553	$1.35(3)\cdot10^{-1}$	$1.48(7)\cdot10^{-1}$	$7.45(4)\cdot10^{-5}$

Continued on next page

Continued: Results of ethane at 205 K, calculated with rRESPA

Δt/fs	ρ/kg/m^3	T/K	p/bar	$\mathcal{T}$/fs	η/mPa s	λ/W m^{-1} K^{-1}	D_{self}/cm^2 s^{-1}
1.0 / 0.1	512.82	205.000(19)	−4.2234(23000)	0.075 33	$1.31(2)\cdot10^{-1}$	$1.55(6)\cdot10^{-1}$	$7.41(6)\cdot10^{-5}$
1.0 / 0.1	512.82	205.010(44)	−4.8826(13000)	0.084 221	$1.34(2)\cdot10^{-1}$	$1.54(6)\cdot10^{-1}$	$7.49(6)\cdot10^{-5}$
1.0 / 0.1	512.82	204.990(36)	−8.3183(6000)	0.119 11	$1.30(2)\cdot10^{-1}$	$1.48(7)\cdot10^{-1}$	$7.52(4)\cdot10^{-5}$

Table A.7: Results of propane at 295 K, calculated with rRESPA

Δt/fs	ρ/kg/m^3	T/K	p/bar	$\mathcal{T}$/fs	η/mPa s	λ/W m^{-1} K^{-1}	D_{self}/cm^2 s^{-1}
2.0 / 0.5	497.2	295.000(51)	−49.237(8500)	0.008 274 8	$1.06(2)\cdot10^{-1}$	$1.03(5)\cdot10^{-1}$	$1.33(1)\cdot10^{-4}$
2.0 / 0.5	497.2	295.010(53)	29.661(7500)	0.011 702	$1.01(2)\cdot10^{-1}$	$1.03(2)\cdot10^{-1}$	$1.32(1)\cdot10^{-4}$
2.0 / 0.5	497.2	295.000(54)	66.258(4900)	0.018 503	$1.02(2)\cdot10^{-1}$	$1.04(1)\cdot10^{-1}$	$1.32(1)\cdot10^{-4}$
2.0 / 0.5	497.2	295.01(4)	61.853(6600)	0.026 167	$9.99(13)\cdot10^{-2}$	$1.03(3)\cdot10^{-1}$	$1.29(1)\cdot10^{-4}$
2.0 / 0.5	497.2	294.990(46)	4.0931(45000)	0.037 006	$9.68(16)\cdot10^{-2}$	$9.44(37)\cdot10^{-2}$	$1.25(1)\cdot10^{-4}$
2.0 / 0.5	497.2	295.010(55)	4.1473(100000)	0.052 334	$9.57(20)\cdot10^{-2}$	$9.65(44)\cdot10^{-2}$	$1.26(1)\cdot10^{-4}$
2.0 / 0.5	497.2	295.000(57)	4.9439(18000)	0.058 511	$9.51(14)\cdot10^{-2}$	$9.80(61)\cdot10^{-2}$	$1.26(1)\cdot10^{-4}$
2.0 / 0.5	497.2	295.010(54)	5.7005(15000)	0.074 012	$9.46(36)\cdot10^{-2}$	$9.59(20)\cdot10^{-2}$	$1.26(1)\cdot10^{-4}$
2.0 / 0.5	497.2	295.010(61)	5.2461(8500)	0.082 748	$9.44(11)\cdot10^{-2}$	$9.45(19)\cdot10^{-2}$	$1.26(1)\cdot10^{-4}$
2.0 / 0.5	497.2	295.000(37)	5.2348(6000)	0.117 02	$9.33(21)\cdot10^{-2}$	$9.82(27)\cdot10^{-2}$	$1.28(1)\cdot10^{-4}$
1.0 / 0.1	497.2	295.01(4)	69.178(7200)	0.008 274 8	$1.00(2)\cdot10^{-1}$	$1.03(4)\cdot10^{-1}$	$1.31(1)\cdot10^{-4}$
1.0 / 0.1	497.2	295.000(45)	75.788(7800)	0.011 702	$1.01(3)\cdot10^{-1}$	$1.04(5)\cdot10^{-1}$	$1.31(1)\cdot10^{-4}$
1.0 / 0.1	497.2	295.000(42)	88.047(4600)	0.018 503	$1.02(2)\cdot10^{-1}$	$1.05(3)\cdot10^{-1}$	$1.31(1)\cdot10^{-4}$
1.0 / 0.1	497.2	294.980(55)	78.46(830)	0.026 167	$9.92(26)\cdot10^{-2}$	$1.05(3)\cdot10^{-1}$	$1.30(1)\cdot10^{-4}$

Continued on next page

Continued: Results of propane at 295 K, calculated with rRESPA

Δt/fs	ρ/kg/m^3	T/K	p/bar	$\mathcal{T}$/fs	η/mPa s	λ/W m^{-1} K^{-1}	D_{self}/cm^2 s^{-1}
1.0 / 0.1	497.2	295.010(48)	4.2512(76000)	0.037 006	$9.33(15)\cdot10^{-2}$	$9.50(29)\cdot10^{-2}$	$1.26(1)\cdot10^{-4}$
1.0 / 0.1	497.2	295.000(45)	6.4127(27000)	0.052 334	$9.61(20)\cdot10^{-2}$	$9.48(30)\cdot10^{-2}$	$1.25(1)\cdot10^{-4}$
1.0 / 0.1	497.2	295.000(51)	6.3677(18000)	0.058 511	$9.57(18)\cdot10^{-2}$	$9.53(18)\cdot10^{-2}$	$1.26(1)\cdot10^{-4}$
1.0 / 0.1	497.2	294.990(48)	6.213(1100)	0.074 012	$9.44(19)\cdot10^{-2}$	$9.31(24)\cdot10^{-2}$	$1.26(1)\cdot10^{-4}$
1.0 / 0.1	497.2	295.00(4)	6.0164(10000)	0.082 748	$9.27(21)\cdot10^{-2}$	$9.40(17)\cdot10^{-2}$	$1.28(1)\cdot10^{-4}$
1.0 / 0.1	497.2	295.010(62)	5.6564(7000)	0.117 02	$9.41(11)\cdot10^{-2}$	$9.63(14)\cdot10^{-2}$	$1.28(1)\cdot10^{-4}$
1.0 / 0.5	497.2	295.000(57)	69.491(6200)	0.008 274 8	$1.02(1)\cdot10^{-1}$	$1.07(6)\cdot10^{-1}$	$1.33(1)\cdot10^{-4}$
1.0 / 0.5	497.2	295.010(51)	74.571(8800)	0.011 702	$1.01(2)\cdot10^{-1}$	$1.04(4)\cdot10^{-1}$	$1.32(1)\cdot10^{-4}$
1.0 / 0.5	497.2	295.010(52)	81.646(5200)	0.018 503	$1.01(2)\cdot10^{-1}$	$1.04(4)\cdot10^{-1}$	$1.29(1)\cdot10^{-4}$
1.0 / 0.5	497.2	294.990(58)	93.123(6100)	0.026 167	$1.02(2)\cdot10^{-1}$	$1.04(2)\cdot10^{-1}$	$1.32(1)\cdot10^{-4}$
1.0 / 0.5	497.2	295.000(56)	6.9193(67000)	0.037 006	$9.32(28)\cdot10^{-2}$	$9.71(44)\cdot10^{-2}$	$1.28(1)\cdot10^{-4}$
1.0 / 0.5	497.2	295.020(45)	7.2282(24000)	0.052 334	$9.45(18)\cdot10^{-2}$	$9.53(25)\cdot10^{-2}$	$1.25(1)\cdot10^{-4}$
1.0 / 0.5	497.2	295.010(51)	7.4308(17000)	0.058 511	$9.59(18)\cdot10^{-2}$	$1.00(8)\cdot10^{-1}$	$1.26(1)\cdot10^{-4}$
1.0 / 0.5	497.2	294.970(48)	5.4418(19000)	0.074 012	$9.57(18)\cdot10^{-2}$	$9.30(50)\cdot10^{-2}$	$1.26\cdot10^{-4}$
1.0 / 0.5	497.2	295.000(56)	6.1665(7900)	0.082 748	$9.11(16)\cdot10^{-2}$	$9.30(11)\cdot10^{-2}$	$1.27(1)\cdot10^{-4}$
1.0 / 0.5	497.2	294.990(51)	5.4778(5200)	0.117 02	$9.12(12)\cdot10^{-2}$	$9.49(19)\cdot10^{-2}$	$1.27(1)\cdot10^{-4}$

Table A.8: Results of propane at 295 K, calculated with Velocity Verlet

Δt/fs	ρ/kg/m^3	T/K	p/bar	$\mathcal{T}$/fs	η/mPa s	λ/W m^{-1} K^{-1}	D_{self}/cm^2 s^{-1}
2.0	497.2	295.010(45)	−111.63(900)	0.011 702	$1.17(3)\cdot10^{-1}$	$1.14(3)\cdot10^{-1}$	$1.31(1)\cdot10^{-4}$
2.0	497.2	295.010(62)	54.482(8800)	0.018 503	$1.03(4)\cdot10^{-1}$	$1.08(3)\cdot10^{-1}$	$1.32(1)\cdot10^{-4}$
2.0	497.2	294.990(56)	72.452(6800)	0.026 167	$1.01(2)\cdot10^{-1}$	$1.07(5)\cdot10^{-1}$	$1.31(1)\cdot10^{-4}$
2.0	497.2	295.000(58)	7.5923(93000)	0.037 006	$9.59(22)\cdot10^{-2}$	$9.78(31)\cdot10^{-2}$	$1.26(1)\cdot10^{-4}$
2.0	497.2	295.010(54)	9.0637(29000)	0.052 334	$9.54(14)\cdot10^{-2}$	$9.56(26)\cdot10^{-2}$	$1.27(1)\cdot10^{-4}$
2.0	497.2	295.010(46)	8.6413(20000)	0.058 511	$9.52(30)\cdot10^{-2}$	$9.53(22)\cdot10^{-2}$	$1.27(1)\cdot10^{-4}$
2.0	497.2	294.99(5)	8.0245(17000)	0.074 012	$9.48(20)\cdot10^{-2}$	$9.67(15)\cdot10^{-2}$	$1.27(1)\cdot10^{-4}$
2.0	497.2	295.020(51)	7.5303(9200)	0.082 748	$9.45(19)\cdot10^{-2}$	$9.78(21)\cdot10^{-2}$	$1.27(1)\cdot10^{-4}$
2.0	497.2	295.000(47)	6.1831(8100)	0.117 02	$9.22(25)\cdot10^{-2}$	$9.50(31)\cdot10^{-2}$	$1.28(1)\cdot10^{-4}$
0.5	497.2	295.000(43)	33.707(8600)	0.008 274 8	$1.03(3)\cdot10^{-1}$	$1.09(3)\cdot10^{-1}$	$1.32(1)\cdot10^{-4}$
0.5	497.2	295.010(36)	72.428(12000)	0.011 702	$1.02(2)\cdot10^{-1}$	$1.04(3)\cdot10^{-1}$	$1.31(1)\cdot10^{-4}$
0.5	497.2	294.98(5)	88.425(9600)	0.018 503	$1.00(2)\cdot10^{-1}$	$1.07(3)\cdot10^{-1}$	$1.32(1)\cdot10^{-4}$
0.5	497.2	295.020(59)	73.759(7700)	0.026 167	$1.01(2)\cdot10^{-1}$	$1.02(2)\cdot10^{-1}$	$1.31(1)\cdot10^{-4}$
0.5	497.2	295.010(43)	7.9425(43000)	0.037 006	$9.58(17)\cdot10^{-2}$	$9.66(36)\cdot10^{-2}$	$1.26(1)\cdot10^{-4}$
0.5	497.2	294.990(63)	7.612(2600)	0.052 334	$9.19(26)\cdot10^{-2}$	$9.72(60)\cdot10^{-2}$	$1.28(1)\cdot10^{-4}$
0.5	497.2	295.010(49)	6.7469(16000)	0.058 511	$9.54(12)\cdot10^{-2}$	$9.38(47)\cdot10^{-2}$	$1.26(1)\cdot10^{-4}$
0.5	497.2	294.98(5)	6.9109(17000)	0.074 012	$9.35(16)\cdot10^{-2}$	$9.72(45)\cdot10^{-2}$	$1.26(1)\cdot10^{-4}$
0.5	497.2	295.010(48)	6.9764(12000)	0.082 748	$9.46(14)\cdot10^{-2}$	$9.33(25)\cdot10^{-2}$	$1.26(1)\cdot10^{-4}$
0.5	497.2	295.000(55)	5.7914(5500)	0.117 02	$9.17(18)\cdot10^{-2}$	$9.82(35)\cdot10^{-2}$	$1.27(1)\cdot10^{-4}$

Table A.9: Results of dimethylether at 300 K, calculated with rRESPA

Δt/fs	ρ/kg/m^3	T/K	p/bar	$\mathcal{T}$/fs	η/mPa s	λ/W m^{-1} K^{-1}	D_{self}/cm^2 s^{-1}
1.0 / 0.5	649.04	300.000(46)	121.25(1000)	0.012 094	$1.45(2)\cdot10^{-1}$	$1.45(5)\cdot10^{-1}$	$1.02(1)\cdot10^{-4}$
1.0 / 0.5	649.04	300.010(49)	100.53(1000)	0.019 123	$1.40(2)\cdot10^{-1}$	$1.42(3)\cdot10^{-1}$	$1.02(1)\cdot10^{-4}$
1.0 / 0.5	649.04	299.990(48)	100.34(780)	0.027 044	$1.41(3)\cdot10^{-1}$	$1.42(6)\cdot10^{-1}$	$1.01(1)\cdot10^{-4}$
1.0 / 0.5	649.04	300.000(45)	1.4783(64000)	0.038 245	$1.34(2)\cdot10^{-1}$	$1.35(9)\cdot10^{-1}$	$9.78(6)\cdot10^{-5}$
1.0 / 0.5	649.04	300.01(6)	1.5315(30000)	0.054 087	$1.33(3)\cdot10^{-1}$	$1.32(4)\cdot10^{-1}$	$9.73(8)\cdot10^{-5}$
1.0 / 0.5	649.04	300.010(67)	1.9463(18000)	0.060 471	$1.35(3)\cdot10^{-1}$	$1.31(3)\cdot10^{-1}$	$9.76(8)\cdot10^{-5}$
1.0 / 0.5	649.04	300.000(71)	2.0271(10000)	0.076 491	$1.34(2)\cdot10^{-1}$	$1.33(5)\cdot10^{-1}$	$9.85(8)\cdot10^{-5}$
1.0 / 0.5	649.04	300.010(54)	1.8268(17000)	0.085 519	$1.34(3)\cdot10^{-1}$	$1.34(5)\cdot10^{-1}$	$9.82(8)\cdot10^{-5}$
1.0 / 0.5	649.04	300.000(72)	2.7582(8100)	0.120 94	$1.32(3)\cdot10^{-1}$	$1.37(7)\cdot10^{-1}$	$9.93(5)\cdot10^{-5}$

Table A.10: Results of propane (vapor) at 360 K, calculated with rRESPA

Δt/fs	ρ/kg/m^3	T/K	p/bar	$\mathcal{T}$/fs	η/mPa s	λ/W m^{-1} K^{-1}	D_{self}/cm^2 s^{-1}
1.0 / 0.5	94.323	360.000(43)	38.118(500)	0.008 274 8	$1.37(12)\cdot10^{-2}$	$2.43(21)\cdot10^{-2}$	$1.57(1)\cdot10^{-3}$
1.0 / 0.5	94.323	359.990(54)	39.529(680)	0.011 702	$1.35(8)\cdot10^{-2}$	$2.24(27)\cdot10^{-2}$	$1.58(2)\cdot10^{-3}$
1.0 / 0.5	94.323	359.960(25)	40.046(570)	0.018 503	$1.24(12)\cdot10^{-2}$	$2.53(47)\cdot10^{-2}$	$1.57(1)\cdot10^{-3}$
1.0 / 0.5	94.323	360.000(48)	40.776(310)	0.026 167	$1.42(15)\cdot10^{-2}$	$2.74(33)\cdot10^{-2}$	$1.60(1)\cdot10^{-3}$
1.0 / 0.5	94.323	359.980(46)	35.038(360)	0.037 006	$1.24(8)\cdot10^{-2}$	$2.37(54)\cdot10^{-2}$	$1.50(1)\cdot10^{-3}$
1.0 / 0.5	94.323	360.010(47)	35.204(240)	0.052 334	$1.17(10)\cdot10^{-2}$	$2.28(23)\cdot10^{-2}$	$1.50(1)\cdot10^{-3}$
1.0 / 0.5	94.323	360.020(37)	35.192(140)	0.058 511	$1.11(12)\cdot10^{-2}$	$2.80(53)\cdot10^{-2}$	$1.49(1)\cdot10^{-3}$

Continued on next page

Continued: Results of propane (vapor) at 360 K, calculated with rRESPA

Δt/fs	ρ/kg/m^3	T/K	p/bar	$\mathcal{T}$/fs	η/mPa s	λ/W m^{-1} K^{-1}	D_{self}/cm^2 s^{-1}
1.0 / 0.5	94.323	359.990(42)	35.227(99)	0.074 012	$1.17(6) \cdot 10^{-2}$	$2.39(20) \cdot 10^{-2}$	$1.50(2) \cdot 10^{-3}$
1.0 / 0.5	94.323	360.000(41)	35.227(90)	0.082 748	$1.17(9) \cdot 10^{-2}$	$2.52(47) \cdot 10^{-2}$	$1.49(1) \cdot 10^{-3}$
1.0 / 0.5	94.323	360.010(38)	35.340(69)	0.117 02	$1.24(8) \cdot 10^{-2}$	$2.09(38) \cdot 10^{-2}$	$1.52(1) \cdot 10^{-3}$

B Supporting Information for: Transferable Anisotropic United-Atom Mie (TAMie) Force-Field: Transport properties from Equilibrium Molecular Dynamic Simulations

The content of this appendix is a literal quote of the supporting information:

M. Fischer, G. Bauer, J. Gross: Supporting Information for: Transferable Anisotropic United-Atom Mie (TAMie) Force Field: Transport Properties from Equilibrium-MD-Simulations. *Industrial & Engineering Chemistry Research*, **59**(18):8855–8869, 2020. doi:10.1021/acs.iecr.0c00848

B.1 SAFT Parameters used in this Study

Table B.1: PC-SAFT Parameters used for the substances in this study

CAS	Substance	Molar Weight / $\mathrm{g\,mol^{-1}}$	m	σ / Å	ϵ/k/K	κ_{ab}	ϵ_{ab}/k/K	DM/D
74840	ethane	30.07	1.6069	3.5206	191.42	0	0	0
74986	propane	44.096	2.002	3.6184	208.11	0	0	0
110543	hexane	86.177	3.0576	3.7983	236.77	0	0	0
111842	nonane	128.25	4.2079	3.8448	244.51	0	0	0
106989	1-butene	56.107	2.2864	3.6431	222	0	0	0
592767	1-heptene	98.1861	3.2863	3.8138	243.756	0	0	0.6296
115106	dimethylether	46.069	2.2634	3.2723	210.29	0	0	1.3
75070	ethanal	44.0526	2.1188	3.246	229.851	0	0	2.6891
123728	butanal	72.107	2.8825	3.4698	247.09	0	0	2.72
111717	heptanal	114.185	3.8527	3.66	260.698	0	0	2.5782
67641	acetone	58.08	2.7447	3.2742	232.99	0	0	2.88
78933	butanone	72.107	2.9835	3.4239	244.99	0	0	2.78

B.2 Parameters of the TAMie force field

Tables B.2–B.5 provide the parameters of the TAMie force field as described in the *Molecular Model* section in the main text. The parameters were all published in previous work[1–3,3], except for the bond constant k_l in table B.3, which was specified by the authors of this study.

United atom i	$M_{ii}/(\mathrm{g\,mol^{-1}})$	$\varepsilon_{ii}/k_\mathrm{B}/\mathrm{K}$	$\sigma_{ii}/\mathrm{Å}$	n_{ii}	q_i/e
CH_3	15.035	136.318	3.6034	14	0.175 (next to ether O)
CH_3 (ethane)	15.035	130.780	3.6463	14	—
CH_2	14.027	52.913	4.0400	14	—
CH_2 (olefins)	14.027	100.681	3.6005	14	—
CH (olefins)	13.019	53.951	3.8234	14	—
O (dimethyl ether)	15.999	54.36	3.213	12	−0.35
O (aldehydes)	15.999	100.58	3.0276	12	−0.422
CH_x (neighbor ald.)					−0.038
CH (aldehydes)	13.019	68.934	3.4941	12	0.46
O (ketones)	15.999	65.55	3.093	12	−0.49
C (ketones)	12.011	32.775	3.919	12	0.49
O (acetone)	15.999	69.184	3.112	12	−0.49
C (acetone)	12.011	34.592	3.942	12	0.49

Table B.2: Pair potential parameters of UA-groups used in this study: Energy parameter ε_{ii}, size parameter σ_{ii}, repulsive exponent n_{ii}, and point charge q_i for the TAMie force field

Bond	$r_0/\mathrm{Å}$	$k_l/\mathrm{K\,Å^{-2}}$
CH_3–CH_3 (ethane)	1.94	100 644
CH_3–CH_x	1.74	100 644
CH_x–CH_y	1.54	100 644
CH=CH_x	1.33	100 644
CH_3–CH[=O_{ald}]	1.74	100 644
CH_2–CH[=O_{ald}]	1.54	100 644
CH=O_{ald}	1.217	100 644
CH_3–C[=O_{ket}]	1.74	100 644
CH_2–C[=O_{ket}]	1.54	100 644
C=O_{ket}	1.229	100 644
CH_3–O_{ether}	1.61	100 644

Table B.3: Bond lengths and constants of the TAMie force field used in this study ($x, y \in \{1, 2\}$)

Bending sites	θ_0/deg	k_θ/k_B/K
CH_x–CH_2–CH_y	114.0	62 500
CH_z=CH–CH_y	119.7	70 420
CH_x–O_{ether}–CH_y	112.0	60 400
CH_x–C_{ket}–CH_y	117.2	62 500
C_{ket}–CH_2–CH_x	114.0	62 500
CH_x–C_{ket}=O_{ket}	121.4	62 500
CH_x–CH=O_{ald}	121.4	62 500

Table B.4: Bending angles and constants of the TAMie force field used in this study ($x, y \in \{2,3\}$ and $z \in \{1,2\}$)

Torsion sites	c_0/k_B/K	c_1/k_B/K	c_2/k_B/K	c_3/k_B/K
CH_x–CH_2–CH_2–CH_y	0.0	355.03	−68.19	791.32
CH_x–CH_2–O_{ether}–CH_y	0.0	725.35	−163.75	558.2
CH_x–CH_2–CH_2–CH_y	0.0	176.62	−53.34	769.93
CH_z=CH–CH_2–CH_y	688.5	86.36	−109.77	−282.24
C–CH_2–CH_2–CH_y	0.0	355.03	−68.19	791.32
CH_x–CH_2–C=O_{ket}	2035.58	−736.90	57.84	−293.23
CH_x–C–CH_2–CH_y	−17.26	752.60	14.89	282.10
CH_x–CH_2–CH_2–CH[=O_{ald}]	11.81	467.80	−274.10	846.80
CH_x–CH_2–CH=O_{ald}	1182.0	−225.60	302.20	−339.30

Table B.5: Torsion potential constants of the TAMie force field used in this study ($x, y \in \{2,3\}$ and $z \in \{1,2\}$)

B.3 Correlation Parameters from Simulation

Tables B.6–B.8 summarize the parameters of the entropy correlations for each transport property adjusted to the simulation results. The corresponding correlation functions can be found in Table 3 in the main text. Additional to the parameters, the AAD of each correlation to all available experiments is given for each substance, along with the number of experimental data points available. The sources of the experiments are given in the column *Lit*.

Table B.6: Entropy Scaling Parameters of the TAMie force field for viscosity

CAS	Substance	A_η	B_η	C_η	D_η	$N_{\text{exp.}}$	$AAD_{\text{exp.}}$	Lit.
74840	ethane	−0.584 82	−1.597	−0.119 57	−0.015 513	2606	5.93 %	[4]
74986	propane	−0.739 04	−1.9377	−0.317 13	−0.051 261	1752	9.47 %	[4]
110543	hexane	−1.3007	−2.6303	−0.508 42	−0.090 849	1804	9.90 %	[4]
111842	nonane	−1.5238	−3.0059	−0.638 05	−0.136 35	382	14.45 %	[4]
106989	1-butene	−0.8661	−2.207	−0.440 46	−0.071 512	22	5.59 %	[4]
592767	1-heptene	−1.1781	−2.5061	−0.489 27	−0.101 39	163	6.79 %	[4]
115106	dimethylether	−0.8927	−2.0926	−0.375 23	−0.070 398	211	6.31 %	[4]
75070	ethanal	−0.978 54	−1.8377	−0.2819	−0.072 213	28	11.61 %	[4]
123728	butanal	−1.084	−2.388	−0.556 46	−0.132 42	233	15.12 %	[4]
111717	heptanal	−1.4179	−2.843	−0.551 04	−0.133 02	12	30.16 %	[4]
67641	acetone	−1.1162	−2.3125	−0.535 79	−0.147 13	512	15.28 %	[4]
78933	butanone	−1.2108	−2.4107	−0.471 33	−0.123 34	246	22.00 %	[4]

Table B.7: Entropy Scaling Parameters of the TAMie force field for thermal conductivity

CAS	Substance	A_λ	B_λ	C_λ	D_λ	$N_{\text{exp.}}$	$AAD_{\text{exp.}}$	Lit.
74840	ethane	−0.416 97	−1.3177	0.538 18	−0.120 65	1629	16.43 %	[4]
74986	propane	−0.3735	−0.745 96	1.2519	−0.027 495	3154	13.35 %	[4]
110543	hexane	−0.128 34	−0.835 16	1.0578	−0.077 646	646	11.23 %	[4]
111842	nonane	−0.043 518	−0.380 23	1.7543	0.031 92	524	6.00 %	[4]
106989	1-butene	−0.127 92	−1.06	0.443 67	−0.075 675	31	11.03 %	[4]
592767	1-heptene	−0.063 358	−0.650 59	1.226	−0.033 603	415	7.69 %	[4]
115106	dimethylether	−0.528 64	−0.732 68	1.4949	−0.026 342	347	15.94 %	[4]
75070	ethanal	−0.549 35	−1.1198	0.824 21	−0.078 127	96	11.57 %	[4]
123728	butanal	−0.247 26	0.187 17	2.4271	0.124 88	82	10.35 %	[4]
111717	heptanal	−0.162	0.307 38	2.7413	0.144 91	12	1.98 %	[4]
67641	acetone	−0.568 02	−0.7099	1.3292	−0.001 708 6	386	9.44 %	[4]
78933	butanone	−0.422 98	−0.132 37	2.0665	0.0883	347	7.99 %	[4]

Table B.8: Entropy Scaling Parameters of the TAMie force field for diffusion

CAS	Substance	$A_{D_{\text{self}}}$	$B_{D_{\text{self}}}$	$C_{D_{\text{self}}}$	$N_{\text{exp.}}$	$AAD_{\text{exp.}}$	Lit.
74840	ethane	−0.373 69	0.148 59	$2.4814 \cdot 10^{-13}$	154	14.40 %	[5–9]
74986	propane	−0.536 49	0.159 84	$9.9011 \cdot 10^{-15}$	75	20.66 %	[7,9]
110543	hexane	−0.707 72	0.268 65	$4.8284 \cdot 10^{-14}$	185	21.16 %	[8–15]
111842	nonane	−0.909 91	0.392 24	$7.1876 \cdot 10^{-13}$	104	18.72 %	[9,10,15–17]
106989	1-butene	−0.682 83	0.142 48	$8.2794 \cdot 10^{-3}$	0	–	–
592767	1-heptene	−0.790 56	0.283 69	$1.9320 \cdot 10^{-14}$	0	–	–
115106	dimethylether	−0.553 05	0.203 44	$3.0468 \cdot 10^{-13}$	40	7.98 %	[9]
75070	ethanal	−0.4574	0.227 17	$1.3107 \cdot 10^{-13}$	0	–	–
123728	butanal	−0.6685	0.300 23	$7.3716 \cdot 10^{-14}$	0	–	–
111717	heptanal	−0.853 65	0.433 13	$1.3380 \cdot 10^{-13}$	0	–	–
67641	acetone	−0.668 09	0.319 03	$1.6004 \cdot 10^{-13}$	48	24.86 %	[9]
78933	butanone	−0.694 77	0.335 19	$1.0136 \cdot 10^{-13}$	0	–	–

B.4 Simulation Results of each Substance

This section contains tables summarizing temperatures T, pressures p, reduced entropies s^*, viscosities η, self-diffusion coefficients D_{self}, and thermal conductivities λ for all investigated substances. The first part of each table describes the simulated state points with the corresponding reduced entropy, calculated using PC-SAFT. The second part provides the simulation results for the transport properties. The respective state points can be assigned via s^*.

Table B.9: Results of ethane

ρ/kg/m^3	T/K	p/bar	s^*
598.62	135.55(4)	8.4677(130000)	−3.3338
540.97	184.27(3)	7.9153(82000)	−2.4914
450.66	247.380(47)	11.396(4200)	−1.6576
308.42	310.470(61)	61.119(1100)	−0.912 27
16.067	246.960(46)	9.3787(510)	−0.064 591

s^*	η/mPa s	λ/W m^{-1} K^{-1}	D_{self}/mm s^{-1}
−3.3338	0.388 15(1300)	0.222 94(1200)	$1.8987(163)\cdot10^{-5}$
−2.4914	0.175 62(530)	0.173 01(600)	$5.2744(447)\cdot10^{-5}$
−1.6576	0.082 168(1700)	0.117 82(860)	$1.3650(96)\cdot10^{-4}$
−0.912 27	0.035 334(980)	0.061 351(2000)	$3.6130(305)\cdot10^{-4}$
−0.064 591	0.008 186 9(8200)	0.015 338(2200)	$6.6563(388)\cdot10^{-3}$

Table B.10: Results of propane

ρ/kg/m^3	T/K	p/bar	s^*
721.87	94.076(17)	2.8624(110000)	−4.5467
671.06	143.09(3)	−4.5537(54000)	−3.4475
592.59	220.060(44)	18.218(2700)	−2.3164
432.67	334.470(59)	23.536(1100)	−1.1917
1.1256	220.060(28)	0.461 98(360)	−0.005 494 6

s^*	η/mPa s	λ/W m^{-1} K^{-1}	D_{self}/mm s^{-1}
−4.5467	3.1202(1500)	0.219 45(850)	$1.5769(230)\cdot10^{-6}$
−3.4475	0.576 41(2100)	0.181 93(530)	$1.1712(104)\cdot10^{-5}$
−2.3164	0.202 68(840)	0.134 54(360)	$4.8891(474)\cdot10^{-5}$
−1.1917	0.062 521(1200)	0.076 826(4400)	$1.9923(191)\cdot10^{-4}$
−0.005 494 6	0.006 318 9(8300)	0.010 204(1200)	$7.4363(914)\cdot10^{-2}$

Table B.11: Results of hexane

ρ/kg/m^3	T/K	p/bar	s^*
723.12	207.730(36)	46.542(2100)	−2.7989
668.69	276.560(43)	47.847(1400)	−2.1205
575.01	383.300(84)	50.235(960)	−1.4148
401.83	510.880(55)	48.334(340)	−0.746 57
7.4016	383.300(54)	2.4913(76)	−0.020 003

s^*	η/mPa s	λ/W m^{-1} K^{-1}	D_{self}/mm s^{-1}
−2.7989	0.8528(420)	0.123 25(780)	$1.1487(124)\cdot10^{-5}$
−2.1205	0.334 26(2700)	0.112 66(620)	$3.4334(340)\cdot10^{-5}$
−1.4148	0.141 19(750)	0.093 022(9600)	$9.8579(909)\cdot10^{-5}$
−0.746 57	0.050 907(1200)	0.064 095(5500)	$3.0435(304)\cdot10^{-4}$
−0.020 003	0.007 597(600)	0.019 846(2200)	$1.5610(150)\cdot10^{-2}$

Table B.12: Results of nonane

ρ/kg/m^3	T/K	p/bar	s^*
761.68	219.700(36)	2.0632(28000)	−2.7275
709.08	291.540(48)	8.9105(14000)	−2.0749
616.51	409.07(6)	8.4399(6900)	−1.3849
437.7	563.990(72)	13.847(300)	−0.723 24
2.0972	409.100(52)	0.528 46(260)	−0.005 734

s^*	η/mPa s	λ/W m^{-1} K^{-1}	D_{self}/mm s^{-1}
−2.7275	1.973(110)	0.158 77(1200)	$4.2517(492)\cdot10^{-6}$
−2.0749	0.5737(220)	0.132 82(770)	$1.9450(153)\cdot10^{-5}$
−1.3849	0.197 07(550)	0.106 63(670)	$6.8291(520)\cdot10^{-5}$
−0.723 24	0.062 104(1900)	0.072 336(3700)	$2.4024(168)\cdot10^{-4}$
−0.005 734	0.007 307 9(7800)	0.017 784(3800)	$4.5883(674)\cdot10^{-2}$

Table B.13: Results of 1-butene

ρ/kg/m^3	T/K	p/bar	s^*
799.96	96.575(20)	20.791(2000)	−4.6778
749.86	147.330(25)	1.3977(24000)	−3.5791
669.04	229.440(37)	9.9527(15000)	−2.4138
496	367.170(56)	19.509(610)	−1.2184
0.423 44	229.440(22)	0.140 55(100)	−0.002 004 2

s^*	η/mPa s	λ/W m^{-1} K^{-1}	D_{self}/mm s^{-1}
−4.6778	7.7496(7000)	0.189 84(550)	$6.3405(941)\cdot 10^{-7}$
−3.5791	0.947 02(4200)	0.176 15(1400)	$7.2819(674)\cdot 10^{-6}$
−2.4138	0.2834(100)	0.135 18(920)	$3.6013(260)\cdot 10^{-5}$
−1.2184	0.080 721(2700)	0.076 723(4400)	$1.7151(120)\cdot 10^{-4}$
−0.002 004 2	0.006 214 3(8600)	0.011 827(3400)	$1.6299(350)\cdot 10^{-1}$

Table B.14: Results of 1-heptene

ρ/kg/m^3	T/K	p/bar	s^*
795.34	169.730(26)	8.0275(25000)	−3.3766
745.48	232.640(39)	11.203(920)	−2.5909
657.97	337.540(46)	9.5989(6700)	−1.7376
476.21	497.05(8)	17.963(400)	−0.890 39
1.1139	337.550(27)	0.307 33(100)	−0.003 625 4

s^*	η/mPa s	λ/W m^{-1} K^{-1}	D_{self}/mm s^{-1}
−3.3766	3.3615(3300)	0.132 87(480)	$2.3048(287)\cdot 10^{-6}$
−2.5909	0.747 97(4200)	0.123 41(570)	$1.3433(144)\cdot 10^{-5}$
−1.7376	0.232 09(740)	0.101 67(380)	$5.3644(340)\cdot 10^{-5}$
−0.890 39	0.071 884(3500)	0.070 874(4500)	$2.1462(188)\cdot 10^{-4}$
−0.003 625 4	0.007 649(940)	0.015 153(1600)	$7.9637(1088)\cdot 10^{-2}$

Table B.15: Results of dimethylether

ρ/kg/m^3	T/K	p/bar	s^*
851.18	144.840(23)	9.2192(47000)	−3.4617
782.33	202.410(41)	14.712(2600)	−2.6175
670.6	286.67(5)	7.5628(21000)	−1.7364
469.54	389.660(69)	52.462(750)	−0.9114
6.9791	286.670(28)	3.3524(150)	−0.020 621

s^*	η/mPa s	λ/W m^{-1} K^{-1}	D_{self}/mm s^{-1}
−3.4617	1.2459(930)	0.246 26(1100)	$6.2692(747)\cdot10^{-6}$
−2.6175	0.3906(200)	0.204 02(870)	$2.5581(237)\cdot10^{-5}$
−1.7364	0.152 26(750)	0.140 48(520)	$8.3276(715)\cdot10^{-5}$
−0.9114	0.058 587(3000)	0.080 419(5800)	$2.7345(259)\cdot10^{-4}$
−0.020 621	0.008 953 3(6500)	0.014 683(1300)	$1.7419(112)\cdot10^{-2}$

Table B.16: Results of ethanal

ρ/kg/m^3	T/K	p/bar	s^*
867.78	240.500(59)	11.111(4300)	−2.7034
767.93	321.960(58)	2.847(2300)	−2.0673
629.33	412.070(87)	23.247(1800)	−1.4241
424.98	483.030(88)	69.886(590)	−0.827 71
28.14	412.06(5)	17.683(72)	−0.090 534

s^*	η/mPa s	λ/W m^{-1} K^{-1}	D_{self}/mm s^{-1}
−2.7034	0.483 34(1500)	0.251 21(1300)	$2.4264(182)\cdot10^{-5}$
−2.0673	0.207 61(490)	0.196 95(1400)	$6.9555(513)\cdot10^{-5}$
−1.4241	0.103 72(290)	0.133 34(1100)	$1.6866(132)\cdot10^{-4}$
−0.827 71	0.046 199(1400)	0.076 707(4500)	$4.0455(412)\cdot10^{-4}$
−0.090 534	0.012 409(1400)	0.023 682(2600)	$5.8509(579)\cdot10^{-3}$

Table B.17: Results of butanal

ρ/kg/m^3	T/K	p/bar	s^*
887.6	194.480(39)	3.9302(31000)	−3.2082
816.6	270.560(39)	5.4477(18000)	−2.4432
700.87	382.520(79)	5.9733(13000)	−1.6255
491.26	519.630(89)	40.601(630)	−0.852 56
5.1518	382.520(36)	2.1243(65)	−0.014 342

s^*	η/mPa s	λ/W m^{-1} K^{-1}	D_{self}/mm s^{-1}
−3.2082	2.7232(1400)	0.168 09(1500)	$3.4614(314)\cdot10^{-6}$
−2.4432	0.565 26(2000)	0.147 87(680)	$1.9936(205)\cdot10^{-5}$
−1.6255	0.201 44(1300)	0.113 26(690)	$7.4787(753)\cdot10^{-5}$
−0.852 56	0.067 213(4400)	0.085 947(12000)	$2.6619(278)\cdot10^{-4}$
−0.014 342	0.010 027(1100)	0.019 798(2100)	$2.4747(231)\cdot10^{-2}$

Table B.18: Results of heptanal

ρ/kg/m^3	T/K	p/bar	s^*
840.85	252.130(36)	11.371(1500)	−2.5729
776.89	332.03(5)	10.004(1100)	−1.9492
666.84	455.240(69)	9.449(690)	−1.3006
470.79	604.82(8)	30.874(430)	−0.695 29
5.3559	455.220(41)	1.6501(57)	−0.012 129

s^*	η/mPa s	λ/W m^{-1} K^{-1}	D_{self}/mm s^{-1}
−2.5729	1.9113(1200)	0.1404(60)	$5.3695(512)\cdot10^{-6}$
−1.9492	0.553 95(4600)	0.128 85(620)	$2.3664(192)\cdot10^{-5}$
−1.3006	0.192 92(720)	0.102 34(390)	$8.0727(427)\cdot10^{-5}$
−0.695 29	0.064 829(2500)	0.079 916(7100)	$2.6343(194)\cdot10^{-4}$
−0.012 129	0.009 236 8(9400)	0.020 528(1700)	$2.2672(221)\cdot10^{-2}$

Table B.19: Results of acetone

ρ/kg/m^3	T/K	p/bar	s^*
867.62	196.340(36)	3.6394(40000)	−2.877
785.39	279.09(5)	6.8071(28000)	−2.1969
660.67	389.350(57)	9.1299(14000)	−1.4677
458.77	508.55(10)	58.237(540)	−0.800 93
8.7917	389.320(34)	4.4061(80)	−0.025 45

s^*	η/mPa s	λ/W m^{-1} K^{-1}	D_{self}/mm s^{-1}
−2.877	1.5422(570)	0.205 21(1200)	$6.0940(641)\cdot10^{-6}$
−2.1969	0.398 05(1400)	0.168 46(950)	$2.9230(228)\cdot10^{-5}$
−1.4677	0.154 58(860)	0.118 94(400)	$9.8146(844)\cdot10^{-5}$
−0.800 93	0.057 889(2100)	0.072 404(3900)	$3.0273(155)\cdot10^{-4}$
−0.025 45	0.010 419(1300)	0.018 319(2100)	$1.4738(103)\cdot10^{-2}$

Table B.20: Results of butanone

ρ/kg/m^3	T/K	p/bar	s^*
848.2	205.160(42)	8.6126(19000)	−2.8524
775.85	281.70(6)	10.668(2000)	−2.167
657.08	393.700(55)	5.8554(8300)	−1.4307
431.71	527.400(71)	43.736(400)	−0.708 43
6.0661	393.710(44)	2.5430(69)	−0.016 154

s^*	η/mPa s	λ/W m^{-1} K^{-1}	D_{self}/mm s^{-1}
−2.8524	1.7406(810)	0.162 44(1100)	$5.6837(614)\cdot10^{-6}$
−2.167	0.454 37(1800)	0.1351(130)	$2.6547(263)\cdot10^{-5}$
−1.4307	0.1593(42)	0.102 49(710)	$9.1637(928)\cdot10^{-5}$
−0.708 43	0.051 395(1400)	0.066 298(5900)	$3.2439(255)\cdot10^{-4}$
−0.016 154	0.009 358 4(7300)	0.017 866(1700)	$2.0597(213)\cdot10^{-2}$

B.5 Verification of the Nosé-Hoover thermostat

We repeated the simulations of hexane with a switched off thermostat in production to check the consistency with the results we obtained with the Nose-Hover thermostat. Figure B.1 shows the results for all transport properties in the entropy scaled depiction. The results are equivalent within statistical uncertainties, wether the thermostat is switched on or not.

The results are summarized in table form in table B.21.

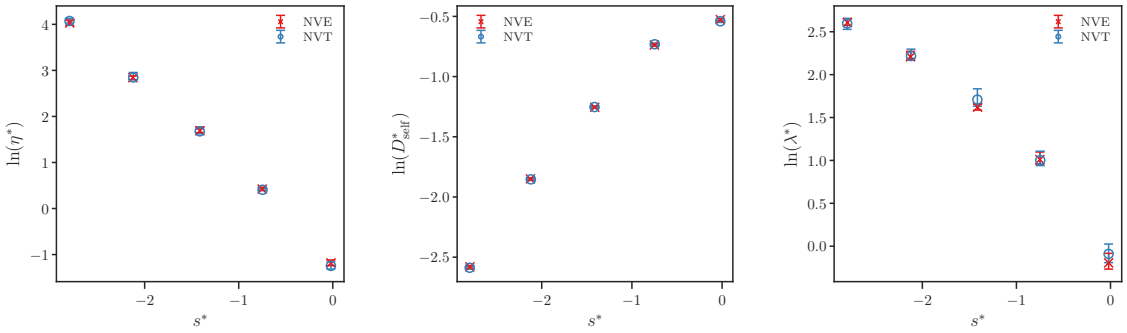

(a) **(b)** **(c)**

Figure B.1: Logarithmic depiction of reduced viscosity η^* (a), self-diffusion D^*_{self} (b), and thermal conductivity λ^* (c) over residual entropy s^* for hexane. The figure compares the results of simulations with an Nosé-Hoover thermostat (NVE) and simulations without any thermostat (NVE)

Table B.21: Results of hexane (NVE)

ρ/kg/m^3	T/K	p/bar	s^*
723.12	208.160(66)	52.036(2200)	−2.796
668.69	275.410(35)	36.59(110)	−2.1252
575.01	384.620(17)	56.929(810)	−1.4124
401.83	504.480(29)	38.499(410)	−0.750 66
7.4016	386.47(11)	2.5158(83)	−0.019 807

s^*	η/mPa s	λ/W m^{-1} K^{-1}	D_{self}/mm s^{-1}
−2.796	0.817 81(4600)	0.124 82(500)	$1.1598(126)\cdot10^{-5}$
−2.1252	0.331(13)	0.111 18(560)	$3.4336(312)\cdot10^{-5}$
−1.4124	0.1433(90)	0.085 467(2900)	$9.8678(711)\cdot10^{-5}$
−0.750 66	0.051 185(1700)	0.063 674(4600)	$2.9936(253)\cdot10^{-4}$
−0.019 807	0.008 165 1(5100)	0.018 118(1700)	$1.5940(158)\cdot10^{-2}$

Bibliography

[1] A. Hemmen, A. Z. Panagiotopoulos, and J. Gross. Grand Canonical Monte Carlo Simulations Guided by an Analytic Equation of State - Transferable Anisotropic Mie Potentials for Ethers. *J. Phys. Chem. B*, **119**(23):7087–7099, 2015. doi:10.1021/acs.jpcb.5b01806.

[2] A. Hemmen and J. Gross. Transferable Anisotropic United-Atom Force Field Based on the Mie Potential for Phase Equilibrium Calculations: n-Alkanes and n-Olefins. *J. Phys. Chem. B*, **119**(35):11695–11707, 2015. doi:10.1021/acs.jpcb.5b01354.

[3] D. Weidler and J. Gross. Transferable Anisotropic United-Atom Force Field Based on the Mie Potential for Phase Equilibria: Aldehydes, Ketones, and Small Cyclic Alkanes. *Ind. Eng. Chem. Res.*, **55**(46):12123–12132, 2016. doi:10.1021/acs.iecr.6b02182.

[4] Dortmund Data Bank. 2018.

[5] A. Boushehri, J. Bzowski, J. Kestin, and E. A. Mason. Equilibrium and Transport Properties of Eleven Polyatomic Gases At Low Density. *J. Phys. Chem. Ref. Data*, **16**(3):445–466, 1987. doi:10.1063/1.555800.

[6] C. R. Mueller and R. W. Cahill. Mass Spectrometric Measurement of Diffusion Coefficients. *J. Chem. Phys.*, **40**(3):651–654, 1964. doi:10.1063/1.1725184.

[7] A. Greiner-Schmid, S. Wappmann, M. Has, and H.-D. Lüdemann. Self-diffusion in the compressed fluid lower alkanes: Methane, ethane, and propane. *J. Chem. Phys.*, **94**(8):5643–5649, 1991. doi:10.1063/1.460474.

[8] M. Helbæk, B. Hafskjold, D. K. Dysthe, and G. H. Sørland. Self-Diffusion Coefficients of Methane or Ethane Mixtures with Hydrocarbons at High Pressure by NMR. *J. Chem. Eng. Data*, **41**(3):598–603, 1996. doi:10.1021/je950293p.

[9] O. Suárez-Iglesias, I. Medina, M. de los Ángeles Sanz, C. Pizarro, and J. L. Bueno. Self-Diffusion in Molecular Fluids and Noble Gases: Available Data. *J. Chem. Eng. Data*, **60**(10):2757–2817, 2015. doi:10.1021/acs.jced.5b00323.

[10] G. Panchenkov and V. Erchenkov. Temperature Variation of the Coordination Number and Diffusion Coefficient in a Liquid. *Russ. J. Phys. Chem.*, **36**:455–457, 1962.

[11] M. Awan and J. Dymond. Transport Properties of Nonelectrolyte Liquid Mixtures. XI. Mutual

Diffusion Coefficients for Toluene + n-Hexane and Toluene + Acetonitrile at Temperatures from 273 to 348 K and at Pressures up to 25 MPa. *Int. J. Thermophys.*, **22**:679–700, 2001. doi:https://doi.org/10.1023/A:1010714713468.

[12] C. D'Agostino, M. Mantle, L. Gladden, and G. Moggridge. Prediction of Binary Diffusion Coefficients in Non-Ideal Mixtures from NMR Data: Hexane-Nitrobenzene near its Consolute Point. *Chem. Eng. Sci.*, **66**:3898–3906, 2011. doi:10.1016/j.ces.2011.05.014.

[13] D. McCall, D. Douglass, and E. Anderson. Self-Diffusion in Liquids: Paraffin Hydrocarbons. *Phys. Fluids*, **2**:87–91, 1959. doi:10.1063/1.1724398.

[14] K. R. Harris. Temperature and density dependence of the self-diffusion coefficient of n-hexane from 223 to 333 K and up to 400 MPa. *J. Chem. Soc., Faraday Trans. 1 F*, **78**(7):2265, 1982. doi:10.1039/f19827802265.

[15] D. W. McCall, D. C. Douglass, and E. W. Anderson. Diffusion in Liquids. *J. Chem. Phys.*, **31**(6):1555–1557, 1959. doi:10.1063/1.1730651.

[16] G. Panchenkov, N. Borisenko, and V. Erchenkov. Self-diffusion of n-paraffins in a wide temperature range. *Zh. Fiz. Khim*, **43**:2369–2370, 1969.

[17] P. Tofts, D. Lloyd, C. Clark, G. Barker, G. Parker, P. McConville, C. Baldock, and J. Pope. Test liquids for quantitative MRI measurements of self-diffusion coefficient in vivo. *Magn. Reson. Med.*, **43**(3):368–374, 2000. doi:10.1002/(SICI)1522-2594(200003)43:3<368::AID-MRM8>3.0.CO;2-B.

C Supporting Information for: Assessing Entropy Scaling for Mixture Viscosities using Molecular Simulations

This supporting information contains the results of all simulations shown in the figures of chapter 3, in tabulated form. The SI is divided into results of the viscosity calculations in appendix C.1, the results of static properties along isotherms from the GCMC simulations (appendix C.2), and results of the vapour-liquid equilibria of the model mixtures at different temperatures, also from GCMC simulations (appendix C.3).

C.1 Tabulated Results of the MD Simulations

This chapter provides the viscosities of the investigated model mixtures at various state points as result of the MD simulations. Additionally, all information that is needed for an entropy scaled analysis of the data are given. Table C.1 thereby shows the results of the model mixture consisting of two fluids with different energy parameters (Mixture I: $\varepsilon_{22}/\varepsilon_{11} = 0.7$), table C.2 presents the results of Mixture II with different diameters ($\sigma_{22}/\sigma_{11} = 1.5$), and table C.3 gives the results of the non-ideal mixture of two identical LJ-fluids ($k_{ij} = 0.25$).

The particle fraction x_1 of the standard LJ fluid with $\sigma_{11} = 1, \varepsilon_{11} = 1$, as well as the number density ρ^* and the temperature T^* are simulation parameters that are held constant during the MD simulation. Pressure p^* and viscosity η^* are direct results of the MD simulations. Entropy s^* and the CE reference viscosity $\eta^*_{\mathrm{ref,CE}}$ are needed for the entropy scaled depiction and to calculate the reduced viscosity $\ln(\eta^\#) = \eta^*/\eta^*_{\mathrm{ref,CE}}$. Entropy s^* is a result of the GCMC simulations (see appendix C.2), $\eta^*_{\mathrm{ref,CE}}$ is calculated according to eq. (4.4). All results are given in reduced LJ units, according to table 4.1. The reported statistical uncertainties are the 95 % confidence interval, calculated as described in the main text in section 4.2.4.

Table C.1: Results of the MD-Simulations of Mixture I

x_1	T^*	p^*	ρ^*	s^*	η^*	$\eta^*_{\mathrm{ref,CE}}$	$\ln(\eta^\#)$
0.00	1.000 00	0.199 86(18)	0.4776	−1.249 85	0.444 94(1206)	0.060 331	1.9981(270)
0.00	1.050 00	0.204 71(15)	0.414 04	−1.054 26	0.368 64(988)	0.063 392	1.7605(270)
0.00	1.100 01	0.198 22(11)	0.331 34	−0.812 21	0.288 62(743)	0.066 438	1.4688(260)
0.00	1.150 01	0.198 40(7)	0.278 15	−0.660 42	0.264 40(929)	0.069 459	1.3367(350)
0.10	1.000 00	0.204 23(21)	0.521 61	−1.419 85	0.532 76(1582)	0.060 331	2.1782(300)
0.10	1.050 00	0.202 19(17)	0.456 81	−1.199 92	0.433 10(1366)	0.063 392	1.9216(310)
0.10	1.100 01	0.197 59(11)	0.374 32	−0.941 56	0.331 59(1115)	0.066 438	1.6076(330)
0.10	1.150 01	0.197 51(9)	0.306 35	−0.745 22	0.280 53(950)	0.069 459	1.3959(340)
0.30	1.000 00	0.199 53(25)	0.584 53	−1.699 98	0.660 00(1481)	0.060 331	2.3924(220)
0.30	1.050 00	0.198 99(25)	0.536 11	−1.498 12	0.571 92(1634)	0.063 392	2.1997(290)
0.30	1.100 00	0.197 97(21)	0.475 45	−1.272 69	0.489 65(2919)	0.066 438	1.9974(590)
0.30	1.150 00	0.197 22(14)	0.399 01	−1.024 04	0.373 97(1361)	0.069 459	1.6834(360)
0.50	1.000 00	0.191 95(36)	0.634 08	−1.949 71	0.854 32(2082)	0.060 331	2.6505(240)
0.50	1.050 00	0.198 13(29)	0.598 41	−1.771 71	0.741 11(2416)	0.063 392	2.4588(320)
0.50	1.100 00	0.196 00(25)	0.553 39	−1.573 28	0.648 48(2580)	0.066 438	2.2784(390)
0.50	1.150 00	0.196 12(24)	0.499 18	−1.362 87	0.546 98(3687)	0.069 459	2.0637(660)
0.70	1.000 00	0.201 43(30)	0.678 39	−2.197 93	1.065 25(4621)	0.060 331	2.8711(430)
0.70	1.050 00	0.197 06(34)	0.6466	−2.016 67	0.912 53(2894)	0.063 392	2.6669(320)
0.70	1.100 00	0.197 01(34)	0.612 24	−1.840 53	0.817 66(2866)	0.066 438	2.5102(350)
0.70	1.150 00	0.194 80(30)	0.571 93	−1.656 02	0.704 69(2861)	0.069 459	2.317(40)
0.90	1.000 00	0.200 74(41)	0.712 64	−2.414 55	1.272 97(4640)	0.060 331	3.0493(360)

Continued on next page

Continued: Results of the MD-Simulations of Mixture I

x_1	T^*	p^*	ρ^*	s^*	η^*	$\eta^*_{\mathrm{ref,CE}}$	$\ln(\eta^\#)$
0.90	1.050 00	0.201 59(43)	0.6867	−2.244 71	1.123 22(2790)	0.063 392	2.8746(250)
0.90	1.100 00	0.190 17(34)	0.655 99	−2.068 62	0.988 31(3683)	0.066 438	2.6997(370)
0.90	1.150 00	0.196 62(33)	0.626 28	−1.910 91	0.863 99(2088)	0.069 459	2.5208(240)
1.00	1.000 00	0.180 32(41)	0.725 11	−2.502 20	1.395 30(5196)	0.060 331	3.141(37)
1.00	1.050 01	0.189 44(39)	0.7016	−2.338 66	1.209 65(3620)	0.063 392	2.9487(300)
1.00	1.100 01	0.193 66(41)	0.675 97	−2.182 34	1.077 59(2629)	0.066 438	2.7862(240)
1.00	1.150 01	0.194 34(34)	0.647 68	−2.024 77	0.982 02(3031)	0.069 459	2.6489(310)

Table C.2: Results of the MD-Simulations of Mixture II

x_1	T^*	p^*	ρ^*	s^*	η^*	$\eta^*_{\mathrm{ref,CE}}$	$\ln(\eta^\#)$
0.00	0.900 66	0.386 38(11)	0.125 45	−3.391 73	1.302 99(3714)	0.024 085	3.9908(280)
0.00	1.000 63	0.434 54(9)	0.122 41	−3.123 80	1.090 51(3846)	0.026 814	3.7055(350)
0.00	1.100 60	0.413 67(10)	0.117 61	−2.843 98	0.857 85(2187)	0.029 528	3.3691(260)
0.00	1.150 58	0.380 30(9)	0.114 39	−2.680 80	0.776 96(2803)	0.030 871	3.2256(360)
0.00	1.200 58	0.410 21(10)	0.1133	−2.599 66	0.749 67(2846)	0.0322	3.1477(380)
0.25	0.900 54	0.397 40(13)	0.151 95	−3.252 38	1.389 62(3805)	0.029 086	3.8665(270)
0.25	1.000 48	0.394 70(12)	0.146 31	−2.948 73	1.113 43(3409)	0.032 381	3.5376(300)
0.25	1.100 45	0.395 53(10)	0.140 76	−2.682 82	0.927 88(3249)	0.035 659	3.2589(350)
0.25	1.150 44	0.392 96(9)	0.137 88	−2.559 77	0.843 78(2860)	0.037 281	3.1194(340)
0.25	1.200 43	0.395 60(9)	0.135 19	−2.448 60	0.768 82(2897)	0.038 885	2.9842(370)

Continued on next page

Continued: Results of the MD-Simulations of Mixture II

x_1	T^*	p^*	ρ^*	s^*	η^*	$\eta^*_{\mathrm{ref,CE}}$	$\ln(\eta^\#)$
0.50	0.900 37	0.403 75(14)	0.192 06	−3.144 69	1.502 69(4414)	0.035 362	3.7494(290)
0.50	1.000 32	0.388 06(13)	0.183 95	−2.824 71	1.203 66(3018)	0.039 369	3.4201(250)
0.50	1.100 31	0.399 48(12)	0.176 69	−2.565 61	0.993 05(4972)	0.043 353	3.1314(490)
0.50	1.150 30	0.398 46(13)	0.172 77	−2.441 09	0.899 90(3217)	0.045 325	2.9884(360)
0.50	1.200 27	0.400 35(12)	0.168 95	−2.326 57	0.834 81(2403)	0.047 276	2.8712(290)
0.75	0.900 18	0.438 38(20)	0.2607	−3.062 82	1.764 97(5746)	0.043 444	3.7044(320)
0.75	1.000 16	0.414 50(15)	0.2487	−2.739 89	1.354 19(3713)	0.048 366	3.3322(270)
0.75	1.100 15	0.403 17(18)	0.236 62	−2.462 54	1.098 31(3805)	0.053 262	3.0263(340)
0.75	1.150 13	0.397 66(15)	0.230 35	−2.325 95	0.992 20(3061)	0.055 684	2.8802(310)
0.75	1.200 14	0.396 77(15)	0.224 19	−2.201 99	0.913 33(1927)	0.058 081	2.7553(210)
1.00	0.900 00	0.217 72(19)	0.387 33	−2.732 33	1.808 48(6025)	0.054 191	3.5077(330)
1.00	1.000 00	0.356 98(23)	0.372 91	−2.543 46	1.583 66(7875)	0.060 331	3.2676(490)
1.00	1.100 00	0.346 91(20)	0.350 24	−2.287 67	1.227 64(4357)	0.066 438	2.9166(350)
1.00	1.150 00	0.447 60(19)	0.346 11	−2.217 85	1.152 17(2175)	0.069 459	2.8087(190)
1.00	1.200 00	0.392 59(19)	0.330 31	−2.046 85	1.011 69(2472)	0.072 449	2.6365(240)

Table C.3: Results of the MD-Simulations of Mixture III

x_1	T^*	p^*	ρ^*	s^*	η^*	$\eta^*_{\mathrm{ref,CE}}$	$\ln(\eta^\#)$
0.00	0.950 00	0.196 98(33)	0.749 82	−2.686 75	1.586 75(3633)	0.057 263	3.3218(230)
0.00	1.000 00	0.187 60(32)	0.725 39	−2.508 00	1.368 99(3395)	0.060 331	3.122(25)

Continued on next page

Continued: Results of the MD-Simulations of Mixture III

x_1	T^*	p^*	ρ^*	s^*	η^*	$\eta^*_{\mathrm{ref,CE}}$	$\ln(\eta^\#)$
0.00	1.050 00	0.210 71(25)	0.704 19	−2.357 26	1.270 43(3656)	0.063 392	2.9978(290)
0.00	1.100 00	0.221 52(27)	0.680 35	−2.210 39	1.132 88(3913)	0.066 438	2.8363(340)
0.00	1.150 00	0.207 60(24)	0.650 03	−2.030 84	0.959 03(2755)	0.069 459	2.6252(290)
0.10	0.950 00	0.208 97(42)	0.7332	−2.566 11	1.428 77(4973)	0.057 263	3.2169(350)
0.10	1.000 00	0.198 21(40)	0.706 46	−2.381 36	1.215 76(3090)	0.060 331	3.0033(250)
0.10	1.050 00	0.198 18(36)	0.679 38	−2.206 02	1.054 15(2739)	0.063 392	2.8111(260)
0.10	1.100 00	0.200 04(38)	0.6506	−2.046 14	0.970 30(2979)	0.066 438	2.6813(310)
0.10	1.150 00	0.190 19(33)	0.615 33	−1.858 24	0.839 45(2823)	0.069 459	2.492(33)
0.10	1.200 00	0.197 74(25)	0.580 73	−1.696 87	0.750 48(3503)	0.072 449	2.3378(470)
0.20	0.950 00	0.277 47(46)	0.727 51	−2.646 62	1.344 36(3972)	0.057 263	3.156(29)
0.20	1.000 00	0.196 98(38)	0.688 71	−2.281 03	1.148 09(4245)	0.060 331	2.946(37)
0.20	1.050 00	0.200 97(38)	0.660 03	−2.104 67	0.994 72(3738)	0.063 392	2.7531(370)
0.20	1.100 00	0.197 01(35)	0.626 77	−1.926 38	0.871 04(3101)	0.066 438	2.5734(350)
0.20	1.150 00	0.200 14(36)	0.591 21	−1.746 62	0.757 80(2721)	0.069 459	2.3897(360)
0.30	1.050 00	0.199 54(40)	0.644 98	−2.035 94	0.899 19(2202)	0.063 392	2.6522(250)
0.30	1.100 00	0.196 85(40)	0.608 91	−1.843 82	0.793 11(3453)	0.066 438	2.4797(430)
0.30	1.150 00	0.197 64(31)	0.568 59	−1.652 27	0.678 94(1962)	0.069 459	2.2798(290)
0.50	1.050 00	0.204 43(44)	0.634 41	−1.996 36	0.875 84(2532)	0.063 392	2.6258(290)
0.50	1.100 00	0.198 54(31)	0.594 74	−1.782 26	0.771 62(3386)	0.066 438	2.4522(430)
0.50	1.150 00	0.198 99(30)	0.550 71	−1.580 50	0.655 42(2546)	0.069 459	2.2445(390)
0.70	1.050 00	0.199 96(42)	0.644 98	−2.035 63	0.917 55(3160)	0.063 392	2.6724(340)

Continued on next page

Continued: Results of the MD-Simulations of Mixture III

x_1	T^*	p^*	ρ^*	s^*	η^*	$\eta^*_{\mathrm{ref,CE}}$	$\ln(\eta^\#)$
0.70	1.100 01	0.197 08(34)	0.608 91	−1.842 52	0.780 62(1952)	0.066 438	2.4638(250)
0.70	1.150 01	0.197 55(32)	0.568 59	−1.654 48	0.676 56(1763)	0.069 459	2.2763(260)
0.80	0.950 00	0.277 18(37)	0.727 51	−2.633 61	1.369 54(5619)	0.057 263	3.1746(410)
0.80	1.000 00	0.197 07(29)	0.688 71	−2.282 80	1.117 20(2031)	0.060 331	2.9187(180)
0.80	1.050 00	0.201 14(24)	0.660 03	−2.105 37	0.991 09(3205)	0.063 392	2.7495(320)
0.80	1.100 00	0.197 52(25)	0.626 77	−1.922 03	0.858 01(2340)	0.066 438	2.5583(270)
0.80	1.150 00	0.200 06(22)	0.591 21	−1.743 19	0.752 06(2681)	0.069 459	2.3821(350)
0.80	1.200 00	0.195 72(19)	0.545 87	−1.555 18	0.639 85(1569)	0.072 449	2.1783(240)
0.90	0.950 00	0.208 99(32)	0.7332	−2.537 10	1.388 14(4001)	0.057 263	3.1881(290)
0.90	1.000 00	0.198 55(30)	0.706 46	−2.372 78	1.232 33(3229)	0.060 331	3.0168(260)
0.90	1.050 00	0.198 07(28)	0.679 38	−2.208 97	1.107 42(4178)	0.063 392	2.8605(370)
0.90	1.100 00	0.200 12(27)	0.6506	−2.034 33	0.982 08(3831)	0.066 438	2.6934(390)
0.90	1.150 00	0.190 27(25)	0.615 33	−1.873 63	0.819 93(1984)	0.069 459	2.4685(240)
0.90	1.200 00	0.197 88(21)	0.580 73	−1.690 65	0.736 11(2067)	0.072 449	2.3185(280)

C.2 Tabulated Results of the isothermal GCMC Simulations

This chapter provides static energetic and entropic properties of the investigated model mixtures at various state points as result of the isothermal GCMC simulations. The tables are structured by mixture and temperature. Tables C.4–C.7 thereby show the results of the model mixture consisting of two fluids with different energy parameters (Mixture I: $\varepsilon_{22}/\varepsilon_{11} = 0.7$), tables C.8–C.13 present the results of Mixture II with different diameters ($\sigma_{22}/\sigma_{11} = 1.5$), and tables C.14–C.20 give the results of the non-ideal mixture of two identical LJ-fluids ($k_{ij} = 0.25$).

The particle fraction x_1 of the standard LJ fluid with $\sigma_{11} = 1, \varepsilon_{11} = 1$, as well as the temperature T^* are simulation parameters that are held constant during the simulations. The specific volume v^* and the number density ρ^*, the specific internal energy u^*_{res}, the specific enthalpy h^*_{res}, and the specific Gibbs energy g^*_{res} are calculated using histogram reweighting as described in section 4.2.3. Entropy s^* is calculated with eq. (4.19). All results are given in reduced LJ units, according to table 4.1.

Table C.4: Results of the GCMC-Simulations of Mixture I at $p^* = 0.20$ and $T^* = 1.00$

x_1	T^*	v^*	ρ^*	u^*_{res}	h^*_{res}	g^*_{res}	s^*
0.001	1.00	2.093 78	0.477 60	−2.245 86	−1.577 25	−2.827 10	−1.249 85
0.050	1.00	2.007 21	0.498 20	−2.393 26	−1.663 95	−2.991 82	−1.327 87
0.100	1.00	1.917 15	0.521 61	−2.558 44	−1.755 16	−3.175 01	−1.419 85
0.150	1.00	1.856 43	0.538 67	−2.699 39	−1.835 27	−3.328 10	−1.492 83
0.200	1.00	1.799 55	0.555 70	−2.842 99	−1.917 34	−3.483 08	−1.565 74
0.250	1.00	1.750 23	0.571 35	−2.984 50	−1.997 86	−3.634 45	−1.636 59
0.300	1.00	1.710 78	0.584 53	−3.117 31	−2.075 17	−3.775 15	−1.699 98
0.350	1.00	1.675 28	0.596 91	−3.249 18	−2.153 55	−3.914 12	−1.760 57
0.400	1.00	1.637 53	0.610 68	−3.391 75	−2.236 81	−4.064 24	−1.827 44
0.450	1.00	1.603 21	0.623 75	−3.534 34	−2.319 69	−4.213 69	−1.894 01
0.500	1.00	1.577 09	0.634 08	−3.664 85	−2.399 72	−4.349 43	−1.949 71
0.550	1.00	1.546 76	0.646 51	−3.810 12	−2.484 48	−4.500 76	−2.016 29
0.600	1.00	1.520 94	0.657 49	−3.950 82	−2.569 02	−4.646 63	−2.077 61
0.650	1.00	1.497 91	0.667 60	−4.089 52	−2.654 68	−4.789 94	−2.135 26
0.700	1.00	1.474 08	0.678 39	−4.235 38	−2.742 64	−4.940 57	−2.197 93
0.750	1.00	1.453 33	0.688 08	−4.377 35	−2.830 49	−5.086 68	−2.256 19

Continued on next page

Continued: Results of the GCMC-Simulations of Mixture I at $p^* = 0.20$ and $T^* = 1.00$

x_1	T^*	v^*	ρ^*	u^*_{res}	h^*_{res}	g^*_{res}	s^*
0.800	1.00	1.435 46	0.696 64	−4.515 07	−2.918 90	−5.227 98	−2.309 08
0.850	1.00	1.422 16	0.703 16	−4.643 38	−3.005 78	−5.358 95	−2.353 17
0.900	1.00	1.403 23	0.712 64	−4.792 89	−3.097 69	−5.512 25	−2.414 55
0.950	1.00	1.387 97	0.720 48	−4.934 23	−3.189 39	−5.656 64	−2.467 25
0.999	1.00	1.379 11	0.725 11	−5.053 85	−3.275 83	−5.778 03	−2.502 20

Table C.5: Results of the GCMC-Simulations of Mixture I at $p^* = 0.20$ and $T^* = 1.05$

x_1	T^*	v^*	ρ^*	u^*_{res}	h^*_{res}	g^*_{res}	s^*
0.001	1.05	2.415 22	0.414 04	−1.947 75	−1.407 73	−2.514 71	−1.054 26
0.050	1.05	2.268 12	0.440 89	−2.114 33	−1.512 42	−2.710 71	−1.141 23
0.100	1.05	2.189 11	0.456 81	−2.238 34	−1.590 60	−2.850 52	−1.199 92
0.150	1.05	2.097 65	0.476 72	−2.385 08	−1.679 88	−3.015 55	−1.272 07
0.200	1.05	2.017 94	0.495 55	−2.530 46	−1.767 81	−3.176 87	−1.341 96
0.250	1.05	1.934 11	0.517 03	−2.692 84	−1.862 17	−3.356 02	−1.422 72
0.300	1.05	1.865 27	0.536 11	−2.848 46	−1.952 38	−3.525 41	−1.498 12
0.350	1.05	1.811 91	0.551 90	−2.991 91	−2.037 28	−3.679 53	−1.564 05
0.400	1.05	1.758 08	0.568 80	−3.144 77	−2.125 54	−3.843 16	−1.635 82
0.450	1.05	1.711 67	0.584 23	−3.294 78	−2.211 68	−4.002 44	−1.705 49
0.500	1.05	1.671 09	0.598 41	−3.441 36	−2.296 84	−4.157 14	−1.771 71
0.550	1.05	1.636 55	0.611 04	−3.583 13	−2.380 75	−4.305 82	−1.833 40
0.600	1.05	1.604 92	0.623 08	−3.725 05	−2.465 18	−4.454 06	−1.894 17
0.650	1.05	1.574 55	0.635 10	−3.869 84	−2.551 37	−4.604 93	−1.955 77
0.700	1.05	1.546 55	0.646 60	−4.015 23	−2.638 42	−4.755 92	−2.016 67
0.750	1.05	1.520 74	0.657 58	−4.161 12	−2.726 24	−4.906 97	−2.076 89
0.800	1.05	1.497 82	0.667 64	−4.303 89	−2.814 55	−5.054 32	−2.133 12
0.850	1.05	1.477 04	0.677 03	−4.446 43	−2.903 42	−5.201 03	−2.188 19
0.900	1.05	1.456 24	0.686 70	−4.592 95	−2.994 75	−5.351 70	−2.244 71
0.950	1.05	1.435 23	0.696 75	−4.745 48	−3.088 46	−5.508 44	−2.304 73
0.999	1.05	1.425 31	0.701 60	−4.864 10	−3.173 44	−5.629 04	−2.338 66

Table C.6: Results of the GCMC-Simulations of Mixture I at $p^* = 0.20$ and $T^* = 1.10$

x_1	T^*	v^*	ρ^*	u^*_{res}	h^*_{res}	g^*_{res}	s^*
0.001	1.10	3.018 07	0.331 34	−1.567 86	−1.170 81	−2.064 24	−0.812 21
0.050	1.10	2.864 92	0.349 05	−1.684 64	−1.260 32	−2.211 66	−0.864 85
0.100	1.10	2.671 51	0.374 32	−1.842 84	−1.372 82	−2.408 54	−0.941 56
0.150	1.10	2.509 45	0.398 49	−2.001 10	−1.479 76	−2.599 21	−1.017 68
0.200	1.10	2.354 74	0.424 68	−2.172 41	−1.590 53	−2.801 46	−1.100 85
0.250	1.10	2.214 73	0.451 52	−2.352 76	−1.701 17	−3.009 82	−1.189 68
0.300	1.10	2.103 29	0.475 45	−2.524 40	−1.803 79	−3.203 74	−1.272 69
0.350	1.10	2.011 05	0.497 25	−2.690 57	−1.901 30	−3.388 36	−1.351 87
0.400	1.10	1.931 41	0.517 76	−2.855 18	−1.996 53	−3.568 89	−1.429 42
0.450	1.10	1.864 20	0.536 42	−3.015 20	−2.088 97	−3.742 36	−1.503 09
0.500	1.10	1.807 05	0.553 39	−3.170 76	−2.178 75	−3.909 35	−1.573 28
0.550	1.10	1.754 89	0.569 84	−3.327 59	−2.268 10	−4.076 61	−1.644 09
0.600	1.10	1.711 29	0.584 36	−3.477 72	−2.355 31	−4.235 47	−1.709 24
0.650	1.10	1.672 71	0.597 83	−3.625 71	−2.442 04	−4.391 17	−1.771 93
0.700	1.10	1.633 35	0.612 24	−3.783 30	−2.532 05	−4.556 63	−1.840 53
0.750	1.10	1.598 70	0.625 51	−3.938 16	−2.622 29	−4.718 42	−1.905 57
0.800	1.10	1.570 12	0.636 90	−4.084 99	−2.711 42	−4.870 97	−1.963 22
0.850	1.10	1.547 03	0.646 40	−4.223 57	−2.798 32	−5.014 16	−2.014 40
0.900	1.10	1.524 40	0.655 99	−4.365 79	−2.885 42	−5.160 91	−2.068 62
0.950	1.10	1.499 68	0.666 81	−4.517 97	−2.975 83	−5.318 03	−2.129 28
0.999	1.10	1.479 35	0.675 97	−4.660 09	−3.063 64	−5.464 22	−2.182 34

Table C.7: Results of the GCMC-Simulations of Mixture I at $p^* = 0.20$ and $T^* = 1.15$

x_1	T^*	v^*	ρ^*	u^*_{res}	h^*_{res}	g^*_{res}	s^*
0.001	1.15	3.595 24	0.278 15	−1.314 91	−0.986 38	−1.745 86	−0.660 42
0.001	1.15	3.595 24	0.278 15	−1.314 91	−0.986 38	−1.745 86	−0.660 42
0.050	1.15	3.441 82	0.290 54	−1.405 71	−1.064 17	−1.867 35	−0.698 41
0.050	1.15	3.441 82	0.290 54	−1.405 71	−1.064 17	−1.867 35	−0.698 41
0.100	1.15	3.264 28	0.306 35	−1.514 62	−1.154 77	−2.011 77	−0.745 22
0.100	1.15	3.264 28	0.306 35	−1.514 62	−1.154 77	−2.011 77	−0.745 22

Continued on next page

Continued: Results of the GCMC-Simulations of Mixture I at $p^* = 0.20$ and $T^* = 1.15$

x_1	T^*	v^*	ρ^*	u^*_{res}	h^*_{res}	g^*_{res}	s^*
0.150	1.15	3.076 07	0.325 09	−1.640 23	−1.254 56	−2.175 02	−0.800 40
0.150	1.15	3.076 07	0.325 09	−1.640 23	−1.254 56	−2.175 02	−0.800 40
0.200	1.15	2.882 10	0.346 97	−1.785 52	−1.363 22	−2.359 10	−0.865 98
0.200	1.15	2.882 10	0.346 97	−1.785 52	−1.363 22	−2.359 10	−0.865 98
0.250	1.15	2.689 48	0.371 82	−1.948 63	−1.479 08	−2.560 74	−0.940 57
0.250	1.15	2.689 48	0.371 82	−1.948 63	−1.479 08	−2.560 74	−0.940 57
0.300	1.15	2.506 21	0.399 01	−2.127 85	−1.598 96	−2.776 60	−1.024 04
0.300	1.15	2.506 21	0.399 01	−2.127 85	−1.598 96	−2.776 60	−1.024 04
0.350	1.15	2.346 17	0.426 23	−2.313 11	−1.716 26	−2.993 88	−1.110 97
0.350	1.15	2.346 17	0.426 23	−2.313 11	−1.716 26	−2.993 88	−1.110 97
0.400	1.15	2.215 24	0.451 42	−2.493 38	−1.826 30	−3.200 33	−1.194 80
0.400	1.15	2.215 24	0.451 42	−2.493 38	−1.826 30	−3.200 33	−1.194 80
0.450	1.15	2.100 50	0.476 08	−2.676 07	−1.934 26	−3.405 97	−1.279 75
0.450	1.15	2.100 50	0.476 08	−2.676 07	−1.934 26	−3.405 97	−1.279 75
0.500	1.15	2.003 29	0.499 18	−2.856 33	−2.038 38	−3.605 67	−1.362 87
0.500	1.15	2.003 29	0.499 18	−2.856 33	−2.038 38	−3.605 67	−1.362 87
0.550	1.15	1.923 50	0.519 89	−3.029 48	−2.137 33	−3.794 78	−1.441 26
0.550	1.15	1.923 50	0.519 89	−3.029 48	−2.137 33	−3.794 78	−1.441 26
0.600	1.15	1.857 69	0.538 30	−3.194 33	−2.231 69	−3.972 79	−1.514 00
0.600	1.15	1.857 69	0.538 30	−3.194 33	−2.231 69	−3.972 79	−1.514 00
0.650	1.15	1.798 38	0.556 06	−3.360 39	−2.325 36	−4.150 71	−1.587 27
0.650	1.15	1.798 38	0.556 06	−3.360 39	−2.325 36	−4.150 71	−1.587 27
0.700	1.15	1.748 48	0.571 93	−3.520 40	−2.416 28	−4.320 71	−1.656 02
0.700	1.15	1.748 48	0.571 93	−3.520 40	−2.416 28	−4.320 71	−1.656 02
0.750	1.15	1.701 48	0.587 72	−3.684 09	−2.508 53	−4.493 79	−1.726 32
0.750	1.15	1.701 48	0.587 72	−3.684 09	−2.508 53	−4.493 79	−1.726 32
0.800	1.15	1.659 51	0.602 59	−3.846 77	−2.601 33	−4.664 87	−1.794 38
0.800	1.15	1.659 51	0.602 59	−3.846 77	−2.601 33	−4.664 87	−1.794 38
0.850	1.15	1.622 97	0.616 15	−4.006 16	−2.693 71	−4.831 57	−1.859 01
0.850	1.15	1.622 97	0.616 15	−4.006 16	−2.693 71	−4.831 57	−1.859 01
0.900	1.15	1.596 74	0.626 28	−4.147 43	−2.780 53	−4.978 08	−1.910 91
0.900	1.15	1.596 74	0.626 28	−4.147 43	−2.780 53	−4.978 08	−1.910 91

Continued on next page

Continued: Results of the GCMC-Simulations of Mixture I at $p^* = 0.20$ and $T^* = 1.15$

x_1	T^*	v^*	ρ^*	u^*_{res}	h^*_{res}	g^*_{res}	s^*
0.950	1.15	1.571 52	0.636 33	−4.290 99	−2.868 32	−5.126 68	−1.963 79
0.950	1.15	1.571 52	0.636 33	−4.290 99	−2.868 32	−5.126 68	−1.963 79
0.999	1.15	1.543 98	0.647 68	−4.445 34	−2.958 05	−5.286 54	−2.024 77
0.999	1.15	1.543 98	0.647 68	−4.445 34	−2.958 05	−5.286 54	−2.024 77

Table C.8: Results of the GCMC-Simulations of Mixture II at $p^* = 0.40$ and $T^* = 0.90$

x_1	T^*	v^*	ρ^*	u^*_{res}	h^*_{res}	g^*_{res}	s^*
0.001	0.90	3.985 80	0.250 89	−5.895 36	−2.148 48	−5.201 04	−3.391 73
0.050	0.90	3.847 77	0.259 89	−5.870 44	−2.204 44	−5.231 34	−3.363 22
0.100	0.90	3.721 77	0.268 69	−5.825 27	−2.259 77	−5.236 56	−3.307 54
0.150	0.90	3.582 22	0.279 16	−5.798 70	−2.316 28	−5.265 81	−3.277 26
0.200	0.90	3.431 12	0.291 45	−5.790 70	−2.373 83	−5.318 25	−3.271 58
0.250	0.90	3.290 50	0.303 91	−5.771 61	−2.428 28	−5.355 42	−3.252 38
0.300	0.90	3.156 22	0.316 83	−5.742 48	−2.480 97	−5.379 99	−3.221 13
0.350	0.90	3.017 50	0.331 40	−5.722 42	−2.535 81	−5.415 42	−3.199 57
0.400	0.90	2.879 68	0.347 26	−5.702 21	−2.590 47	−5.450 34	−3.177 64
0.450	0.90	2.741 98	0.364 70	−5.684 89	−2.644 40	−5.488 09	−3.159 66
0.500	0.90	2.603 41	0.384 11	−5.671 72	−2.700 14	−5.530 36	−3.144 69
0.550	0.90	2.468 28	0.405 14	−5.653 25	−2.755 98	−5.565 94	−3.122 18
0.600	0.90	2.331 24	0.428 96	−5.640 86	−2.813 80	−5.608 37	−3.105 08
0.650	0.90	2.197 88	0.454 98	−5.623 36	−2.872 27	−5.644 21	−3.079 93
0.700	0.90	2.058 99	0.485 68	−5.620 50	−2.934 54	−5.696 90	−3.069 29
0.750	0.90	1.917 92	0.521 40	−5.627 16	−3.003 45	−5.759 99	−3.062 82
0.800	0.90	1.778 67	0.562 22	−5.635 29	−3.081 34	−5.823 82	−3.047 20
0.850	0.90	1.656 83	0.603 56	−5.596 54	−3.155 35	−5.833 81	−2.976 07
0.900	0.90	1.536 43	0.650 86	−5.553 71	−3.226 47	−5.839 14	−2.902 97
0.950	0.90	1.426 44	0.701 04	−5.463 49	−3.270 39	−5.792 91	−2.802 80
0.999	0.90	1.290 89	0.774 66	−5.444 47	−3.369 01	−5.828 11	−2.732 33

Table C.9: Results of the GCMC-Simulations of Mixture II at $p^* = 0.40$ and $T^* = 1.00$

x_1	T^*	v^*	ρ^*	u^*_{res}	h^*_{res}	g^*_{res}	s^*
0.001	1.00	4.084 72	0.244 81	−5.677 55	−1.919 87	−5.043 66	−3.123 80
0.050	1.00	3.961 86	0.252 41	−5.634 69	−1.968 21	−5.049 95	−3.081 74
0.100	1.00	3.830 80	0.261 04	−5.592 59	−2.017 87	−5.060 27	−3.042 40
0.150	1.00	3.701 17	0.270 19	−5.549 76	−2.070 20	−5.069 29	−2.999 09
0.200	1.00	3.561 67	0.280 77	−5.519 16	−2.125 52	−5.094 50	−2.968 97
0.250	1.00	3.417 39	0.292 62	−5.497 75	−2.182 06	−5.130 79	−2.948 73
0.300	1.00	3.274 73	0.305 37	−5.473 93	−2.237 76	−5.164 04	−2.926 28
0.350	1.00	3.133 44	0.319 14	−5.450 02	−2.293 64	−5.196 64	−2.903 01
0.400	1.00	2.991 52	0.334 28	−5.428 52	−2.350 55	−5.231 91	−2.881 36
0.450	1.00	2.852 92	0.350 52	−5.402 94	−2.406 23	−5.261 77	−2.855 54
0.500	1.00	2.718 17	0.367 89	−5.372 02	−2.460 04	−5.284 75	−2.824 71
0.550	1.00	2.578 83	0.387 77	−5.350 57	−2.516 12	−5.319 03	−2.802 92
0.600	1.00	2.433 53	0.410 93	−5.342 81	−2.576 33	−5.369 40	−2.793 07
0.650	1.00	2.291 94	0.436 31	−5.330 23	−2.636 12	−5.413 45	−2.777 33
0.700	1.00	2.145 58	0.466 08	−5.330 59	−2.701 80	−5.472 36	−2.770 56
0.750	1.00	2.010 47	0.497 40	−5.308 27	−2.764 19	−5.504 08	−2.739 89
0.800	1.00	1.877 80	0.532 54	−5.282 46	−2.828 38	−5.531 34	−2.702 97
0.850	1.00	1.742 36	0.573 93	−5.263 38	−2.897 56	−5.566 43	−2.668 88
0.900	1.00	1.596 58	0.626 34	−5.276 19	−2.971 30	−5.637 56	−2.666 25
0.950	1.00	1.473 44	0.678 69	−5.223 35	−3.018 78	−5.633 97	−2.615 19
0.999	1.00	1.340 81	0.745 82	−5.201 72	−3.121 94	−5.665 40	−2.543 46

Table C.10: Results of the GCMC-Simulations of Mixture II at $p^* = 0.40$ and $T^* = 1.05$

x_1	T^*	v^*	ρ^*	u^*_{res}	h^*_{res}	g^*_{res}	s^*
0.001	1.05	4.191 91	0.238 55	−5.516 86	−1.800 71	−4.890 10	−2.942 28
0.050	1.05	4.055 88	0.246 56	−5.480 38	−1.851 94	−4.908 02	−2.910 56
0.100	1.05	3.911 73	0.255 64	−5.450 57	−1.905 04	−4.935 88	−2.886 51
0.150	1.05	3.767 70	0.265 41	−5.422 55	−1.958 35	−4.965 47	−2.863 92
0.200	1.05	3.625 52	0.275 82	−5.393 46	−2.012 37	−4.993 26	−2.838 94
0.250	1.05	3.481 48	0.287 23	−5.367 28	−2.067 89	−5.024 69	−2.816 00

Continued on next page

Continued: Results of the GCMC-Simulations of Mixture II at $p^* = 0.40$ and $T^* = 1.05$

x_1	T^*	v^*	ρ^*	u^*_{res}	h^*_{res}	g^*_{res}	s^*
0.300	1.05	3.338 75	0.299 51	−5.339 92	−2.123 77	−5.054 42	−2.791 10
0.350	1.05	3.197 45	0.312 75	−5.312 31	−2.179 99	−5.083 33	−2.765 08
0.400	1.05	3.054 68	0.327 37	−5.287 72	−2.237 05	−5.115 84	−2.741 71
0.450	1.05	2.912 57	0.343 34	−5.263 61	−2.293 62	−5.148 58	−2.719 01
0.500	1.05	2.770 67	0.360 92	−5.239 90	−2.351 01	−5.181 63	−2.695 82
0.550	1.05	2.629 64	0.380 28	−5.216 62	−2.408 48	−5.214 77	−2.672 65
0.600	1.05	2.488 61	0.401 83	−5.195 04	−2.466 18	−5.249 60	−2.650 87
0.650	1.05	2.343 57	0.426 70	−5.183 48	−2.527 29	−5.296 05	−2.636 92
0.700	1.05	2.203 39	0.453 85	−5.163 22	−2.586 85	−5.331 86	−2.614 29
0.750	1.05	2.059 81	0.485 48	−5.152 65	−2.651 80	−5.378 73	−2.597 08
0.800	1.05	1.925 65	0.519 30	−5.121 68	−2.713 18	−5.401 42	−2.560 22
0.850	1.05	1.781 88	0.561 21	−5.115 76	−2.776 25	−5.453 01	−2.549 29
0.900	1.05	1.640 84	0.609 44	−5.105 61	−2.840 63	−5.499 27	−2.532 04
0.950	1.05	1.524 25	0.656 06	−5.020 75	−2.884 20	−5.461 05	−2.454 15
0.999	1.05	1.373 46	0.728 09	−5.049 69	−2.979 33	−5.550 30	−2.448 54

Table C.11: Results of the GCMC-Simulations of Mixture II at $p^* = 0.40$ and $T^* = 1.10$

x_1	T^*	v^*	ρ^*	u^*_{res}	h^*_{res}	g^*_{res}	s^*
0.001	1.10	4.251 21	0.235 23	−5.410 80	−1.681 93	−4.810 32	−2.843 98
0.050	1.10	4.118 98	0.242 78	−5.365 31	−1.736 29	−4.817 72	−2.801 31
0.100	1.10	3.983 90	0.251 01	−5.324 46	−1.790 44	−4.830 90	−2.764 06
0.150	1.10	3.842 07	0.260 28	−5.290 81	−1.846 06	−4.853 98	−2.734 47
0.200	1.10	3.697 43	0.270 46	−5.260 33	−1.903 07	−4.881 35	−2.707 53
0.250	1.10	3.552 08	0.281 53	−5.231 98	−1.960 05	−4.911 14	−2.682 82
0.300	1.10	3.406 31	0.293 57	−5.205 70	−2.017 15	−4.943 18	−2.660 02
0.350	1.10	3.261 11	0.306 64	−5.180 11	−2.074 47	−4.975 66	−2.637 45
0.400	1.10	3.118 20	0.320 70	−5.152 21	−2.131 21	−5.004 93	−2.612 47
0.450	1.10	2.974 59	0.336 18	−5.125 39	−2.188 80	−5.035 55	−2.587 96
0.500	1.10	2.829 85	0.353 38	−5.101 74	−2.247 63	−5.069 80	−2.565 61
0.550	1.10	2.686 22	0.372 27	−5.078 03	−2.306 19	−5.103 54	−2.543 04

Continued on next page

Continued: Results of the GCMC-Simulations of Mixture II at $p^* = 0.40$ and $T^* = 1.10$

x_1	T^*	v^*	ρ^*	u^*_{res}	h^*_{res}	g^*_{res}	s^*
0.600	1.10	2.542 73	0.393 28	−5.055 86	−2.364 18	−5.138 77	−2.522 35
0.650	1.10	2.398 32	0.416 96	−5.037 21	−2.423 14	−5.177 89	−2.504 31
0.700	1.10	2.256 86	0.443 09	−5.012 80	−2.481 47	−5.210 06	−2.480 54
0.750	1.10	2.113 05	0.473 25	−4.995 17	−2.541 16	−5.249 95	−2.462 54
0.800	1.10	1.971 32	0.507 27	−4.974 37	−2.603 88	−5.285 84	−2.438 15
0.850	1.10	1.831 98	0.545 86	−4.948 50	−2.662 08	−5.315 71	−2.412 39
0.900	1.10	1.683 67	0.593 94	−4.947 97	−2.728 76	−5.374 50	−2.405 22
0.950	1.10	1.544 41	0.647 49	−4.923 94	−2.789 04	−5.406 17	−2.379 21
0.999	1.10	1.427 58	0.700 49	−4.835 79	−2.848 31	−5.364 76	−2.287 67

Table C.12: Results of the GCMC-Simulations of Mixture II at $p^* = 0.40$ and $T^* = 1.15$

x_1	T^*	v^*	ρ^*	u^*_{res}	h^*_{res}	g^*_{res}	s^*
0.001	1.15	4.371 09	0.228 78	−5.235 41	−1.554 05	−4.636 97	−2.680 80
0.050	1.15	4.194 36	0.238 42	−5.241 99	−1.619 63	−4.714 25	−2.690 97
0.100	1.15	4.063 58	0.246 09	−5.194 04	−1.676 41	−4.718 61	−2.645 39
0.150	1.15	3.917 73	0.255 25	−5.162 23	−1.737 07	−4.745 14	−2.615 72
0.200	1.15	3.772 00	0.265 11	−5.129 99	−1.796 53	−4.771 19	−2.586 66
0.250	1.15	3.626 33	0.275 76	−5.099 02	−1.854 75	−4.798 48	−2.559 77
0.300	1.15	3.479 09	0.287 43	−5.070 83	−1.913 32	−4.829 20	−2.535 54
0.350	1.15	3.331 74	0.300 14	−5.044 65	−1.972 25	−4.861 95	−2.512 78
0.400	1.15	3.185 94	0.313 88	−5.015 61	−2.030 35	−4.891 23	−2.487 72
0.450	1.15	3.040 30	0.328 92	−4.987 37	−2.088 41	−4.921 25	−2.463 33
0.500	1.15	2.894 05	0.345 54	−4.961 96	−2.147 08	−4.954 33	−2.441 09
0.550	1.15	2.749 13	0.363 75	−4.934 95	−2.205 16	−4.985 30	−2.417 51
0.600	1.15	2.605 73	0.383 77	−4.906 40	−2.263 21	−5.014 10	−2.392 08
0.650	1.15	2.461 95	0.406 18	−4.879 40	−2.322 25	−5.044 62	−2.367 27
0.700	1.15	2.315 41	0.431 89	−4.858 63	−2.382 47	−5.082 46	−2.347 82
0.750	1.15	2.170 58	0.460 71	−4.835 68	−2.442 60	−5.117 44	−2.325 95
0.800	1.15	2.025 46	0.493 71	−4.814 96	−2.503 59	−5.154 78	−2.305 38
0.850	1.15	1.881 73	0.531 43	−4.791 05	−2.565 49	−5.188 36	−2.280 76

Continued on next page

Continued: Results of the GCMC-Simulations of Mixture II at $p^* = 0.40$ and $T^* = 1.15$

x_1	T^*	v^*	ρ^*	u^*_{res}	h^*_{res}	g^*_{res}	s^*
0.900	1.15	1.741 39	0.574 25	−4.758 54	−2.623 20	−5.211 99	−2.251 12
0.950	1.15	1.600 23	0.624 91	−4.728 40	−2.683 29	−5.238 30	−2.221 75
0.999	1.15	1.444 61	0.692 23	−4.751 74	−2.773 37	−5.323 90	−2.217 85

Table C.13: Results of the GCMC-Simulations of Mixture II at $p^* = 0.40$ and $T^* = 1.20$

x_1	T^*	v^*	ρ^*	u^*_{res}	h^*_{res}	g^*_{res}	s^*
0.001	1.20	4.412 91	0.226 61	−5.156 85	−1.472 10	−4.591 69	−2.599 66
0.050	1.20	4.280 87	0.233 60	−5.112 62	−1.522 95	−4.600 27	−2.564 44
0.100	1.20	4.136 42	0.241 76	−5.075 16	−1.579 70	−4.620 59	−2.534 08
0.150	1.20	3.992 09	0.250 50	−5.038 63	−1.637 15	−4.641 80	−2.503 87
0.200	1.20	3.845 10	0.260 07	−5.005 85	−1.696 19	−4.667 81	−2.476 36
0.250	1.20	3.698 58	0.270 37	−4.973 50	−1.755 75	−4.694 07	−2.448 60
0.300	1.20	3.550 35	0.281 66	−4.943 23	−1.815 98	−4.723 08	−2.422 59
0.350	1.20	3.401 39	0.294 00	−4.914 73	−1.875 47	−4.754 17	−2.398 92
0.400	1.20	3.252 77	0.307 43	−4.886 72	−1.934 32	−4.785 61	−2.376 08
0.450	1.20	3.106 07	0.321 95	−4.856 42	−1.992 33	−4.813 99	−2.351 38
0.500	1.20	2.959 41	0.337 91	−4.826 19	−2.050 54	−4.842 43	−2.326 57
0.550	1.20	2.814 53	0.355 30	−4.794 30	−2.108 88	−4.868 48	−2.299 67
0.600	1.20	2.669 03	0.374 67	−4.764 44	−2.168 44	−4.896 83	−2.273 66
0.650	1.20	2.522 16	0.396 49	−4.736 68	−2.227 77	−4.927 81	−2.250 03
0.700	1.20	2.376 90	0.420 72	−4.706 69	−2.285 84	−4.955 93	−2.225 07
0.750	1.20	2.230 23	0.448 39	−4.680 33	−2.345 86	−4.988 24	−2.201 99
0.800	1.20	2.080 91	0.480 56	−4.659 69	−2.407 00	−5.027 33	−2.183 60
0.850	1.20	1.929 25	0.518 34	−4.645 67	−2.473 12	−5.073 98	−2.167 38
0.900	1.20	1.794 96	0.557 12	−4.591 60	−2.525 75	−5.073 62	−2.123 22
0.950	1.20	1.652 45	0.605 16	−4.553 91	−2.582 28	−5.092 93	−2.092 20
0.999	1.20	1.513 74	0.660 62	−4.510 52	−2.648 81	−5.105 02	−2.046 85

Table C.14: Results of the GCMC-Simulations of Mixture III at $p^* = 0.20$ and $T^* = 0.90$

x_1	T^*	v^*	ρ^*	u^*_{res}	h^*_{res}	g^*_{res}	s^*
0.001	0.90	1.317 51	0.759 01	−5.356 49	−3.498 14	−5.992 99	−2.772 05
0.050	0.90	1.310 57	0.763 03	−5.246 20	−3.380 21	−5.884 08	−2.782 08
0.100	0.90	1.318 44	0.758 47	−5.145 31	−3.265 13	−5.781 63	−2.796 11
0.150	0.90	1.318 71	0.758 31	−5.142 93	−3.178 22	−5.779 19	−2.889 97
0.200	0.90	1.318 90	0.758 21	−5.141 58	−3.109 23	−5.777 80	−2.965 08
0.250	0.90	1.319 04	0.758 12	−5.140 57	−3.054 41	−5.776 76	−3.024 84
0.300	0.90	1.319 17	0.758 05	−5.139 75	−3.011 63	−5.775 92	−3.071 43
0.350	0.90	1.319 29	0.757 98	−5.139 06	−2.979 58	−5.775 20	−3.106 25
0.400	0.90	1.319 40	0.757 92	−5.138 47	−2.957 42	−5.774 59	−3.130 19
0.450	0.90	1.319 50	0.757 86	−5.137 97	−2.944 65	−5.774 07	−3.143 80
0.500	0.90	1.319 59	0.757 81	−5.137 55	−2.940 96	−5.773 63	−3.147 41
0.550	0.90	1.319 67	0.757 76	−5.137 20	−2.946 27	−5.773 26	−3.141 10
0.600	0.90	1.319 75	0.757 72	−5.136 92	−2.960 67	−5.772 97	−3.124 77
0.650	0.90	1.319 81	0.757 68	−5.136 72	−2.984 45	−5.772 76	−3.098 12
0.700	0.90	1.311 67	0.762 38	−5.258 88	−3.112 15	−5.896 55	−3.093 78
0.750	0.90	1.314 33	0.760 84	−5.193 37	−3.129 23	−5.830 50	−3.001 41
0.800	0.90	1.316 02	0.759 87	−5.200 31	−3.144 03	−5.837 10	−2.992 31
0.850	0.90	1.315 16	0.760 37	−5.214 07	−3.211 27	−5.851 03	−2.933 08
0.900	0.90	1.305 19	0.766 17	−5.312 29	−3.314 49	−5.951 25	−2.929 73
0.950	0.90	1.313 92	0.761 08	−5.232 86	−3.392 87	−5.870 07	−2.752 44
0.999	0.90	1.318 31	0.758 54	−5.352 40	−3.510 80	−5.988 74	−2.753 26

Table C.15: Results of the GCMC-Simulations of Mixture III at $p^* = 0.20$ and $T^* = 0.95$

x_1	T^*	v^*	ρ^*	u^*_{res}	h^*_{res}	g^*_{res}	s^*
0.001	0.95	1.333 65	0.749 82	−5.257 00	−3.387 85	−5.940 27	−2.686 75
0.050	0.95	1.347 72	0.741 99	−5.070 50	−3.258 74	−5.750 96	−2.623 39
0.100	0.95	1.363 88	0.733 20	−4.900 72	−3.140 13	−5.577 94	−2.566 11
0.150	0.95	1.374 01	0.727 80	−4.813 33	−3.042 81	−5.488 53	−2.574 44
0.200	0.95	1.374 55	0.727 51	−4.809 15	−2.969 95	−5.484 24	−2.646 62
0.250	0.95	1.374 83	0.727 36	−4.807 09	−2.912 15	−5.482 12	−2.705 23

Continued on next page

Continued: Results of the GCMC-Simulations of Mixture III at $p^* = 0.20$ and $T^* = 0.95$

x_1	T^*	v^*	ρ^*	u^*_{res}	h^*_{res}	g^*_{res}	s^*
0.300	0.95	1.375 02	0.727 26	−4.805 78	−2.867 09	−5.480 77	−2.751 25
0.350	0.95	1.375 16	0.727 19	−4.804 90	−2.833 37	−5.479 87	−2.785 79
0.400	0.95	1.375 25	0.727 14	−4.804 34	−2.810 11	−5.479 29	−2.809 67
0.450	0.95	1.375 31	0.727 11	−4.804 04	−2.796 75	−5.478 97	−2.823 39
0.500	0.95	1.375 35	0.727 09	−4.803 95	−2.792 99	−5.478 88	−2.827 25
0.550	0.95	1.375 36	0.727 08	−4.804 07	−2.798 74	−5.479 00	−2.821 32
0.600	0.95	1.375 34	0.727 09	−4.804 40	−2.814 09	−5.479 33	−2.805 52
0.650	0.95	1.375 29	0.727 12	−4.804 96	−2.839 34	−5.479 90	−2.779 54
0.700	0.95	1.375 20	0.727 16	−4.805 79	−2.875 04	−5.480 75	−2.742 85
0.750	0.95	1.375 08	0.727 23	−4.806 98	−2.922 08	−5.481 96	−2.694 61
0.800	0.95	1.374 88	0.727 33	−4.808 74	−2.981 84	−5.483 77	−2.633 61
0.850	0.95	1.374 52	0.727 53	−4.811 99	−3.056 60	−5.487 09	−2.558 41
0.900	0.95	1.367 25	0.731 40	−4.887 38	−3.153 68	−5.563 93	−2.537 10
0.950	0.95	1.355 14	0.737 93	−5.044 19	−3.268 21	−5.723 16	−2.584 15
0.999	0.95	1.340 43	0.746 03	−5.230 18	−3.395 36	−5.912 09	−2.649 19

Table C.16: Results of the GCMC-Simulations of Mixture III at $p^* = 0.20$ and $T^* = 1.00$

x_1	T^*	v^*	ρ^*	u^*_{res}	h^*_{res}	g^*_{res}	s^*
0.001	1.00	1.378 57	0.725 39	−5.056 14	−3.272 43	−5.780 43	−2.508 00
0.050	1.00	1.394 51	0.717 10	−4.873 82	−3.146 12	−5.594 92	−2.448 81
0.100	1.00	1.415 50	0.706 46	−4.693 23	−3.028 77	−5.410 13	−2.381 36
0.150	1.00	1.435 41	0.696 66	−4.538 20	−2.927 53	−5.251 12	−2.323 59
0.200	1.00	1.451 99	0.688 71	−4.414 12	−2.842 69	−5.123 72	−2.281 03
0.250	1.00	1.462 41	0.683 80	−4.339 96	−2.775 07	−5.047 47	−2.272 40
0.300	1.00	1.465 55	0.682 34	−4.318 68	−2.725 15	−5.025 57	−2.300 43
0.350	1.00	1.466 89	0.681 71	−4.309 65	−2.688 21	−5.016 28	−2.328 07
0.400	1.00	1.467 45	0.681 45	−4.305 79	−2.662 70	−5.012 30	−2.349 60
0.450	1.00	1.467 51	0.681 43	−4.305 23	−2.647 88	−5.011 73	−2.363 85
0.500	1.00	1.467 17	0.681 59	−4.307 29	−2.643 37	−5.013 86	−2.370 49
0.550	1.00	1.466 46	0.681 91	−4.311 74	−2.649 05	−5.018 45	−2.369 40

Continued on next page

Continued: Results of the GCMC-Simulations of Mixture III at $p^* = 0.20$ and $T^* = 1.00$

x_1	T^*	v^*	ρ^*	u^*_{res}	h^*_{res}	g^*_{res}	s^*
0.600	1.00	1.465 38	0.682 42	−4.318 65	−2.665 02	−5.025 57	−2.360 55
0.650	1.00	1.463 86	0.683 12	−4.328 45	−2.691 65	−5.035 68	−2.344 03
0.700	1.00	1.461 74	0.684 12	−4.342 30	−2.729 60	−5.049 95	−2.320 35
0.750	1.00	1.458 47	0.685 65	−4.363 97	−2.780 13	−5.072 28	−2.292 15
0.800	1.00	1.450 44	0.689 44	−4.419 79	−2.846 90	−5.129 70	−2.282 80
0.850	1.00	1.434 66	0.697 03	−4.540 59	−2.932 21	−5.253 66	−2.321 45
0.900	1.00	1.416 92	0.705 76	−4.688 09	−3.031 92	−5.404 70	−2.372 78
0.950	1.00	1.397 26	0.715 69	−4.863 99	−3.147 21	−5.584 54	−2.437 32
0.999	1.00	1.377 82	0.725 78	−5.059 74	−3.275 33	−5.784 17	−2.508 85

Table C.17: Results of the GCMC-Simulations of Mixture III at $p^* = 0.20$ and $T^* = 1.05$

x_1	T^*	v^*	ρ^*	u^*_{res}	h^*_{res}	g^*_{res}	s^*
0.001	1.05	1.420 06	0.704 19	−4.882 07	−3.172 93	−5.648 06	−2.357 26
0.050	1.05	1.449 38	0.689 95	−4.663 45	−3.041 28	−5.423 57	−2.268 85
0.100	1.05	1.471 93	0.679 38	−4.487 91	−2.927 21	−5.243 53	−2.206 02
0.150	1.05	1.494 97	0.668 91	−4.332 12	−2.826 26	−5.083 12	−2.149 40
0.200	1.05	1.515 07	0.660 03	−4.203 37	−2.740 45	−4.950 35	−2.104 67
0.250	1.05	1.534 26	0.651 78	−4.094 42	−2.668 01	−4.837 57	−2.066 25
0.300	1.05	1.550 45	0.644 98	−4.007 69	−2.609 87	−4.747 61	−2.035 94
0.350	1.05	1.562 26	0.640 10	−3.945 82	−2.566 05	−4.683 36	−2.016 49
0.400	1.05	1.570 05	0.636 92	−3.905 33	−2.535 66	−4.641 32	−2.005 40
0.450	1.05	1.574 64	0.635 07	−3.881 65	−2.517 72	−4.616 73	−1.999 05
0.500	1.05	1.576 27	0.634 41	−3.873 23	−2.511 80	−4.607 98	−1.996 36
0.550	1.05	1.574 83	0.634 99	−3.880 53	−2.517 87	−4.615 56	−1.997 80
0.600	1.05	1.570 13	0.636 89	−3.904 54	−2.536 11	−4.640 51	−2.004 19
0.650	1.05	1.562 03	0.640 19	−3.946 35	−2.566 86	−4.683 94	−2.016 27
0.700	1.05	1.550 31	0.645 03	−4.008 16	−2.610 69	−4.748 10	−2.035 63
0.750	1.05	1.534 59	0.651 64	−4.093 49	−2.668 44	−4.836 57	−2.064 88
0.800	1.05	1.514 61	0.660 23	−4.204 85	−2.741 29	−4.951 92	−2.105 37
0.850	1.05	1.491 57	0.670 43	−4.341 29	−2.829 73	−5.092 97	−2.155 47

Continued on next page

Continued: Results of the GCMC-Simulations of Mixture III at $p^* = 0.20$ and $T^* = 1.05$

x_1	T^*	v^*	ρ^*	u^*_{res}	h^*_{res}	g^*_{res}	s^*
0.900	1.05	1.469 11	0.680 68	−4.495 38	−2.932 14	−5.251 56	−2.208 97
0.950	1.05	1.448 50	0.690 37	−4.666 13	−3.045 73	−5.426 43	−2.267 33
0.999	1.05	1.425 32	0.701 60	−4.863 68	−3.172 23	−5.628 62	−2.339 42

Table C.18: Results of the GCMC-Simulations of Mixture III at $p^* = 0.20$ and $T^* = 1.10$

x_1	T^*	v^*	ρ^*	u^*_{res}	h^*_{res}	g^*_{res}	s^*
0.001	1.10	1.469 84	0.680 35	−4.690 27	−3.064 87	−5.496 30	−2.210 39
0.050	1.10	1.505 80	0.664 10	−4.464 98	−2.932 42	−5.263 82	−2.119 46
0.100	1.10	1.537 05	0.650 60	−4.274 69	−2.816 52	−5.067 27	−2.046 14
0.150	1.10	1.568 63	0.637 50	−4.106 59	−2.715 32	−4.892 86	−1.979 59
0.200	1.10	1.595 48	0.626 77	−3.968 48	−2.630 36	−4.749 38	−1.926 38
0.250	1.10	1.620 30	0.617 17	−3.851 84	−2.558 41	−4.627 78	−1.881 24
0.300	1.10	1.642 27	0.608 91	−3.756 21	−2.499 56	−4.527 76	−1.843 82
0.350	1.10	1.660 34	0.602 29	−3.681 91	−2.453 89	−4.449 84	−1.814 50
0.400	1.10	1.673 32	0.597 61	−3.629 53	−2.421 67	−4.394 86	−1.793 81
0.450	1.10	1.680 08	0.595 21	−3.601 16	−2.403 18	−4.365 15	−1.783 61
0.500	1.10	1.681 40	0.594 74	−3.594 45	−2.397 68	−4.358 17	−1.782 26
0.550	1.10	1.678 15	0.595 90	−3.606 18	−2.404 64	−4.370 55	−1.787 19
0.600	1.10	1.670 40	0.598 66	−3.636 41	−2.424 12	−4.402 33	−1.798 37
0.650	1.10	1.658 35	0.603 01	−3.686 17	−2.456 15	−4.454 50	−1.816 68
0.700	1.10	1.642 10	0.608 98	−3.756 26	−2.501 07	−4.527 84	−1.842 52
0.750	1.10	1.621 21	0.616 82	−3.848 90	−2.559 79	−4.624 66	−1.877 15
0.800	1.10	1.596 39	0.626 41	−3.965 95	−2.632 43	−4.746 67	−1.922 03
0.850	1.10	1.571 03	0.636 52	−4.099 90	−2.717 24	−4.885 69	−1.971 32
0.900	1.10	1.542 06	0.648 48	−4.262 44	−2.816 26	−5.054 03	−2.034 33
0.950	1.10	1.505 07	0.664 42	−4.466 94	−2.935 48	−5.265 93	−2.118 59
0.999	1.10	1.475 86	0.677 57	−4.671 56	−3.062 84	−5.476 39	−2.194 14

Table C.19: Results of the GCMC-Simulations of Mixture III at $p^* = 0.20$ and $T^* = 1.15$

x_1	T^*	v^*	ρ^*	u^*_{res}	h^*_{res}	g^*_{res}	s^*
0.001	1.15	1.538 38	0.650 03	−4.457 71	−2.964 57	−5.300 03	−2.030 84
0.050	1.15	1.577 34	0.633 98	−4.241 08	−2.835 02	−5.075 61	−1.948 34
0.100	1.15	1.625 15	0.615 33	−4.024 56	−2.712 55	−4.849 53	−1.858 24
0.150	1.15	1.657 95	0.603 15	−3.864 84	−2.614 59	−4.683 25	−1.798 84
0.200	1.15	1.691 46	0.591 21	−3.723 79	−2.526 88	−4.535 49	−1.746 62
0.250	1.15	1.727 43	0.578 90	−3.594 09	−2.449 56	−4.398 60	−1.694 82
0.300	1.15	1.758 73	0.568 59	−3.488 65	−2.386 80	−4.286 91	−1.652 27
0.350	1.15	1.783 57	0.560 67	−3.408 37	−2.338 55	−4.201 66	−1.620 10
0.400	1.15	1.801 24	0.555 17	−3.352 67	−2.304 52	−4.142 42	−1.598 17
0.450	1.15	1.811 64	0.551 99	−3.320 12	−2.284 35	−4.107 79	−1.585 60
0.500	1.15	1.815 82	0.550 71	−3.307 89	−2.277 14	−4.094 72	−1.580 50
0.550	1.15	1.813 55	0.551 41	−3.316 11	−2.282 94	−4.103 40	−1.583 01
0.600	1.15	1.802 76	0.554 71	−3.349 28	−2.303 08	−4.138 73	−1.596 22
0.650	1.15	1.783 47	0.560 70	−3.408 15	−2.337 92	−4.201 45	−1.620 47
0.700	1.15	1.757 41	0.569 02	−3.491 08	−2.386 94	−4.289 60	−1.654 48
0.750	1.15	1.727 34	0.578 92	−3.594 82	−2.449 07	−4.399 35	−1.695 90
0.800	1.15	1.694 54	0.590 13	−3.717 71	−2.524 14	−4.528 80	−1.743 19
0.850	1.15	1.656 29	0.603 76	−3.869 62	−2.614 33	−4.688 36	−1.803 51
0.900	1.15	1.615 59	0.618 97	−4.046 85	−2.719 06	−4.873 74	−1.873 63
0.950	1.15	1.579 93	0.632 94	−4.234 30	−2.834 02	−5.068 32	−1.942 87
0.999	1.15	1.544 15	0.647 61	−4.443 04	−2.960 12	−5.284 21	−2.020 95

Table C.20: Results of the GCMC-Simulations of Mixture III at $p^* = 0.20$ and $T^* = 1.20$

x_1	T^*	v^*	ρ^*	u^*_{res}	h^*_{res}	g^*_{res}	s^*
0.001	1.20	1.608 33	0.621 76	−4.244 17	−2.862 73	−5.122 51	−1.883 15
0.050	1.20	1.655 34	0.604 10	−4.022 61	−2.732 05	−4.891 54	−1.799 57
0.100	1.20	1.721 96	0.580 73	−3.781 54	−2.600 91	−4.637 15	−1.696 87
0.150	1.20	1.774 96	0.563 39	−3.596 49	−2.494 43	−4.441 50	−1.622 55
0.200	1.20	1.831 95	0.545 87	−3.426 07	−2.397 69	−4.259 68	−1.551 65
0.250	1.20	1.882 07	0.531 33	−3.287 53	−2.317 16	−4.111 12	−1.494 96

Continued on next page

Continued: Results of the GCMC-Simulations of Mixture III at $p^* = 0.20$ and $T^* = 1.20$

x_1	T^*	v^*	ρ^*	u^*_{res}	h^*_{res}	g^*_{res}	s^*
0.300	1.20	1.928 20	0.518 62	−3.171 35	−2.249 65	−3.985 71	−1.446 71
0.350	1.20	1.967 08	0.508 37	−3.080 22	−2.196 38	−3.886 80	−1.408 68
0.400	1.20	1.996 32	0.500 92	−3.015 11	−2.158 08	−3.815 84	−1.381 47
0.450	1.20	2.016 37	0.495 94	−2.973 40	−2.133 91	−3.770 13	−1.363 52
0.500	1.20	2.024 41	0.493 97	−2.957 50	−2.125 20	−3.752 62	−1.356 18
0.550	1.20	2.017 05	0.495 77	−2.971 87	−2.133 62	−3.768 46	−1.362 36
0.600	1.20	1.996 82	0.500 80	−3.014 06	−2.157 77	−3.814 69	−1.380 77
0.650	1.20	1.966 98	0.508 39	−3.080 13	−2.196 37	−3.886 73	−1.408 63
0.700	1.20	1.927 53	0.518 80	−3.172 17	−2.250 00	−3.986 67	−1.447 22
0.750	1.20	1.880 87	0.531 67	−3.289 54	−2.317 98	−4.113 37	−1.496 16
0.800	1.20	1.828 75	0.546 82	−3.432 35	−2.400 39	−4.266 60	−1.555 18
0.850	1.20	1.775 64	0.563 18	−3.595 73	−2.495 28	−4.440 60	−1.621 10
0.900	1.20	1.725 89	0.579 41	−3.773 75	−2.599 79	−4.628 57	−1.690 65
0.950	1.20	1.669 98	0.598 81	−3.988 77	−2.721 82	−4.854 78	−1.777 46
0.999	1.20	1.616 95	0.618 45	−4.222 59	−2.855 03	−5.099 20	−1.870 14

C.3 Tabulated Results of the Vapor Liquid Equilibrium GCMC Simulations

This supporting information contains tables summarizing vapor liquid equilibrium data for the investigated model mixtures at several temperatures. The tables are structured by mixture and temperature. Tables C.21–C.25 thereby show the results of the model mixture consisting of two fluids with different energy parameters (Mixture I: $\varepsilon_{22}/\varepsilon_{11} = 0.7$), tables C.26–C.30 present the results of Mixture II with different diameters ($\sigma_{22}/\sigma_{11} = 1.5$), and tables C.31–C.34 give the results of the non-ideal mixture of two identical LJ-fluids ($k_{ij} = 0.25$).

The tables show the composition of the liquid x_2^{liq} and the vapor phase x_2^{vap}, the vapor pressure p^*_{sat}, and the liquid and vapor densities ($\rho^{*\text{liq}}$ & $\rho^{*\text{vap}}$). All results are given in reduced LJ units, according to table 4.1.

Table C.21: VLE-Data from GCMC-Simulations of Mixture I at $T^* = 0.90$

x_2^{vap}	x_2^{liq}	p^*_{sat}	$\rho^{*\text{vap}}$	$\rho^{*\text{liq}}$
0.006 21	0.001 00	0.010 10	0.012 18	0.739 21
0.008 20	0.025 00	0.010 11	0.012 19	0.703 46
0.010 05	0.050 00	0.010 03	0.012 10	0.673 65
0.018 88	0.075 00	0.009 70	0.011 68	0.642 22
0.039 26	0.100 00	0.009 26	0.011 14	0.619 78
0.046 54	0.125 00	0.009 13	0.010 99	0.592 76
0.072 18	0.150 00	0.008 77	0.010 55	0.571 32
0.088 86	0.175 00	0.008 59	0.010 35	0.548 61
0.096 67	0.200 00	0.008 51	0.010 26	0.525 80
0.103 03	0.225 00	0.008 43	0.010 17	0.504 88
0.110 63	0.250 00	0.008 33	0.010 05	0.485 85
0.119 55	0.275 00	0.008 21	0.009 91	0.467 81
0.128 52	0.300 00	0.008 09	0.009 76	0.450 64
0.141 66	0.325 00	0.007 91	0.009 54	0.435 09
0.162 70	0.350 00	0.007 64	0.009 22	0.421 38
0.178 42	0.375 00	0.007 46	0.009 00	0.408 11
0.192 64	0.400 00	0.007 30	0.008 81	0.395 35
0.211 09	0.425 00	0.007 11	0.008 57	0.383 36
0.232 49	0.450 00	0.006 89	0.008 32	0.372 15
0.253 01	0.475 00	0.006 71	0.008 09	0.361 47

Continued on next page

Continued: VLE-Data from GCMC-Simulations of Mixture I at $T^* = 0.90$

x_2^{vap}	x_2^{liq}	p^*_{sat}	$\rho^{*\mathrm{vap}}$	$\rho^{*\mathrm{liq}}$
0.274 70	0.500 00	0.006 52	0.007 87	0.351 37
0.298 19	0.525 00	0.006 33	0.007 64	0.341 90
0.321 50	0.550 00	0.006 15	0.007 43	0.332 93
0.345 35	0.575 00	0.005 99	0.007 23	0.324 40
0.371 91	0.600 00	0.005 81	0.007 02	0.316 31
0.401 08	0.625 00	0.005 63	0.006 81	0.308 51
0.430 64	0.650 00	0.005 46	0.006 60	0.300 96
0.460 02	0.675 00	0.005 31	0.006 42	0.293 69
0.491 43	0.700 00	0.005 15	0.006 23	0.286 70
0.525 52	0.725 00	0.004 99	0.006 04	0.279 91
0.559 79	0.750 00	0.004 84	0.005 87	0.273 38
0.594 30	0.775 00	0.004 70	0.005 70	0.267 27
0.630 95	0.800 00	0.004 56	0.005 53	0.261 57
0.671 30	0.825 00	0.004 41	0.005 36	0.256 11
0.714 48	0.850 00	0.004 27	0.005 19	0.250 75
0.758 48	0.875 00	0.004 13	0.005 03	0.245 50
0.803 43	0.900 00	0.004 01	0.004 88	0.240 37
0.849 92	0.925 00	0.003 88	0.004 74	0.235 36
0.898 18	0.950 00	0.003 76	0.004 60	0.230 36
0.946 33	0.975 00	0.003 65	0.004 46	0.225 41
0.997 85	0.999 00	0.003 54	0.004 33	0.220 90

Table C.22: VLE-Data from GCMC-Simulations of Mixture I at $T^* = 1.00$

x_2^{vap}	x_2^{liq}	p^*_{sat}	$\rho^{*\mathrm{vap}}$	$\rho^{*\mathrm{liq}}$
0.005 17	0.001 00	0.022 40	0.025 96	0.715 15
0.008 94	0.025 00	0.022 40	0.026 00	0.667 04
0.010 55	0.050 00	0.022 27	0.025 83	0.627 29
0.019 63	0.075 00	0.021 42	0.024 75	0.606 86
0.034 99	0.100 00	0.020 55	0.023 69	0.580 64
0.044 94	0.125 00	0.020 07	0.023 11	0.556 39

Continued on next page

Continued: VLE-Data from GCMC-Simulations of Mixture I at $T^* = 1.00$

x_2^{vap}	x_2^{liq}	p^*_{sat}	$\rho^{*\mathrm{vap}}$	$\rho^{*\mathrm{liq}}$
0.059 78	0.150 00	0.019 46	0.022 40	0.534 59
0.070 08	0.175 00	0.019 07	0.021 94	0.510 98
0.083 72	0.200 00	0.018 58	0.021 36	0.489 66
0.095 57	0.225 00	0.018 17	0.020 89	0.470 58
0.108 89	0.250 00	0.017 73	0.020 38	0.453 09
0.127 87	0.275 00	0.017 17	0.019 73	0.437 66
0.141 80	0.300 00	0.016 78	0.019 30	0.422 23
0.153 21	0.325 00	0.016 48	0.018 94	0.407 29
0.166 37	0.350 00	0.016 12	0.018 53	0.393 44
0.184 44	0.375 00	0.015 65	0.018 00	0.380 88
0.206 29	0.400 00	0.015 14	0.017 41	0.369 32
0.226 26	0.425 00	0.014 71	0.016 92	0.358 29
0.244 88	0.450 00	0.014 33	0.016 49	0.347 75
0.265 54	0.475 00	0.013 94	0.016 04	0.337 73
0.290 13	0.500 00	0.013 50	0.015 54	0.328 30
0.316 25	0.525 00	0.013 07	0.015 06	0.319 50
0.342 87	0.550 00	0.012 67	0.014 61	0.311 16
0.369 98	0.575 00	0.012 29	0.014 19	0.303 12
0.396 56	0.600 00	0.011 95	0.013 81	0.295 30
0.423 34	0.625 00	0.011 62	0.013 44	0.287 73
0.451 32	0.650 00	0.011 30	0.013 08	0.280 48
0.481 09	0.675 00	0.010 97	0.012 72	0.273 61
0.513 07	0.700 00	0.010 64	0.012 36	0.267 07
0.546 39	0.725 00	0.010 33	0.012 00	0.260 88
0.580 39	0.750 00	0.010 02	0.011 67	0.255 04
0.615 88	0.775 00	0.009 72	0.011 34	0.249 45
0.653 07	0.800 00	0.009 43	0.011 02	0.243 96
0.691 35	0.825 00	0.009 15	0.010 71	0.238 60
0.731 34	0.850 00	0.008 88	0.010 40	0.233 42
0.773 65	0.875 00	0.008 61	0.010 11	0.228 41
0.816 72	0.900 00	0.008 35	0.009 83	0.223 52
0.861 44	0.925 00	0.008 10	0.009 56	0.218 78

Continued on next page

Continued: VLE-Data from GCMC-Simulations of Mixture I at $T^* = 1.00$

x_2^{vap}	x_2^{liq}	p^*_{sat}	$\rho^{*\mathrm{vap}}$	$\rho^{*\mathrm{liq}}$
0.907 57	0.950 00	0.007 87	0.009 30	0.214 04
0.951 48	0.975 00	0.007 65	0.009 07	0.209 78
0.998 06	0.999 00	0.007 43	0.008 83	0.205 84

Table C.23: VLE-Data from GCMC-Simulations of Mixture I at $T^* = 1.05$

x_2^{vap}	x_2^{liq}	p^*_{sat}	$\rho^{*\mathrm{vap}}$	$\rho^{*\mathrm{liq}}$
0.003 18	0.001 00	0.031 88	0.036 97	0.669 96
0.007 22	0.025 00	0.031 83	0.036 98	0.636 22
0.014 21	0.050 00	0.031 06	0.035 98	0.606 91
0.022 61	0.075 00	0.030 20	0.034 87	0.583 29
0.032 99	0.100 00	0.029 31	0.033 74	0.558 91
0.041 31	0.125 00	0.028 64	0.032 91	0.531 74
0.051 60	0.150 00	0.027 83	0.031 91	0.508 22
0.065 62	0.175 00	0.026 86	0.030 73	0.488 85
0.084 53	0.200 00	0.025 79	0.029 45	0.471 86
0.101 25	0.225 00	0.025 00	0.028 52	0.454 74
0.114 25	0.250 00	0.024 43	0.027 86	0.437 30
0.126 34	0.275 00	0.023 90	0.027 25	0.420 45
0.139 76	0.300 00	0.023 34	0.026 59	0.404 87
0.156 76	0.325 00	0.022 65	0.025 80	0.391 06
0.177 48	0.350 00	0.021 90	0.024 93	0.378 63
0.198 66	0.375 00	0.021 21	0.024 14	0.366 72
0.217 88	0.400 00	0.020 62	0.023 48	0.355 17
0.236 06	0.425 00	0.020 10	0.022 89	0.344 30
0.256 38	0.450 00	0.019 55	0.022 27	0.334 24
0.280 39	0.475 00	0.018 94	0.021 58	0.324 79
0.305 03	0.500 00	0.018 36	0.020 94	0.315 62
0.328 64	0.525 00	0.017 85	0.020 37	0.306 77
0.352 69	0.550 00	0.017 36	0.019 82	0.298 45
0.378 91	0.575 00	0.016 85	0.019 27	0.290 66

Continued on next page

Continued: VLE-Data from GCMC-Simulations of Mixture I at $T^* = 1.05$

x_2^{vap}	x_2^{liq}	p^*_{sat}	ρ^{*vap}	ρ^{*liq}
0.407 74	0.600 00	0.016 33	0.018 70	0.283 27
0.438 42	0.625 00	0.015 82	0.018 15	0.276 22
0.469 46	0.650 00	0.015 35	0.017 63	0.269 51
0.499 76	0.675 00	0.014 92	0.017 17	0.263 08
0.530 13	0.700 00	0.014 51	0.016 73	0.256 89
0.561 78	0.725 00	0.014 11	0.016 30	0.250 95
0.594 63	0.750 00	0.013 71	0.015 87	0.245 24
0.628 01	0.775 00	0.013 33	0.015 46	0.239 75
0.662 18	0.800 00	0.012 96	0.015 07	0.234 50
0.698 08	0.825 00	0.012 59	0.014 67	0.229 51
0.736 00	0.850 00	0.012 22	0.014 27	0.224 75
0.775 51	0.875 00	0.011 85	0.013 87	0.220 16
0.817 97	0.900 00	0.011 49	0.013 47	0.215 73
0.862 22	0.925 00	0.011 13	0.013 09	0.211 28
0.906 58	0.950 00	0.010 79	0.012 73	0.206 70
0.952 59	0.975 00	0.010 47	0.012 38	0.202 61
0.998 09	0.999 00	0.010 16	0.012 05	0.199 48

Table C.24: VLE-Data from GCMC-Simulations of Mixture I at $T^* = 1.10$

x_2^{vap}	x_2^{liq}	p^*_{sat}	ρ^{*vap}	ρ^{*liq}
0.001 64	0.001 00	0.043 86	0.051 48	0.652 30
0.007 33	0.025 00	0.043 40	0.050 96	0.616 86
0.014 36	0.050 00	0.042 36	0.049 54	0.583 95
0.024 29	0.075 00	0.040 95	0.047 62	0.555 37
0.034 56	0.100 00	0.039 74	0.046 04	0.532 22
0.044 61	0.125 00	0.038 65	0.044 62	0.508 66
0.056 27	0.150 00	0.037 47	0.043 11	0.486 50
0.072 05	0.175 00	0.036 08	0.041 38	0.469 08
0.086 75	0.200 00	0.034 97	0.040 02	0.450 41
0.100 15	0.225 00	0.034 02	0.038 89	0.431 93

Continued on next page

Continued: VLE-Data from GCMC-Simulations of Mixture I at $T^* = 1.10$

x_2^{vap}	x_2^{liq}	p_{sat}^*	$\rho^{*\mathrm{vap}}$	$\rho^{*\mathrm{liq}}$
0.114 05	0.250 00	0.033 10	0.037 77	0.415 61
0.130 58	0.275 00	0.032 07	0.036 55	0.401 05
0.148 94	0.300 00	0.031 03	0.035 33	0.387 49
0.166 70	0.325 00	0.030 12	0.034 27	0.374 58
0.184 22	0.350 00	0.029 27	0.033 29	0.362 30
0.203 35	0.375 00	0.028 40	0.032 29	0.350 82
0.224 50	0.400 00	0.027 52	0.031 28	0.340 03
0.246 80	0.425 00	0.026 66	0.030 31	0.329 66
0.270 20	0.450 00	0.025 83	0.029 38	0.319 81
0.293 99	0.475 00	0.025 05	0.028 52	0.310 53
0.318 08	0.500 00	0.024 32	0.027 71	0.301 80
0.342 97	0.525 00	0.023 61	0.026 94	0.293 51
0.368 61	0.550 00	0.022 93	0.026 19	0.285 59
0.395 27	0.575 00	0.022 27	0.025 47	0.277 99
0.423 15	0.600 00	0.021 62	0.024 77	0.270 71
0.451 98	0.625 00	0.020 99	0.024 10	0.263 77
0.481 45	0.650 00	0.020 39	0.023 45	0.257 23
0.511 58	0.675 00	0.019 81	0.022 84	0.251 04
0.542 61	0.700 00	0.019 25	0.022 24	0.245 12
0.574 92	0.725 00	0.018 70	0.021 66	0.239 38
0.608 85	0.750 00	0.018 16	0.021 09	0.233 81
0.643 94	0.775 00	0.017 64	0.020 54	0.228 44
0.679 38	0.800 00	0.017 14	0.020 02	0.223 31
0.715 14	0.825 00	0.016 66	0.019 53	0.218 42
0.751 67	0.850 00	0.016 20	0.019 05	0.213 74
0.789 75	0.875 00	0.015 75	0.018 57	0.209 30
0.830 16	0.900 00	0.015 29	0.018 10	0.205 08
0.871 51	0.925 00	0.014 86	0.017 64	0.201 04
0.912 63	0.950 00	0.014 45	0.017 22	0.197 16
0.954 74	0.975 00	0.014 04	0.016 80	0.193 48
0.998 16	0.999 00	0.013 63	0.016 36	0.190 03

Table C.25: VLE-Data from GCMC-Simulations of Mixture I at $T^* = 1.15$

x_2^{vap}	x_2^{liq}	p^*_{sat}	$\rho^{*\mathrm{vap}}$	$\rho^{*\mathrm{liq}}$
0.001 20	0.001 00	0.057 49	0.069 07	0.631 73
0.009 02	0.025 00	0.056 46	0.067 71	0.585 50
0.016 98	0.050 00	0.055 15	0.065 86	0.554 47
0.025 92	0.075 00	0.053 60	0.063 60	0.526 94
0.037 67	0.100 00	0.051 76	0.060 99	0.505 54
0.050 62	0.125 00	0.050 05	0.058 65	0.484 33
0.064 20	0.150 00	0.048 45	0.056 53	0.463 55
0.077 90	0.175 00	0.046 98	0.054 63	0.444 64
0.092 65	0.200 00	0.045 54	0.052 79	0.427 37
0.107 07	0.225 00	0.044 22	0.051 15	0.410 62
0.122 56	0.250 00	0.042 90	0.049 51	0.395 01
0.139 72	0.275 00	0.041 54	0.047 85	0.380 78
0.159 17	0.300 00	0.040 14	0.046 18	0.368 01
0.179 53	0.325 00	0.038 82	0.044 64	0.356 06
0.200 07	0.350 00	0.037 61	0.043 24	0.344 63
0.221 01	0.375 00	0.036 47	0.041 95	0.333 54
0.242 08	0.400 00	0.035 41	0.040 75	0.322 88
0.263 76	0.425 00	0.034 38	0.039 60	0.312 95
0.286 41	0.450 00	0.033 38	0.038 49	0.303 70
0.309 80	0.475 00	0.032 41	0.037 42	0.294 88
0.334 54	0.500 00	0.031 45	0.036 37	0.286 41
0.360 52	0.525 00	0.030 52	0.035 36	0.278 33
0.386 79	0.550 00	0.029 63	0.034 41	0.270 66
0.413 74	0.575 00	0.028 78	0.033 50	0.263 46
0.441 80	0.600 00	0.027 95	0.032 61	0.256 65
0.470 45	0.625 00	0.027 16	0.031 77	0.250 10
0.499 66	0.650 00	0.026 40	0.030 97	0.243 79
0.529 98	0.675 00	0.025 65	0.030 18	0.237 75
0.561 49	0.700 00	0.024 92	0.029 42	0.231 96
0.593 90	0.725 00	0.024 22	0.028 69	0.226 41
0.627 07	0.750 00	0.023 54	0.028 00	0.221 07
0.661 13	0.775 00	0.022 89	0.027 33	0.215 93

Continued on next page

Continued: VLE-Data from GCMC-Simulations of Mixture I at $T^* = 1.15$

x_2^{vap}	x_2^{liq}	p_{sat}^*	$\rho^{*\mathrm{vap}}$	$\rho^{*\mathrm{liq}}$
0.696 09	0.800 00	0.022 25	0.026 69	0.210 96
0.731 57	0.825 00	0.021 65	0.026 08	0.206 12
0.767 50	0.850 00	0.021 06	0.025 50	0.201 44
0.804 41	0.875 00	0.020 50	0.024 94	0.196 93
0.842 27	0.900 00	0.019 95	0.024 39	0.192 58
0.881 65	0.925 00	0.019 41	0.023 87	0.188 41
0.920 64	0.950 00	0.018 92	0.023 39	0.184 38
0.959 47	0.975 00	0.018 44	0.022 94	0.180 67
0.998 33	0.999 00	0.017 97	0.022 48	0.177 42

Table C.26: VLE-Data from GCMC-Simulations of Mixture II at $T^* = 0.90$

x_2^{vap}	x_2^{liq}	p_{sat}^*	$\rho^{*\mathrm{vap}}$	$\rho^{*\mathrm{liq}}$
0.006 21	0.001 00	0.010 10	0.012 18	0.739 21
0.008 20	0.025 00	0.010 11	0.012 19	0.703 46
0.010 05	0.050 00	0.010 03	0.012 10	0.673 65
0.018 88	0.075 00	0.009 70	0.011 68	0.642 22
0.039 26	0.100 00	0.009 26	0.011 14	0.619 78
0.046 54	0.125 00	0.009 13	0.010 99	0.592 76
0.072 18	0.150 00	0.008 77	0.010 55	0.571 32
0.088 86	0.175 00	0.008 59	0.010 35	0.548 61
0.096 67	0.200 00	0.008 51	0.010 26	0.525 80
0.103 03	0.225 00	0.008 43	0.010 17	0.504 88
0.110 63	0.250 00	0.008 33	0.010 05	0.485 85
0.119 55	0.275 00	0.008 21	0.009 91	0.467 81
0.128 52	0.300 00	0.008 09	0.009 76	0.450 64
0.141 66	0.325 00	0.007 91	0.009 54	0.435 09
0.162 70	0.350 00	0.007 64	0.009 22	0.421 38
0.178 42	0.375 00	0.007 46	0.009 00	0.408 11
0.192 64	0.400 00	0.007 30	0.008 81	0.395 35
0.211 09	0.425 00	0.007 11	0.008 57	0.383 36

Continued on next page

Continued: VLE-Data from GCMC-Simulations of Mixture II at $T^* = 0.90$

x_2^{vap}	x_2^{liq}	p^*_{sat}	$\rho^{*\mathrm{vap}}$	$\rho^{*\mathrm{liq}}$
0.232 49	0.450 00	0.006 89	0.008 32	0.372 15
0.253 01	0.475 00	0.006 71	0.008 09	0.361 47
0.274 70	0.500 00	0.006 52	0.007 87	0.351 37
0.298 19	0.525 00	0.006 33	0.007 64	0.341 90
0.321 50	0.550 00	0.006 15	0.007 43	0.332 93
0.345 35	0.575 00	0.005 99	0.007 23	0.324 40
0.371 91	0.600 00	0.005 81	0.007 02	0.316 31
0.401 08	0.625 00	0.005 63	0.006 81	0.308 51
0.430 64	0.650 00	0.005 46	0.006 60	0.300 96
0.460 02	0.675 00	0.005 31	0.006 42	0.293 69
0.491 43	0.700 00	0.005 15	0.006 23	0.286 70
0.525 52	0.725 00	0.004 99	0.006 04	0.279 91
0.559 79	0.750 00	0.004 84	0.005 87	0.273 38
0.594 30	0.775 00	0.004 70	0.005 70	0.267 27
0.630 95	0.800 00	0.004 56	0.005 53	0.261 57
0.671 30	0.825 00	0.004 41	0.005 36	0.256 11
0.714 48	0.850 00	0.004 27	0.005 19	0.250 75
0.758 48	0.875 00	0.004 13	0.005 03	0.245 50
0.803 43	0.900 00	0.004 01	0.004 88	0.240 37
0.849 92	0.925 00	0.003 88	0.004 74	0.235 36
0.898 18	0.950 00	0.003 76	0.004 60	0.230 36
0.946 33	0.975 00	0.003 65	0.004 46	0.225 41
0.997 85	0.999 00	0.003 54	0.004 33	0.220 90

Table C.27: VLE-Data from GCMC-Simulations of Mixture II at $T^* = 1.00$

x_2^{vap}	x_2^{liq}	p^*_{sat}	$\rho^{*\mathrm{vap}}$	$\rho^{*\mathrm{liq}}$
0.005 17	0.001 00	0.022 40	0.025 96	0.715 15
0.008 94	0.025 00	0.022 40	0.026 00	0.667 04
0.010 55	0.050 00	0.022 27	0.025 83	0.627 29
0.019 63	0.075 00	0.021 42	0.024 75	0.606 86

Continued on next page

Continued: VLE-Data from GCMC-Simulations of Mixture II at $T^* = 1.00$

x_2^{vap}	x_2^{liq}	p^*_{sat}	$\rho^{*\mathrm{vap}}$	$\rho^{*\mathrm{liq}}$
0.034 99	0.100 00	0.020 55	0.023 69	0.580 64
0.044 94	0.125 00	0.020 07	0.023 11	0.556 39
0.059 78	0.150 00	0.019 46	0.022 40	0.534 59
0.070 08	0.175 00	0.019 07	0.021 94	0.510 98
0.083 72	0.200 00	0.018 58	0.021 36	0.489 66
0.095 57	0.225 00	0.018 17	0.020 89	0.470 58
0.108 89	0.250 00	0.017 73	0.020 38	0.453 09
0.127 87	0.275 00	0.017 17	0.019 73	0.437 66
0.141 80	0.300 00	0.016 78	0.019 30	0.422 23
0.153 21	0.325 00	0.016 48	0.018 94	0.407 29
0.166 37	0.350 00	0.016 12	0.018 53	0.393 44
0.184 44	0.375 00	0.015 65	0.018 00	0.380 88
0.206 29	0.400 00	0.015 14	0.017 41	0.369 32
0.226 26	0.425 00	0.014 71	0.016 92	0.358 29
0.244 88	0.450 00	0.014 33	0.016 49	0.347 75
0.265 54	0.475 00	0.013 94	0.016 04	0.337 73
0.290 13	0.500 00	0.013 50	0.015 54	0.328 30
0.316 25	0.525 00	0.013 07	0.015 06	0.319 50
0.342 87	0.550 00	0.012 67	0.014 61	0.311 16
0.369 98	0.575 00	0.012 29	0.014 19	0.303 12
0.396 56	0.600 00	0.011 95	0.013 81	0.295 30
0.423 34	0.625 00	0.011 62	0.013 44	0.287 73
0.451 32	0.650 00	0.011 30	0.013 08	0.280 48
0.481 09	0.675 00	0.010 97	0.012 72	0.273 61
0.513 07	0.700 00	0.010 64	0.012 36	0.267 07
0.546 39	0.725 00	0.010 33	0.012 00	0.260 88
0.580 39	0.750 00	0.010 02	0.011 67	0.255 04
0.615 88	0.775 00	0.009 72	0.011 34	0.249 45
0.653 07	0.800 00	0.009 43	0.011 02	0.243 96
0.691 35	0.825 00	0.009 15	0.010 71	0.238 60
0.731 34	0.850 00	0.008 88	0.010 40	0.233 42
0.773 65	0.875 00	0.008 61	0.010 11	0.228 41

Continued on next page

Continued: VLE-Data from GCMC-Simulations of Mixture II at $T^* = 1.00$

x_2^{vap}	x_2^{liq}	p^*_{sat}	$\rho^{*\mathrm{vap}}$	$\rho^{*\mathrm{liq}}$
0.816 72	0.900 00	0.008 35	0.009 83	0.223 52
0.861 44	0.925 00	0.008 10	0.009 56	0.218 78
0.907 57	0.950 00	0.007 87	0.009 30	0.214 04
0.951 48	0.975 00	0.007 65	0.009 07	0.209 78
0.998 06	0.999 00	0.007 43	0.008 83	0.205 84

Table C.28: VLE-Data from GCMC-Simulations of Mixture II at $T^* = 1.05$

x_2^{vap}	x_2^{liq}	p^*_{sat}	$\rho^{*\mathrm{vap}}$	$\rho^{*\mathrm{liq}}$
0.003 18	0.001 00	0.031 88	0.036 97	0.669 96
0.007 22	0.025 00	0.031 83	0.036 98	0.636 22
0.014 21	0.050 00	0.031 06	0.035 98	0.606 91
0.022 61	0.075 00	0.030 20	0.034 87	0.583 29
0.032 99	0.100 00	0.029 31	0.033 74	0.558 91
0.041 31	0.125 00	0.028 64	0.032 91	0.531 74
0.051 60	0.150 00	0.027 83	0.031 91	0.508 22
0.065 62	0.175 00	0.026 86	0.030 73	0.488 85
0.084 53	0.200 00	0.025 79	0.029 45	0.471 86
0.101 25	0.225 00	0.025 00	0.028 52	0.454 74
0.114 25	0.250 00	0.024 43	0.027 86	0.437 30
0.126 34	0.275 00	0.023 90	0.027 25	0.420 45
0.139 76	0.300 00	0.023 34	0.026 59	0.404 87
0.156 76	0.325 00	0.022 65	0.025 80	0.391 06
0.177 48	0.350 00	0.021 90	0.024 93	0.378 63
0.198 66	0.375 00	0.021 21	0.024 14	0.366 72
0.217 88	0.400 00	0.020 62	0.023 48	0.355 17
0.236 06	0.425 00	0.020 10	0.022 89	0.344 30
0.256 38	0.450 00	0.019 55	0.022 27	0.334 24
0.280 39	0.475 00	0.018 94	0.021 58	0.324 79
0.305 03	0.500 00	0.018 36	0.020 94	0.315 62
0.328 64	0.525 00	0.017 85	0.020 37	0.306 77

Continued on next page

Continued: VLE-Data from GCMC-Simulations of Mixture II at $T^* = 1.05$

x_2^{vap}	x_2^{liq}	p^*_{sat}	$\rho^{*\mathrm{vap}}$	$\rho^{*\mathrm{liq}}$
0.352 69	0.550 00	0.017 36	0.019 82	0.298 45
0.378 91	0.575 00	0.016 85	0.019 27	0.290 66
0.407 74	0.600 00	0.016 33	0.018 70	0.283 27
0.438 42	0.625 00	0.015 82	0.018 15	0.276 22
0.469 46	0.650 00	0.015 35	0.017 63	0.269 51
0.499 76	0.675 00	0.014 92	0.017 17	0.263 08
0.530 13	0.700 00	0.014 51	0.016 73	0.256 89
0.561 78	0.725 00	0.014 11	0.016 30	0.250 95
0.594 63	0.750 00	0.013 71	0.015 87	0.245 24
0.628 01	0.775 00	0.013 33	0.015 46	0.239 75
0.662 18	0.800 00	0.012 96	0.015 07	0.234 50
0.698 08	0.825 00	0.012 59	0.014 67	0.229 51
0.736 00	0.850 00	0.012 22	0.014 27	0.224 75
0.775 51	0.875 00	0.011 85	0.013 87	0.220 16
0.817 97	0.900 00	0.011 49	0.013 47	0.215 73
0.862 22	0.925 00	0.011 13	0.013 09	0.211 28
0.906 58	0.950 00	0.010 79	0.012 73	0.206 70
0.952 59	0.975 00	0.010 47	0.012 38	0.202 61
0.998 09	0.999 00	0.010 16	0.012 05	0.199 48

Table C.29: VLE-Data from GCMC-Simulations of Mixture II at $T^* = 1.10$

x_2^{vap}	x_2^{liq}	p^*_{sat}	$\rho^{*\mathrm{vap}}$	$\rho^{*\mathrm{liq}}$
0.001 64	0.001 00	0.043 86	0.051 48	0.652 30
0.007 33	0.025 00	0.043 40	0.050 96	0.616 86
0.014 36	0.050 00	0.042 36	0.049 54	0.583 95
0.024 29	0.075 00	0.040 95	0.047 62	0.555 37
0.034 56	0.100 00	0.039 74	0.046 04	0.532 22
0.044 61	0.125 00	0.038 65	0.044 62	0.508 66
0.056 27	0.150 00	0.037 47	0.043 11	0.486 50
0.072 05	0.175 00	0.036 08	0.041 38	0.469 08

Continued on next page

Continued: VLE-Data from GCMC-Simulations of Mixture II at $T^* = 1.10$

x_2^{vap}	x_2^{liq}	p^*_{sat}	$\rho^{*\mathrm{vap}}$	$\rho^{*\mathrm{liq}}$
0.086 75	0.200 00	0.034 97	0.040 02	0.450 41
0.100 15	0.225 00	0.034 02	0.038 89	0.431 93
0.114 05	0.250 00	0.033 10	0.037 77	0.415 61
0.130 58	0.275 00	0.032 07	0.036 55	0.401 05
0.148 94	0.300 00	0.031 03	0.035 33	0.387 49
0.166 70	0.325 00	0.030 12	0.034 27	0.374 58
0.184 22	0.350 00	0.029 27	0.033 29	0.362 30
0.203 35	0.375 00	0.028 40	0.032 29	0.350 82
0.224 50	0.400 00	0.027 52	0.031 28	0.340 03
0.246 80	0.425 00	0.026 66	0.030 31	0.329 66
0.270 20	0.450 00	0.025 83	0.029 38	0.319 81
0.293 99	0.475 00	0.025 05	0.028 52	0.310 53
0.318 08	0.500 00	0.024 32	0.027 71	0.301 80
0.342 97	0.525 00	0.023 61	0.026 94	0.293 51
0.368 61	0.550 00	0.022 93	0.026 19	0.285 59
0.395 27	0.575 00	0.022 27	0.025 47	0.277 99
0.423 15	0.600 00	0.021 62	0.024 77	0.270 71
0.451 98	0.625 00	0.020 99	0.024 10	0.263 77
0.481 45	0.650 00	0.020 39	0.023 45	0.257 23
0.511 58	0.675 00	0.019 81	0.022 84	0.251 04
0.542 61	0.700 00	0.019 25	0.022 24	0.245 12
0.574 92	0.725 00	0.018 70	0.021 66	0.239 38
0.608 85	0.750 00	0.018 16	0.021 09	0.233 81
0.643 94	0.775 00	0.017 64	0.020 54	0.228 44
0.679 38	0.800 00	0.017 14	0.020 02	0.223 31
0.715 14	0.825 00	0.016 66	0.019 53	0.218 42
0.751 67	0.850 00	0.016 20	0.019 05	0.213 74
0.789 75	0.875 00	0.015 75	0.018 57	0.209 30
0.830 16	0.900 00	0.015 29	0.018 10	0.205 08
0.871 51	0.925 00	0.014 86	0.017 64	0.201 04
0.912 63	0.950 00	0.014 45	0.017 22	0.197 16
0.954 74	0.975 00	0.014 04	0.016 80	0.193 48

Continued on next page

Continued: VLE-Data from GCMC-Simulations of Mixture II at $T^* = 1.10$

x_2^{vap}	x_2^{liq}	p^*_{sat}	$\rho^{*\mathrm{vap}}$	$\rho^{*\mathrm{liq}}$
0.998 16	0.999 00	0.013 63	0.016 36	0.190 03

Table C.30: VLE-Data from GCMC-Simulations of Mixture II at $T^* = 1.15$

x_2^{vap}	x_2^{liq}	p^*_{sat}	$\rho^{*\mathrm{vap}}$	$\rho^{*\mathrm{liq}}$
0.001 20	0.001 00	0.057 49	0.069 07	0.631 73
0.009 02	0.025 00	0.056 46	0.067 71	0.585 50
0.016 98	0.050 00	0.055 15	0.065 86	0.554 47
0.025 92	0.075 00	0.053 60	0.063 60	0.526 94
0.037 67	0.100 00	0.051 76	0.060 99	0.505 54
0.050 62	0.125 00	0.050 05	0.058 65	0.484 33
0.064 20	0.150 00	0.048 45	0.056 53	0.463 55
0.077 90	0.175 00	0.046 98	0.054 63	0.444 64
0.092 65	0.200 00	0.045 54	0.052 79	0.427 37
0.107 07	0.225 00	0.044 22	0.051 15	0.410 62
0.122 56	0.250 00	0.042 90	0.049 51	0.395 01
0.139 72	0.275 00	0.041 54	0.047 85	0.380 78
0.159 17	0.300 00	0.040 14	0.046 18	0.368 01
0.179 53	0.325 00	0.038 82	0.044 64	0.356 06
0.200 07	0.350 00	0.037 61	0.043 24	0.344 63
0.221 01	0.375 00	0.036 47	0.041 95	0.333 54
0.242 08	0.400 00	0.035 41	0.040 75	0.322 88
0.263 76	0.425 00	0.034 38	0.039 60	0.312 95
0.286 41	0.450 00	0.033 38	0.038 49	0.303 70
0.309 80	0.475 00	0.032 41	0.037 42	0.294 88
0.334 54	0.500 00	0.031 45	0.036 37	0.286 41
0.360 52	0.525 00	0.030 52	0.035 36	0.278 33
0.386 79	0.550 00	0.029 63	0.034 41	0.270 66
0.413 74	0.575 00	0.028 78	0.033 50	0.263 46
0.441 80	0.600 00	0.027 95	0.032 61	0.256 65
0.470 45	0.625 00	0.027 16	0.031 77	0.250 10

Continued on next page

Continued: VLE-Data from GCMC-Simulations of Mixture II at $T^* = 1.15$

x_2^{vap}	x_2^{liq}	p^*_{sat}	$\rho^{*\text{vap}}$	$\rho^{*\text{liq}}$
0.499 66	0.650 00	0.026 40	0.030 97	0.243 79
0.529 98	0.675 00	0.025 65	0.030 18	0.237 75
0.561 49	0.700 00	0.024 92	0.029 42	0.231 96
0.593 90	0.725 00	0.024 22	0.028 69	0.226 41
0.627 07	0.750 00	0.023 54	0.028 00	0.221 07
0.661 13	0.775 00	0.022 89	0.027 33	0.215 93
0.696 09	0.800 00	0.022 25	0.026 69	0.210 96
0.731 57	0.825 00	0.021 65	0.026 08	0.206 12
0.767 50	0.850 00	0.021 06	0.025 50	0.201 44
0.804 41	0.875 00	0.020 50	0.024 94	0.196 93
0.842 27	0.900 00	0.019 95	0.024 39	0.192 58
0.881 65	0.925 00	0.019 41	0.023 87	0.188 41
0.920 64	0.950 00	0.018 92	0.023 39	0.184 38
0.959 47	0.975 00	0.018 44	0.022 94	0.180 67
0.998 33	0.999 00	0.017 97	0.022 48	0.177 42

Table C.31: VLE-Data from GCMC-Simulations of Mixture III at $T^* = 1.00$

x_2^{vap}	x_2^{liq}	p^*_{sat}	$\rho^{*\text{vap}}$	$\rho^{*\text{liq}}$
0.004 45	0.001 00	0.024 76	0.029 25	0.700 50
0.101 71	0.025 00	0.027 29	0.032 53	0.696 54
0.188 60	0.050 00	0.030 09	0.036 26	0.692 97
0.256 02	0.075 00	0.032 65	0.039 75	0.687 51
0.311 53	0.100 00	0.035 08	0.043 15	0.681 94
0.364 91	0.125 00	0.037 78	0.047 02	0.678 64
0.410 41	0.150 00	0.040 43	0.050 96	0.675 71
0.449 89	0.175 00	0.043 06	0.055 00	0.671 22
0.482 25	0.200 00	0.045 48	0.058 83	0.664 75
0.511 77	0.225 00	0.047 91	0.062 80	0.658 32
0.539 57	0.250 00	0.050 43	0.067 04	0.652 73
0.562 08	0.275 00	0.052 65	0.070 87	0.647 05

Continued on next page

Continued: VLE-Data from GCMC-Simulations of Mixture III at $T^* = 1.00$

x_2^{vap}	x_2^{liq}	p_{sat}^*	ρ^{*vap}	ρ^{*liq}
0.583 98	0.300 00	0.054 95	0.074 98	0.641 36
0.606 23	0.325 00	0.057 49	0.079 64	0.635 67
0.626 57	0.350 00	0.060 02	0.084 42	0.629 35
0.643 63	0.375 00	0.062 30	0.088 86	0.622 31
0.658 77	0.400 00	0.064 44	0.093 13	0.614 65
0.672 90	0.425 00	0.066 53	0.097 41	0.606 51
0.686 50	0.450 00	0.068 62	0.101 86	0.598 69
0.700 61	0.475 00	0.070 88	0.106 91	0.591 63
0.715 31	0.500 00	0.073 37	0.112 86	0.584 23
0.729 04	0.525 00	0.075 87	0.119 32	0.575 43
0.741 15	0.550 00	0.078 22	0.125 94	0.566 10
0.752 47	0.575 00	0.080 55	0.133 15	0.556 77
0.763 50	0.600 00	0.083 00	0.141 60	0.546 67
0.773 51	0.625 00	0.085 41	0.151 14	0.534 50
0.782 53	0.650 00	0.087 73	0.161 34	0.519 62
0.790 82	0.675 00	0.090 05	0.173 25	0.502 94
0.681 54	0.681 54	0.013 19	0.013 88	0.013 88
0.799 27	0.700 00	0.092 39	0.185 62	0.484 50
0.614 76	0.725 00	0.012 27	0.012 88	0.018 80

Table C.32: VLE-Data from GCMC-Simulations of Mixture III at $T^* = 1.05$

x_2^{vap}	x_2^{liq}	p_{sat}^*	ρ^{*vap}	ρ^{*liq}
0.004 08	0.001 08	0.033 89	0.039 86	0.674 21
0.010 74	0.002 84	0.034 11	0.040 15	0.674 18
0.017 33	0.004 59	0.034 33	0.040 45	0.674 18
0.023 83	0.006 34	0.034 56	0.040 74	0.674 20
0.030 27	0.008 09	0.034 78	0.041 04	0.674 21
0.036 62	0.009 83	0.035 00	0.041 33	0.674 21
0.042 91	0.011 57	0.035 22	0.041 63	0.674 18
0.049 13	0.013 34	0.035 45	0.041 93	0.674 11

Continued on next page

Continued: VLE-Data from GCMC-Simulations of Mixture III at $T^* = 1.05$

x_2^{vap}	x_2^{liq}	p^*_{sat}	$\rho^{*\mathrm{vap}}$	$\rho^{*\mathrm{liq}}$
0.055 27	0.015 14	0.035 67	0.042 23	0.674 00
0.061 35	0.016 96	0.035 89	0.042 53	0.673 85
0.067 36	0.018 81	0.036 12	0.042 83	0.673 67
0.073 31	0.020 66	0.036 34	0.043 13	0.673 45
0.079 19	0.022 50	0.036 56	0.043 43	0.673 20
0.085 01	0.024 28	0.036 79	0.043 73	0.672 92
0.090 76	0.026 00	0.037 01	0.044 03	0.672 64
0.096 46	0.027 63	0.037 24	0.044 34	0.672 34
0.102 08	0.029 16	0.037 46	0.044 65	0.672 03
0.107 65	0.030 59	0.037 69	0.044 95	0.671 71
0.113 15	0.031 94	0.037 92	0.045 27	0.671 38
0.118 59	0.033 24	0.038 14	0.045 58	0.671 03
0.123 97	0.034 51	0.038 37	0.045 90	0.670 66
0.129 29	0.035 79	0.038 61	0.046 22	0.670 26
0.134 55	0.037 12	0.038 84	0.046 54	0.669 83
0.139 75	0.038 53	0.039 07	0.046 86	0.669 35
0.144 89	0.040 07	0.039 31	0.047 19	0.668 83
0.149 98	0.041 75	0.039 54	0.047 51	0.668 25
0.155 01	0.043 58	0.039 78	0.047 84	0.667 63
0.160 00	0.045 57	0.040 01	0.048 17	0.666 96
0.164 93	0.047 69	0.040 25	0.048 50	0.666 27
0.169 81	0.049 91	0.040 48	0.048 83	0.665 58
0.174 65	0.052 19	0.040 71	0.049 15	0.664 89
0.179 45	0.054 48	0.040 95	0.049 48	0.664 22
0.184 20	0.056 74	0.041 18	0.049 81	0.663 59
0.188 90	0.058 96	0.041 41	0.050 13	0.663 01
0.193 56	0.061 10	0.041 64	0.050 46	0.662 48
0.198 18	0.063 18	0.041 87	0.050 79	0.661 99
0.202 75	0.065 18	0.042 10	0.051 11	0.661 54
0.207 28	0.067 13	0.042 33	0.051 44	0.661 14
0.211 77	0.069 03	0.042 56	0.051 77	0.660 76
0.216 22	0.070 89	0.042 80	0.052 10	0.660 41

Continued on next page

Continued: VLE-Data from GCMC-Simulations of Mixture III at $T^* = 1.05$

x_2^{vap}	x_2^{liq}	p_{sat}^*	$\rho^{*\mathrm{vap}}$	$\rho^{*\mathrm{liq}}$
0.220 62	0.072 72	0.043 03	0.052 43	0.660 08
0.224 98	0.074 54	0.043 26	0.052 77	0.659 76
0.229 31	0.076 35	0.043 49	0.053 10	0.659 44
0.233 59	0.078 17	0.043 72	0.053 44	0.659 13
0.237 83	0.079 99	0.043 96	0.053 77	0.658 81
0.242 03	0.081 82	0.044 19	0.054 11	0.658 49
0.246 20	0.083 66	0.044 42	0.054 45	0.658 15
0.250 33	0.085 52	0.044 66	0.054 79	0.657 81
0.254 42	0.087 40	0.044 89	0.055 13	0.657 45
0.258 47	0.089 29	0.045 12	0.055 48	0.657 07
0.262 49	0.091 19	0.045 36	0.055 82	0.656 68
0.266 48	0.093 11	0.045 59	0.056 17	0.656 27
0.270 43	0.095 03	0.045 83	0.056 51	0.655 85
0.274 34	0.096 95	0.046 06	0.056 86	0.655 40
0.278 22	0.098 88	0.046 30	0.057 21	0.654 94
0.282 07	0.100 82	0.046 53	0.057 56	0.654 47
0.285 89	0.102 75	0.046 77	0.057 92	0.653 98
0.289 67	0.104 69	0.047 01	0.058 27	0.653 47
0.293 42	0.106 63	0.047 24	0.058 63	0.652 96
0.297 14	0.108 57	0.047 48	0.058 98	0.652 42
0.300 83	0.110 52	0.047 72	0.059 34	0.651 88
0.304 49	0.112 48	0.047 95	0.059 70	0.651 33
0.308 12	0.114 44	0.048 19	0.060 06	0.650 77
0.311 72	0.116 42	0.048 43	0.060 42	0.650 21
0.315 28	0.118 40	0.048 67	0.060 79	0.649 64
0.318 82	0.120 39	0.048 90	0.061 15	0.649 08
0.322 33	0.122 39	0.049 14	0.061 52	0.648 52
0.325 81	0.124 39	0.049 38	0.061 89	0.647 96
0.329 26	0.126 39	0.049 62	0.062 25	0.647 42
0.332 68	0.128 40	0.049 86	0.062 62	0.646 88
0.336 07	0.130 39	0.050 10	0.063 00	0.646 36
0.339 44	0.132 38	0.050 34	0.063 37	0.645 86

Continued on next page

Continued: VLE-Data from GCMC-Simulations of Mixture III at $T^* = 1.05$

x_2^{vap}	x_2^{liq}	p^*_{sat}	$\rho^{*\mathrm{vap}}$	$\rho^{*\mathrm{liq}}$
0.342 78	0.134 35	0.050 58	0.063 74	0.645 37
0.346 09	0.136 31	0.050 82	0.064 12	0.644 89
0.349 37	0.138 24	0.051 06	0.064 50	0.644 44
0.352 63	0.140 16	0.051 30	0.064 88	0.643 99
0.355 86	0.142 06	0.051 54	0.065 26	0.643 56
0.359 06	0.143 94	0.051 78	0.065 64	0.643 14
0.362 23	0.145 81	0.052 02	0.066 02	0.642 73
0.365 38	0.147 67	0.052 26	0.066 40	0.642 33
0.368 51	0.149 52	0.052 51	0.066 79	0.641 93
0.371 60	0.151 37	0.052 75	0.067 18	0.641 53
0.374 67	0.153 23	0.052 99	0.067 57	0.641 13
0.377 72	0.155 10	0.053 24	0.067 96	0.640 73
0.380 74	0.156 99	0.053 48	0.068 35	0.640 32
0.383 73	0.158 90	0.053 73	0.068 74	0.639 91
0.386 70	0.160 85	0.053 97	0.069 14	0.639 49
0.389 65	0.162 82	0.054 22	0.069 53	0.639 06
0.392 58	0.164 83	0.054 46	0.069 93	0.638 62
0.395 48	0.166 87	0.054 71	0.070 33	0.638 18
0.398 36	0.168 94	0.054 95	0.070 73	0.637 72
0.401 21	0.171 03	0.055 20	0.071 14	0.637 25
0.404 05	0.173 15	0.055 45	0.071 54	0.636 78
0.406 86	0.175 29	0.055 69	0.071 94	0.636 30
0.409 66	0.177 43	0.055 94	0.072 35	0.635 82
0.412 43	0.179 58	0.056 19	0.072 76	0.635 32
0.415 18	0.181 72	0.056 43	0.073 17	0.634 83
0.417 92	0.183 85	0.056 68	0.073 58	0.634 33
0.420 63	0.185 96	0.056 93	0.073 99	0.633 83
0.423 32	0.188 06	0.057 18	0.074 40	0.633 32
0.426 00	0.190 15	0.057 42	0.074 82	0.632 81
0.428 65	0.192 22	0.057 67	0.075 24	0.632 30
0.431 29	0.194 27	0.057 92	0.075 65	0.631 78
0.433 91	0.196 32	0.058 17	0.076 07	0.631 25

Continued on next page

Continued: VLE-Data from GCMC-Simulations of Mixture III at $T^* = 1.05$

x_2^{vap}	x_2^{liq}	p^*_{sat}	$\rho^{*\mathrm{vap}}$	$\rho^{*\mathrm{liq}}$
0.436 51	0.198 36	0.058 42	0.076 50	0.630 72
0.439 09	0.200 40	0.058 67	0.076 92	0.630 19
0.441 65	0.202 46	0.058 92	0.077 35	0.629 64
0.444 19	0.204 53	0.059 17	0.077 78	0.629 08
0.446 72	0.206 62	0.059 42	0.078 21	0.628 51
0.449 23	0.208 73	0.059 67	0.078 64	0.627 93
0.451 72	0.210 88	0.059 92	0.079 07	0.627 33
0.454 19	0.213 06	0.060 17	0.079 51	0.626 72
0.456 65	0.215 27	0.060 42	0.079 95	0.626 11
0.459 09	0.217 51	0.060 67	0.080 38	0.625 48
0.461 52	0.219 79	0.060 93	0.080 83	0.624 84
0.463 93	0.222 09	0.061 18	0.081 27	0.624 20
0.466 32	0.224 41	0.061 43	0.081 72	0.623 55
0.468 71	0.226 76	0.061 68	0.082 16	0.622 89
0.471 07	0.229 11	0.061 94	0.082 61	0.622 24
0.473 42	0.231 46	0.062 19	0.083 06	0.621 59
0.475 76	0.233 82	0.062 44	0.083 52	0.620 95
0.478 08	0.236 16	0.062 69	0.083 97	0.620 31
0.480 39	0.238 50	0.062 95	0.084 43	0.619 67
0.482 68	0.240 82	0.063 20	0.084 89	0.619 05
0.484 96	0.243 12	0.063 45	0.085 35	0.618 44
0.487 23	0.245 40	0.063 71	0.085 81	0.617 83
0.489 48	0.247 65	0.063 96	0.086 27	0.617 24
0.491 72	0.249 89	0.064 22	0.086 74	0.616 66
0.493 95	0.252 10	0.064 47	0.087 21	0.616 08
0.496 16	0.254 30	0.064 72	0.087 68	0.615 52
0.498 35	0.256 48	0.064 98	0.088 16	0.614 96
0.500 54	0.258 64	0.065 24	0.088 63	0.614 41
0.502 70	0.260 79	0.065 49	0.089 11	0.613 86
0.504 86	0.262 92	0.065 75	0.089 60	0.613 32
0.507 00	0.265 05	0.066 00	0.090 08	0.612 77
0.509 13	0.267 18	0.066 26	0.090 57	0.612 23

Continued on next page

Continued: VLE-Data from GCMC-Simulations of Mixture III at $T^* = 1.05$

x_2^{vap}	x_2^{liq}	p^*_{sat}	$\rho^{*\mathrm{vap}}$	$\rho^{*\mathrm{liq}}$
0.511 24	0.269 29	0.066 52	0.091 06	0.611 68
0.513 35	0.271 41	0.066 77	0.091 55	0.611 14
0.515 43	0.273 53	0.067 03	0.092 05	0.610 58
0.517 51	0.275 65	0.067 29	0.092 55	0.610 03
0.519 57	0.277 78	0.067 55	0.093 05	0.609 46
0.521 62	0.279 91	0.067 81	0.093 55	0.608 89
0.523 66	0.282 06	0.068 07	0.094 06	0.608 30
0.525 68	0.284 21	0.068 33	0.094 57	0.607 71
0.527 69	0.286 38	0.068 59	0.095 08	0.607 11
0.529 69	0.288 57	0.068 85	0.095 60	0.606 50
0.531 68	0.290 77	0.069 11	0.096 11	0.605 87
0.533 65	0.292 99	0.069 37	0.096 64	0.605 23
0.535 61	0.295 22	0.069 63	0.097 16	0.604 58
0.537 56	0.297 48	0.069 90	0.097 69	0.603 92
0.539 50	0.299 76	0.070 16	0.098 22	0.603 25
0.541 43	0.302 06	0.070 42	0.098 75	0.602 56
0.543 35	0.304 38	0.070 68	0.099 29	0.601 87
0.545 25	0.306 72	0.070 95	0.099 83	0.601 16
0.547 15	0.309 08	0.071 21	0.100 37	0.600 45
0.549 03	0.311 46	0.071 47	0.100 91	0.599 73
0.550 90	0.313 86	0.071 74	0.101 46	0.599 00
0.552 77	0.316 26	0.072 00	0.102 01	0.598 26
0.554 62	0.318 68	0.072 27	0.102 57	0.597 52
0.556 46	0.321 12	0.072 53	0.103 12	0.596 77
0.558 29	0.323 55	0.072 80	0.103 68	0.596 02
0.560 11	0.326 00	0.073 06	0.104 25	0.595 27
0.561 92	0.328 44	0.073 33	0.104 81	0.594 51
0.563 72	0.330 89	0.073 60	0.105 38	0.593 76
0.565 52	0.333 33	0.073 86	0.105 95	0.593 00
0.567 30	0.335 77	0.074 13	0.106 53	0.592 24
0.569 07	0.338 21	0.074 39	0.107 11	0.591 49
0.570 83	0.340 64	0.074 66	0.107 69	0.590 73

Continued on next page

Continued: VLE-Data from GCMC-Simulations of Mixture III at $T^* = 1.05$

x_2^{vap}	x_2^{liq}	p^*_{sat}	$\rho^{*\mathrm{vap}}$	$\rho^{*\mathrm{liq}}$
0.572 58	0.343 06	0.074 93	0.108 28	0.589 97
0.574 32	0.345 47	0.075 20	0.108 87	0.589 21
0.576 05	0.347 88	0.075 47	0.109 46	0.588 46
0.577 77	0.350 28	0.075 73	0.110 05	0.587 70
0.579 48	0.352 67	0.076 00	0.110 65	0.586 94
0.581 18	0.355 05	0.076 27	0.111 26	0.586 18
0.582 87	0.357 43	0.076 54	0.111 86	0.585 41
0.584 55	0.359 81	0.076 81	0.112 47	0.584 65
0.586 22	0.362 18	0.077 08	0.113 09	0.583 87
0.587 88	0.364 56	0.077 35	0.113 71	0.583 10
0.589 53	0.366 93	0.077 62	0.114 33	0.582 32
0.591 17	0.369 30	0.077 89	0.114 96	0.581 53
0.592 80	0.371 68	0.078 16	0.115 59	0.580 73
0.594 43	0.374 06	0.078 43	0.116 22	0.579 93
0.596 04	0.376 44	0.078 71	0.116 86	0.579 11
0.597 64	0.378 84	0.078 98	0.117 51	0.578 29
0.599 23	0.381 23	0.079 25	0.118 15	0.577 46
0.600 81	0.383 64	0.079 52	0.118 81	0.576 62
0.602 39	0.386 06	0.079 80	0.119 46	0.575 77
0.603 95	0.388 48	0.080 07	0.120 13	0.574 90
0.605 50	0.390 91	0.080 35	0.120 79	0.574 03
0.607 05	0.393 35	0.080 62	0.121 47	0.573 15
0.608 58	0.395 80	0.080 90	0.122 14	0.572 26
0.610 11	0.398 26	0.081 17	0.122 82	0.571 36
0.611 63	0.400 72	0.081 45	0.123 51	0.570 44
0.613 14	0.403 19	0.081 72	0.124 20	0.569 53
0.614 64	0.405 67	0.082 00	0.124 90	0.568 60
0.616 13	0.408 15	0.082 27	0.125 61	0.567 66
0.617 61	0.410 64	0.082 55	0.126 31	0.566 72
0.619 09	0.413 13	0.082 83	0.127 03	0.565 77
0.620 56	0.415 63	0.083 11	0.127 75	0.564 82
0.622 01	0.418 13	0.083 38	0.128 48	0.563 86

Continued on next page

Continued: VLE-Data from GCMC-Simulations of Mixture III at $T^* = 1.05$

x_2^{vap}	x_2^{liq}	p^*_{sat}	$\rho^{*\mathrm{vap}}$	$\rho^{*\mathrm{liq}}$
0.623 46	0.420 63	0.083 66	0.129 21	0.562 89
0.624 90	0.423 13	0.083 94	0.129 95	0.561 93
0.626 34	0.425 64	0.084 22	0.130 70	0.560 95
0.627 76	0.428 15	0.084 50	0.131 45	0.559 97
0.629 19	0.430 66	0.084 78	0.132 20	0.558 98
0.630 60	0.433 17	0.085 06	0.132 97	0.557 99
0.631 99	0.435 69	0.085 34	0.133 75	0.557 00
0.633 38	0.438 20	0.085 62	0.134 53	0.556 01
0.634 77	0.440 72	0.085 90	0.135 33	0.555 01
0.636 14	0.443 23	0.086 18	0.136 13	0.554 00
0.637 50	0.445 75	0.086 46	0.136 94	0.552 99
0.638 86	0.448 26	0.086 74	0.137 77	0.551 98
0.640 21	0.450 78	0.087 03	0.138 59	0.550 96
0.641 56	0.453 30	0.087 31	0.139 42	0.549 91
0.642 90	0.455 81	0.087 59	0.140 27	0.548 87
0.644 22	0.458 33	0.087 88	0.141 12	0.547 82
0.645 53	0.460 84	0.088 16	0.142 00	0.546 77
0.646 83	0.463 35	0.088 44	0.142 88	0.545 71
0.648 16	0.465 87	0.088 73	0.143 75	0.544 61
0.649 45	0.468 38	0.089 02	0.144 65	0.543 52
0.650 73	0.470 89	0.089 30	0.145 57	0.542 42
0.652 00	0.473 40	0.089 59	0.146 49	0.541 31
0.653 24	0.475 90	0.089 87	0.147 46	0.540 21
0.654 49	0.478 41	0.090 16	0.148 41	0.539 08
0.655 72	0.480 93	0.090 45	0.149 38	0.537 93
0.656 98	0.483 45	0.090 74	0.150 34	0.536 74
0.658 20	0.485 97	0.091 03	0.151 34	0.535 57
0.659 41	0.488 50	0.091 32	0.152 35	0.534 37
0.660 59	0.491 02	0.091 61	0.153 40	0.533 18
0.661 78	0.493 56	0.091 90	0.154 44	0.531 95
0.662 93	0.496 10	0.092 19	0.155 53	0.530 74
0.664 12	0.498 67	0.092 48	0.156 58	0.529 45

Continued on next page

Continued: VLE-Data from GCMC-Simulations of Mixture III at $T^* = 1.05$

x_2^{vap}	x_2^{liq}	p^*_{sat}	$\rho^{*\mathrm{vap}}$	$\rho^{*\mathrm{liq}}$
0.665 23	0.501 22	0.092 77	0.157 73	0.528 22
0.666 40	0.503 81	0.093 07	0.158 81	0.526 89
0.667 57	0.506 41	0.093 36	0.159 90	0.525 54
0.668 86	0.509 07	0.093 65	0.160 86	0.524 02
0.669 92	0.511 67	0.093 95	0.162 09	0.522 73
0.671 03	0.514 30	0.094 24	0.163 25	0.521 34
0.672 13	0.516 95	0.094 54	0.164 44	0.519 95
0.673 23	0.519 61	0.094 83	0.165 63	0.518 51
0.674 21	0.522 25	0.095 13	0.166 97	0.517 20
0.675 28	0.524 93	0.095 43	0.168 21	0.515 74
0.676 29	0.527 61	0.095 73	0.169 53	0.514 33
0.677 34	0.530 31	0.096 03	0.170 81	0.512 85
0.678 47	0.533 06	0.096 32	0.172 00	0.511 24
0.679 50	0.535 78	0.096 62	0.173 31	0.509 73
0.680 78	0.538 61	0.096 92	0.174 33	0.507 89
0.681 81	0.541 34	0.097 22	0.175 65	0.506 33
0.682 85	0.544 09	0.097 52	0.176 96	0.504 75
0.683 89	0.546 83	0.097 82	0.178 29	0.503 14
0.684 68	0.549 46	0.098 13	0.179 95	0.501 87
0.685 68	0.552 18	0.098 43	0.181 34	0.500 29
0.687 01	0.555 05	0.098 72	0.182 31	0.498 25
0.688 02	0.557 77	0.099 03	0.183 69	0.496 63
0.688 93	0.560 43	0.099 33	0.185 23	0.495 15
0.689 94	0.563 12	0.099 64	0.186 63	0.493 53
0.691 08	0.565 87	0.099 94	0.187 87	0.491 71
0.691 97	0.568 49	0.100 24	0.189 44	0.490 24
0.692 99	0.571 16	0.100 55	0.190 84	0.488 59
0.693 58	0.573 59	0.100 86	0.192 87	0.487 57
0.694 57	0.576 21	0.101 17	0.194 34	0.485 98
0.696 59	0.579 34	0.101 45	0.194 32	0.482 79
0.697 62	0.581 95	0.101 76	0.195 74	0.481 12
0.698 65	0.584 55	0.102 07	0.197 15	0.479 46

Continued on next page

Continued: VLE-Data from GCMC-Simulations of Mixture III at $T^* = 1.05$

x_2^{vap}	x_2^{liq}	p^*_{sat}	$\rho^{*\mathrm{vap}}$	$\rho^{*\mathrm{liq}}$
0.699 69	0.587 16	0.102 37	0.198 53	0.477 76
0.700 73	0.589 74	0.102 68	0.199 93	0.476 07
0.701 61	0.592 22	0.102 99	0.201 58	0.474 68
0.702 83	0.594 88	0.103 30	0.202 72	0.472 71
0.704 05	0.597 53	0.103 60	0.203 86	0.470 75
0.705 30	0.600 19	0.103 90	0.204 95	0.468 72
0.706 37	0.602 74	0.104 21	0.206 31	0.467 02
0.707 04	0.605 01	0.104 53	0.208 33	0.466 10
0.708 11	0.607 53	0.104 85	0.209 71	0.464 45
0.709 39	0.610 18	0.105 15	0.210 73	0.462 39
0.710 49	0.612 72	0.105 46	0.212 04	0.460 68
0.713 25	0.616 42	0.105 71	0.210 63	0.455 56
0.714 39	0.618 98	0.106 02	0.211 86	0.453 77
0.715 29	0.621 34	0.106 34	0.213 51	0.452 55
0.715 95	0.623 51	0.106 67	0.215 57	0.451 88
0.717 52	0.626 39	0.106 96	0.216 05	0.449 17
0.718 68	0.628 92	0.107 27	0.217 27	0.447 45
0.719 85	0.631 46	0.107 58	0.218 45	0.445 71
0.720 98	0.633 94	0.107 89	0.219 73	0.444 12
0.722 17	0.636 47	0.108 20	0.220 88	0.442 39
0.723 58	0.639 21	0.108 50	0.221 63	0.440 13
0.723 22	0.640 36	0.108 89	0.225 64	0.442 13
0.724 29	0.642 75	0.109 21	0.227 03	0.440 79
0.682 91	0.682 91	0.109 85	0.337 66	0.337 66

Table C.33: VLE-Data from GCMC-Simulations of Mixture III at $T^* = 1.10$

x_2^{vap}	x_2^{liq}	p^*_{sat}	$\rho^{*\mathrm{vap}}$	$\rho^{*\mathrm{liq}}$
0.003 36	0.001 00	0.045 67	0.054 32	0.641 25
0.073 60	0.025 00	0.049 08	0.059 15	0.636 60
0.138 11	0.050 00	0.052 67	0.064 40	0.629 87

Continued on next page

Continued: VLE-Data from GCMC-Simulations of Mixture III at $T^* = 1.10$

x_2^{vap}	x_2^{liq}	p^*_{sat}	$\rho^{*\mathrm{vap}}$	$\rho^{*\mathrm{liq}}$
0.188 71	0.075 00	0.055 83	0.069 17	0.621 31
0.237 84	0.100 00	0.059 24	0.074 47	0.615 06
0.288 22	0.125 00	0.063 26	0.081 02	0.610 07
0.329 75	0.150 00	0.067 10	0.087 56	0.605 90
0.364 99	0.175 00	0.070 77	0.094 09	0.600 26
0.396 14	0.200 00	0.074 38	0.100 83	0.593 59
0.424 87	0.225 00	0.078 08	0.108 17	0.586 12
0.448 04	0.250 00	0.081 35	0.115 17	0.577 86
0.467 35	0.275 00	0.084 27	0.121 84	0.568 21
0.485 73	0.300 00	0.087 22	0.129 07	0.557 70
0.504 21	0.325 00	0.090 43	0.137 60	0.547 07
0.521 76	0.350 00	0.093 79	0.147 42	0.536 22
0.537 39	0.375 00	0.097 18	0.158 42	0.524 56
0.550 76	0.400 00	0.100 51	0.170 76	0.511 80
0.562 78	0.425 00	0.103 73	0.183 29	0.497 61
0.574 00	0.450 00	0.106 89	0.196 07	0.482 93
0.584 81	0.475 00	0.110 10	0.209 81	0.468 85
0.598 08	0.500 00	0.113 08	0.218 70	0.451 66
0.609 92	0.525 00	0.116 85	0.236 12	0.441 24
0.560 97	0.560 97	0.116 19	0.340 38	0.340 38

Table C.34: VLE-Data from GCMC-Simulations of Mixture III at $T^* = 1.15$

x_2^{vap}	x_2^{liq}	p^*_{sat}	$\rho^{*\mathrm{vap}}$	$\rho^{*\mathrm{liq}}$
0.006 92	0.002 56	0.060 09	0.073 54	0.605 15
0.006 92	0.002 56	0.060 09	0.073 54	0.605 15
0.011 08	0.004 17	0.060 34	0.073 92	0.604 44
0.011 08	0.004 17	0.060 34	0.073 92	0.604 44
0.015 21	0.005 78	0.060 59	0.074 30	0.603 84
0.015 21	0.005 78	0.060 59	0.074 30	0.603 84
0.019 31	0.007 38	0.060 85	0.074 68	0.603 31

Continued on next page

Continued: VLE-Data from GCMC-Simulations of Mixture III at $T^* = 1.15$

x_2^{vap}	x_2^{liq}	p^*_{sat}	$\rho^{*\mathrm{vap}}$	$\rho^{*\mathrm{liq}}$
0.019 31	0.007 38	0.060 85	0.074 68	0.603 31
0.023 38	0.008 96	0.061 10	0.075 07	0.602 84
0.023 38	0.008 96	0.061 10	0.075 07	0.602 84
0.027 42	0.010 53	0.061 35	0.075 46	0.602 39
0.027 42	0.010 53	0.061 35	0.075 46	0.602 39
0.031 43	0.012 10	0.061 61	0.075 85	0.601 97
0.031 43	0.012 10	0.061 61	0.075 85	0.601 97
0.035 41	0.013 67	0.061 86	0.076 24	0.601 56
0.035 41	0.013 67	0.061 86	0.076 24	0.601 56
0.039 36	0.015 24	0.062 12	0.076 63	0.601 17
0.039 36	0.015 24	0.062 12	0.076 63	0.601 17
0.043 29	0.016 82	0.062 37	0.077 03	0.600 78
0.043 29	0.016 82	0.062 37	0.077 03	0.600 78
0.047 18	0.018 40	0.062 63	0.077 43	0.600 40
0.047 18	0.018 40	0.062 63	0.077 43	0.600 40
0.051 04	0.019 98	0.062 89	0.077 83	0.600 02
0.051 04	0.019 98	0.062 89	0.077 83	0.600 02
0.054 88	0.021 56	0.063 14	0.078 23	0.599 65
0.054 88	0.021 56	0.063 14	0.078 23	0.599 65
0.058 68	0.023 13	0.063 40	0.078 63	0.599 29
0.058 68	0.023 13	0.063 40	0.078 63	0.599 29
0.062 46	0.024 71	0.063 66	0.079 04	0.598 94
0.062 46	0.024 71	0.063 66	0.079 04	0.598 94
0.066 21	0.026 28	0.063 92	0.079 45	0.598 59
0.066 21	0.026 28	0.063 92	0.079 45	0.598 59
0.069 93	0.027 84	0.064 17	0.079 85	0.598 24
0.069 93	0.027 84	0.064 17	0.079 85	0.598 24
0.073 62	0.029 40	0.064 43	0.080 26	0.597 90
0.073 62	0.029 40	0.064 43	0.080 26	0.597 90
0.077 29	0.030 96	0.064 69	0.080 68	0.597 56
0.077 29	0.030 96	0.064 69	0.080 68	0.597 56
0.080 93	0.032 51	0.064 95	0.081 09	0.597 22

Continued on next page

Continued: VLE-Data from GCMC-Simulations of Mixture III at $T^* = 1.15$

x_2^{vap}	x_2^{liq}	p^*_{sat}	$\rho^{*\mathrm{vap}}$	$\rho^{*\mathrm{liq}}$
0.080 93	0.032 51	0.064 95	0.081 09	0.597 22
0.084 55	0.034 05	0.065 21	0.081 51	0.596 88
0.084 55	0.034 05	0.065 21	0.081 51	0.596 88
0.088 13	0.035 60	0.065 47	0.081 92	0.596 54
0.088 13	0.035 60	0.065 47	0.081 92	0.596 54
0.091 70	0.037 15	0.065 73	0.082 34	0.596 19
0.091 70	0.037 15	0.065 73	0.082 34	0.596 19
0.095 23	0.038 71	0.065 99	0.082 77	0.595 84
0.095 23	0.038 71	0.065 99	0.082 77	0.595 84
0.098 75	0.040 28	0.066 25	0.083 19	0.595 48
0.098 75	0.040 28	0.066 25	0.083 19	0.595 48
0.102 24	0.041 86	0.066 51	0.083 62	0.595 11
0.102 24	0.041 86	0.066 51	0.083 62	0.595 11
0.105 70	0.043 46	0.066 78	0.084 04	0.594 73
0.105 70	0.043 46	0.066 78	0.084 04	0.594 73
0.109 14	0.045 08	0.067 04	0.084 47	0.594 34
0.109 14	0.045 08	0.067 04	0.084 47	0.594 34
0.112 56	0.046 71	0.067 30	0.084 90	0.593 95
0.112 56	0.046 71	0.067 30	0.084 90	0.593 95
0.115 95	0.048 36	0.067 56	0.085 33	0.593 54
0.115 95	0.048 36	0.067 56	0.085 33	0.593 54
0.119 32	0.050 01	0.067 83	0.085 77	0.593 13
0.119 32	0.050 01	0.067 83	0.085 77	0.593 13
0.122 67	0.051 67	0.068 09	0.086 20	0.592 72
0.122 67	0.051 67	0.068 09	0.086 20	0.592 72
0.126 00	0.053 34	0.068 35	0.086 64	0.592 30
0.126 00	0.053 34	0.068 35	0.086 64	0.592 30
0.129 31	0.055 00	0.068 61	0.087 07	0.591 89
0.129 31	0.055 00	0.068 61	0.087 07	0.591 89
0.132 59	0.056 65	0.068 88	0.087 51	0.591 47
0.132 59	0.056 65	0.068 88	0.087 51	0.591 47
0.135 85	0.058 30	0.069 14	0.087 95	0.591 06

Continued on next page

Continued: VLE-Data from GCMC-Simulations of Mixture III at $T^* = 1.15$

x_2^{vap}	x_2^{liq}	p^*_{sat}	$\rho^{*\mathrm{vap}}$	$\rho^{*\mathrm{liq}}$
0.135 85	0.058 30	0.069 14	0.087 95	0.591 06
0.139 09	0.059 94	0.069 40	0.088 39	0.590 65
0.139 09	0.059 94	0.069 40	0.088 39	0.590 65
0.142 31	0.061 56	0.069 67	0.088 84	0.590 25
0.142 31	0.061 56	0.069 67	0.088 84	0.590 25
0.145 51	0.063 16	0.069 93	0.089 28	0.589 85
0.145 51	0.063 16	0.069 93	0.089 28	0.589 85
0.148 69	0.064 75	0.070 20	0.089 73	0.589 46
0.148 69	0.064 75	0.070 20	0.089 73	0.589 46
0.151 84	0.066 32	0.070 46	0.090 18	0.589 08
0.151 84	0.066 32	0.070 46	0.090 18	0.589 08
0.154 98	0.067 88	0.070 73	0.090 63	0.588 70
0.154 98	0.067 88	0.070 73	0.090 63	0.588 70
0.158 10	0.069 42	0.070 99	0.091 09	0.588 33
0.158 10	0.069 42	0.070 99	0.091 09	0.588 33
0.161 19	0.070 94	0.071 26	0.091 55	0.587 96
0.161 19	0.070 94	0.071 26	0.091 55	0.587 96
0.164 27	0.072 45	0.071 52	0.092 01	0.587 60
0.164 27	0.072 45	0.071 52	0.092 01	0.587 60
0.167 32	0.073 94	0.071 79	0.092 47	0.587 24
0.167 32	0.073 94	0.071 79	0.092 47	0.587 24
0.170 35	0.075 43	0.072 06	0.092 94	0.586 88
0.170 35	0.075 43	0.072 06	0.092 94	0.586 88
0.173 37	0.076 91	0.072 33	0.093 41	0.586 52
0.173 37	0.076 91	0.072 33	0.093 41	0.586 52
0.176 36	0.078 38	0.072 60	0.093 88	0.586 15
0.176 36	0.078 38	0.072 60	0.093 88	0.586 15
0.179 34	0.079 86	0.072 87	0.094 36	0.585 79
0.179 34	0.079 86	0.072 87	0.094 36	0.585 79
0.182 29	0.081 34	0.073 14	0.094 84	0.585 42
0.182 29	0.081 34	0.073 14	0.094 84	0.585 42
0.185 22	0.082 83	0.073 41	0.095 32	0.585 04

Continued on next page

Continued: VLE-Data from GCMC-Simulations of Mixture III at $T^* = 1.15$

x_2^{vap}	x_2^{liq}	p^*_{sat}	$\rho^{*\mathrm{vap}}$	$\rho^{*\mathrm{liq}}$
0.185 22	0.082 83	0.073 41	0.095 32	0.585 04
0.188 14	0.084 33	0.073 68	0.095 81	0.584 65
0.188 14	0.084 33	0.073 68	0.095 81	0.584 65
0.191 04	0.085 84	0.073 96	0.096 30	0.584 25
0.191 04	0.085 84	0.073 96	0.096 30	0.584 25
0.193 92	0.087 38	0.074 23	0.096 79	0.583 85
0.193 92	0.087 38	0.074 23	0.096 79	0.583 85
0.196 77	0.088 93	0.074 50	0.097 29	0.583 43
0.196 77	0.088 93	0.074 50	0.097 29	0.583 43
0.199 62	0.090 51	0.074 78	0.097 79	0.583 00
0.199 62	0.090 51	0.074 78	0.097 79	0.583 00
0.202 44	0.092 12	0.075 05	0.098 29	0.582 55
0.202 44	0.092 12	0.075 05	0.098 29	0.582 55
0.205 24	0.093 75	0.075 33	0.098 79	0.582 10
0.205 24	0.093 75	0.075 33	0.098 79	0.582 10
0.208 03	0.095 40	0.075 60	0.099 30	0.581 63
0.208 03	0.095 40	0.075 60	0.099 30	0.581 63
0.210 80	0.097 07	0.075 88	0.099 81	0.581 15
0.210 80	0.097 07	0.075 88	0.099 81	0.581 15
0.213 55	0.098 77	0.076 15	0.100 33	0.580 66
0.213 55	0.098 77	0.076 15	0.100 33	0.580 66
0.216 29	0.100 48	0.076 43	0.100 84	0.580 16
0.216 29	0.100 48	0.076 43	0.100 84	0.580 16
0.219 01	0.102 21	0.076 71	0.101 36	0.579 65
0.219 01	0.102 21	0.076 71	0.101 36	0.579 65
0.221 71	0.103 94	0.076 98	0.101 88	0.579 13
0.221 71	0.103 94	0.076 98	0.101 88	0.579 13
0.224 39	0.105 68	0.077 26	0.102 40	0.578 60
0.224 39	0.105 68	0.077 26	0.102 40	0.578 60
0.227 06	0.107 43	0.077 54	0.102 93	0.578 07
0.227 06	0.107 43	0.077 54	0.102 93	0.578 07
0.229 71	0.109 17	0.077 81	0.103 46	0.577 54

Continued on next page

Continued: VLE-Data from GCMC-Simulations of Mixture III at $T^* = 1.15$

x_2^{vap}	x_2^{liq}	p^*_{sat}	$\rho^{*\mathrm{vap}}$	$\rho^{*\mathrm{liq}}$
0.229 71	0.109 17	0.077 81	0.103 46	0.577 54
0.232 35	0.110 90	0.078 09	0.103 99	0.577 01
0.232 35	0.110 90	0.078 09	0.103 99	0.577 01
0.234 96	0.112 63	0.078 37	0.104 52	0.576 47
0.234 96	0.112 63	0.078 37	0.104 52	0.576 47
0.237 56	0.114 35	0.078 65	0.105 05	0.575 93
0.237 56	0.114 35	0.078 65	0.105 05	0.575 93
0.240 15	0.116 06	0.078 93	0.105 59	0.575 39
0.240 15	0.116 06	0.078 93	0.105 59	0.575 39
0.242 72	0.117 75	0.079 21	0.106 13	0.574 86
0.242 72	0.117 75	0.079 21	0.106 13	0.574 86
0.245 27	0.119 44	0.079 48	0.106 67	0.574 32
0.245 27	0.119 44	0.079 48	0.106 67	0.574 32
0.247 80	0.121 11	0.079 76	0.107 22	0.573 79
0.247 80	0.121 11	0.079 76	0.107 22	0.573 79
0.250 32	0.122 77	0.080 04	0.107 77	0.573 26
0.250 32	0.122 77	0.080 04	0.107 77	0.573 26
0.252 82	0.124 43	0.080 32	0.108 32	0.572 73
0.252 82	0.124 43	0.080 32	0.108 32	0.572 73
0.255 30	0.126 08	0.080 61	0.108 88	0.572 20
0.255 30	0.126 08	0.080 61	0.108 88	0.572 20
0.257 77	0.127 72	0.080 89	0.109 44	0.571 68
0.257 77	0.127 72	0.080 89	0.109 44	0.571 68
0.260 22	0.129 37	0.081 17	0.110 00	0.571 15
0.260 22	0.129 37	0.081 17	0.110 00	0.571 15
0.262 65	0.131 01	0.081 45	0.110 56	0.570 62
0.262 65	0.131 01	0.081 45	0.110 56	0.570 62
0.265 07	0.132 66	0.081 73	0.111 13	0.570 10
0.265 07	0.132 66	0.081 73	0.111 13	0.570 10
0.267 47	0.134 32	0.082 02	0.111 70	0.569 56
0.267 47	0.134 32	0.082 02	0.111 70	0.569 56
0.269 85	0.135 99	0.082 30	0.112 28	0.569 03

Continued on next page

Continued: VLE-Data from GCMC-Simulations of Mixture III at $T^* = 1.15$

x_2^{vap}	x_2^{liq}	p_{sat}^*	$\rho^{*\mathrm{vap}}$	$\rho^{*\mathrm{liq}}$
0.269 85	0.135 99	0.082 30	0.112 28	0.569 03
0.272 22	0.137 67	0.082 58	0.112 86	0.568 49
0.272 22	0.137 67	0.082 58	0.112 86	0.568 49
0.274 57	0.139 36	0.082 87	0.113 44	0.567 94
0.274 57	0.139 36	0.082 87	0.113 44	0.567 94
0.276 91	0.141 07	0.083 15	0.114 03	0.567 38
0.276 91	0.141 07	0.083 15	0.114 03	0.567 38
0.279 23	0.142 79	0.083 44	0.114 62	0.566 82
0.279 23	0.142 79	0.083 44	0.114 62	0.566 82
0.281 53	0.144 53	0.083 72	0.115 21	0.566 24
0.281 53	0.144 53	0.083 72	0.115 21	0.566 24
0.283 82	0.146 29	0.084 01	0.115 81	0.565 65
0.283 82	0.146 29	0.084 01	0.115 81	0.565 65
0.286 10	0.148 07	0.084 29	0.116 41	0.565 05
0.286 10	0.148 07	0.084 29	0.116 41	0.565 05
0.288 36	0.149 86	0.084 58	0.117 02	0.564 44
0.288 36	0.149 86	0.084 58	0.117 02	0.564 44
0.290 60	0.151 66	0.084 87	0.117 62	0.563 81
0.290 60	0.151 66	0.084 87	0.117 62	0.563 81
0.292 84	0.153 48	0.085 15	0.118 24	0.563 16
0.292 84	0.153 48	0.085 15	0.118 24	0.563 16
0.295 05	0.155 31	0.085 44	0.118 85	0.562 50
0.295 05	0.155 31	0.085 44	0.118 85	0.562 50
0.297 26	0.157 15	0.085 73	0.119 47	0.561 82
0.297 26	0.157 15	0.085 73	0.119 47	0.561 82
0.299 44	0.159 00	0.086 01	0.120 10	0.561 13
0.299 44	0.159 00	0.086 01	0.120 10	0.561 13
0.301 62	0.160 86	0.086 30	0.120 72	0.560 42
0.301 62	0.160 86	0.086 30	0.120 72	0.560 42
0.303 78	0.162 72	0.086 59	0.121 36	0.559 69
0.303 78	0.162 72	0.086 59	0.121 36	0.559 69
0.305 93	0.164 59	0.086 88	0.121 99	0.558 95

Continued on next page

Continued: VLE-Data from GCMC-Simulations of Mixture III at $T^* = 1.15$

x_2^{vap}	x_2^{liq}	p^*_{sat}	$\rho^{*\mathrm{vap}}$	$\rho^{*\mathrm{liq}}$
0.305 93	0.164 59	0.086 88	0.121 99	0.558 95
0.308 06	0.166 46	0.087 17	0.122 63	0.558 20
0.308 06	0.166 46	0.087 17	0.122 63	0.558 20
0.310 18	0.168 33	0.087 45	0.123 28	0.557 43
0.310 18	0.168 33	0.087 45	0.123 28	0.557 43
0.312 29	0.170 21	0.087 74	0.123 93	0.556 65
0.312 29	0.170 21	0.087 74	0.123 93	0.556 65
0.314 38	0.172 08	0.088 03	0.124 58	0.555 86
0.314 38	0.172 08	0.088 03	0.124 58	0.555 86
0.316 46	0.173 96	0.088 32	0.125 24	0.555 06
0.316 46	0.173 96	0.088 32	0.125 24	0.555 06
0.318 53	0.175 83	0.088 61	0.125 91	0.554 25
0.318 53	0.175 83	0.088 61	0.125 91	0.554 25
0.320 58	0.177 71	0.088 90	0.126 58	0.553 43
0.320 58	0.177 71	0.088 90	0.126 58	0.553 43
0.322 64	0.179 59	0.089 19	0.127 23	0.552 58
0.322 64	0.179 59	0.089 19	0.127 23	0.552 58
0.324 67	0.181 47	0.089 48	0.127 91	0.551 75
0.324 67	0.181 47	0.089 48	0.127 91	0.551 75
0.326 69	0.183 35	0.089 77	0.128 59	0.550 91
0.326 69	0.183 35	0.089 77	0.128 59	0.550 91
0.328 69	0.185 23	0.090 06	0.129 28	0.550 06
0.328 69	0.185 23	0.090 06	0.129 28	0.550 06
0.330 68	0.187 12	0.090 35	0.129 98	0.549 22
0.330 68	0.187 12	0.090 35	0.129 98	0.549 22
0.332 65	0.189 01	0.090 64	0.130 69	0.548 37
0.332 65	0.189 01	0.090 64	0.130 69	0.548 37
0.334 61	0.190 91	0.090 93	0.131 40	0.547 51
0.334 61	0.190 91	0.090 93	0.131 40	0.547 51
0.336 56	0.192 81	0.091 23	0.132 11	0.546 65
0.336 56	0.192 81	0.091 23	0.132 11	0.546 65
0.338 50	0.194 72	0.091 52	0.132 83	0.545 78

Continued on next page

Continued: VLE-Data from GCMC-Simulations of Mixture III at $T^* = 1.15$

x_2^{vap}	x_2^{liq}	p^*_{sat}	$\rho^{*\mathrm{vap}}$	$\rho^{*\mathrm{liq}}$
0.338 50	0.194 72	0.091 52	0.132 83	0.545 78
0.340 42	0.196 63	0.091 81	0.133 56	0.544 91
0.340 42	0.196 63	0.091 81	0.133 56	0.544 91
0.342 33	0.198 56	0.092 10	0.134 29	0.544 03
0.342 33	0.198 56	0.092 10	0.134 29	0.544 03
0.344 22	0.200 49	0.092 40	0.135 04	0.543 15
0.344 22	0.200 49	0.092 40	0.135 04	0.543 15
0.346 10	0.202 43	0.092 69	0.135 79	0.542 26
0.346 10	0.202 43	0.092 69	0.135 79	0.542 26
0.347 97	0.204 39	0.092 98	0.136 55	0.541 37
0.347 97	0.204 39	0.092 98	0.136 55	0.541 37
0.349 83	0.206 35	0.093 28	0.137 32	0.540 47
0.349 83	0.206 35	0.093 28	0.137 32	0.540 47
0.351 67	0.208 33	0.093 57	0.138 09	0.539 55
0.351 67	0.208 33	0.093 57	0.138 09	0.539 55
0.353 56	0.210 33	0.093 86	0.138 80	0.538 57
0.353 56	0.210 33	0.093 86	0.138 80	0.538 57
0.355 38	0.212 33	0.094 16	0.139 59	0.537 63
0.355 38	0.212 33	0.094 16	0.139 59	0.537 63
0.357 19	0.214 35	0.094 45	0.140 38	0.536 69
0.357 19	0.214 35	0.094 45	0.140 38	0.536 69
0.358 99	0.216 37	0.094 75	0.141 17	0.535 71
0.358 99	0.216 37	0.094 75	0.141 17	0.535 71
0.360 78	0.218 41	0.095 04	0.141 98	0.534 74
0.360 78	0.218 41	0.095 04	0.141 98	0.534 74
0.362 54	0.220 46	0.095 34	0.142 79	0.533 76
0.362 54	0.220 46	0.095 34	0.142 79	0.533 76
0.364 28	0.222 52	0.095 63	0.143 64	0.532 79
0.364 28	0.222 52	0.095 63	0.143 64	0.532 79
0.366 04	0.224 59	0.095 93	0.144 46	0.531 76
0.366 04	0.224 59	0.095 93	0.144 46	0.531 76
0.367 74	0.226 67	0.096 23	0.145 32	0.530 77

Continued on next page

Continued: VLE-Data from GCMC-Simulations of Mixture III at $T^* = 1.15$

x_2^{vap}	x_2^{liq}	p^*_{sat}	$\rho^{*\mathrm{vap}}$	$\rho^{*\mathrm{liq}}$
0.367 74	0.226 67	0.096 23	0.145 32	0.530 77
0.369 48	0.228 76	0.096 52	0.146 16	0.529 72
0.369 48	0.228 76	0.096 52	0.146 16	0.529 72
0.371 18	0.230 86	0.096 82	0.147 02	0.528 68
0.371 18	0.230 86	0.096 82	0.147 02	0.528 68
0.372 87	0.232 97	0.097 11	0.147 89	0.527 64
0.372 87	0.232 97	0.097 11	0.147 89	0.527 64
0.374 54	0.235 08	0.097 41	0.148 78	0.526 58
0.374 54	0.235 08	0.097 41	0.148 78	0.526 58
0.376 19	0.237 19	0.097 71	0.149 69	0.525 54
0.376 19	0.237 19	0.097 71	0.149 69	0.525 54
0.377 82	0.239 31	0.098 01	0.150 61	0.524 49
0.377 82	0.239 31	0.098 01	0.150 61	0.524 49
0.379 45	0.241 43	0.098 30	0.151 53	0.523 42
0.379 45	0.241 43	0.098 30	0.151 53	0.523 42
0.381 11	0.243 57	0.098 60	0.152 41	0.522 31
0.381 11	0.243 57	0.098 60	0.152 41	0.522 31
0.382 76	0.245 70	0.098 90	0.153 30	0.521 20
0.382 76	0.245 70	0.098 90	0.153 30	0.521 20
0.384 68	0.247 92	0.099 19	0.153 87	0.519 78
0.384 68	0.247 92	0.099 19	0.153 87	0.519 78
0.386 29	0.250 05	0.099 49	0.154 80	0.518 69
0.386 29	0.250 05	0.099 49	0.154 80	0.518 69
0.387 89	0.252 18	0.099 79	0.155 74	0.517 59
0.387 89	0.252 18	0.099 79	0.155 74	0.517 59
0.389 46	0.254 30	0.100 09	0.156 70	0.516 51
0.389 46	0.254 30	0.100 09	0.156 70	0.516 51
0.391 07	0.256 43	0.100 38	0.157 61	0.515 37
0.391 07	0.256 43	0.100 38	0.157 61	0.515 37
0.392 63	0.258 55	0.100 68	0.158 57	0.514 28
0.392 63	0.258 55	0.100 68	0.158 57	0.514 28
0.394 22	0.260 67	0.100 98	0.159 51	0.513 15

Continued on next page

Continued: VLE-Data from GCMC-Simulations of Mixture III at $T^* = 1.15$

x_2^{vap}	x_2^{liq}	p^*_{sat}	$\rho^{*\mathrm{vap}}$	$\rho^{*\mathrm{liq}}$
0.394 22	0.260 67	0.100 98	0.159 51	0.513 15
0.395 69	0.262 76	0.101 28	0.160 58	0.512 15
0.395 69	0.262 76	0.101 28	0.160 58	0.512 15
0.397 21	0.264 86	0.101 58	0.161 58	0.511 07
0.397 21	0.264 86	0.101 58	0.161 58	0.511 07
0.398 70	0.266 94	0.101 88	0.162 62	0.510 02
0.398 70	0.266 94	0.101 88	0.162 62	0.510 02
0.400 24	0.269 04	0.102 18	0.163 59	0.508 91
0.400 24	0.269 04	0.102 18	0.163 59	0.508 91
0.401 73	0.271 12	0.102 48	0.164 63	0.507 85
0.401 73	0.271 12	0.102 48	0.164 63	0.507 85
0.403 35	0.273 24	0.102 78	0.165 51	0.506 62
0.403 35	0.273 24	0.102 78	0.165 51	0.506 62
0.404 72	0.275 28	0.103 08	0.166 68	0.505 68
0.404 72	0.275 28	0.103 08	0.166 68	0.505 68
0.406 25	0.277 36	0.103 38	0.167 66	0.504 53
0.406 25	0.277 36	0.103 38	0.167 66	0.504 53
0.407 67	0.279 42	0.103 68	0.168 77	0.503 50
0.407 67	0.279 42	0.103 68	0.168 77	0.503 50
0.409 42	0.281 57	0.103 98	0.169 47	0.502 06
0.409 42	0.281 57	0.103 98	0.169 47	0.502 06
0.410 85	0.283 63	0.104 28	0.170 56	0.500 99
0.410 85	0.283 63	0.104 28	0.170 56	0.500 99
0.412 25	0.285 68	0.104 59	0.171 69	0.499 94
0.412 25	0.285 68	0.104 59	0.171 69	0.499 94
0.413 66	0.287 73	0.104 89	0.172 81	0.498 87
0.413 66	0.287 73	0.104 89	0.172 81	0.498 87
0.415 06	0.289 78	0.105 20	0.173 94	0.497 79
0.415 06	0.289 78	0.105 20	0.173 94	0.497 79
0.416 52	0.291 86	0.105 50	0.174 99	0.496 62
0.416 52	0.291 86	0.105 50	0.174 99	0.496 62
0.417 86	0.293 90	0.105 80	0.176 19	0.495 57

Continued on next page

Continued: VLE-Data from GCMC-Simulations of Mixture III at $T^* = 1.15$

x_2^{vap}	x_2^{liq}	p^*_{sat}	$\rho^{*\mathrm{vap}}$	$\rho^{*\mathrm{liq}}$
0.417 86	0.293 90	0.105 80	0.176 19	0.495 57
0.419 23	0.295 96	0.106 11	0.177 35	0.494 47
0.419 23	0.295 96	0.106 11	0.177 35	0.494 47
0.420 59	0.298 02	0.106 42	0.178 53	0.493 38
0.420 59	0.298 02	0.106 42	0.178 53	0.493 38
0.421 93	0.300 08	0.106 72	0.179 73	0.492 28
0.421 93	0.300 08	0.106 72	0.179 73	0.492 28
0.423 18	0.302 12	0.107 03	0.181 05	0.491 27
0.423 18	0.302 12	0.107 03	0.181 05	0.491 27
0.424 61	0.304 22	0.107 34	0.182 14	0.490 04
0.424 61	0.304 22	0.107 34	0.182 14	0.490 04
0.426 07	0.306 35	0.107 64	0.183 18	0.488 74
0.426 07	0.306 35	0.107 64	0.183 18	0.488 74
0.427 37	0.308 43	0.107 95	0.184 42	0.487 61
0.427 37	0.308 43	0.107 95	0.184 42	0.487 61
0.428 67	0.310 52	0.108 26	0.185 67	0.486 47
0.428 67	0.310 52	0.108 26	0.185 67	0.486 47
0.430 03	0.312 63	0.108 57	0.186 85	0.485 25
0.430 03	0.312 63	0.108 57	0.186 85	0.485 25
0.431 31	0.314 73	0.108 88	0.188 12	0.484 11
0.431 31	0.314 73	0.108 88	0.188 12	0.484 11
0.432 60	0.316 84	0.109 19	0.189 39	0.482 95
0.432 60	0.316 84	0.109 19	0.189 39	0.482 95
0.434 58	0.319 24	0.109 49	0.189 68	0.480 85
0.434 58	0.319 24	0.109 49	0.189 68	0.480 85
0.435 62	0.321 26	0.109 80	0.191 28	0.480 00
0.435 62	0.321 26	0.109 80	0.191 28	0.480 00
0.436 89	0.323 39	0.110 12	0.192 57	0.478 84
0.436 89	0.323 39	0.110 12	0.192 57	0.478 84
0.438 15	0.325 51	0.110 43	0.193 87	0.477 68
0.438 15	0.325 51	0.110 43	0.193 87	0.477 68
0.439 12	0.327 53	0.110 75	0.195 58	0.476 90

Continued on next page

Continued: VLE-Data from GCMC-Simulations of Mixture III at $T^* = 1.15$

x_2^{vap}	x_2^{liq}	p^*_{sat}	$\rho^{*\mathrm{vap}}$	$\rho^{*\mathrm{liq}}$
0.439 12	0.327 53	0.110 75	0.195 58	0.476 90
0.440 57	0.329 74	0.111 06	0.196 61	0.475 48
0.440 57	0.329 74	0.111 06	0.196 61	0.475 48
0.441 81	0.331 88	0.111 37	0.197 92	0.474 33
0.441 81	0.331 88	0.111 37	0.197 92	0.474 33
0.445 49	0.335 16	0.111 61	0.195 66	0.469 53
0.445 49	0.335 16	0.111 61	0.195 66	0.469 53
0.446 72	0.337 30	0.111 93	0.196 96	0.468 40
0.446 72	0.337 30	0.111 93	0.196 96	0.468 40
0.448 02	0.339 48	0.112 24	0.198 16	0.467 17
0.448 02	0.339 48	0.112 24	0.198 16	0.467 17
0.449 31	0.341 65	0.112 55	0.199 38	0.465 96
0.449 31	0.341 65	0.112 55	0.199 38	0.465 96
0.450 74	0.343 89	0.112 86	0.200 39	0.464 53
0.450 74	0.343 89	0.112 86	0.200 39	0.464 53
0.451 80	0.345 94	0.113 18	0.201 93	0.463 71
0.451 80	0.345 94	0.113 18	0.201 93	0.463 71
0.452 99	0.348 05	0.113 50	0.203 30	0.462 71
0.452 99	0.348 05	0.113 50	0.203 30	0.462 71
0.454 17	0.350 14	0.113 81	0.204 68	0.461 72
0.454 17	0.350 14	0.113 81	0.204 68	0.461 72
0.455 34	0.352 23	0.114 13	0.206 05	0.460 76
0.455 34	0.352 23	0.114 13	0.206 05	0.460 76
0.456 23	0.354 17	0.114 46	0.207 86	0.460 25
0.456 23	0.354 17	0.114 46	0.207 86	0.460 25
0.457 37	0.356 21	0.114 78	0.209 30	0.459 36
0.457 37	0.356 21	0.114 78	0.209 30	0.459 36
0.458 22	0.358 11	0.115 11	0.211 18	0.458 94
0.458 22	0.358 11	0.115 11	0.211 18	0.458 94
0.460 39	0.360 70	0.115 39	0.210 96	0.456 43
0.460 39	0.360 70	0.115 39	0.210 96	0.456 43
0.461 80	0.362 87	0.115 70	0.211 95	0.455 14

Continued on next page

Continued: VLE-Data from GCMC-Simulations of Mixture III at $T^* = 1.15$

x_2^{vap}	x_2^{liq}	p^*_{sat}	$\rho^{*\mathrm{vap}}$	$\rho^{*\mathrm{liq}}$
0.461 80	0.362 87	0.115 70	0.211 95	0.455 14
0.463 04	0.364 95	0.116 02	0.213 19	0.454 15
0.463 04	0.364 95	0.116 02	0.213 19	0.454 15
0.464 16	0.366 94	0.116 34	0.214 63	0.453 37
0.464 16	0.366 94	0.116 34	0.214 63	0.453 37
0.465 69	0.369 18	0.116 65	0.215 35	0.451 89
0.465 69	0.369 18	0.116 65	0.215 35	0.451 89
0.467 10	0.371 32	0.116 96	0.216 31	0.450 66
0.467 10	0.371 32	0.116 96	0.216 31	0.450 66
0.468 33	0.373 34	0.117 28	0.217 54	0.449 75
0.468 33	0.373 34	0.117 28	0.217 54	0.449 75
0.469 12	0.375 09	0.117 61	0.219 52	0.449 61
0.469 12	0.375 09	0.117 61	0.219 52	0.449 61
0.470 33	0.377 08	0.117 93	0.220 78	0.448 75
0.470 33	0.377 08	0.117 93	0.220 78	0.448 75
0.472 07	0.379 37	0.118 23	0.221 16	0.447 02
0.472 07	0.379 37	0.118 23	0.221 16	0.447 02
0.473 94	0.381 77	0.118 52	0.221 27	0.445 01
0.473 94	0.381 77	0.118 52	0.221 27	0.445 01
0.475 17	0.383 74	0.118 84	0.222 48	0.444 16
0.475 17	0.383 74	0.118 84	0.222 48	0.444 16
0.476 40	0.385 71	0.119 16	0.223 68	0.443 32
0.476 40	0.385 71	0.119 16	0.223 68	0.443 32
0.477 34	0.387 49	0.119 49	0.225 35	0.443 01
0.477 34	0.387 49	0.119 49	0.225 35	0.443 01
0.478 20	0.389 20	0.119 83	0.227 18	0.442 85
0.478 20	0.389 20	0.119 83	0.227 18	0.442 85
0.479 41	0.391 14	0.120 16	0.228 38	0.442 07
0.479 41	0.391 14	0.120 16	0.228 38	0.442 07
0.478 75	0.391 91	0.120 58	0.232 82	0.444 41
0.478 75	0.391 91	0.120 58	0.232 82	0.444 41
0.481 32	0.394 64	0.120 83	0.231 68	0.441 44

Continued on next page

Continued: VLE-Data from GCMC-Simulations of Mixture III at $T^* = 1.15$

x_2^{vap}	x_2^{liq}	p_{sat}^*	$\rho^{*\mathrm{vap}}$	$\rho^{*\mathrm{liq}}$
0.481 32	0.394 64	0.120 83	0.231 68	0.441 44
0.482 73	0.396 68	0.121 14	0.232 52	0.440 35
0.482 73	0.396 68	0.121 14	0.232 52	0.440 35
0.441 44	0.441 44	0.121 59	0.333 78	0.333 78
0.441 44	0.441 44	0.121 59	0.333 78	0.333 78